Surface and Electrical Characterization of Conjugated Molecular Wires

A DISSERTATION
SUBMITTED TO THE FACULTY OF THE GRADUATE SCHOOL OF THE
UNIVERSITY OF MINNESOTA
BY

Abel Tesfahun Demissie

IN PARTIAL FULFILLMENT OF THE REQUIREMENTS
FOR THE DEGREE OF
DOCTOR OF PHILOSOPHY

Prof. C. Daniel Frisbie

October, 2016

Acknowledgments

I would like to thank my advisor, Prof. C. Daniel Frisbie for providing me an opportunity to conduct research in his group. The toughest challenge any graduate student in PhD program encounters is the decision whom to work for, because it directly impacts the successful completion of a PhD degree verses others. I am very thankful for the continuous encouragement, advice, and support that Dan has provided me in order to accomplish my thesis. His enthusiasm in discussing good and not-so good data has challenged me to push myself above and beyond. Despite dealing with all of the department business associated with being the department head, he always found time to meet with his students, and to visit labs more frequently. He also gave me an invaluable help in writing manuscripts, preparing presentations, and recommendations for future career plans.

I would also like to thank Dr. Greg Haugstad for all his help with the ion beam analysis experiments. I am very grateful for all of the scientific exchanges, and help with RBS and NRA experiments which are very crucial contributions to this document. I would also like to thank researchers at the National University of Singapore; Prof. Christian Nijhuis, Dr. Suchand Sangeeth, Dr. Li Yuan, and Mr. Tao Wang. I am very pleased with the successful outcome of our experiments.

I would also like to acknowledge funding sources from NSF, IPRIME, and MRSEC.

I owe a debt of gratitude to past and current Frisbie group members: Dr. Liang Luo, Dr. Zuoti Xie, Dr. Davood Taherinia, Dr. Christopher Smith, Dr. Stuart Oram, Dr. Ankit Mahajan, Dr. Wei Xie, Dr. Yanfei Wu, Elliot Schmidt, Scott White, Xinglong Ren, Boxin Tang, Motao Cao, Fazel Bidoky, Chang-Hyun Kim, Dr. Bryan Paulsen, Dr. Tao He, Bonssa Teizazu, Dr. Geoff Rojas, Yan Wang and others. I would like to thank all of them for taking pains in maintaining our lab equipment and facilities that made this project possible. I would also like to acknowledge all of the characterization facility and clean room staff members, especially Dr. Bing Luo, Mr, Paul Kimani, Mr. Kevin Roberts, and Mr. Mark Fisher for all their support and useful discussion regarding equipments.

Lastly, I would like to thank my family for their continuous support and motivation to help me get through difficult times. I especially would like to acknowledge my wife Etu for her unyielding encouragement and support, and for understanding the rigorous time demands of graduate school. I would like to dedicate this thesis to my parents who made sure that my dreams and aspirations would not be decided by an ethnocentric government of Ethiopia. I would like to thank Mahi, Meron, Pomy, Sly, Oli, Mely, Roman, Miza, Bini, Zizi, Soli, Martha, Ezra, Hana, Mesfin, Dr. Solomon, Mimi, Dr. Story, Dr. Brown, and Dr. Lawrence for their support and encouragement.

Dedicated to

my mom and dad who made sacrifices for my success

Abstract

This thesis describes the surface and electrical characterization of ultrathin organic films and interfaces. These films were synthesized on the surface of gold by utilizing layer by layer synthesis via imine condensation. Film growth by imine click (condensation) chemistry is particularly useful for molecular electronics experiments because it provides a convenient means to obtain and extend π-conjugation in the growth direction. However, in the context of film growth from a solid substrate, the reaction yield per step has not been characterized previously, though it is critically important. To address these issues, my research focused on a comprehensive characterization of oligophenyleneimine (OPI) wires via Rutherford backscattering spectrometry (RBS), X-ray photoelectron spectroscopy (XPS), spectroscopic ellipsometry (SE), reflection-absorption infrared spectroscopy (RAIRS), and cyclic voltammetry (CV). In addition, we had the unique opportunity of developing the first of its kind implementation of nuclear reaction analysis (NRA) to probe the intensity of carbon atoms after each addition step. Overall the combination of various techniques indicated that film growth proceeds in a quantitative manner. Furthermore, the NRA experiment was optimized to measure the carbon content in self-assembled monolayers of alkyl thiols. The results indicated well-resolved coverage values for ultrathin films with consecutive steps of 2 carbon atoms per molecule.

Another fundamental problem in molecular electronics is the vast discrepancy in the values of measured resistance per molecule between small and large area molecular junctions. In collaboration with researchers at the National University of Singapore, we addressed these issues by comparing the electrical properties of OPI wires with the

eutectic gallium indium alloy (EGaIn) junction (1000 μm^2), and conducting probe atomic force microscopy (CP-AFM) junction (50 nm^2). Our results showed that intensive (i.e., area independent) observables such as crossover length, activation energy, and decay constants agreed very well across the two junction platforms. On the other hand, the extensive (area dependent) resistance per molecule values was 100 times higher for EGaIn junction verses CP-AFM after normalizing to contact area. This was most likely due to differences in metal-molecule contact resistances. *My contribution to this collaborative work is in synthesis and timely delivery of OPI wires.*

The structure-property relationships of OPI wires with 5 terminal F atoms were studied extensively by XPS. The results show similar crossover behavior obtained by molecular junction experiments. Saturated spacers (conjugation disruption units) were introduced into the molecular backbone, and their effects on the intensity of F 1s counts were measured. Overall, there was good correlation between the position and number of saturated units verses F 1s peak area. Even though core hole spectroscopy and time dependent density functional theory (TDDFT) calculations are required to fully understand the charge transport dynamics, the preliminary results point to a new ultrahigh vacuum method of measuring charge transfer rates. Overall, these experiments open significant opportunities to synthesize ultra-thin films and characterize a variety of donor-block-acceptor and metal complex systems in molecular electronics.

Table of Contents

List of Figures and Tables

1. Molecular Wires

One of the first to coin the term molecular wire is Jean-Marie Lehn, the 1988 Chemistry Nobel prize winner, who described a caroviologen molecule where charges can easily transfer through conjugated pathways between the terminal groups of the molecule as shown below.[1,2]

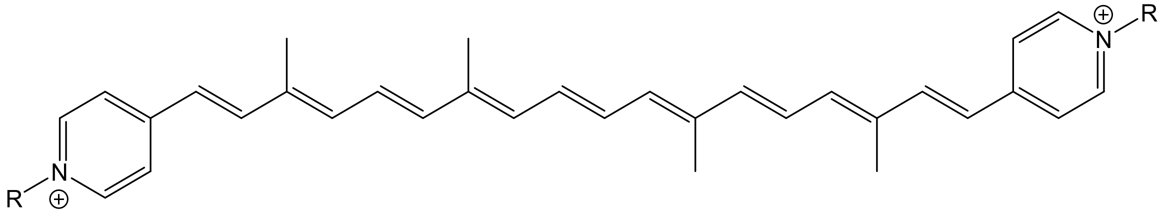

Figure 1.1 Caroviologen trans-membrane molecular wire proposed by Lehn.

However, the definition of the term "molecular wire" is still controversial. It ranges from description of a specific behavior of a system to the structural parameters of the molecules examined.[1] Nitzan and Ratner defined molecular wire as a molecule that conducts electrical current between two electrodes.[3] Wasielewski defined molecular wires as a device that conducts in a regime, wherein the distance dependence of electron transfer (ET) may be very weak.[4] The former definition applies well for the systems investigated in this thesis, whereas the latter is appropriate for ultrafast spectroscopy of photoinduced ET experiments.

In the context of molecular electronics, the study of fundamental charge transport through molecular wires is an important research topic. *Molecular electronics is defined as the field of science that investigates the electronic and thermal properties of circuits in which the individual molecules or an assembly of molecules are used as building blocks*.[5] The concept of using organic molecules as active components in electrical junctions was proposed by Aviram and Ratner in 1974.[6] As the demands for high density circuitry of conventional top down reaches its technical limit, many researchers believe or speculate that molecular electronics will be an alternative solution.[5,7,8] This currently seems like an ambitious goal because an emerging technology without fundamental understanding of mechanisms that govern charge transport is impractical. Nevertheless, molecular electronics in principle offers the following advantages[5]:

1) *Size*. Molecules are inherently small (0.5 – 10 nm). The current state of the art 14 nm Fin field effect transistors have 42 nm pitch width.[9] Due to their small size, molecules can lead to higher packing density.
2) *Synthesis tailorability*. The tools of molecular synthesis are well developed thanks to organic chemistry. Thus, the effects of molecular geometry and composition on charge transport can be largely explored.
3) *Speed*. Although most of the molecules investigated to date have poor conductivities in comparison to metals and inorganic semiconductors, new molecular wires with very high conductivities have been reported recently.[10] Thus, the transient time can be reduced.
4) *Assembly and recognition*. Specific intermolecular interaction and chemisorption to surfaces can be used to form structures by nanoscale assembly. Furthermore, switching and sensing capabilities can be realized by modifying the electronic behavior via molecular recognition (For example, DNA sensors).
5) *New functionalities*. The study of charge transport properties of stable isotopes and isomers could lead to new electronic functionality that has not been explored.

There are dozens of techniques to study charge transport through molecular wires. They can generally be classified into 3 categories[1]: molecular junctions, photo-induced electron transfer, and theoretical Landauer approach. In molecular junctions, a single molecule or arrays of molecules are connected between two metal electrodes as shown in Figure 1.2. Some examples of molecular testbeds include but not limited to; break junction,[11,12] the conducting probe atomic force microscope (CP-AFM),[13] the scanning tunneling microscope,[14] the eutectic gallium indium alloy (EGaIn) junction,[15–17] the Hg drop junction,[18,19] the conducting polymer junction,[20,21] the surface diffusion mediated junction,[22] and others. The ability to contact molecules easily and reproducibly as a function of length, bias, architecture, temperature and surface linkers has led to exciting discoveries in single molecules (or an ensemble of single molecules) such as; Coulomb blockade,[23] Kondo resistance,[24] switching,[25] negative differential resistance,[26] and rectification.[27] However, when the measured resistances are normalized to single molecule resistance, there are vast differences among the different types of molecular junctions; thus, creating a huge controversy in molecular electronics. Akkerman et al., reviewed this topic and found that large area junctions (10^3 – 10^{12} molecules) have

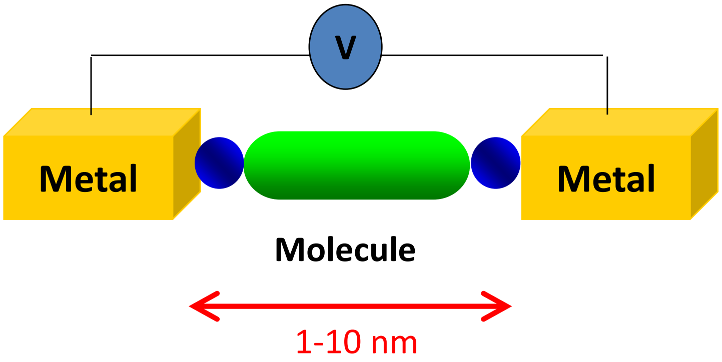

Figure 1.2 Schematic illustration of a metal-molecule-metal junction.

consistently larger single molecule resistance of up to 8-9 orders of magnitude than small area junctions (1-10^2 molecules) for a given molecular structure.[28] For this reason, one of the central questions in molecular electronics is: “How reproducible are the electrical characteristics for a given molecular architecture across different types of junctions?” To address this issue, I and my coworkers compared prior CP-AFM and new EGaIn measurements on conjugated oligophenylene imine (OPI) wires. We were able to explain the vast discrepancy of the resistance per molecule values to contact resistance and effective contact area. On the other hand, area intensive quantities agreed very well.

The stepwise growth of OPI wires was first reported by Rosink et al.[29] Film synthesis began with a self-assembled monolayer (SAM) of 4-aminothiophenol on Au, followed by repetitive, alternate addition of terephthalaldehyde (benzene-1,4-dicarbaldehyde) or 1,4-benzenediamine to form π-conjugated films ranging from 0.6 – 7.5 nm in length.[29] In their pioneering work, Choi et al., showed the crossover from tunneling to hopping transport of OPI wires near 4 nm via CP-AFM junction.[30] The crossover was also confirmed by variable temperature direct current (DC) measurements, which revealed thermally activated hopping transport for long wires, and thermally inactivated tunneling transport for short wires. However, in the context of film growth from a solid substrate, the reaction yield per step and surface coverage (molecules per unit area) have not been characterized previously, though it is critically important.[30–34] For example, a 90 % yield for each step can give rise to undesirable dispersity such that any measured transport properties cannot be assigned to a monodisperse system. Thus, central questions for film synthesis via stepwise approach are: “What is the reaction yield and surface coverage of each growth? How do we optimize the reaction yield to obtain monodisperse system?" To address these issues, I and my coworkers utilized a battery of surface characterization tools. We also demonstrated the first of its kind implementation of nuclear reaction analysis (NRA) to calculate surface coverage of C atoms after each growth step.

The vast majority of work in my thesis builds upon decades of prior work on DC transport and solution ET measurements process. Even though both experiments are different, they yield complimentary results. In DC transport, charges are injected from one electrode, and driven to the other contact by the applied potential (electric field). The amount of charges injected is controlled by the overlap of the wire frontier orbitals with the electrode, and applied bias. In solution ET experiments, charge transfer is induced by photo excitation of an electron from HOMO to LUMO level, and the resulting charge separation and recombination rates are measured by transient absorption and fluorescence spectroscopy.[35] Elegant examples of the influence of length, conjugation, electron affinity of bridge unit between donor and acceptor moieties on ET studies are available.[36–38] Ultimately a better picture of conduction gained through both DC and ET experiments will aid in design of π conjugated polymers for improved device performance in solar cells, thin film transistors, and diodes.

1.1 Thesis Overview

My dissertation focuses on two important topics – surface and electrical characterization of OPI wires. In particular it involves demonstrating a comprehensive characterization of surface coverage and reaction yield for each growth step, which are important in establishing structure-property relationships. These experiments directly address the effectiveness of Schiff base chemistry in synthesizing long π conjugated wires on metal platforms, which are crucial for probing the physical chemistry of charge conduction. Furthermore, the methods employed can be extended to other stepwise growth such as cycloaddition, and knovenagel condensation. Our unique approach to calculate the surface coverage of C atoms was extended to characterization of alkyl thiol self-assembled monolayers (SAMs), the most commonly studied benchmark systems in molecular junctions. Our results indicated that NRA is impressively sensitive, up to increments of 2 C atoms per monolayer.

The DC and alternating current (AC) electrical transport behaviors of OPI wires were studied by EGaIn junctions. The area intensive transport properties such as cross over length, slope, and activation energy agreed very well with prior CP-AFM measurements. The area extensive property such as resistance per molecule varied by two orders of magnitude after normalizing to effective contact area primarily due to contact resistance. It is gratifying that these different molecular junctions that vary by orders of magnitude in the total size of molecules probed (10^2 for CP-AFM vs 10^9 for EGaIn) can give such similar results. It also established the utility of OPI wires as excellent platforms when comparing different testbeds, due to broad range of observable transport characteristics.

A preliminary work on the properties of perfluoro capped OPI wires will also be discussed. The XPS spectra of F1s were collected as a function of wire length. The results revealed two different slopes for the peak area of F 1s vs molecular length. At first glance, the crossover looks very similar to molecular junction experiments. More work needs to be done to confirm this previously unreported characteristic of OPI wires such as chemical calculations and core hole clock spectroscopy. It is noteworthy that the XPS measurements were performed in an ultra-high vacuum (10^{-9} Torr) as compared to ambient transport measurements in molecular junctions and solution ET study. We conclude with an outlook section for future transport experiments on synthesis of more conductive wires, and donor-block-acceptor systems.

Chapter 2 is devoted to provide general information on self-assembly of organothiols, and stepwise growth of π-conjugated OPI wires. In addition, a brief introduction on the characterization tools will be discussed. Chapter 3 is intended to introduce a few of the molecular junction techniques. A comparison of a few of the techniques on alkyl thiols systems will be discussed.

Chapter 4 through 7 presents my publications and preliminary work. Chapter 4 has been published as A. T. Demissie, G. Haugstad, and C. D. Frisbie "Growth of Thin, Anisotropic, π-Conjugated Molecular Films by Stepwise 'Click' Assembly of Molecular Building Blocks: Characterizing Reaction Yield, Surface Coverage, and Film Thickness vs. Addition Step Number" *Journal of the American Chemical Society* **2015**, 137, 8819–8828. In this work, we systematically measured the coverage and surface reaction yield for a set of π-conjugated molecular wires ranging in length between 0.6 and 5.5 nm. The OPI wires were grown from SAMs of 4-aminothiophenol or 4-formylthiophenol, and reacted stepwise with alternating addition of terephthalaldehyde (22 °C) or 1,4-benzenediamine (40 °C). We employed 6 different analysis techniques – spectroscopic ellipsometry, cyclic voltammetry, reflection-absorption infrared spectroscopy, Rutherford backscattering spectrometry, X-ray photoelectron spectroscopy, and NRA to demonstrate that the surface reaction yields via imine click chemistry are high, approximately 99%. The high yields and correspondingly high surface coverages of π-conjugated molecular wires (3.5 molecules/nm^2) bode well for continued use of these systems in ongoing molecular electronics experiments. Additionally, these OPI wires serve as an excellent platform for quantitative comparison of different surface analytical techniques and in particular for demonstrating the effective use of NRA for SAM characterization for the first time.

Chapter 5 has been published as A. T. Demissie, G. Haugstad, and C. D. Frisbie "Quantitative Surface Coverage Measurements of Self-Assembled Monolayers by Nuclear Reaction Analysis of Carbon-12" *Journal of the Physical Chemistry Letters* **2016**, 7, 3477−348. This work describes surface coverage measurements by RBS for alkyl thiols consisting of 8, 10, 12, 14, 16, and 18 C atoms per chain and oligophenylene thiols consisting of 1, 2, and 3 phenyl rings per chain on Au coated on mica, Si, and pyrolytic graphite sheet. The consistency of the C atom coverage values obtained by NRA was cross-checked by measuring the S atom concentration by conventional RBS. From these data, we obtained an average coverage value of 3.5 ± 0.2 molecules per nm^2 for both alkyl thiols and oligophenylene thiols on polycrystalline Au surfaces.

Chapter 6 has been published as C. S. S Sangeeth, A. T. Demissie, L. Yuan, T. Wang, C. D. Frisbie, and C. A. Nijhuis "Comparison of DC and AC Transport in 1.5-7.5 nm Oligophenylene Imine Molecular Wires across Two Junction Platforms: Eutectic Ga-In versus Conducting Probe Atomic Force Microscope Junctions" *Journal of the American Chemical Society* **2016**, 138, 7305-7314. This work describes the DC and AC impedance spectroscopy measurements on systematically varied OPI wires via EGaIn junctions, and comparisons of obtained results to prior reported CP-AFM results. We obtained a clear crossover from tunneling to hopping transport near 4 nm, which has not been reported before for large area junctions. Variable temperature measurements indicated that thermally activated transport for long wires have activation energy of 0.245 ± 0.008 eV in line with previously reported CP-AFM data. AC impedance spectroscopy measurements were utilized to calculate the wire resistance, wire capacitance, and for the first time, the dielectric constant of the wires. The AC results also indicated a similar crossover from tunneling to hopping transport near 4 nm with a decay constant β of 2.92 ± 0.13 nm^{-1} in the tunneling regime, and 1.01 ± 0.08 nm^{-1} in the hopping regime. Our results show excellent overall agreement between EGaIn and CP-AFM junctions for the measured intensive quantities such as the tunneling decay constant, crossover length, and activation energy. Based on these results, we conclude the differences in absolute resistance per molecule in our large and small area junctions reflect correction factors due to contact resistance. *My contribution to this work was in the synthesis and timely delivery of the OPI wires. Dr. Sangeeth performed all of the transport measurements at the National University of Singapore. We both contributed equally in data analysis, and in preparation of the manuscript.*

Chapter 7 will be prepared for submission to the *Journal of the American Chemical Society*. This chapter examines the connection between electronic structure and x-ray photoelectron emission counts of F 1s for a set of π-conjugated molecular wires ranging in length between 0.6 and 4.5 nm. The OPI wires were grown from SAMs of 4-aminothiophenol or 4-formylthiophenol, and reacted step-wise with alternating addition of terephthalaldehyde (22 °C) or 1,4-Benzenediamine (40 °C). The perfluoro termini (cap) were introduced by reacting amine terminated wires with pentafluorobenzaldehyde. The XPS F 1s peak area from the pentafluoro termini decreased with wire length. The slope of peak area versus estimated thickness was large for short wires than long wires. A crossover in slope was observed near 3 nm. NRA experiments revealed that the surface coverages for the wires were similar, and do not account for the obtained XPS results. To rule out surface charging or chemical shifts, OPI wires were synthesized on Si substrate starting from SAMs of 4-aminopropyl silane, and the results indicated no such effects. To further investigate the role of molecular structure on the observed F 1s counts, conjugation blocking alkyl chains were inserted at different positions along the wire backbone. The results show that conjugation blocking units significantly impact the intensity of F 1s counts. Overall, we obtained good correlation between the wire structure and its corresponding effects on the intensity of F 1s counts. Future work will focus on density functional theory and core-hole clock spectroscopy to identify potential charge transport mechanism and to develop a new ultra-high vacuum method of electronic characterization of ultra-thin organic films.

Chapter 8 is intended to summarize future interesting experiments for the group. Recent success on the chemisorption of alkynes to Au via Au-C σ bond indicates a potential new approach to synthesize very conductive molecular wires. We will also explore methods to reduce steric strain by incorporation of Ru complex ligands with COOH groups that can adapt a co-planar geometry. A brief synthesis of terpyridine bis complexes with a variety of metal complexes will be discussed. This opens the opportunity to explore new I-V characteristics in the hopping regime. We will also explore synthesis of donor-block-acceptor molecular wires with metal complex donor units, and fullerene acceptor moieties.

1.2 References

(1) *Charge and Exciton Transport through Molecular Wires*; Siebbeles, L. D. .; Grozeman, F. C., Eds.; John Wiley & Sons, 2011.

(2) Arrhenius, T. S.; Blanchard-Desce, M.; Dvolaitzky, M.; Lehn, J.-M.; Malthete, J. *Proc. Natl. Acad. Sci.* **1986**, *83*, 5355.

(3) Nitzan, A.; Ratner, M. a. *Science* **2003**, *300*, 1384.

(4) Davis, W. B.; Svec, W. A.; Ratner, M. A.; Wasielewski, M. R. **1998**, *396*, 60.

(5) Scheer, E. *Molecular Electronics: An Introduction to Theory and Experiment*; World Scientific, 2010.

(6) Aviram, A.; Ratner, M. A. *Chem. Phys. Lett.* **1974**, *29*, 277.

(7) Cheng, H.; Shen, H.; Yang, F.; Tang, J. *Nucl. Instruments Methods Phys. Res. Sect. B Beam Interact. with Mater. Atoms* **1994**, *85*, 47.

(8) Altmann, J. *Military Nanotechnology: Potential Applications and Preventive Arms Control*; Routledge, 2007.

(9) Natarajan, S.; Agostinelli, M.; Akbar, S.; Bost, M.; Bowonder, A.; Chikarmane, V.; Chouksey, S.; Dasgupta, A.; Fischer, K.; Fu, Q.; Ghani, T.; Giles, M.; Govindaraju, S.; Grover, R.; Han, W.; Hanken, D.; Haralson, E.; Haran, M.; Heckscher, M.; Heussner, R.; Jain, P.; James, R.; Jhaveri, R.; Jin, I.; Kam, H.; Karl, E.; Kenyon, C.; Liu, M.; Luo, Y.; Mehandru, R.; Morarka, S.; Neiberg, L.; Packan, P.; Paliwal, A.; Parker, C.; Patel, P.; Patel, R.; Pelto, C.; Pipes, L.; Plekhanov, P.; Prince, M.; Rajamani, S.; Sandford, J.; Sell, B.; Sivakumar, S.; Smith, P.; Song, B.; Tone, K.; Troeger, T.; Wiedemer, J.; Yang, M.; Zhang, K. In *2014 IEEE International Electron Devices Meeting*; IEEE, 2014; pp. 3.7.1–3.7.3.

(10) Chen, W.; Widawsky, J. R.; Vázquez, H.; Schneebeli, S. T.; Hybertsen, M. S.; Breslow, R.; Venkataraman, L. *J. Am. Chem. Soc.* **2011**, *133*, 17160.

(11) Perrin, M. L.; Frisenda, R.; Koole, M.; Seldenthuis, J. S.; Gil, J. A. C.; Valkenier, H.; Hummelen, J. C.; Renaud, N.; Grozema, F. C.; Thijssen, J. M.; Dulić, D.; van der Zant, H. S. J. *Nat. Nanotechnol.* **2014**, *9*, 830.

(12) Hines, T.; Diez-Perez, I.; Hihath, J.; Liu, H.; Wang, Z. S.; Zhao, J.; Zhou, G.; Müllen, K.; Tao, N. *J. Am. Chem. Soc.* **2010**, *132*, 11658.

(13) Wold, D. J.; Frisbie, C. D. *J. Am. Chem. Soc.* **2001**, *123*, 5549.

(14) Lauhon, L. J.; Ho, W. *Phys. Rev. Lett.* **2000**, *85*, 4566.

(15) Nijhuis, C. A.; Reus, W. F.; Whitesides, G. M. *J. Am. Chem. Soc.* **2009**, *131*, 17814.

(16) Nijhuis, C. A.; Reus, W. F.; Barber, J. R.; Whitesides, G. M. *J. Phys. Chem. C* **2012**, *116*, 14139.

(17) Chiechi, R. C.; Weiss, E. A.; Dickey, M. D.; Whitesides, G. M. *Angew. Chem. Int. Ed. Engl.* **2008**, *47*, 142.

(18) Yaffe, O.; Ely, T.; Har-Lavan, R.; Egger, D. A.; Johnston, S.; Cohen, H.; Kronik, L.; Vilan, A.; Cahen, D. *J. Phys. Chem. C. Nanomater. Interfaces* **2013**, *117*, 22351.

(19) Tran, E.; Rampi, M. A.; Whitesides, G. M. *Angew. Chem. Int. Ed. Engl.* **2004**, *43*, 3835.

(20) Akkerman, H. B.; Blom, P. W. M.; de Leeuw, D. M.; de Boer, B. *Nature* **2006**, *441*, 69.

(21) Neuhausen, A. B.; Hosseini, A.; Sulpizio, J. A.; Chidsey, C. E. D.; Goldhaber-Gordon, D. *ACS Nano* **2012**, *6*, 9920.

(22) Bonifas, A. P.; McCreery, R. L. *Nat. Nanotechnol.* **2010**, *5*, 612.

(23) Park, J.; Pasupathy, A. N.; Goldsmith, J. I.; Chang, C.; Yaish, Y.; Petta, J. R.; Rinkoski, M.; Sethna, J. P.; Abruña, H. D.; McEuen, P. L.; Ralph, D. C. *Nature* **2002**, *417*, 722.

(24) Kubatkin, S.; Danilov, A.; Hjort, M.; Cornil, J.; Brédas, J.-L.; Stuhr-Hansen, N.; Hedegård, P.; Bjørnholm, T. *Nature* **2003**, *425*, 698.

(25) Liao, J.; Agustsson, J. S.; Wu, S.; Schönenberger, C.; Calame, M.; Leroux, Y.; Mayor, M.; Jeannin, O.; Ran, Y.-F.; Liu, S.-X.; Decurtins, S. *Nano Lett.* **2010**, *10*, 759.

(26) Rawlett, A. M.; Hopson, T. J.; Nagahara, L. A.; Tsui, R. K.; Ramachandran, G. K.; Lindsay, S. M. *Appl. Phys. Lett.* **2002**, *81*, 3043.

(27) Yuan, L.; Nerngchamnong, N.; Cao, L.; Hamoudi, H.; del Barco, E.; Roemer, M.; Sriramula, R. K.; Thompson, D.; Nijhuis, C. A. *Nat. Commun.* **2015**, *6*, 6324.

(28) Akkerman, H. B.; de Boer, B. *J. Phys. Condens. Matter* **2008**, *20*, 013001.

(29) Rosink, J. J. W. M.; Blauw, M. A.; Geerligs, L. J.; van der Drift, E.; Rousseeuw, B. A. C.; Radelaar, S.; Sloof, W. G.; Fakkeldij, E. J. M. *Langmuir* **2000**, *16*, 4547.

(30) Choi, S. H.; Kim, B.; Frisbie, C. D. *Science* **2008**, *320*, 1482.

(31) Luo, L.; Choi, S. H.; Frisbie, C. D. *Chem. Mater.* **2011**, *23*, 631.

(32) Choi, S. H.; Frisbie, C. D. *J. Am. Chem. Soc.* **2010**, *132*, 16191.

(33) Choi, S. H.; Risko, C.; Delgado, M. C. R.; Kim, B.; Brédas, J.-L.; Frisbie, C. D. *J. Am. Chem. Soc.* **2010**, *132*, 4358.

(34) Luo, L.; Balhorn, L.; Vlaisavljevich, B.; Ma, D.; Gagliardi, L.; Frisbie, C. D. *J. Phys. Chem. C* **2014**, *118*, 26485.

(35) *Charge and Exciton Transport through Molecular Wires*; John Wiley & Sons, 2011.

(36) Eng, M. P.; Albinsson, B. *Angew. Chem. Int. Ed. Engl.* **2006**, *45*, 5626.

(37) Segawa, H.; Takehara, C.; Honda, K.; Shimidzu, T.; Asahi, T.; Mataga, N. *J. Phys. Chem.* **1992**, *96*, 503.

(38) Segal, D.; Nitzan, A.; Davis, W. B.; Wasielewski, M. R.; Ratner, M. A. *J. Phys. Chem. B* **2000**, *104*, 3817.

2. Molecular Self-Assembly and Wire Growth

Self-assembly is the spontaneous formation of discrete nanometer-sized units from simpler sub units or building blocks. While biological membranes, cellular structures and viruses can be regarded as highly sophisticated self-assembled systems, the simplest examples are self-assembled monolayers (SAMs). These are arrangements of molecules adsorbed on solid surfaces in which intermolecular forces play a key role and which can be spontaneously formed from solution or vapor phase.[1] The pioneering work of Langmuir and Blodgett involves the modification of single and multilayer films by dipping the substrate beneath a water surface covered with fatty acids, and slowly withdrawing it (substrate).[2,3] Such processes depend on pH, temperature, and the presence of salts of divalent metals.[4] Furthermore, the roughness of the substrate significantly affects the quality of the film since the interface is formed by physically contacting the film with the substrate.

A common approach to form well-ordered SAMs is via chemisorption of particular functional groups with the substrate. For examples, thiols have a high affinity towards coinage metals such as Au, Ag, Pt, Cu etc. Table 2.1 shows a list of the commonly employed functional groups and their binding affinity towards substrates. Due to their reproducibility, and ease of formation, SAMs of alkyl thiols are the most commonly studied systems in molecular electronics. Furthermore, the availability of alkyl chain length with various numbers of C atoms from commercial sources makes them ideal systems to investigate length-dependent transport measurements. On the other hand, it is difficult to systematically examine hopping transport in conjugated systems because it requires longer chain length (> 4nm), which are difficult to synthesize. Such rigid, well packed and conjugated systems require a layer-by-layer growth approach method which will be discussed later.

Table 2.1 List of various functional groups (anchoring units) and substrates used for forming SAMs. R is the molecular backbone.[5–16]

Ligand	**Substrate**
RSH	Au, Ag, Pt, Cu, Pd, Zn, GaAs
RSAc	Au
RSSH	Au
ROH	Si, Fe_2O_3
RCOOH	Fe_2O_3, Al_2O_3
R-NH_2	FeS_2, Mica, Steel
$RC\equiv N$	Ag, Au
$RN\equiv N^+BF_4^-$	Si, GaAs, Pd
RSeH	Ag, Au, CdTe
$R_3P=O$	Co, CdSe, CdTe
RPO_3^{-2} / $RP(O)OH_2$	Al, GaAs, ITO, TiO_2, ZrO_2, CdTe
$RN\equiv C$	Pt
$RC=CH_2$	Si
R-SiX_3, X = H, Cl, OCH_2CH_3	SiO_2, HfO_2, TiO_2

2.1 Self-Assembly of Organothiols

2.1.1. Substrate Preparation

Au substrates were prepared using two different methods: conventional thermal evaporation and template stripping. For thermal evaporation, 50 Å of Cr was first evaporated on bare Si wafer or mica as an adhesion layer followed by 700 Å of Au in a home-built evaporator at a rate of approximately 1-2 Å/s and base pressure $\leq 2 \times 10^{-6}$ Torr. For template-stripped Au, an epoxy adhesive (EPO-TEK 377) was employed to bond small Si wafer pieces onto a 5000 Å thick Au film deposited by e-beam evaporation on bare Si without any adhesion layer. The samples were then cured at approximately 150 °C for 1.5 h, and the Au layer was stripped off the bottom Si layer by a razor blade. Template stripped Au surfaces yield an atomically flat layer because the evaporated Au adopts the topography of the Si; thus, this quality makes them better suited for charge transport studies than thermal evaporated Au. For example, Beebe et al., showed that rough or thermally evaporated Au resulted in 2 orders of magnitude change in resistance for SAMs, whereas the variance for template stripped Au was small.[17] On the other hand, use of template Au is limited by their incompatibility in certain polar solvents such as DMSO that results in the formation of bubbles across the metal surface, and subsequently delaminates or peels off the film from the Si substrate. Low temperatures such as 40°C also result in film delamination.

2.1.2 Monolayer Formation

Since their discovery in 1980s by Nuzzo and Allara, thiol and dithiol SAMs on gold have been extensively studied with a variety of surface characterization techniques.[18] It is beyond the scope of this thesis to examine carefully the complexities associated with SAM formation. A brief review of the kinetics and structure of SAMs will be discussed next.

Self-assembly of thiols can be done in gas or solution phase, the latter being the most common method. A solution ranging from 10-1000 µM in concentration is typically used to form SAMs. A thiol SAM consists of three parts[19]: (1) the S head group that forms a strong covalent bond with the substrate (50 kcal mol^{-1} for thiolate bond), (2) the hydrocarbon or aromatic chain that forms van der Waals interaction and stabilizes the chain (1-2 kcal mol^{-1} per methylene), and (3) the terminal group that changes the physical and chemical properties of the SAM (few kT). The kinetics of self-assembly can be divided into 4 steps as shown in Figure 2.1a. In the first step, the thiol molecules

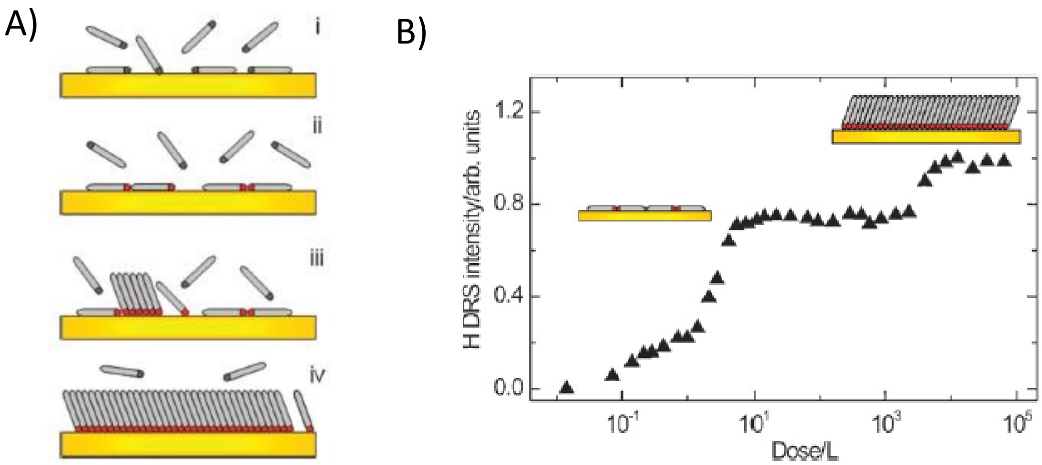

Figure 2.1 A) Schematics of the kinetics of self-assembly of alkane thiol on Au: (i) physisorption, (ii) lying down phase, (iii) nucleation of standing up phase, and (iv) completion of standing up phase. B) DRS intensity of Hydrogen from Au verses exposure to hexane thiol in UHV.[20] The first plateau corresponds to completion of step (ii), and the second plateau to completion of step iv. Spectrum taken from references 19 and 20, with permission of the Royal society of Chemistry, and American Chemical society, respectively.

physisorbs on the surface of Au followed by chemisorption, where it loses the mercaptan H atom. Chemisorption is easier at defective sites of Au, where preferred nucleation of islands containing lying down molecules takes place.[19] This growth has been monitored by time of flight direct recoil spectroscopy (TOF-DRS), where H signals from the terminal methyl group of hexane thiol were detected after exposure to Au (111).[20] The first rise in the H DRS intensity corresponds to growth of lying down islands, followed by plateau after completion of this step. The next step is the nucleation of molecules in the standing up phase (step 3) which corresponds to the second rise in H DRS in Figure 2.1b. The completion of this step is believed to take several hours (step 4). Thus, the self-assembly of thiols that involves transitions between lying down and standing up phases is governed by balance between intermolecular and molecule-substrate interactions.[1]

2.1.3 Monolayer Structure

The existence of stable hexagonal lattice symmetry of alkane thiol ($\sqrt{3}\,x\,\sqrt{3}\ R30°$) on Au (111) has been reported via scanning tunneling microscopy (STM),[19] atomic force microscopy (AFM), [21] grazing incidence x-ray diffraction (GIXD). [22] However, other stable high coverage c(4 × 2) (super lattice of √3 × √3 R30° lattice, or better described as 3√3 × 2√3 R30° with respect to substrate registry) unit cell with orthorhombic symmetry that involves reconstruction of the Au surface and presence of adatoms was discovered by STM and other diffraction techniques.[19] The question of which of the structures, $\sqrt{3}\,x\,\sqrt{3}\ R30°$ versus c (4 x 2) is energetically favored, and its dependence on chain length remains unclear.[1] The adsorption site of the thiol on Au (111) surface is an active area of research that has drawn much attention over the past few years, and various models have been suggested to coincide with experimental data.

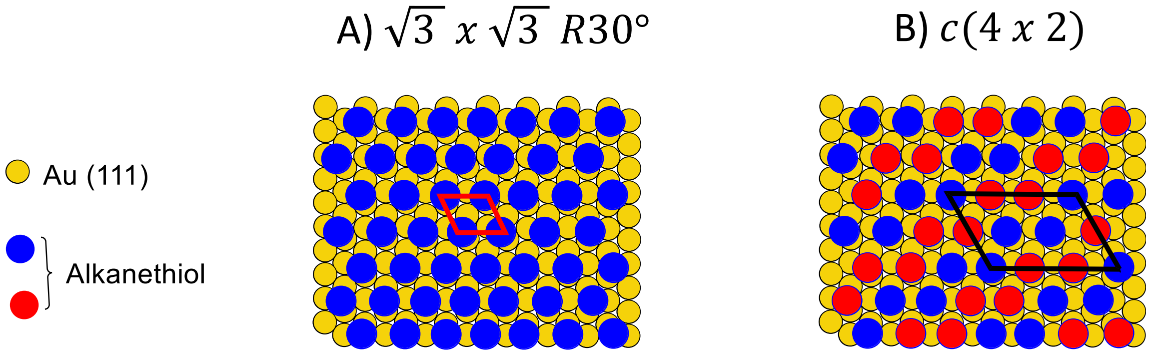

Figure 2.2 Alkane thiol hexagonal lattices on Au(111). A) $\sqrt{3}\,x\,\sqrt{3}\ R30°$ lattice with unit cell drawn in red. B) c(4 x 2) or $3\sqrt{3} \times 2\sqrt{3}\ \mathrm{R30°}$ super lattice with unit cell drawn in black. The red and blue circles correspond to alkyl thiol monolayer with different twist angles.

Nevertheless, adatom model involving $(RS)_2Au$ moieties seems to be well-grounded both from GIXD data and theoretical stability for the c(4 x 2) lattice, but could not explain the existence $\sqrt{3}\,x\,\sqrt{3}\ R30°$ lattice.[23]

Since the molecular cross section for aromatic thiols is bigger than alkane thiols, it is expected that all binding sites on the Au will not be occupied. However, well ordered and reproducible $\sqrt{3}\,x\,\sqrt{3}\ R30°$ structures were reported for 4-aminothiophenol and 4-terphenyl thiol on Au (111).[24,25] Here, it is interesting to note that the presence of terminal groups makes a significant difference on the structure of the SAMs. Sabatani et al., found a tilt angle of 80° for benzene thiol; whereas, 4-ATP has a tilt angle of 30°.[26] This observation is in agreement with the reflection absorption infrared spectroscopy which shows the absence of strong C=C stretch mode for phenyl thiol SAMs. On the other hand, SAMs of 4-ATP have strong C=C and C-N stretch modes as shown in Figure 2.4.[27]

2.1.4 Monolayer Defects

Even though SAMs are ideally sketched as perfect monolayers, they are far from what the real structure looks like. It is impossible to find SAMs without any defects. The defects constitute of a small number of missing atoms (pin holes), vacancy islands, domain boundaries, step edges, chemical impurities, and substrate (film) impurities. Typical polycrystalline Au substrates are replete with lots of defects and structural irregularities such as dense arrangements of inter-grain boundaries, twins, faceting, and occlusions.[16]

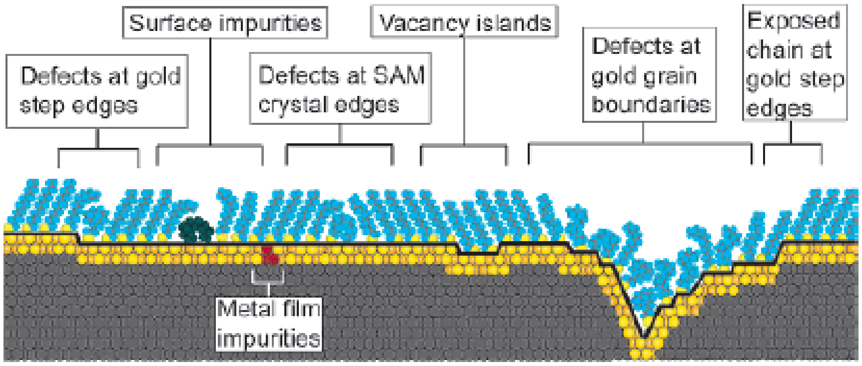

Figure 2.3 Schematic illustrations of extrinsic and intrinsic defects. Adapted from reference 16 with permission from Chemical Reviews.

2.2 Step Wise Growth of Molecular Wires

An ingenious method for the synthesis of π-conjugated phenylene imine was first reported by Rosink et al.[28] The growth begins by adsorption of SAMs of 4-aminothiophenol on Au. The SAMs were then thoroughly rinsed with absolute ethanol, and immersed into solution of terephthalaldehyde (benzene-1,4-dicarbaldehyde) in ethanol. One of the carbonyl units reacts with the terminal amine unit of the SAM, and the resulting imine bond extends the length and conjugation of the monolayer by a phenyl ring. The SAMs are now refereed to as oligophenylene imine wires: the "oligo" term refers to a few repeating units, the "phenylene" term refers to the benzene molecules, and the "imine" term stands for the nature of the bond that links the repeat units. The OPI wires are now terminated with carbonyl units as shown in Figure 2.4a (OPI-2). The Au wafer was then thoroughly rinsed, and immersed into a solution of 1,4-Benzenediamine in ethanol. The carbonyl terminal unit on the wire now reacts with one of the amine functional group to further extend the length and conjugation of the wire (OPI-3). Thus,

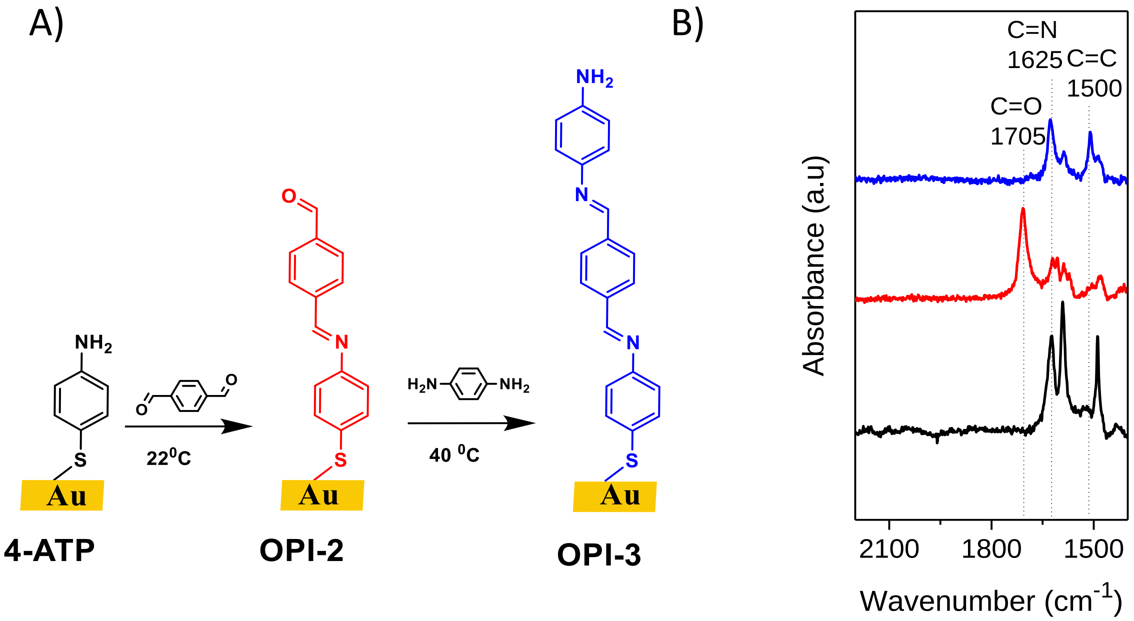

Figure 2.4 A) Molecular structure and synthetic route to OPI wires on Au shown up to 3rd layer. B) The corresponding RAIRS spectra. Vertical dashed lines indicated the position of carbonyl (C=O) stretch (1705 cm^{-1}), imine (C=N) stretch (1625 cm^{-1}), and phenyl (C=C) stretch (1500 cm^{-1}) peaks.

an alternate reaction with terephthalaldehyde and 1,4-Benzenediamine was used to extend the length of the wires in a step-wise fashion. Using a similar stepwise growth approach, Choi et al., synthesized oligonapthalenefluoroeneimine (ONI) wires with naphathalene-2,6-dicarboxaldehyde and fluorene-2,7-diamine repeat units (Figure 2.5a).[29] The same authors also synthesized alternating donor-acceptor oligo-tetrathiafulvalene-pyromelliticdiimide-imine (OTPI) wires, with tetrathiafulvalene (donor), and pyromelliticdiimide, (acceptor) repeat units (Figure 2.5b).[30] Thus, imine click chemistry is compatible with a variety of repeating units, which is important for fundamental charge

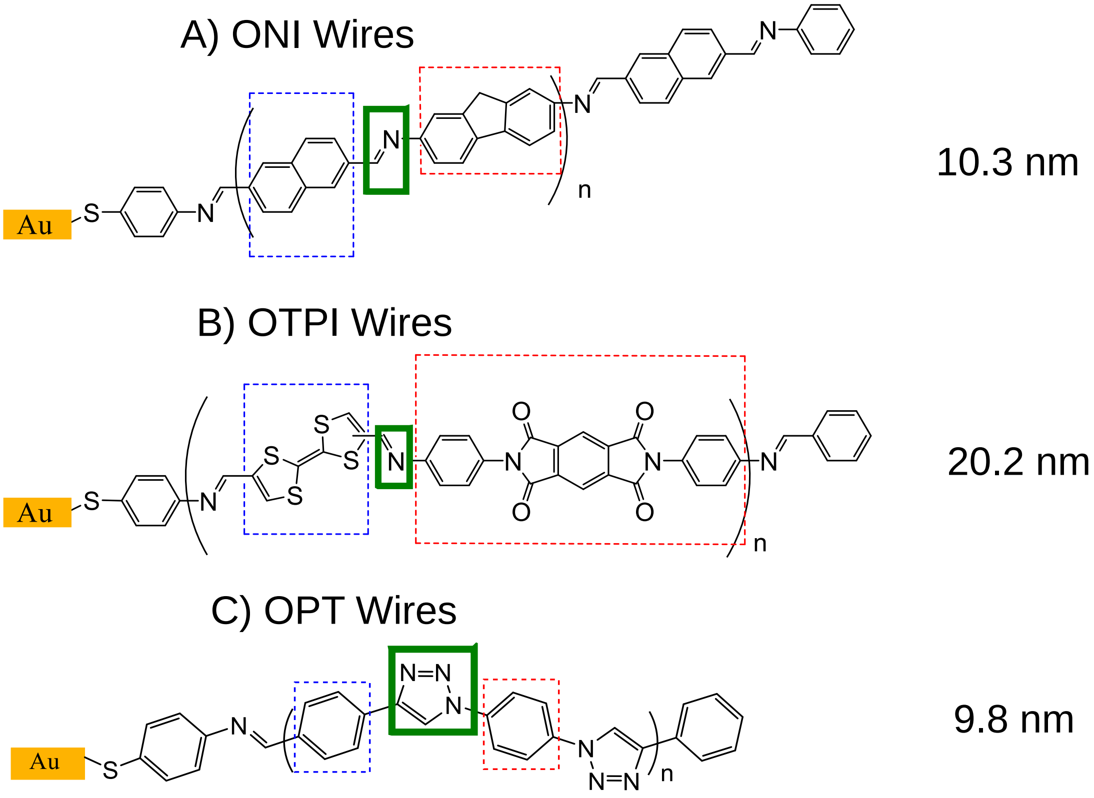

Figure 2.5 Molecular structures of the longest ONI wires (A)[29], OTPI wires (B)[30], and OPT wires (C)[42]. The repeat units are circled in red and blue rectangles, and the linkers are circled in bold green.

transport study of π-conjugated oligomers. Luo et al., also reported using a stepwise approach to grow molecular wires via Cu(I) catalyzed cycloaddition reaction between alkynes and azide to form triazole linkages as shown in Figure 2.5c.[31]

2.3 Characterization of SAMs and Molecular Wires

SAMs and molecular wires have been characterized by nearly all of the surface analysis tools up to date. In this section, a few representative techniques will be discussed in details.

2.3.1 Spectroscopic ellipsometry. Ellipsometry is used to measure optical properties and thickness of samples by measuring change in polarization states that occurs when a polarized light is reflected at non-normal incidence from a film surface. The incident light polarized with Ep and Es components, which are respectively parallel and perpendicular to the plane of incidence, become elliptically polarized after reflection from the sample. The experimental data is expressed in terms of tan ψ and Δ, which are related to

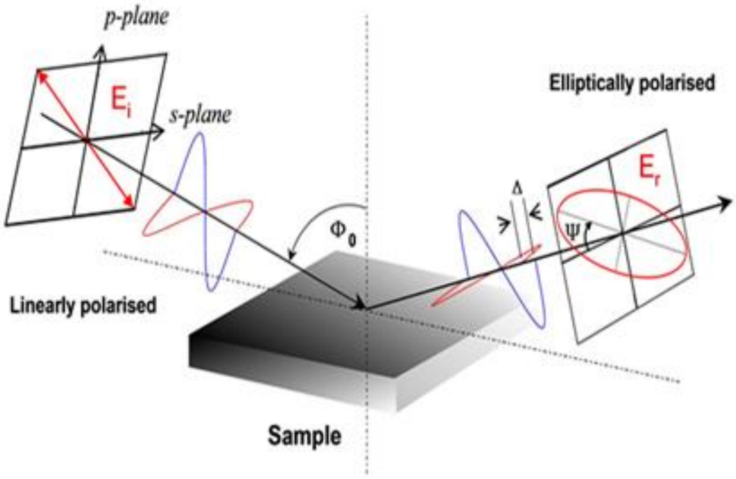

Figure 2.6 Schematics of an optical ellipsometry. Adapted from reference 32.

amplitude ratio and phase difference that develops from the s and p field components after reflection, respectively.[32] When multiple layers are present on the substrate, a similar but slightly complicated equation applies since the Fresnel-reflection coefficient depends on wavelength, incidence angle, layer thickness, and complex refractive indices (n and k) for both film and substrate. Thickness of OPI wires was determined according to the following procedures. Spectra for a bare Au wafer were first measured at incident angles of 45°, 55°, and 65° over a range of wavelength (300– 1100 nm). Instrument software was then used to extrapolate for film thickness. Measurements on the same wafer were repeated after wire growth, and the thickness was fitted on top of the previous model. The refractive index was assumed to be 1.45, and dielectric constant of 0 for fitted wavelength range of 600 – 1000 nm.

2.3.2 Fourier transform infrared spectroscopy. Fourier transform infrared spectroscopy (FTIR) is a powerful method for analysis of composition, film crystallinity, surface coverage, and film orientation.[9,18,33] The excitation of normal vibrational mode is active if the projection of the change in dipole moment of the molecule (**p**) is non-zero along the direction of infra-red electric field. The integral intensity (A) of the absorption is proportional to the probability of transition between an initial state i and final state j per unit time. Quantum mechanical selection rules allow a change of ±1 for the quantized vibrational energy level:

$$A \sim E^2 \langle j|\boldsymbol{p}|i\rangle^2 cos^2\theta \tag{2.1}$$

where, E is the electric field of the IR light, and θ is the angle between E and **p**.

IR light of various frequencies is generated via Michelson interferometer. A beam splitter separates IR light (produced by heating KBr source) to two beams. One of the beams is directed towards a fixed mirror, while the other is directed towards a moving mirror which is controlled by a laser. Once the mirrors reflect back the IR light, they combine constructively and destructively since they travelled different distances back and forth from the mirrors. This produces an interferogram, and contains information about each infrared frequency. The beam is then directed towards the sample, where certain frequencies are absorbed and then travel towards liquid N_2 cooled mercury cadmium telluride (MCT) detector. Fourier transform program then converts the modified interferogram to an absorption versus frequency plot.

Reflection-absorption infrared spectroscopy (RAIRS) is a well-established technique for studying the absorption of chemisorbed molecules on metal surfaces. A Harrick Seagull accessory, which contains a bunch of mirrors that reflects the IR light at a grazing angle of 84° from the surface normal, was used to excite vibrational states of the dipoles in the SAMs a shown in Figure 2.7. This method takes advantage of the great

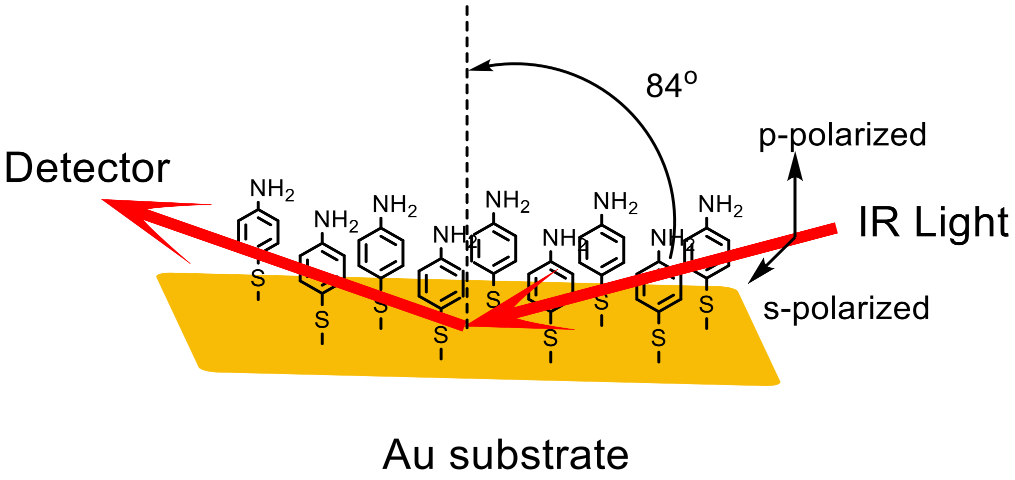

Figure 2.7 Schematics of a reflection absorption infrared spectroscopy.

difference in absorption of polarized light along the sample normal. For each sample and background, an average of 300 scans at a resolution of 2 cm^{-1} were collected after 15-20 min of purging with dry air followed by ~ 300 - 1000 sample scans. A representative example of RAIRS is displayed in Figure 2.4.

2.3.3 X-ray photoelectron spectroscopy. X-ray photoelectron spectroscopy (XPS) is one of the most commonly employed tools for surface analysis. Unlike FTIR where only vibrational states are perturbed, XPS ejects core electrons from their respective energy levels. The popularity of XPS is due to its ability to identify and quantify all elements except H and He (due to low photoionization cross-section) as well as measure the thickness of substrates. Core electrons are used for analysis because most elements have a characteristic binding energy that can be used for identification. Electrons are ejected via the photoelectric effect, for which Albert Einstein was awarded the Nobel Prize in 1929. Sample is exposed to irradiation in an ultrahigh vacuum chamber (~10^{-9} Torr) by x-rays and the kinetic energy (KE) and photoelectron counts are measured. The KE of the photo-emitted electron is given by the formula:

$$K.E = hv - \phi - BE \tag{2.2}$$

where, φ is the work function of the spectrometer, and BE is the binding energy (measured from core level to fermi level, see Figure 2.9).[34] Once electrons are photo-emitted from the sample, they pass through a retarding grid/lens system which decelerates the electrons to some constant energy known as pass energy (E) before reaching the entrance slit of the analyzer. Reducing their energy is critical for peak resolution because ΔE is directly related to the radius of the analyzer (R) by the relation ΔE/E α w/R where w is slit width. Once the electrons are resolved by the hemi-spherical analyzer, a four-probe resistive anode detector with a micro-channel plate is used to count them. The x-ray source used in this thesis is Al K_α (1486.6 eV).

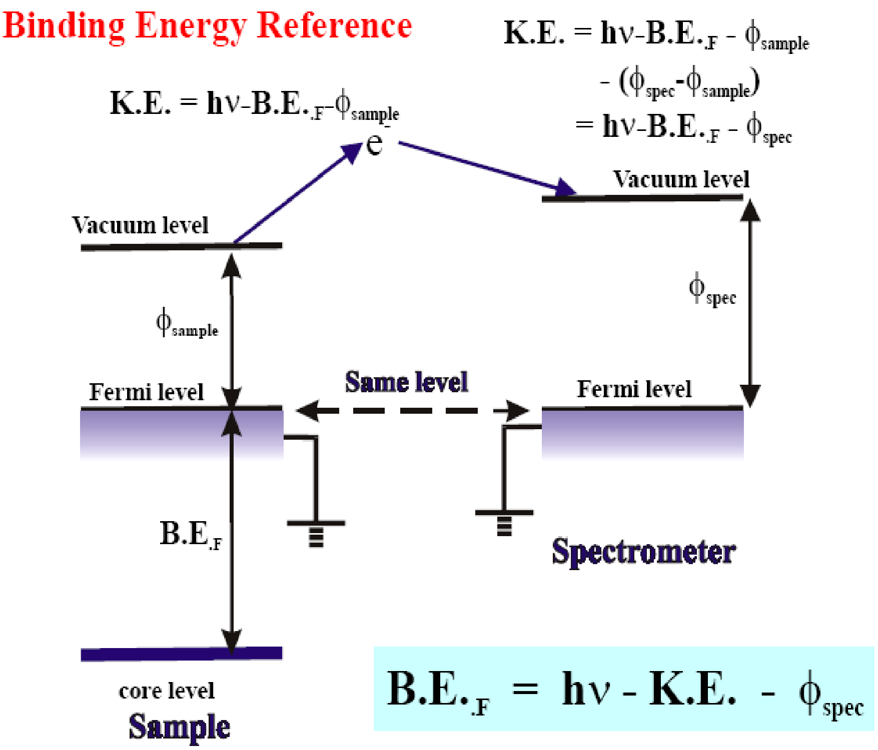

Figure 2.8 Schematics of binding energy reference from the core level, and its relation to the work function of the instrument. Adapted from reference 34.

One of the prime advantages of XPS is its ability to detect degenerate energy levels (dictated by the laws of quantum mechanics). Each electron has principal quantum number (*n*), angular momentum quantum number (*l*), magnetic quantum number (*m*) and spin quantum number (*s*). Spin orbit coupling results from the coupling of magnetic field set up by the electrons motion around the nucleus and on their own axis. Two coupling schemes exist, j-j coupling and Russell-Saunders. The former applies to high atomic number elements (Z>30), while the latter applies to low Z elements. For example, Br 3p electrons couple to give the following values

$$J = l + s = 1 \pm 0.5 = {}^{3}/_{2}\,, {}^{1}/_{2} \tag{2.3}$$

The degeneracy of each level can be calculated by using the relation 2j+1. Thus for the above example, there are twice as many electrons in 3p-3/2 states than 3p-1/2 states. It is customary in XPS to leave out the half- term and express the levels as 3p-3 and 3p-1. However, we will not adapt such notations in this thesis.

The common formalism of XPS is based on the assumptions which are as follows[35]:

1. X-ray reflection, attenuation and refraction are negligible.
2. The surface of the sample is flat and amorphous.
3. The composition of the sample is uniform over the thickness range analyzed.
4. The sample area irradiated by the X-ray is larger than the analyzed area (A_0).
5. Elastic scattering of the photoelectrons are negligible.
6. Photoelectrons are attenuated exponentially as they travel towards the detector in the sample (Beer's law).

If elastic scattering is neglected, the photoelectron intensity (I) from a sample of uniform composition can be expressed as[35]:

$$I = F_X\left(\frac{d\sigma_x}{d\Omega}\right)\lambda_{in}MxfA_oTD\Delta\Omega$$

$where,\ F_X$ is the average flux of the x-rays on the sample.

$\left(\frac{d\sigma_x}{d\Omega}\right)$ is the differential photoionization cross section.

λ_{in} is the Inelastic mean free path of photoelectrons in the sample.

M is the total atomic density of sample (number/ volume).

x is the fraction of atoms emitting photoelectrons from element of interest.

f is the fraction of photoemitted electrons that appear in the main peak.

A_o is the area of sample irradiated by x-ray that is viewed by analyzer.

D is the detector efficiency.

T is the transmission function of analyzer.

$\Delta\Omega$ is the acceptor solid angle.

In order to make quantitative analysis, it is convenient to compare the relative measurements of peak intensities for a particular element in the sample with corresponding peak and element in a reference material. The comparison is done as shown below:

$$I = F_X\left(\frac{d\sigma_x}{d\Omega}\right)\lambda_{in}MxfA_oTD\Delta\Omega$$

$I = F_X\left(\frac{d\sigma_x}{d\Omega}\right)\lambda_{in}MxfAB,\ where$ B ($A_oTD\Delta\Omega$) is an instrumental term for sample of interest.

$$\frac{I_i^{sample}}{I_i^{ref}} = \frac{\left(F_X\left(\frac{d\sigma_x}{d\Omega}\right)\lambda_{in}MxfB\right)_i^{sample}}{\left(F_X\left(\frac{d\sigma_x}{d\Omega}\right)\lambda_{in}MxfB\right)_i^{ref}}$$

$$x_i^{sample} = \frac{I_i^{sample}\left(\left(\frac{d\sigma_x}{d\Omega}\right)\lambda_{in}MfB\right)^{ref} x^{ref}}{I_i^{ref}\left(\left(\frac{d\sigma_x}{d\Omega}\right)\lambda_{in}MfB\right)^{sample}} = x_i^{ref}\left[\frac{I_i^{sample}}{I_i^{ref}}\right]F$$

Most XPS instruments use either fluorine or carbon as a standard element (I*) and ignore the F term.

$$S_i^E = \frac{I_i^{ref}}{I^*}$$

$$x_i^{sample} = \frac{\left(\frac{I_i^{sample}}{S_i^E}\right)}{\sum_{j=1}^{n}\left(\frac{I_j^{sample}}{S_i^E}\right)} \tag{2.4}$$

However, it has been shown F (Matrix correction factor) can vary between 0.3 and 3.[36] Since the sensitivity factor for most XPS instruments is primarily concerned with variation of B and λ with energy, the influence of *M, f,* and $\frac{d\sigma}{d\Omega}$ terms on sensitivity factor are not well established.[35]

The attenuation of photoelectron intensity with depth can be expressed as follows if elastic scattering is neglected:

$$\begin{aligned} I_{Au} &= F_X\left(\frac{d\sigma_x}{d\Omega}\right)\lambda_{in} M x f A_o T D \Delta\Omega \exp\left(-\frac{t}{\lambda(E)\cos\alpha}\right) \\ I_{Au} &= I_{Au_0}\exp\left(-\frac{t}{\lambda(E)\cos\alpha}\right) \end{aligned} \tag{2.5}$$

where, t is for sample thickness and α is take off angle (angle between the substrate normal and analyzer, 35°). For an over layer film such as carbon, the attenuation can be expressed as:

$$\begin{aligned} I_C &= F_X\left(\frac{d\sigma_x}{d\Omega}\right)\lambda_{in} M x f A_o T D \Delta\Omega\left[1-\exp\left(-\frac{t}{\lambda(E)\cos\alpha}\right)\right] \\ I_C &= I_{C_o}\left[1-\exp\left(-\frac{t}{\lambda(E)\cos\alpha}\right)\right] \end{aligned} \tag{2.6}$$

Therefore by comparing the intensity of C and Au to a reference SAMs such as octadecanethiol, sample thickness can be extracted by simplifying the following equation.[37,30,38]

$$\frac{\frac{I_c}{I_{Au}}(sample)}{\frac{I_c}{I_{Au}}(ref)} = \frac{\left\{1-\exp(-\frac{t_{sample}}{\lambda(E)\cos\alpha})\right\}\exp(-\frac{t_{ref}}{\lambda(E)\cos\alpha})}{\left\{1-\exp(-\frac{t_{ref}}{\lambda(E)\cos\alpha})\right\}\exp(-\frac{t_{sample}}{\lambda(E)\cos\alpha})} \tag{2.7}$$

2.3.4 Rutherford Backscattering Spectrometry. Rutherford backscattering spectrometry (RBS) is a non-destructive technique that is used to measure the elemental composition of a sample. A beam of high energy ${}^{4}_{2}He^{2+}$ ions impinges on a sample and the backscattered counts *versus* energy of the ions are used to calculate the surface coverage and elemental composition. The basic principle that describes RBS is an elastic (hard sphere) collision. From first principles[39], the kinematic factor (K), which is the ratio of backscattered ${}^{4}_{2}He^{2+}$energy (E_1) to incident ${}^{4}_{2}He^{2+}$ energy (E_0) is used to calculate the mass of the target atom. The Ortec silicon ion detector was positioned at a scattering angle (θ) of 165° with respect to the incident beam and subtended a solid angle of 3.6 msr.

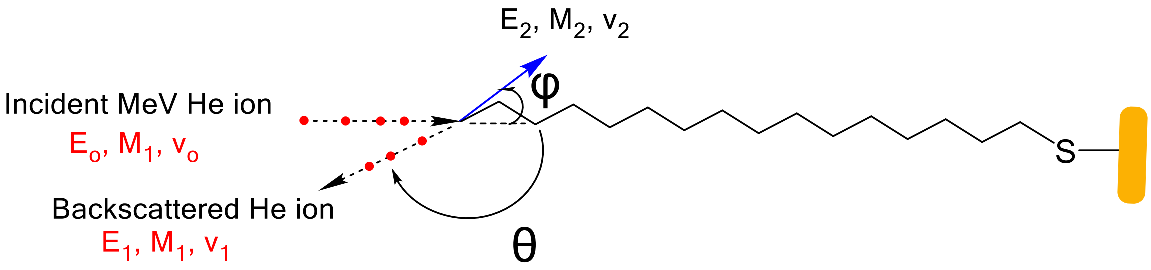

Figure 2.9 Schematics of elastic hard sphere collision between ${}^{4}_{2}He^{2+}$ion and C target.

Conservation of Energy

$$\frac{1}{2}M_1v_0^2 = \frac{1}{2}M_1v_1^2 + \frac{1}{2}M_2v_2^2,$$

Conservation of Momentum

$$M_1v_0 = M_1v_1\cos\theta + M_2v_2\cos\phi,$$

$$0 = M_1v_1\sin\theta - M_2v_2\sin\phi.$$

$\boxed{E_1 = KE_0}$ Backscattering

$\boxed{E_2 = K_{rec}E_0}$ Forward Recoil

Eliminating ϕ and v_2

$$\frac{v_1}{v_0} = \left[\frac{(M_2^2 - M_1^2\sin^2\theta)^{\frac{1}{2}} + M_1\cos\theta}{(M_1+M_2)}\right] \text{ for } M_1 \le M_2$$

$$\boxed{K_{rec} = \left[\frac{4M_1M_2\cos^2\phi}{(M_1+M_2)^2}\right]}$$

$$\boxed{K = \left[\frac{(M_2^2 - M_1^2\sin^2\theta)^{\frac{1}{2}} + M_1\cos\theta}{M_1+M_2}\right]^2} \qquad (2.8)$$

Note: In the above equation, phi (φ) and theta (θ) are not the azimuthal and sample normal angles.

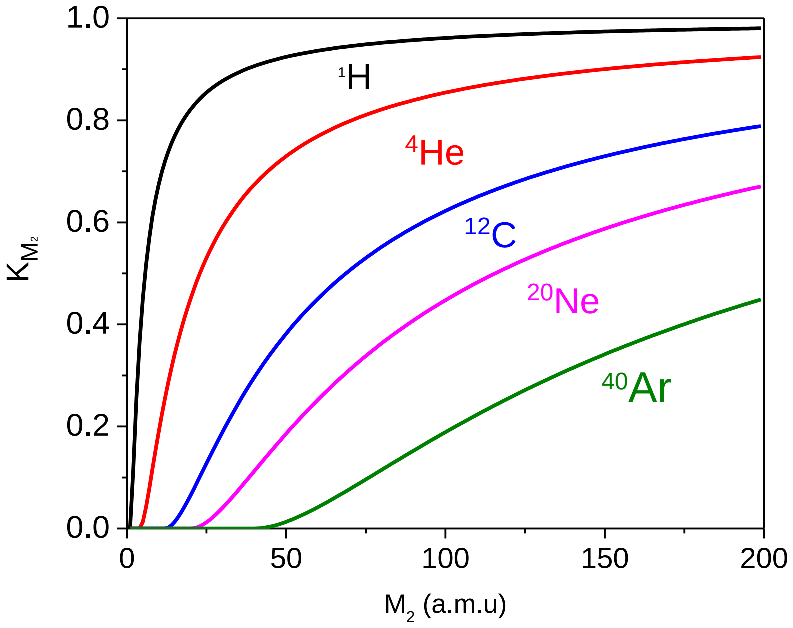

Figure 2.10 Plot of kinematic factor verses target mass in atomic mass unit for various incident particles (H, He, C, Ne, and Ar). (Equation 2.8)

The implication of the kinematic factor as function of different incident particle mass is shown in Figure 2.10. In general, there is a good mass resolution for a light element and their isotopes. However, mass resolution decreases with target mass M_2, i.e., the slope of K_{M2} vs M_2 plateaus as M_2 increases. In contrast, the mass resolution for heavier elements increases as the mass of the incident particle increases. An alternate strategy to increase mass resolution is by increasing the energy of the incident particle.[40] Figure 2.11 displays the RBS spectra of GaAs substrate at various incident beam energy. As the incident beam energy increases, it is clear that mass resolution of peaks is significantly improved. This can be directly inferred from the relation $E_1=KE_0$, where E_0 is the incident beam energy. Note that isotopes of Ga and As are resolved for high incident beam energy.

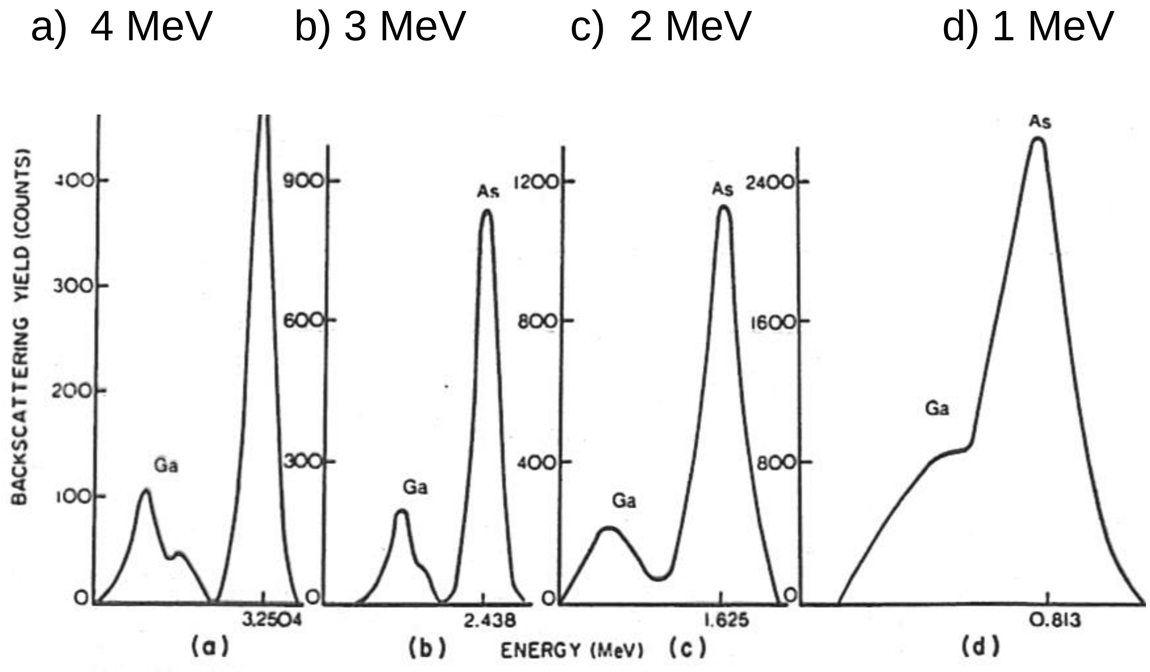

Figure 2.11 RBS spectra of GaAs substrate at various incident beam energy. The Ga and As peaks are well resolved for high incident beam energy. Adapted with permission from reference 40.

The probability that a scattering event will result in a signal at the detector for certain backscattering angle θ is given by the differential scattering cross section, $\frac{d\sigma}{d\Omega}$. It has units of area per unit angle. If S is the surface area of the target that is uniformly illuminated by the beam, then the total number of atoms that are available from scattering is equal to SNt where N is the density of the sample and t is its thickness. The ratio of the total cross sectional area per unit angle of all eligible atoms ($SNt\frac{d\sigma}{d\Omega}$) to the beam area S is interpreted as the probability that the scattering event will be recorded by the detector; that is, this ratio is set equal to $(1/d\Omega)(dQ/Q)$, where Q is the total number of incident particles and dQ is the number of particles recorded by the detector.[39]

$$\frac{SNt\frac{d\sigma}{d\Omega}}{S} = \left(\frac{1}{d\Omega}\right)\left(\frac{dQ}{Q}\right) \tag{2.9}$$

Upon rearranging the above,

$$\frac{d\sigma}{d\Omega} = \left(\frac{1}{Nt}\right)\left[\frac{\frac{dQ}{d\Omega}}{Q}\right] \tag{2.10}$$

This assumption only holds for randomly distributed atoms in the nuclei such that the cross sections of the nuclei do not overlap.

For classical Rutherford scattering, the force that acts during the collision between the projectile and target mass is described by Coulomb repulsion of the two nuclei. This holds when the distance of closes approach is large compared to nuclear distances, but small compared with the Bohr radius (0.53 Å). When these assumptions along with the conservation of momentum and kinetic energy are made, the differential scattering cross section can be described by:

$$\frac{d\sigma}{d\Omega} = \left(\frac{Z_1 Z_2 e^2}{4E_0}\right)^2 \frac{4}{\sin^4\theta} \frac{\left\{\left[1-\left(\left(M_1/M_2\right)\sin\theta\right)^2\right]^{1/2} + \cos\theta\right\}^2}{\left[1-\left(\left(M_1/M_2\right)\sin\theta\right)^2\right]^{1/2}} \tag{2.11}$$

for the laboratory reference frame. A series of expansion for $M_1/M_2 << 1$, yields

$$\frac{d\sigma}{d\Omega} = \left(\frac{Z_1 Z_2 e^2}{4E}\right)^2 \left[\sin^{-4}\frac{\theta}{2} - 2\left(\frac{M_1}{M_2}\right)^2 + \ldots\right] \tag{2.12}$$

Equation 2.12 shows that $\frac{d\sigma}{d\Omega}$ is proportional to Z_1^2 and Z_2^2. That is, heavy target and projectile are efficient scatterers than light target and projectile. On the other hand, $\frac{d\sigma}{d\Omega}$ is inversely proportional to E_0^2 and $\sin^4(\theta/2)$, which indicates that low bombarding energy and scattering angle gives rise to high backscattering yield.

Low atomic mass elements such as C are difficult to detect with RBS because their signal lies spectrally atop the much stronger substrate signal (Rutherford backscattering peak counts being proportional to atomic number squared) and it has a correspondingly substantial noise. In nuclear reaction analysis (NRA), an incident ${}^4_2He^{2+}$ ion may initiate a nuclear reaction by penetrating a target nucleus if it has enough energy to overcome the Coulomb barrier, forming an intermediate excited nuclear state that immediately decays back to the ground state by emission of a particle in the case of *prompt* reactions. Some nuclear reactions generate more slowly decaying radioactive states, on the scale of minutes to hours. This non-Rutherford scattering process can result in a distinct enhancement of the signal (peak intensity) of target nuclei because the quantum mechanics for activation of such nuclear states produces a scattering cross section that is much higher than classical Columbic scattering as shown below. For example, NRA enhancement of the cross section of carbon is displayed in Figure 2.12 as a function of the incident beam energy.

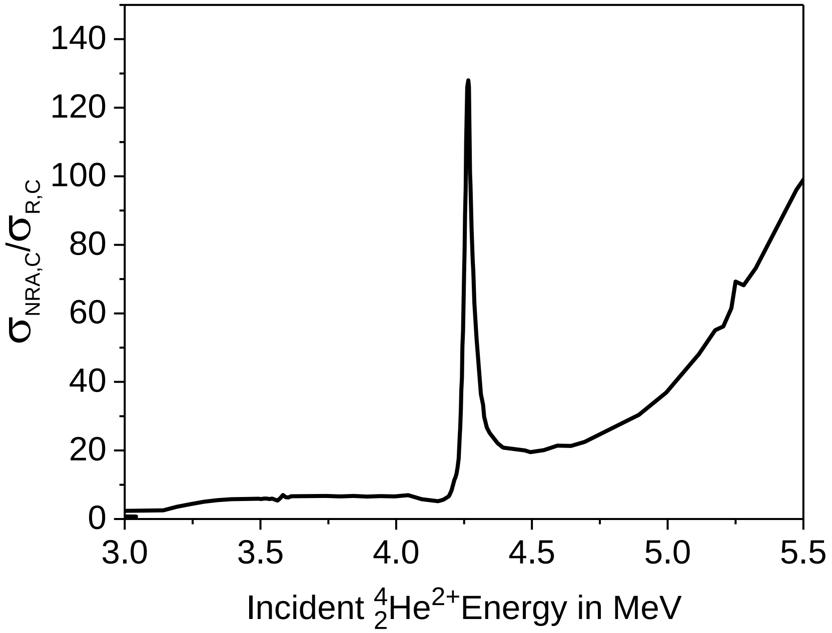

Figure 2.12 Ratio of nuclear resonant scattering cross section to rutherford scattering cross section of C veres incident beam energy at backscattering angle of 165°.[43]

RBS quantifies the areal concentration of a sample (molecules per unit area) not thickness. One must know the density of the film in order to calculate film thickness. The areal density (N_s) can be calculated according to equation 2.13[39]:

$$N_s = A \cos \theta / [(\frac{d\sigma}{d\Omega}) \Omega Q] \tag{2.13}$$

where, A is the total number of ions detected, and θ is the tilt angle of the sample relative to the ion beam, $\frac{d\sigma}{d\Omega}$ is the differential scattering cross section per unit angle, Ω is the detector solid angle, and Q is the total number of incident ions.

2.3.5 Cyclic Voltammetry. Cyclic voltammetry is a type of potentiodynamic electrochemical measurement that measures the current as a function of electrode potential. The utility of CV depends on the analyte under study, which has to be redox active within the scanned potential. In order to measure both current and potential simultaneously, 3 electrodes are required. A Pt electrode is used as counter electrode, Ag electrode is used as reference electrode, and monolayer coated electrode serves as the working electrode. To obtain a cyclic voltammogram, a sawtooth potential is applied between the working electrode and reference electrode, and the resulting current between the counter and electrode is measured.

While XPS, IR, and RBS are used to provide information about composition and structure of the monolayer, CV is used to probe the nature of defects and charge transfer rates.[41]

2.4 References

(1) Vericat, C.; Vela, M. E.; Corthey, G.; Pensa, E.; Cortés, E.; Fonticelli, M. H.; Ibañez, F.; Benitez, G. E.; Carro, P.; Salvarezza, R. C. *RSC Adv.* **2014**, *4*, 27730.

(2) Blodgett, K. B. *J. Am. Chem. Soc.* **1934**, *56*, 495.

(3) Blodgett, K. B. *J. Am. Chem. Soc.* **1935**, *57*, 1007.

(4) Langmuir, I.; Schaefer, V. J. *J. Am. Chem. Soc.* **1936**, *58*, 284.

(5) Bonifas, A. P.; McCreery, R. L. *Nat. Nanotechnol.* **2010**, *5*, 612.

(6) Cai, L.; Yao, Y.; Yang, J.; Price, D. W.; Tour, J. M. *Chem. Mater.* **2002**, *14*, 2905.

(7) Küller, a.; El-Desawy, M. a.; Stadler, V.; Geyer, W.; Eck, W.; Gölzhäuser, a. *J. Vac. Sci. Technol. B Microelectron. Nanom. Struct.* **2004**, *22*, 1114.

(8) Zharnikov, M.; Küller, A.; Shaporenko, A.; Schmidt, E.; Eck, W. *Langmuir* **2003**, *19*, 4682.

(9) Allara, D. L.; Nuzzo, R. G. *Langmuir* **1985**, *1*, 52.

(10) Himmel, H.-J.; Kaschke, M.; Harder, P.; Wöll, C. *Thin Solid Films* **1996**, *284-285*, 275.

(11) Frey, S.; Shaporenko, A.; Zharnikov, M.; Harder, P.; Allara, D. L. *J. Phys. Chem. B* **2003**, *107*, 7716.

(12) Willicut, R. J.; McCarley, R. L. *Langmuir* **1995**, *11*, 296.

(13) Han, S. W.; Lee, S. J.; Kim, K. *Langmuir* **2001**, *17*, 6981.

(14) Fadeev, A. Y.; Helmy, R.; Marcinko, S. *Langmuir* **2002**, *18*, 7521.

(15) Wollman, E. W.; Kang, D.; Frisbie, C. D.; Lorkovic, I. M.; Wrighton, M. S. *Society* **1994**, 4395.

(16) Love, J. C.; Estroff, L. A.; Kriebel, J. K.; Nuzzo, R. G.; Whitesides, G. M. *Chem. Rev.* **2005**, *105*, 1103.

(17) Beebe, J. M.; Engelkes, V. B.; Miller, L. L.; Frisbie, C. D. *J. Am. Chem. Soc.* **2002**, *124*, 11268.

(18) Nuzzo, R. G.; Allara, D. L. *J. Am. Chem. Soc.* **1983**, *105*, 4481.

(19) Vericat, C.; Vela, M. E.; Benitez, G.; Carro, P.; Salvarezza, R. C. *Chem. Soc. Rev.* **2010**, *39*, 1805.

(20) Rodríguez, L. M.; Gayone, J. E.; Sánchez, E. A.; Grizzi, O.; Blum, B.; Salvarezza, R. C.; Xi, L.; Lau, W. M. *J. Am. Chem. Soc.* **2007**, *129*, 7807.

(21) Caldwell, W. B.; Campbell, D. J.; Chen, K.; Herr, B. R.; Mirkin, C. A.; Malik, A.; Durbin, M. K.; Dutta, P.; Huang, K. G. *J. Am. Chem. Soc.* **1995**, *117*, 6071.

(22) Torrelles, X.; Barrena, E.; Munuera, C.; Rius, J.; Ferrer, S.; Ocal, C. *Langmuir* **2004**, *20*, 9396.

(23) Walter, M.; Akola, J.; Lopez-Acevedo, O.; Jadzinsky, P. D.; Calero, G.; Ackerson, C. J.; Whetten, R. L.; Grönbeck, H.; Häkkinen, H. *Proc. Natl. Acad. Sci. U. S. A.* **2008**, *105*, 9157.

(24) Fuxen, C.; Azzam, W.; Arnold, R.; Witte, G.; Terfort, A.; Wöll, C. *Langmuir* **2001**, *17*, 3689.

(25) Kim, Y. T.; McCarley, R. L.; Bard, A. J. *J. Phys. Chem.* **1992**, *96*, 7416.

(26) Sabatani, E.; Cohen-Boulakia, J.; Bruening, M.; Rubinstein, I. *Langmuir* **1993**, *9*, 2974.

(27) Demissie, A. T.; Haugstad, G.; Frisbie, C. D. *J. Am. Chem. Soc.* **2015**, *137*, 8819.

(28) Rosink, J. J. W. M.; Blauw, M. A.; Geerligs, L. J.; van der Drift, E.; Rousseeuw, B. A. C.; Radelaar, S.; Sloof, W. G.; Fakkeldij, E. J. M. *Langmuir* **2000**, *16*, 4547.

(29) Choi, S. H.; Risko, C.; Delgado, M. C. R.; Kim, B.; Brédas, J.-L.; Frisbie, C. D. *J. Am. Chem. Soc.* **2010**, *132*, 4358.

(30) Choi, S. H.; Frisbie, C. D. *J. Am. Chem. Soc.* **2010**, *132*, 16191.

(31) Luo, L.; Frisbie, C. D. *J. Am. Chem. Soc.* **2010**, *132*, 8854.

(32) Ellipsometry http://america.pink/ellipsometry_1415432.html (accessed Apr 4, 2016).

(33) Ulman, A.; Eilers, J. E.; Tillman, N. *Langmuir* **1989**, *5*.

(34) Smart, R.; McIntyre, S.; Bancroft, M.; Bello, I. X-ray Photoelectron Spectroscopy - Powerpoint slides http://mmrc.caltech.edu/SS_XPS/XPS_PPT/XPS_Slides.pdf (accessed Jan 20, 2004).

(35) Powell, C. J.; Jablonski, a. *J. Electron Spectros. Relat. Phenomena* **2010**, *178-179*, 331.

(36) Powell, C. J.; Werner, W. S. M.; Smekal, W. *Surf. Interface Anal.* **2011**, *43*, 1046.

(37) Choi, S. H.; Kim, B.; Frisbie, C. D. *Science* **2008**, *320*, 1482.

(38) Luo, L.; Choi, S. H.; Frisbie, C. D. *Chem. Mater.* **2011**, *23*, 631.

(39) Chu, W.-K.; Mayer, J. W.; Nicolet, M. *Backscattering Spectrometry*; Academic Press, INC: New York, 1978.

(40) Haugstad, G. Ion Beam Analysis - Powerpoint slides, 2011, 51.

(41) Chidsey, C. E. D.; Bertozzi, C. R.; Putvinski, T. M.; Mujsce, A. M. *J. Am. Chem. Soc.* **1990**, *112*, 4301.

(42) Luo, L.; Frisbie, C. D. *J. Am. Chem. Soc.* **2010**, *132*, 8854.

(43) Feng, Y.; Zhou, Z.; Zhou, Y.; Zhao, G. *Nucl. Instruments Methods Phys. Res. Sect. B Beam Interact. with Mater. Atoms* **1994**, *86*, 225.

3 Molecular Junctions

The influence of structure on charge transport in molecules is a central goal in molecular electronics.[1–12] To realize this goal, one must bring molecules into contact between two conducting electrode separated by a few nanometers as shown in Figure 1.2. This chapter explores some of the methods used to form nanoscopic junctions with molecules. Molecular junctions can be divided into 2 categories: soft contact and hard contact. In soft contact, the top electrode gently approaches the molecules and makes a temporary contact. In hard contact, a permanent contact is made with molecules between the top and bottom electrodes. Hard contacts such as thermally evaporated top metal contact on self-assembled monolayers (SAMs) have very low yield of working junctions due to electrical short. On the other hand, soft contacts have feedback mechanisms that allow the user to control multiple variables such as approach speed and applied load on the molecules.

Recent advances of organic electronics in devices such as organic light emitting diodes (OLEDs), thin film transistors (TFTs), and roll to roll organic photovoltaic (OPV) solar cells have demonstrated the utility of organic molecules.[13,14] For example, Samsung Galaxy S6 and Galaxy S6 Edge smart phones have OLED displays.[15] Bulk film properties such as defects, and morphological complexities associated with thin films play a significant role in determining the electrical properties of such devices. On the other hand, nanoscopic junctions probe the electrical properties of a molecule or ensemble of molecules where the effects of defects and morphology are absent. This also opens the door to explore the charge transport phenomena in chemical and biological systems. It should be noted that the transport characteristics of a molecular junction depends on the nature of the metal-molecule interface (chemisorbed vs physisorbed) and contact type in addition to the molecules.

3.1 Molecular Junction Fabrication Techniques

3.1.1. Scanning Tunneling Microscope Junctions

Scanning Tunneling Microscope junctions involve the use of atomically flat tips to contact a single molecule or couple of molecules depending on the sharpness of the tip. In STM measurements, the tip is initially brought closer to the sample via current feedback mechanism. A bias is applied between the STM tip and the conducting substrate, and the tunneling current between both is monitored.[16] When the tunneling current is kept constant (constant current mode), the height profile of the surface is recorded. When the position of the probe is kept constant (constant height mode), the change in current is recorded. Once the tip has formed contact with the substrate, the feedback is turned off and I-V measurements are taken. In addition to transport measurements, STM is heavily used to image molecules on the surface. Much of our understanding about the kinetics and structures of self-assembly is due to STM images on conductive substrates.[17] For example, mixed monolayer assembly of insulating and conducting molecules were imaged by Nakasa et al., and the results showed obvious contrast difference between the two types of molecules.[18] Thus, the sub-molecular resolution of STM is critically important for studying the influence of intermolecular interaction on charge transport.

Since the I-V measurements are not under any feedback mechanisms, a major disadvantage of STM for charge transport study is in the ambiguity of the tunneling barrier height. Therefore, it is not clear whether a given change in current corresponds to change in height or change in conductance of a molecule.[19] Other problems associated with lack of feedback mechanism include lateral tip drift.

Tao et al., developed STM-break junction method by repeatedly moving a STM tip into and out of contact with substrate electrode that contains the sample molecules in solution.[20] As shown in Figure 3.1, the conductance of Au contact between the STM tip and Au substrate decreased in quantum unit of conductance (Go) as Au tip is pulled away from the substrate. When the last contact is completely broken, new series of

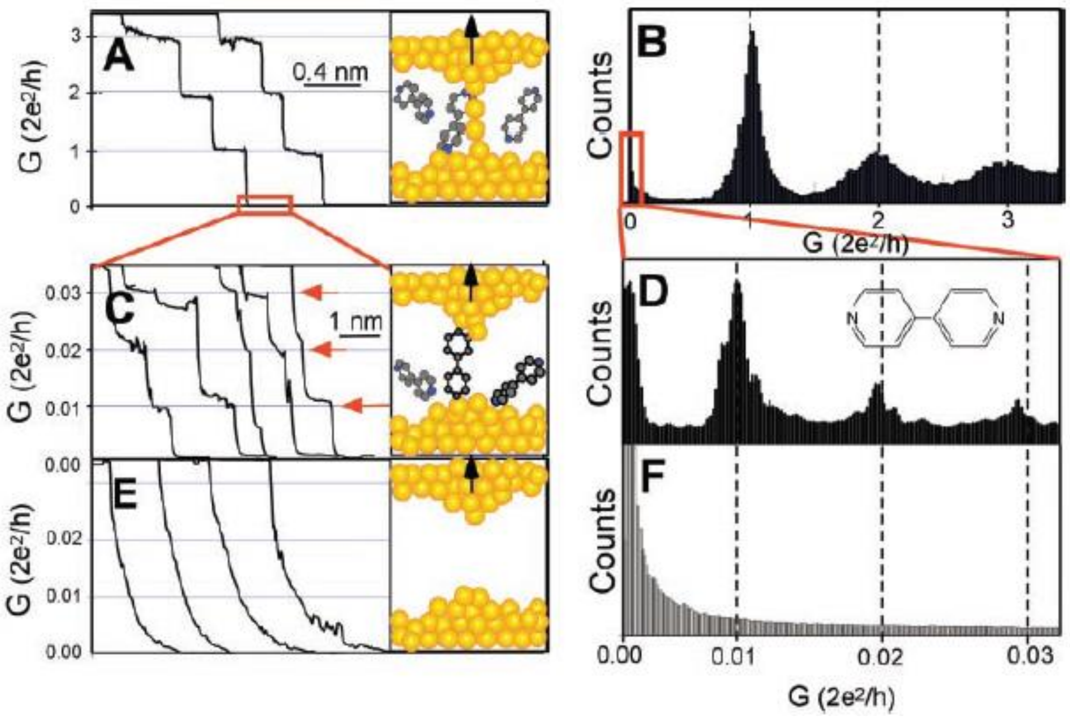

Figure 3.1 (A) Conductance decrease of Au-Au contact between Au substrate and Au tip as the tip is pulled away. (B) Corresponding histogram plot for 100 curves as shown in A. The conductance decreases near quantum steps of Go. (C) New series of conductance steps formed by molecules that bridged the gap between the broken Au contacts. (D) Conductance histograms from the stable molecular junctions formed in C. The peaks near 0.01, 0.02 and 0.03 G0 corresponds to 1,2, and 3 molecule(s) in the junction. (E) In the absence of molecules, there were no steps were observed in the same conductance range as shown in F. Adapted from reference 20 with permission from the American Association for the Advancement of Science.

conductance steps appear if molecules that can bridge the gap between the substrate and STM tip are present in solution, as shown in Figure 3.1c. The corresponding histogram (1000 curves) from the molecular junction formed is shown in Figure 3.1d. The conductance values at 0.01Go, 0.02Go, and 0.03 Go correspond to 1, 2 and 3 molecules in the junction, respectively.[20] Figure 3.1e and 3.1f show the absence of conductance steps without bridging molecules.

3.1.2 Break Junctions

Break junctions comprises of two types, mechanically controlled break junctions and electromigration break junctions. The mechanically controlled break junctions consists of lithographically defined metallic free suspended bridge or a notched wire above a gap etched in an insulating (polymer or oxide) layer on a, preferably, bendable substrate.[21] A piezo element then pushes the substrate and splits the wire, while counter

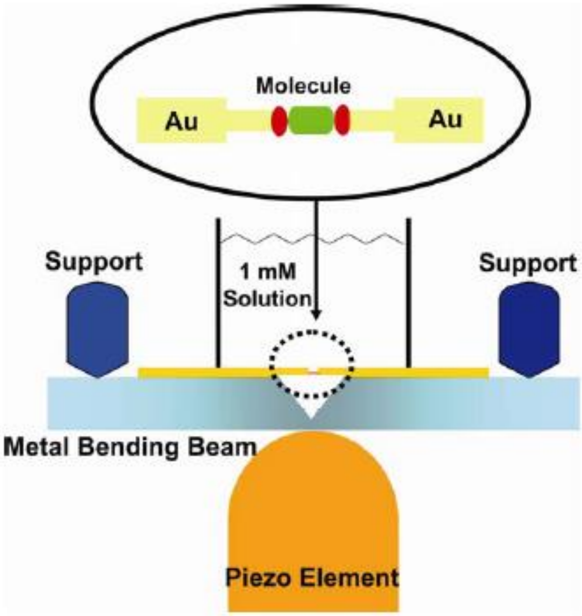

Figure 3.2 Schematic of mechanically controllable break junction. Adapted from reference 21 with permission from the American Association for the Advancement of Science.

supports at the sides of the sample keeps the substrate fixed at a certain position as shown in Figure 3.2. A molecule can then bridge the gap and form a junction. Due to the high reduction factor between the piezo micrometer precision and the in plane elongation, the separation between electrodes can be altered with sub-nm resolution.[16] The back and forth bending allows for performing statistically relevant large number of junctions in a single experiment.

Electromigration is another method for forming break junctions, where the gap between the electrodes is formed by application of large bias.[22] Typically, the gap ranges from 1-2 nm. However, if the gaps are formed on rigid substrates like Si, it cannot be altered after formation. Break junctions are compatible for variable temperature study. Some problems include formation of cluster of molecules on the electrodes which could complicate analysis of the obtained result.

3.1.3 Conducting Probe Atomic Force Microscopy

Conducting probe atomic force microscopy is another type of scanning probe technique similar to STM, but different in probe size and feedback mechanism. Over the past decade, our group and others demonstrated that CP-AFM is a convenient and reproducible approach for forming molecular junctions.[11,12,23–28] A metal coated AFM tip is brought into contact with molecules under controlled load. The tip is coated by conventional thermal evaporation of 5 nm Cr as adhesion layer followed by 50-100 nm of metal (Au, Ag or Pt). An optical feedback mechanism that uses a laser beam reflected off the back surface of the AFM tip is used to precisely control the load on the molecules. Typically, the applied load ranges between 1-10 nN. CP-AFM offers the flexibility to study the influence of contact type (physisorbed or chemisorbed), and metal contact

(contact resistance) on I-V measurements. For example, Beebe et al., reported that the value of the contact resistance and SAM resistance decreased by 2 orders of magnitude with increasing work function of the metal contacts.[29]

CP-AFM is also compatible for variable temperature measurements, which are extremely important for verifying transport mechanisms such as tunneling or hopping. For example, OPI molecular wires have temperature independent I-V characteristics for wires less than 4 nm in length, and thermally activated transport mechanism for wires longer than 4 nm.[30]

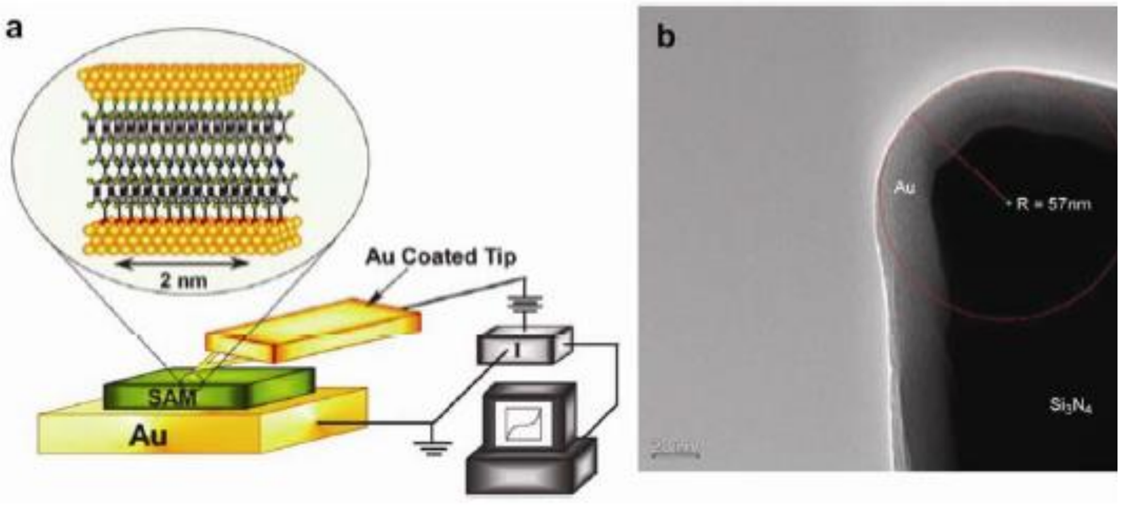

Figure 3.3 (A) Schematic of conducting probe atomic force microscopy (CP-AFM). (B) Transmission electron microscopy image of AFM tip. Adapted from reference 30 with permission from WILEY-VH Verlag & Co.

3.1.4 Eutectic Gallium Indium Mixture

Eutectic Gallium Indium (75% Ga and 25% In) mixture junctions consists of conformal, soft contacts to molecules. EGaIn junctions can be classified into two types: conical and microfluidic stabilized junctions. The conical EGaIn junctions are made by slowly retracting a needle that is in contact with a drop of liquid EGaIn until it bifurcated into two parts (one attached to syringe and another one attached to the bulk EGaIn).[31] Using a micromanipulator, the needle tip is slowly brought into contact with SAMs, and the I-V measurements are then executed. EGaIn mixtures have a sacrificial conducting gallium oxide layer (GaOx) that forms instantaneously, and prevents alloying of the liquid EGaIn with bottom electrode (short). Some disadvantages of conical EGaIn include variations in tip formation among users, tip drift and vibrations.

Microfluidic stabilized EGaIn junction was recently reported by Nijhuis et al.[32–34] Here, the GaOx/EGaIn was stabilized in a microfluidic device made of a transparent rubber of polydimethylsiloxane (PDMS). This requires a few lithography steps to make two microchannels as shown in Figure 3.4. Channel 1 and 2 were then filled with the EGaIn mixture by applying vacuum at the outlets, respectively. The dimensions of channel 2 were chosen such that the high surface tension of the liquid metal prevented it from completely filling the channel. The top electrode was then carefully placed on the SAMs, and electrical measurements were performed by forming one contact between the GaOx/EGaIn at the inlet of the channel of the top-electrode via a tungsten probe mounted on a micromanipulator, and another contact was placed on the substrate. Microfluidic EGaIn junctions have lots of advantage versus conical EGaIn junctions: highly reproducible data sets among users, small log distribution of conductance histograms, high electrical stability (up to 2500 cycles), high yield (78%) of working junctions, and compatibility with variable temperature and AC measurements.[32]

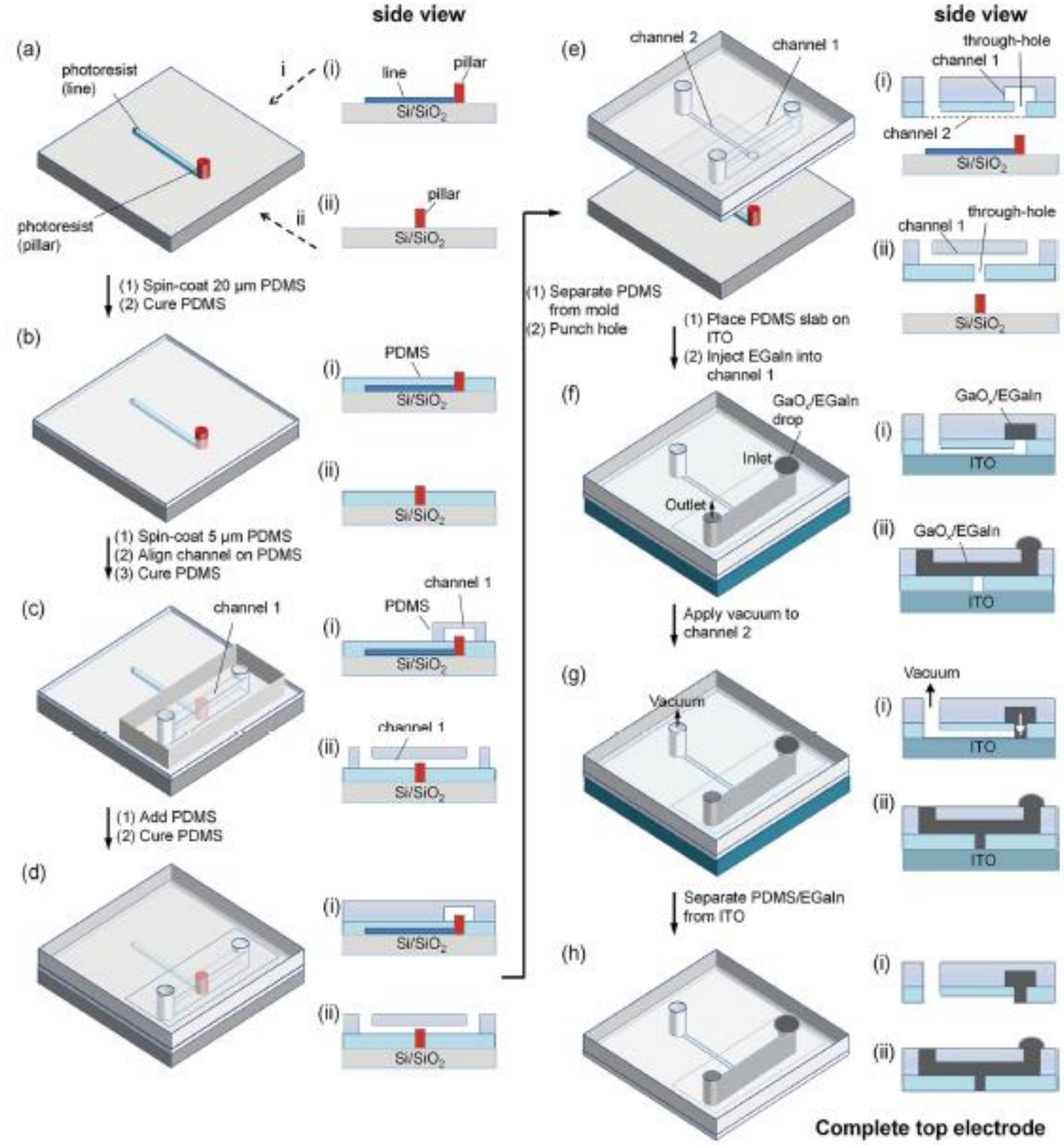

Figure 3.4 Schematics of microfluidic stabilized EGaIn junction fabrication process. a) The mold consists of a line and a pillar on a Si/SiO$_2$ wafer with a layer of FOTS (FOTS is not indicated for clarity). b) A layer of PDMS (20 μm) was spin-coated on the mold to fully cover the photoresist line, but not the pillar, and cured. c) A thin layer of PDMS (5 μm) was spin-coated on the first layer of PDMS and channel 1 in PDMS was aligned over the pillar perpendicularly with respect to the line of the mold. The thin layer of PDMS was cured. d) More uncured PDMS was added to stabilize the thin layer of PDMS and cured. e) The microfluidic device was peeled off from the mold and a hole was punched at the end of the small channel. f) We placed the microfluidic device on an ITO substrate and injected GaOx / EGaIn into the PDMS channel. g) The through-hole was filled with GaOx / EGaIn by applying vacuum to channel 2. h) Separation of the microfluidic device from the ITO yielded a complete top-electrode. Adapted from reference 32 with permission from Nature Materials.

3.1.5 Surface Diffusion Metal Deposition

Recently, Bonifas and McCreery reported a novel method to contact individual molecules one at a time using surface diffusion metal deposition (SDMD), and to perform in-situ current monitoring during formation of contact.[35] As shown in Figure 2, the monolayers are shielded by a layer of SiO_2 to avoid penetration of the evaporated atoms. Once the metal atoms land on the substrate, they diffuse and contact the molecules without damaging the monolayers since their kinetic energy is dissipated by the time they approach the molecular interface. Thus, measurements of current during diffusion step permits observations of conductance steps for junctions as small as a molecule as shown in Figure 3.5b.

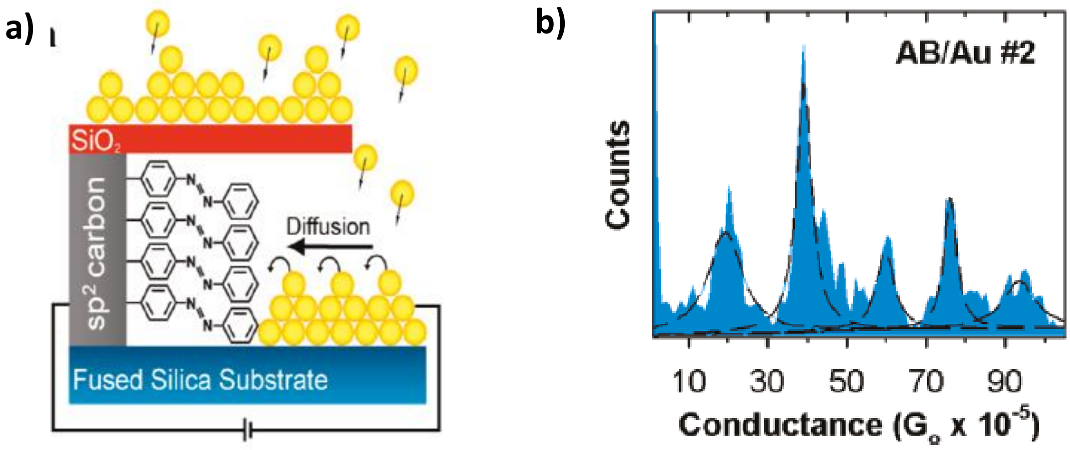

Figure 3.5 (A) Schematics of in-situ SDMD technique with azobenzene monolayer attached to conductive sp^2 carbon. (B) Histogram of >24,000 data points collected every 50 ms. Adapted from reference 35 with permission from Nano Letters.

3.2 Comparison of CP-AFM, STM, and EGaIn Testbeds

Akkerman, et al. noticed a striking 7-8 orders of magnitude difference in the resistance per molecule verses the junction area, but a good explanation for this general observation across testbeds is lacking.[36] We and other have shown that SAMs of alkyl dithiols (i.e., molecules with terminal –SH group that can chemically bond with the top electrode after contact) has nearly 2 orders of magnitude lower resistance than SAMs with alkyl monothiols.[2,29,37] Thus, when comparisons are made between different testbeds, it is important to compare measurements performed on the same type of molecules or SAMs only. Furthermore, the contacts need to be of similar type (Au/Au junctions to Au/Au) since the barrier height changes with the work function of the electrode. For example, for HOMO mediated tunneling, the fermi level-HOMO offset (barrier height) increases with decreasing contact work function for Pt (5.6 eV), Au (5.1 eV), and Ag (4.3 eV), respectively.

3.2.1 Comparison of alkyl dithiols via CP-AFM and STM junctions

Electrical transport measurement of alkyl dithiols on CP-AFM[29] and STM[20] molecular junctions are compared in this section. In both junctions, the molecules are contacted by Au/Au electrodes. The STM conductance measurements by Tao et al.,[20] were converted to resistance per molecule simply by taking the inverse of the conductance values. The high conductance (HC) and low conductance (LC) correspond to different geometries of the anchoring molecule.

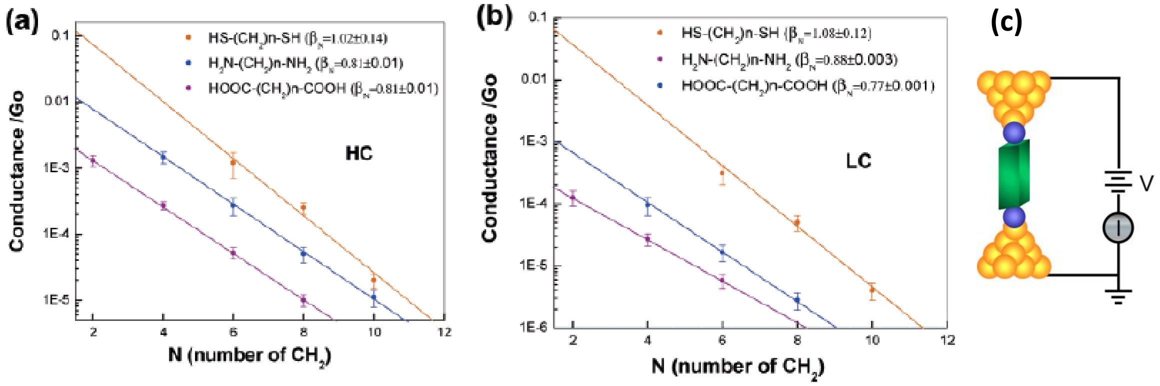

Figure 3.6 A semilog plot of conductance verses number of methyl groups for dithiol (orange), diamine (blue), and dicarboxylic acid (purple) terminated alkanes for a) HC and b) LC. It is clear that the measured resistance and contact resistance depends on terminal groups. Adapted from reference 20 with permission from the journal of the American Chemical Society. Schematic illustration of STM junction (c).

Sample calculation for single molecule resistance (r) for C6 from Figure 3.6

$$r = G^{-1}$$

$$\text{C6, } G = 1.5 \times 10^{-3}\ \text{Go} = 1.5 \times 10^{-3} \times 7.748 \times 10^{-5}\ \text{S}$$

$$= 1.2 \times 10^{-7}\ \text{S}$$

$$\text{C6, } r = 1/G = 1/(1.2 \times 10^{-7}\ \text{S}) = 8.6\ \text{M}\Omega$$

C 8 = 48 MΩ, C 10 = 645 MΩ

Similarly for LC,

C6 = 43 MΩ, C8 = 258 MΩ, C10 = 3230 MΩ

For CP-AFM, the reported resistance values for dithiol SAMs on Au/Au junctions were taken from Figure 3.7. The molecules were then treated as parallel combination of resistors.

Single molecule resistance (r) calculation for C6;

$$\frac{1}{R}=\frac{\Gamma}{r},$$

where, Γ is the total number of molecules in contact

For tip size of 50 nm^2 and coverage of 3.5 molecule/nm^2

$$\Gamma = 175$$

$$\text{C6,} \qquad r = \Gamma \times R \; (R = 3 \times 10^5\ \Omega)$$

$$= 175 \times 3 \times 10^5\ \Omega$$

$$= 61.3\ \text{M}\Omega$$

Similarly, r(C4) = 4.38 MΩ, and r(C8) = 525 MΩ

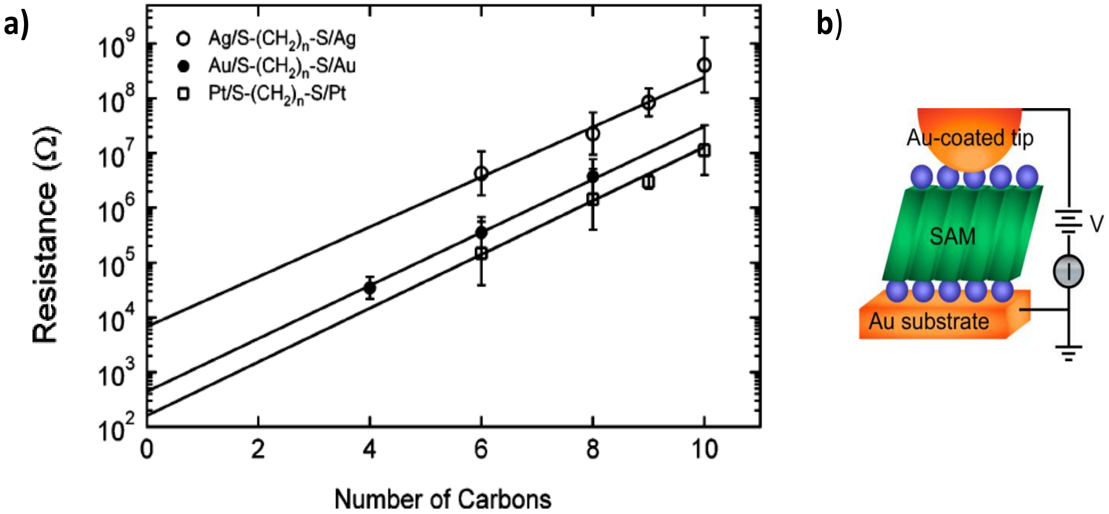

Figure 3.7 A semilog plot of the measured resistance for alkyl dithiols for Au/Au, Ag/Ag, and Pt/Pt junctions. B) Schematics of the CP-AFM junction (not drawn to scale). Adapted from reference 29 with permission from Journal of the American Chemical Society

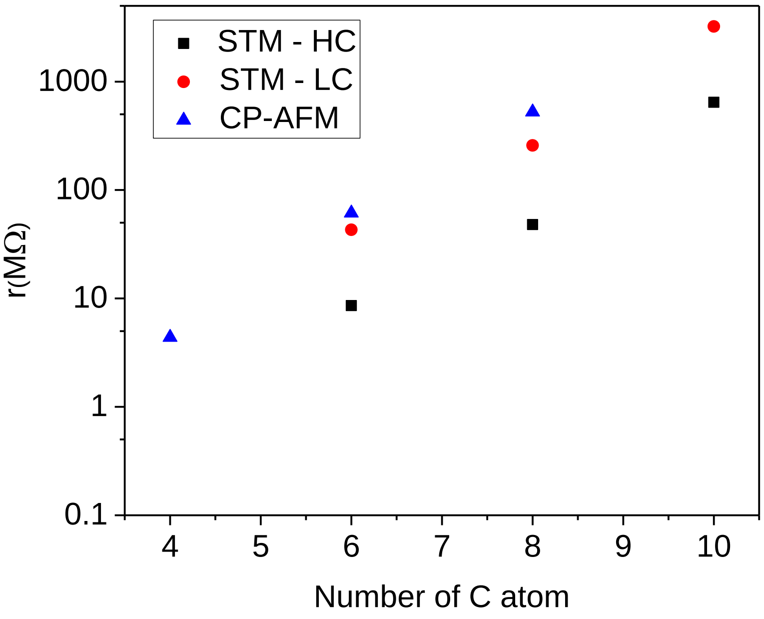

Figure 3.8 A Semi log plot of resistance per molecule (r) values number of C atoms in the junction for CP-AFM and STM measurements.

The resistance per molecule (r) values for CP-AFM and STM-LC are in good agreement. The geometry of the SAM arrays is better described in CP-AFM than single molecule experiments, where the molecules are floating around in solution. Furthermore, the value of the contact work function for a point contact is not necessarily similar to its bulk value, and can be a potential source of variation between the CP-AFM and STM-HC values in Figure 3.8.

3.2.2 Comparison of alkyl monothiols via CP-AFM and EGaIn junctions

Electrical transport measurement of alkyl monothiols on EGaIn and CP-AFM molecular junctions are compared in this section. In EGaIn junctions, the molecules were assembled on template stripped Ag substrate and contacted by EGaIn top electrode. EGaIn has relatively similar work function as Ag. In CP-AFM junctions, the molecules were assembled on template stripped Ag substrate and contacted by Ag coated AFM tip. The resistances per molecule calculations for EGaIn junctions are shown below. The low bias resistance (-0.1 V to 0.1 V) were tabulated from the J-V plot reported by Nijhuis et al.[38]

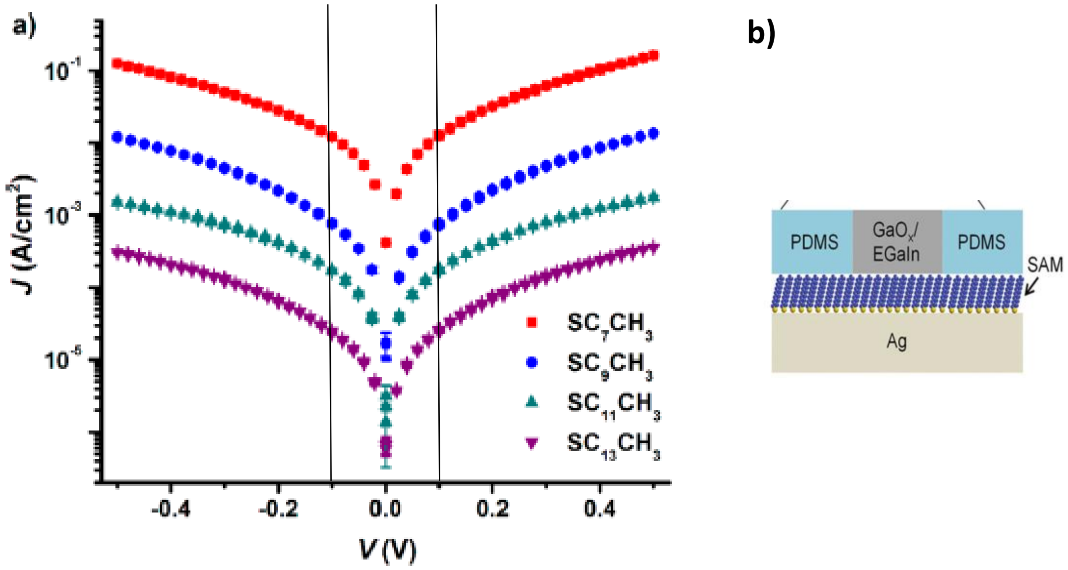

Figure 3.9 a) Semilog plots of current density (J) vs applied voltage for alkyl monothiol SAMs. The low bias resistance (±0.1V) was calculated from the linear fit of J vs V. b) Schematic illustration of EGaIn molecular junctions. Adapted from reference 38 with permission from the journal of the American Chemical Society.

Single molecule resistance (r) calculation for C10

$$\frac{1}{R} = \frac{\gamma \Gamma}{r},$$

Where, R is low bias resistance (-0.1 V to 0.1 V)

γ is the area correction factor (10^{-4})

Γ is the total number of molecules in junction

For EGaIn junction size of 960 μm^2 (geometrical) and coverage of 4.5 molecules /nm^2

$$\text{C10, R} = \frac{1262.62\ \Omega.cm^2}{960 \times 10^{-8} cm^2} = 1.32 \times 10^8\ \Omega$$

$$r = \gamma \times \Gamma \times R$$

$$= 10^{-4} \times 4.5 \times 960 \times 10^{6} \times 1.32 \times 10^{8}\ \Omega$$

$$= 5.68 \times 10^{7}\ \mathrm{M\Omega}$$

C8, $r = 4.10 \times 10^{6}\ \mathrm{M\Omega}$ C14, $r = 1.84 \times 10^{9}\ \mathrm{M\Omega}$ C12, $r = 2.38 \times 10^{8}\ \mathrm{M\Omega}$

The area correction factor (γ) in the EGaIn junction accounts for the effective contact area (not geometrical area), or the true area of the electrodes that is in direct intimate contact with the molecules. This number was adapted from the work of Simeone et al., who measured J-V characteristics of thermally grown Fe_2O_3 on template stripped Fe substrates via the Hg drop junction and conical EGaIn junctions.[39] Since the Fe_2O_3 layer has a much higher resistivity than the electrodes, it was expected that the measured current density would be the same for both molecular junctions. However, the obtained current density (J) for conical EGaIn junctions were 3 orders of magnitude lower than that of Hg junctions as shown in Figure 3.10.[39] This discrepancy was attributed to the area correction factor from the top electrode (EGaIn contact – 10^{-3}). A second area correction for the bottom substrate was calculated from the STM image. The contact area

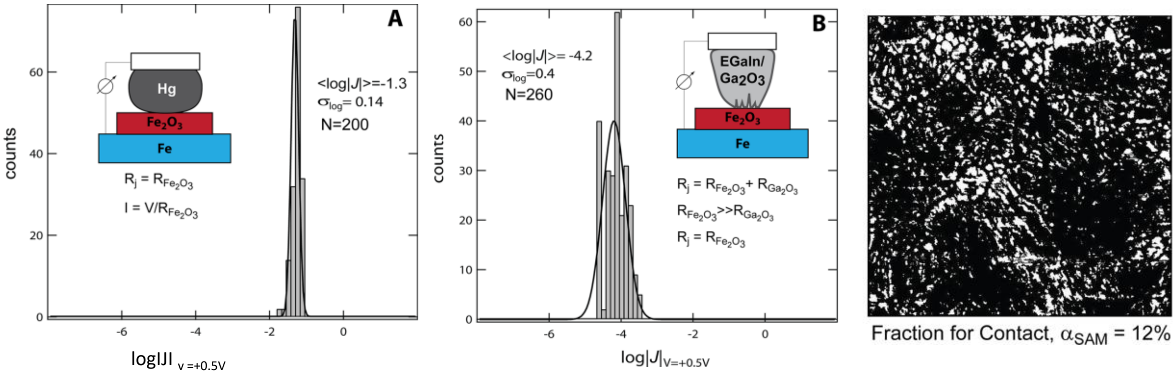

Figure 3.10 Histograms of the value of logJ at V=-0.5V for Fe/Fe_2O_3//Hg junctions (A) and Fe/Fe_2O_3//EGaIn junctions (B). (C) Surface area available for contact estimated from digital analysis of STM image of the bottom template stripped electrode (white). Adapted from reference 39 with permission from the journal of the American Chemical Society.

was estimated within 2 Å from the top most average plane of the image, which resulted in ~ 12% of the geometrical area.[39] Thus, a total area correction factor of 10^{-4} was used.

For CP-AFM, the reported resistance values for dithiol SAMs on Au/Au junctions were taken from the plot in Figure 3.11. The single molecule resistance was calculated as shown below.

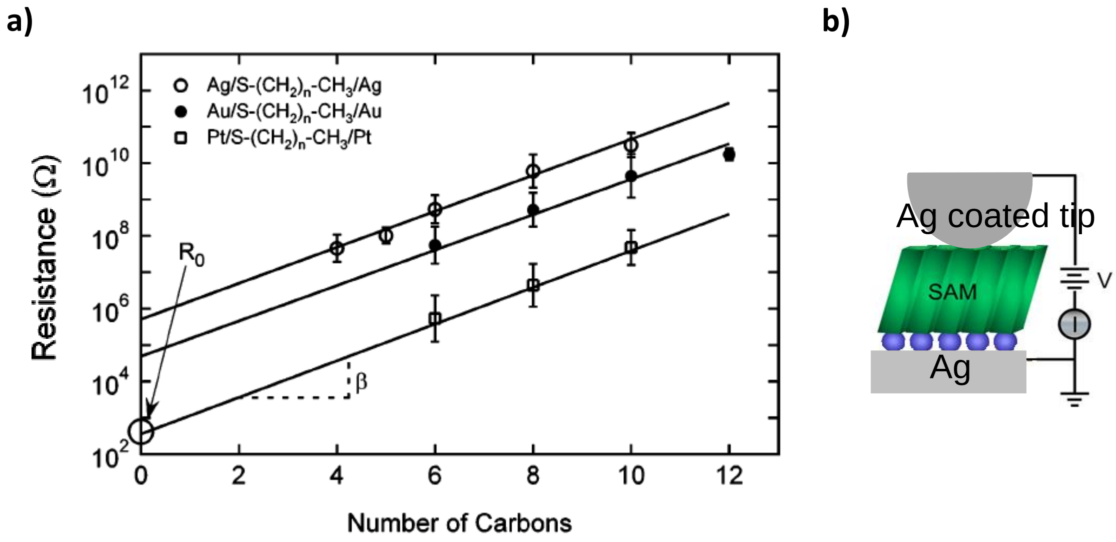

Figure 3.11 Semi-log plot of the measured resistance for alkyl dithiols for Au/Au, Ag/Ag, and Pt/Pt junctions. B) Schematics of the CP-AFM junction (not drawn to scale). Adapted from reference 29 with permission from Journal of the American Chemical Society.

Single molecule resistance (r) calculation for C4

$$\frac{1}{R} = \frac{\Gamma}{r},$$

Where, Γ is the total number of molecules in junction

For tip size of 50 nm^2 and coverage of 4.5 molecule / nm^2

$\Gamma = 225$

C4 $R = 5 \times 10^7\ \Omega$, $r = \Gamma \times R$

$r = 225 \times 5 \times 10^7\ \Omega$

$= 1.13 \times 10^4$ MΩ

C6, $r = 1.35 \times 10^5$ MΩ C10, $r = 1.01 \times 10^7$ MΩ C8, $r = 1.8 \times 10^6$ MΩ

Figure 3.12 displays the area normalized single molecule resistance for CP-AFM and EGaIn monothiol junctions. It is clear that both junctions yield similar r values after correcting for contact area.

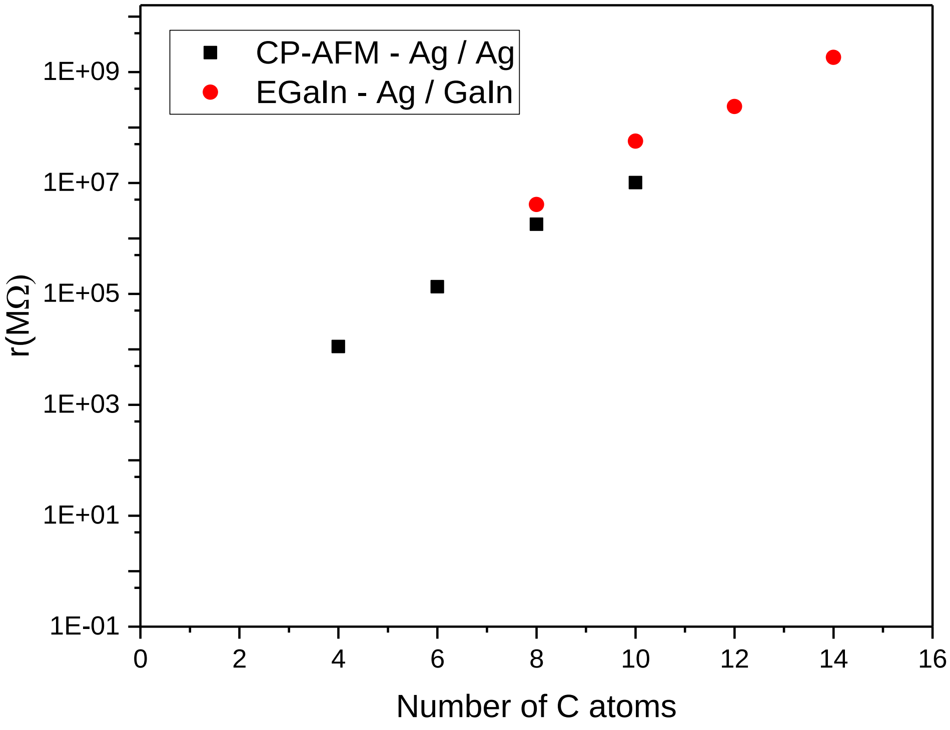

Figure 3.12 A Semi log plot of resistance per molecule (r) values number of C atoms in the junction for CP-AFM and STM measurements.

3.3 References

(1) Love, J. C.; Estroff, L. A.; Kriebel, J. K.; Nuzzo, R. G.; Whitesides, G. M. *Chem. Rev*. **2005**, *105*, 1103.

(2) Chen, W.; Widawsky, J. R.; Vázquez, H.; Schneebeli, S. T.; Hybertsen, M. S.; Breslow, R.; Venkataraman, L. *J. Am. Chem. Soc*. **2011**, *133*, 17160.

(3) Hines, T.; Díez-Pérez, I.; Nakamura, H.; Shimazaki, T.; Asai, Y.; Tao, N. *J. Am. Chem. Soc*. **2013**, *135*, 3319.

(4) Cademartiri, L.; Thuo, M. M.; Nijhuis, C. A.; Reus, W. F.; Tricard, S.; Barber, J. R.; Sodhi, R. N. S.; Brodersen, P.; Kim, C.; Chiechi, R. C.; Whitesides, G. M. *J. Phys. Chem. C* **2012**, *116*, 10848.

(5) Yuan, L.; Jiang, L.; Zhang, B.; Nijhuis, C. A. *Angew. Chemie - Int. Ed.* **2014**, *53*, 3377.

(6) Sayed, S. Y.; Bayat, A.; Kondratenko, M.; Leroux, Y.; Hapiot, P.; McCreery, R. L. *J. Am. Chem. Soc.* **2013**, *135*, 12972.

(7) Alloway, D. M.; Graham, A. L.; Yang, X.; Mudalige, A.; Colorado, R.; Wysocki, V. H.; Pemberton, J. E.; Randall Lee, T.; Wysocki, R. J.; Armstrong, N. R. *J. Phys. Chem. C* **2009**, *113*, 20328.

(8) Reuter, M. G.; Solomon, G. C.; Hansen, T.; Seideman, T.; Ratner, M. A. *J. Phys. Chem. Lett.* **2011**, *2*, 1667.

(9) Yaffe, O.; Ely, T.; Har-Lavan, R.; Egger, D. A.; Johnston, S.; Cohen, H.; Kronik, L.; Vilan, A.; Cahen, D. *J. Phys. Chem. C. Nanomater. Interfaces* **2013**, *117*, 22351.

(10) Bâldea, I.; Xie, Z.; Frisbie, C. D. *Nanoscale* **2015**, *7*, 10465.

(11) Taherinia, D.; Smith, C. E.; Ghosh, S.; Odoh, S. O.; Balhorn, L.; Gagliardi, L.; Cramer, C. J.; Frisbie, C. D. *ACS Nano* **2016**.

(12) Smith, C. E.; Odoh, S. O.; Ghosh, S.; Gagliardi, L.; Cramer, C. J.; Frisbie, C. D. *J. Am. Chem. Soc.* **2015**.

(13) Sirringhaus, H. *Adv. Mater.* **2014**, *26*, 1319.

(14) Dou, L.; You, J.; Hong, Z.; Xu, Z.; Li, G.; Street, R. A.; Yang, Y. *Adv. Mater.* **2013**, *25*, 6642.

(15) Samsung Galaxy S7 display, possibilities for future http://www.igalaxys7.com/samsung-galaxy-s7-display/ (accessed Apr 1, 2016).

(16) Akkerman, H. B.; de Boer, B. *J. Phys. Condens. Matter* **2008**, *20*, 013001.

(17) Vericat, C.; Vela, M. E.; Benitez, G.; Carro, P.; Salvarezza, R. C. *Chem. Soc. Rev.* **2010**, *39*, 1805.

(18) Nakasa, A.; Akiba, U.; Fujihira, M. *Appl. Surf. Sci.* **2000**, *157*, 326.

(19) Akkerman, H. B.; Blom, P. W. M.; de Leeuw, D. M.; de Boer, B. *Nature* **2006**, *441*, 69.

(20) Chen, F.; Li, X.; Hihath, J.; Huang, Z.; Tao, N. *J. Am. Chem. Soc.* **2006**, *128*, 15874.

(21) Reed, M. a. *Science (80-.).* **1997**, *278*, 252.

(22) Park, J.; Pasupathy, A. N.; Goldsmith, J. I.; Chang, C.; Yaish, Y.; Petta, J. R.; Rinkoski, M.; Sethna, J. P.; Abruña, H. D.; McEuen, P. L.; Ralph, D. C. *Nature* **2002**, *417*, 722.

(23) Beebe, J. M.; Engelkes, V. B.; Miller, L. L.; Frisbie, C. D. *J. Am. Chem. Soc.* **2002**, *124*, 11268.

(24) Kim, B.; Choi, S. H.; Zhu, X.-Y.; Frisbie, C. D. *J. Am. Chem. Soc.* **2011**, *133*, 19864.

(25) Luo, L.; Benameur, A.; Brignou, P.; Choi, S. H.; Rigaut, S.; Frisbie, C. D. *J. Phys. Chem. C* **2011**, *115*, 19955.

(26) Xie, Z.; Bâldea, I.; Smith, C. E.; Wu, Y.; Frisbie, C. D. *ACS Nano* **2015**, *9*, 8022.

(27) Engelkes, V. B.; Beebe, J. M.; Frisbie, C. D. *J. Phys. Chem. B* **2005**, *109*, 16801.

(28) Cai, L. T.; Skulason, H.; Kushmerick, J. G.; Pollack, S. K.; Naciri, J.; Shashidhar, R.; Allara, D. L.; Mallouk, T. E.; Mayer, T. S. *J. Phys. Chem. B* **2004**, *108*, 2827.

(29) Engelkes, V. B.; Beebe, J. M.; Frisbie, C. D. *J. Am. Chem. Soc.* **2004**, *126*, 14287.

(30) *Charge and Exciton Transport through Molecular Wires*; John Wiley & Sons, 2011.

(31) Chiechi, R. C.; Weiss, E. A.; Dickey, M. D.; Whitesides, G. M. *Angew. Chem. Int. Ed. Engl.* **2008**, *47*, 142.

(32) Wan, A.; Jiang, L.; Sangeeth, C. S. S.; Nijhuis, C. A. *Adv. Funct. Mater.* **2014**, *24*, 4442.

(33) Sangeeth, C. S.; Wan, A.; Nijhuis, C. A. *Nanoscale* **2015**, *7*, 12061.

(34) Yuan, L.; Nerngchamnong, N.; Cao, L.; Hamoudi, H.; del Barco, E.; Roemer, M.; Sriramula, R. K.; Thompson, D.; Nijhuis, C. A. *Nat. Commun.* **2015**, *6*, 6324.

(35) Bonifas, A. P.; McCreery, R. L. *Nano Lett.* **2011**, *11*, 4725.

(36) Bergren, A. J.; Harris, K. D.; Deng, F.; McCreery, R. L. *J. Phys. Condens. Matter* **2008**, *20*, 374117.

(37) Kim, T.; Vázquez, H.; Hybertsen, M. S.; Venkataraman, L. *Nano Lett.* **2013**, *13*, 3358.

(38) Sangeeth, C. S. S.; Wan, A.; Nijhuis, C. a. *J. Am. Chem. Soc.* **2014**, *136*, 11134.

(39) Simeone, F. C.; Yoon, H. J.; Thuo, M. M.; Barber, J. R.; Smith, B.; Whitesides, G. M. *J. Am. Chem. Soc.* **2013**, *135*, 18131.

4. Growth and Comprehensive Characterization of Oligophenylene Imine Molecular Wires

4.1 Abstract

We report systematic characterization of anisotropic, π-conjugated oligophenyleneimine (OPI) films synthesized using stepwise imine condensation, or ‘click’ chemistry. Film synthesis began with a self-assembled monolayer (SAM) of 4-formylthiophenol or 4-aminothiophenol on Au, followed by repetitive, alternate addition of terephthalaldehyde (benzene-1,4-dicarbaldehyde) or 1,4-benzenediamine to form π-conjugated films ranging from 0.6 – 5.5 nm in thickness. By systematically capping the OPI films with a redox or halogen label, we were able to measure relative surface coverage after each monomer addition via Rutherford backscattering spectrometry (RBS), X-ray photoelectron spectroscopy (XPS), spectroscopic ellipsometry (SE), reflection-absorption infrared spectroscopy (RAIRS), and cyclic voltammetry (CV). Nuclear reaction analysis (NRA) was also employed for the first time on a SAM to calculate the surface coverage of carbon atoms after each stepwise addition. These 6 different analysis methods indicate that the average extent of reaction is greater than 99% for each addition step. The high yield and molecular surface coverage confirm the efficacy of Schiff base chemistry, at least with the terephthalaldehyde and 1,4-benzenediamine monomers, for preparing high quality molecular films with π-conjugation normal to the substrate.

4.2 Introduction

Functional organic thin films with precisely tailored electronic and optical properties can be prepared using a variety of controlled stepwise monomer addition techniques. Marks, *et al.*, for example, have prepared dielectric thin films for flexible electronics applications via siloxane mediated stepwise reactions.[1–3] Others have employed metal ion coordination chemistry to build oriented organometallic films for molecular electronics experiments.[4] In our previous work, we have utilized Schiff-base (imine) chemistry to assemble oriented, π-conjugated organic films from simple diamine- and dialdehyde-substituted building blocks.[5–8] Alternatively, we have employed the well-known azide-alkyne reaction chemistry to make π-conjugated films.[9] Each of these approaches relies on efficient ‘click’ or ‘click-like’ reactions to ensure high reaction yields in a simple, sequential monomer addition process. Furthermore, click chemistry is self-limiting, much like atomic layer deposition (ALD) chemistry, so that one has precise nanometer level control over film architecture perpendicular to the substrate.

Film growth by imine click (condensation) chemistry is particularly useful for molecular electronics experiments because it provides a convenient means to obtain extended π-conjugation in the growth direction. However, in the context of film growth from a solid substrate, the reaction yield per step has not been characterized previously, though it is obviously critically important. Low reaction yields – or even not very low yields, of order 90% – give rise to substantial and undesirable polydispersity in the molecular lengths normal to the substrate.

Here we have employed a battery of methods including spectroscopic ellipsometry (SE), reflection-absorption infrared spectroscopy (RAIRS), Rutherford backscattering spectrometry (RBS), nuclear reaction analysis (NRA), X-ray photoelectron spectroscopy (XPS), and cyclic voltammetry (CV) to characterize the condensation reaction efficiency. To our knowledge, detailed characterization of stepwise grown conjugated molecular wire films has not been reported previously. Furthermore, we have found new optimized conditions for growing the OPI wires that were not employed in our earlier work.[5] The characterization experiments are challenging because the films are extremely thin. Indeed, we find that our samples are an excellent platform for comparing a variety of surface analysis methods. A particularly unique aspect of this work is the use of NRA, which has not been employed before for analysis of self-assembled monolayers (SAMs) or ultra-thin organic layers. Most importantly, we find that, within error for all techniques we employed, these oligoimine condensation steps proceed essentially quantitatively, and thus produce films of oriented π-conjugated molecules with low polydispersities, which is advantageous for continued application of these systems in ongoing molecular electronics experiments.[10–25]

4.3 Experimental Methods

Materials. Au nuggets were purchased from Mowery Inc. (St. Paul, MN). Silicon wafers were purchased from Wafer Net (San Jose, CA). 4-chlorothiophenol and aminoferrocene were purchased from TCI America (Portland, OR). Tetrabutylammonium hexafluorophosphate, 4-aminothiophenol (4-ATP), 1,4-benzenediamine, terephthalaldehyde, 4-iodobenzaldehyde, 4-iodoaniline, 4-cholorobenzaldehyde, 4-chloroaniline, 4-fluorobenzaldehyde, and 4-fluoroaniline were purchased from Sigma Aldrich (St. Louis, MO). Absolute ethanol was purchased from Decon Labs (King of Prussia, PA), dimethyl sulfoxide (DMSO) was purchased from Fisher Scientific

(Waltham, MA), and acetonitrile was purchased from ACROS Organics (Geel, Belgium). 4-formyl thiophenol (4-FTP) was synthesized according to the literature.[26,27]

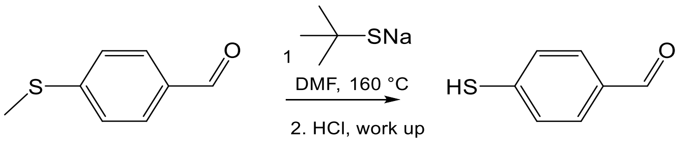

Scheme 4.1 Synthesis of 4-formylthiophenol (4-FTP)

Wire Growth and Characterization. Au substrates were prepared using two different methods; conventional thermal evaporation and template stripping. For thermal evaporation, 50 Å of Cr was first evaporated on bare Si wafer or mica as an adhesion layer followed by 700 Å of Au in a home-built evaporator at a rate of approximately 1-2 Å/s and base pressure ≤ 2 x 10^{-6} Torr. For template-stripped Au (*used only for XPS data in additional Information*), an epoxy adhesive was employed to bond small Si wafer pieces onto a 5000 Å thick Au film deposited by e-beam evaporation on bare Si without any adhesion layer. The samples were then cured at approximately 150 °C for 1.5 h, and the Au layer was stripped off the bottom Si layer by a razor blade.

The Au substrates were then immersed into 1 mM 4-ATP (absolute ethanol) or 4-FTP (DMSO). After 24 h, the SAM-coated Au substrates were removed from the thiophenol solution and rinsed thoroughly with absolute ethanol to remove physisorbed molecules before immersing them into a 20 mM solution containing the next dialdehyde or diamine derivative depending on the wire design. Thus, the lengths of the wires were precisely controlled by alternate addition of the amine and aldehyde derivatives. In order to optimize wire growth, aldehyde-terminated wires were reacted at 40 ± 2 °C with 1,4-benzenediamine for 24 h, and amine-terminated wires were reacted at room temperature (22 °C) with terephthalaldehyde for 24 h. OPI wires were kept in absolute ethanol before any surface characterization. Upon removal, the samples were rinsed again with absolute ethanol, and blown dry with N_2 or Ar. The ferrocene capping reaction was carried out in a glove box with < 0.1 ppm O_2 because aminoferrocene decomposes in air. The aldehyde-terminated wires were reacted with 2 mM aminoferrocene in absolute ethanol for a period of 24 h at room temperature. The samples were then rinsed, dried and transferred to a clean centrifuge tube that contained absolute ethanol before taking them out of the glove box for further rinsing (ethanol) and characterization.

Reflection-absorption infrared spectra (RAIRS) were collected with a Nicolet iS50 spectrometer with a Harrick Seagull accessory for grazing angle specular reflectance measurements. The incident angle for the p-polarized IR beam was 84° from the surface normal. For each sample and background, an average of 300 scans at a resolution of 2 cm^{-1} were collected after 15 min of purging with dry air.

Ellipsometry measurements were accomplished on a variable angle spectroscopic ellipsometer (J.A. Woolam Co., Inc). The change in polarization angles (ψ and Δ) were measured as a function of wavelength (λ) over 600-1000 nm at incident angles of 55°, 65° and 75°. To obtain accurate measurements, the background for each sample was measured before any wire growth to fit for Cr and Au thickness. Measurements for the polarization angles were performed again after completion of wire growth at the same position and incident angles as the background. The new ψ and Δ values along with the measured background thickness were used to fit for thickness of the monolayers for fixed values of the indices of refraction (n=1.45) and absorption coefficient (k=0). From prior UV-visible spectroscopy work, the absorption coefficient for OPI wires was estimated to be approximately zero over the wavelength range of 600-1000 nm.[5]

XPS spectra were collected by an SSX-100-XPS system (Surface Science), which is equipped with a monochromatic Al K_α X-ray source (1486.3 eV), at a base pressure of $\leq 10^{-9}$ Torr. The Al X-ray anode was operated at 200 W, the illuminated spot size on the sample was 0.64 mm^2, and a hemi-spherical analyzer (at a 35° take-off angle with respect to the sample normal) with constant pass energy was used to guide the photo-emitted electrons towards the detector. The pass energy for survey scans was 150 eV, and 50 eV for high resolution scans. For each high resolution scan, the binding energy was referenced to Au $4f_{7/2}$ (84.0 eV). The areas under the peaks of interest were fit using the Shirley background subtraction method, which removes the contribution of inelastically scattered electrons from the main peak.[28]

Cyclic voltammetry (CV) measurements were undertaken to measure the surface coverage of redox-capped wires. A three-necked cylindrical electrochemical cell with a hole in the bottom was employed. An O-ring was placed between the bottom of the cell (0.9 cm in diameter), and the monolayer coated Au substrate, which acted as the working electrode. The cell was then filled with 0.1 M $[Bu_4N^+][PF_6^-]$ (tetrabutylammonium hexafluorophosphate) in extra dry acetonitrile (< 10 ppm H_2O). A Pt wire was employed as the counter electrode, and Ag wire as the quasi-reference electrode. The cell was purged with either N_2 or Ar gas prior to and during electrochemical measurements. For each monolayer, the scans were recorded at sweep rates of 100 – 500 mV/s, and the voltammograms were reproducible and stable to electrochemical cycling up to 1.2 V vs Ag wire.

Rutherford backscattering spectrometry (RBS) was performed as a second measure of the surface coverage of monolayers capped with ferrocene. A MAS 1700 pelletron tandem ion accelerator (5SDH) equipped with a charge exchange RF plasma source (National Electrostatics Corporation, NEC: Middleton, WI) was used to generate a 3.0 MeV ${}_{2}^{4}He^{2+}$ beam with a current of 30-40 nA measured at the sample. ${}_{2}^{4}He^{2+}$ ions backscattered by nuclear collisions (via Coulomb repulsion) were counted by an Ortec silicon ion detector that was positioned at a scattering angle of 165° with respect to the incident beam and subtending a solid angle of 3.6 msr. Spectra consisting of counts versus backscattered ion energy (with energetics described by classical billiard-ball kinematics) were acquired with a multichannel analyzer controlled by NEC RC43 software. The substrates were prepared by thermally evaporating 20 nm of Au onto bare Si (100) without a Cr adhesion layer. Cr was not used because its backscattered peak position lies close to the Fe peaks. The total integrated incident charge on the sample was Q = 100 μC per spectrum (40-60 min). The beam cross section was approximately 2 × 2 mm (square), but the sample was tilted by 75° (sample normal with respect to beam) to improve depth resolution, thereby elongating the analytical spot size to ~ 8 mm along one dimension (sample size was ~ 15 mm along this dimension). Luminescent control samples of the same thickness were employed to precisely locate the beam position per sample goniometer coordinates. Quantitative comparisons between spectra (vertical scale) were achieved by normalizing to the signal intensity of the Si substrate. This treatment accounted for small variations in the accuracy of beam current integration (i.e., error in determination of Q).

For nuclear reaction analysis (NRA), the ${}^{4}_{2}He^{2+}$ ions were accelerated to 4.289 MeV in order to produce prompt nuclear reactions with carbon nuclei (described later) using a beam current of 30-40 nA at normal incidence (0° sample tilt, thus 2 × 2 mm analytical spot size). Backscattering ${}^{4}_{2}He^{2+}$ ions were detected as above but with a *strong enhancement in carbon sensitivity* due to a non-Rutherford, nuclear-resonance scattering cross section[29] (i.e., with probability determined by nuclear quantum mechanics rather than classical Coulomb repulsion), but with energetics still described by classical billiard-ball kinematics (*i.e. elastic collision*) as in conventional RBS. The NRA substrates were prepared by thermal evaporation of 5 nm Cr followed by 50 nm Au on mica.

4.4 Results and Discussion

Verification of wire growth and length. Oligophenyleneimine (OPI) wires were prepared on Au surfaces by imine condensation click chemistry with alternate addition of terephthalaldehyde and 1,4-benzenediamine. As shown in Figure 4.1, room temperature reaction of aldehyde capped wires with 1,4-benzenediamine resulted in incomplete disappearance of aldehyde peaks in the RAIRS spectra. In the notation OPI-X-Y, X represents the number of phenylene rings, and Y represents either a halogen or ferrocene capping unit (if present). Figures 4.2a and 4.2b display the RAIRS spectra of OPI wires grown from SAMs of 4-FTP and 4-ATP, respectively under optimized conditions. Wires capped with carbonyl units appear at odd positions (OPI-3, OPI-5, OPI-7, and OPI-9) for wires grown from 4-FTP (Figure 4.2a), and even positions (OPI-2, OPI-4, OPI-6, OPI-8, and OPI-10) for wires grown from 4-ATP (Figure 4.2b). The alternate appearance and

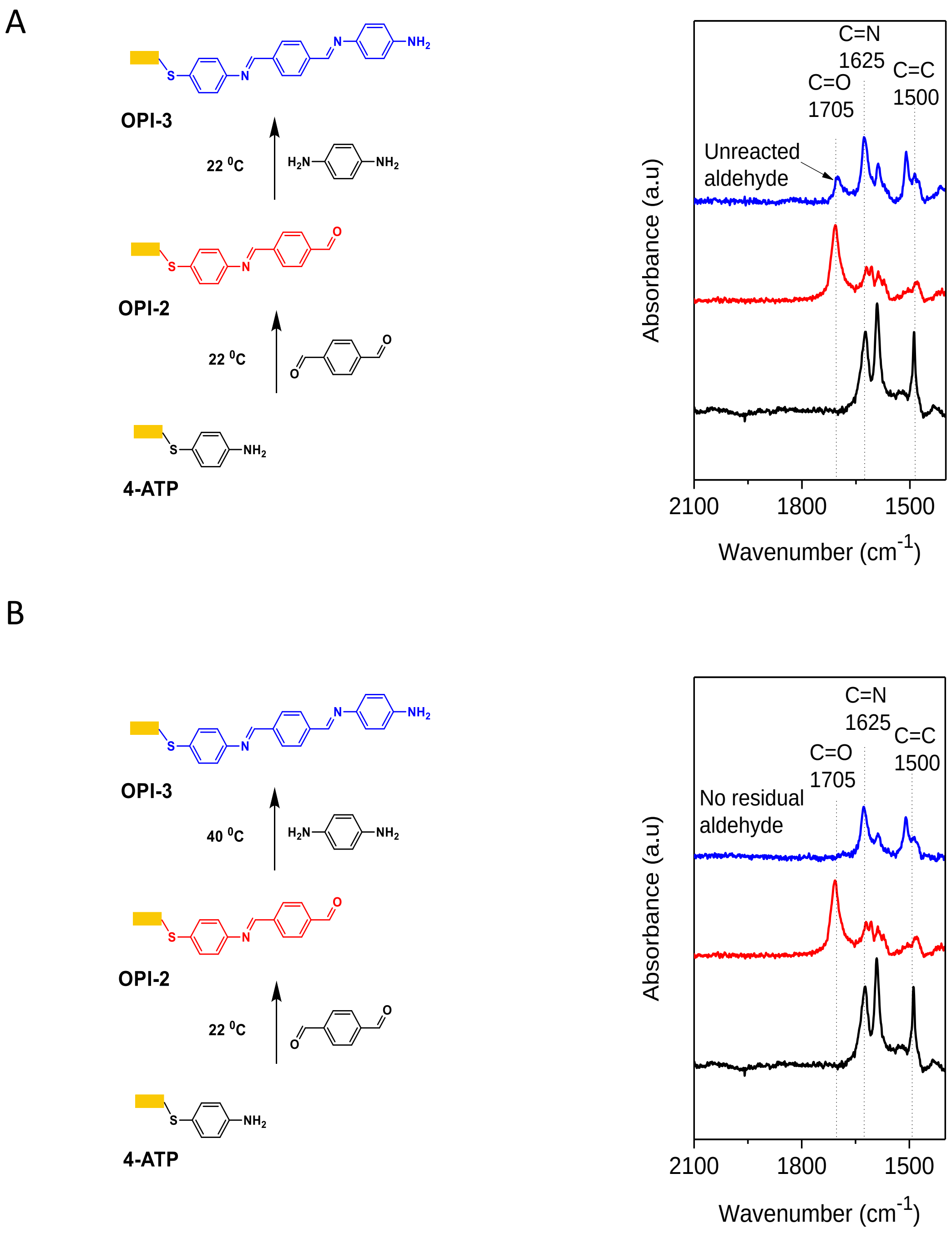

Figure 4.1 (A) Molecular structure and un-optimized stepwise growth of OPI wires, and the corresponding RAIRS spectra on the right. The residual carbonyl peak at 1705 cm^{-1} for reaction of OPI-2 with benzene-1,4-diamine indicates an incomplete reaction at room temperature. (B) Molecular structure and optimized stepwise growth of OPI wires, and the corresponding RAIRS spectra on the right. The absence of residual carbonyl peak at 1705 cm^{-1} for reaction of OPI-2 with benzene-1,4-diamine indicates near quantitative reaction of formyl units.

disappearance of carbonyl stretch peaks[30] (1705 cm^{-1}) suggests an extent of reaction near completion for each step. The intensity of the imine stretch[30,31] (C=N, 1625 cm^{-1}) and benzene ring stretch mode[30] (C=C, 1500 cm^{-1}) increased with the number of repeat units, as expected. The sample dimensions for all of the RAIRS spectra were kept the same, so that quantitative information about the extent of reaction can be reliably extracted from the carbonyl peak.

The extent of reaction for the n^{th} click step by FTIR was calculated from the carbonyl peak area ratio of OPI-n to OPI-(n-1). The method assumes that the orientation of carbonyl peaks with respect to the p-plane of the IR light electric field is the same for wires of different lengths. It should be noted that baseline correction of the spectra could easily introduce errors in peak areas. As shown later (Figure 4.20), the obtained results are scattered around a mean value of 98 ± 7.9%. This value does not deviate significantly from other quantitative characterization methods as will become clear later.

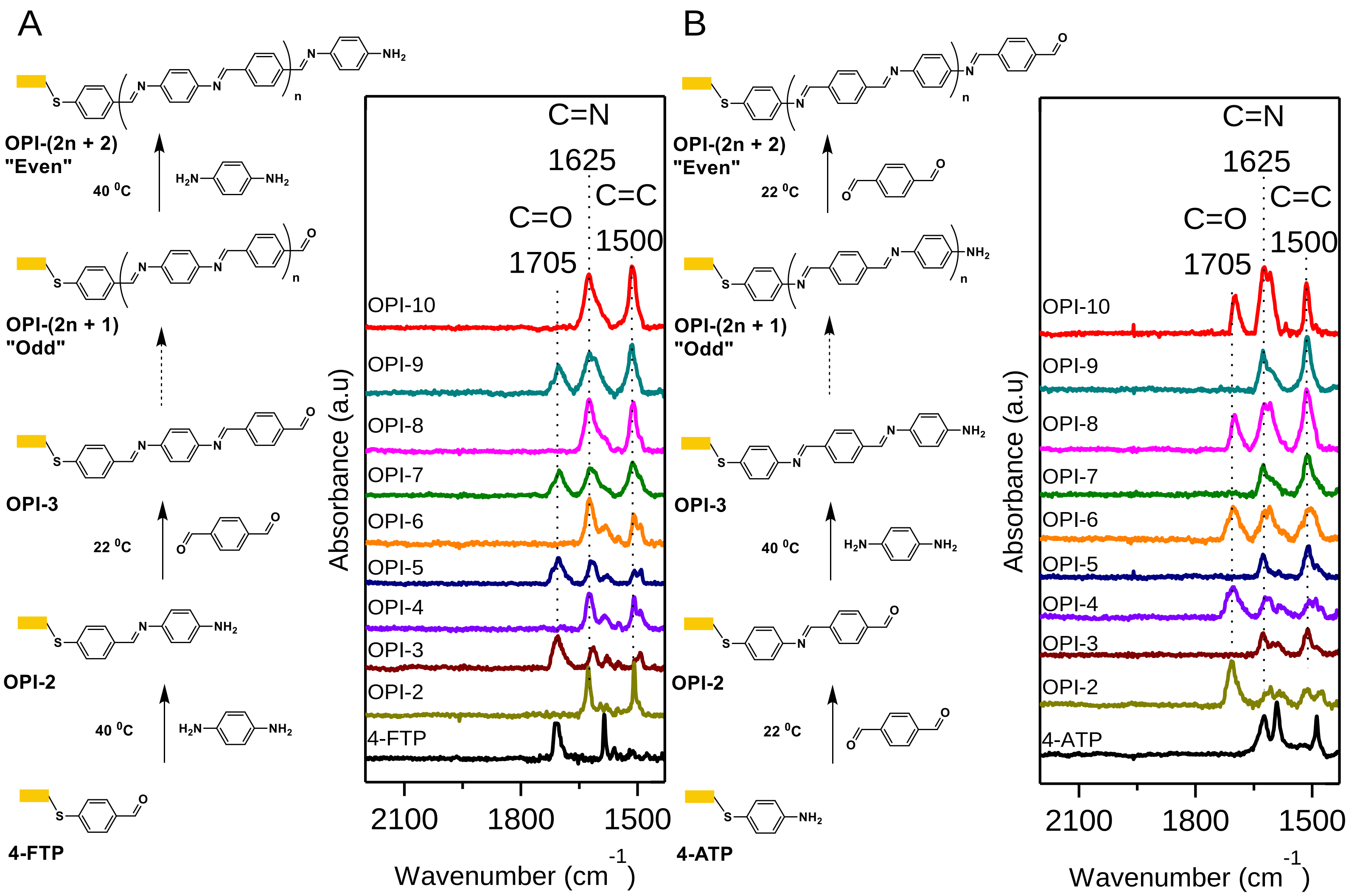

Figure 4.2 (A) Molecular structure and stepwise growth of OPI wires starting from 4-FTP (left) and corresponding RAIRS spectra (right) showing the alternate appearance and disappearance of aldehyde peaks. The aldehyde peaks appear for odd numbers of phenyl rings. (B) Molecular structure and stepwise growth of OPI wires starting from 4-ATP (left) and corresponding RAIRS spectra (right) showing the alternate appearance and disappearance of aldehyde peaks. The aldehyde peaks appear for even numbers of phenyl rings.

Ellipsometry was employed to determine the thickness of the wire films. As shown in Figure 4.3, the length of the wires increased with the number of repeat units. The estimated (theoretical) thickness was calculated by assuming perpendicular orientation and trans-configuration for each chain length. The index of refraction (n) and absorption coefficient (k) for ellipsometry were assumed to be 1.45 and 0, respectively, over the wavelength region 600-1000 nm. The ellipsometry data are reasonably well matched to theoretical expectations. It is clear that films up to 5.5 nm in thickness are synthesized. Comparison of the measured thickness with theoretical prediction suggests an average tilt angle of 30° with respect to the surface normal.

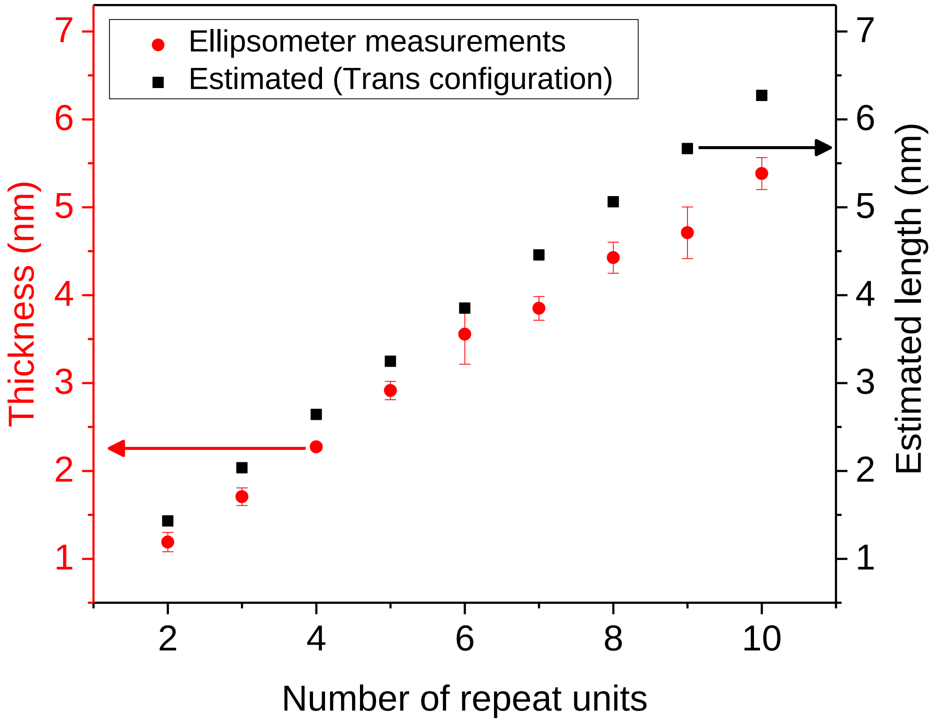

Figure 4.3 Measured and estimated thicknesses of OPI films as a function of number of repeat units. The estimated thicknesses were calculated using Cambridge Scientific ChemBio 3D, assuming trans configuration of the molecules oriented normal to the substrate; the Au-S bond length was taken to be 2.36 Å.[5,47] Tilt angle was calculated from the inverse cosine of the ratio of ellipsometer values to theoretical predictions. Error bars represent one standard deviation.

Wire surface coverage by cyclic voltammetry. CV measurements were employed to calculate the surface coverage and extent of reaction for OPI wires capped with redox-active ferrocene. As shown in Figure 4.4a, aldehyde-terminated OPI wires were reacted with aminoferrocene to yield OPI-X-Fc wires. For each wire, CVs were recorded at sweep rates of 100, 200, 300, 400, and 500 mV/s, and displayed reversible redox peaks characteristic of ferrocene. A representative CV of OPI-5-Fc is shown in Figure 4.4b for the various sweep rates (CV for other wires are plotted in Figure 4.5). Figure 4.4c displays a CV plot of OPI-2 that is not capped with ferrocene, but was left in the aminoferrocene solution for a period of 24 h. As expected the CV spectra does not show redox behavior characteristic of ferrocene tagged wires. Thus, this control experiment verifies that aminoferrocene reacts only with the aldehyde termini of the wire, and does not bond with Au substrate.

For each wire length, at least 3 scans were averaged for each sweep rate on 3 different samples. The CV spectra of all OPI-Fc wires exhibit a linear dependence on sweep rate and excellent reversibility. Previous work by others has shown that electron transfer from Fc to metals through conjugated bridges can be very fast, though to our knowledge the OPI bridges reported here are longer than oligophenylenevinylene (OPV) and oligophenyleneethynylene (OPE) bridges probed previously.[32,33] A detailed examination of electron transfer kinetics will be the subject of a future study. We focus here on the surface analytical aspects, namely that the Fc coverage is reasonably constant for all wire lengths.

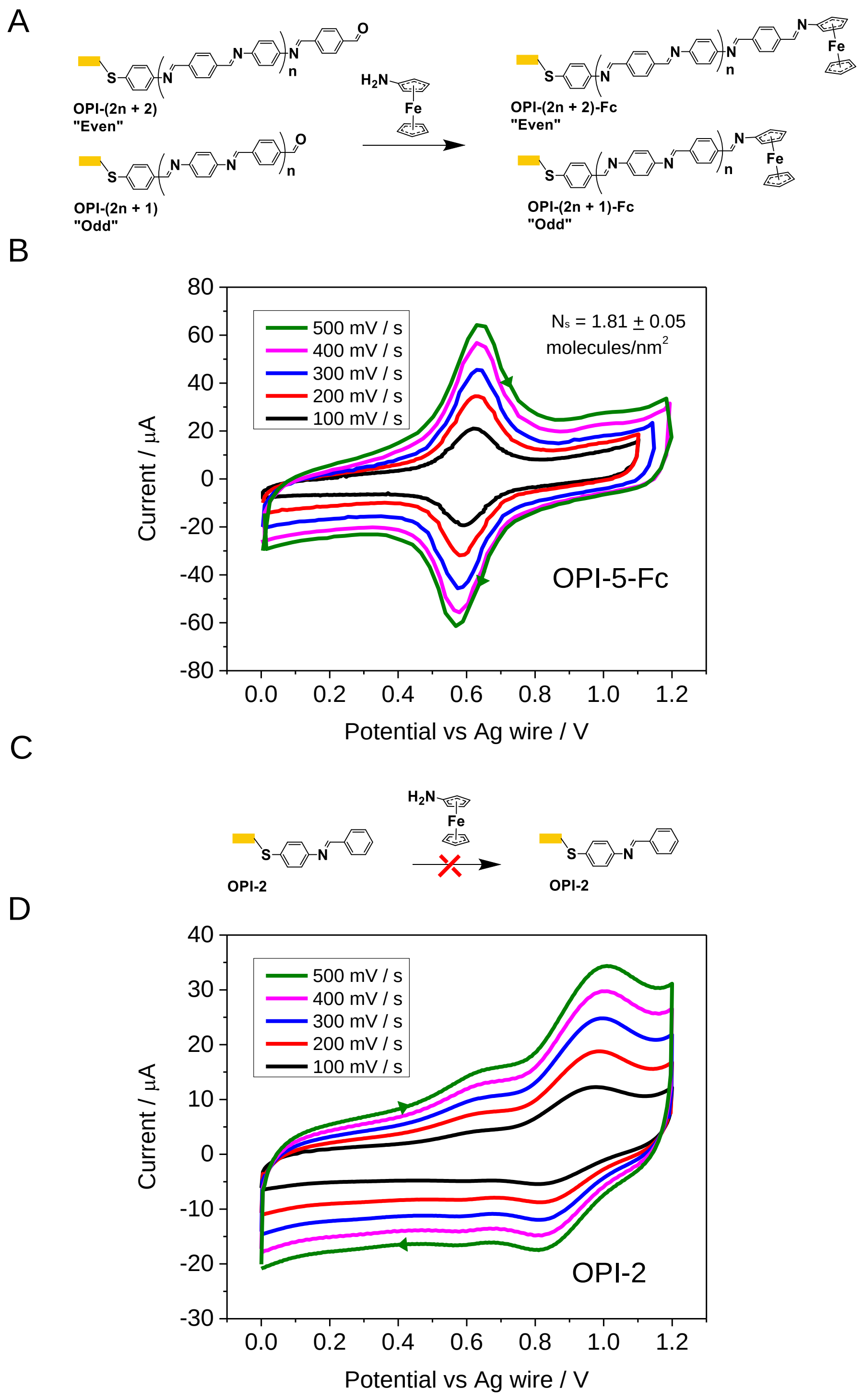

Figure 4.4 (A) Molecular structure for aldehyde terminated wires (left) on Au before and after capping with aminoferrocene (right). (B) CV OPI-5-Fc at different sweep rates. The electrolyte was 0.1 M $[Bu_4N^+][PF_6^-]$ in acetonitrile. The reference and counter electrodes were Ag and Pt wires, respectively. (C) Molecular structure of OPI-2, a control sample that was left in the aminoferrocene solution for 24h. (D) CV of OPI-2. The absence of redox peaks characteristics of ferrocene indicates that aminoferrocene only reacts with aldehyde terminated wires.

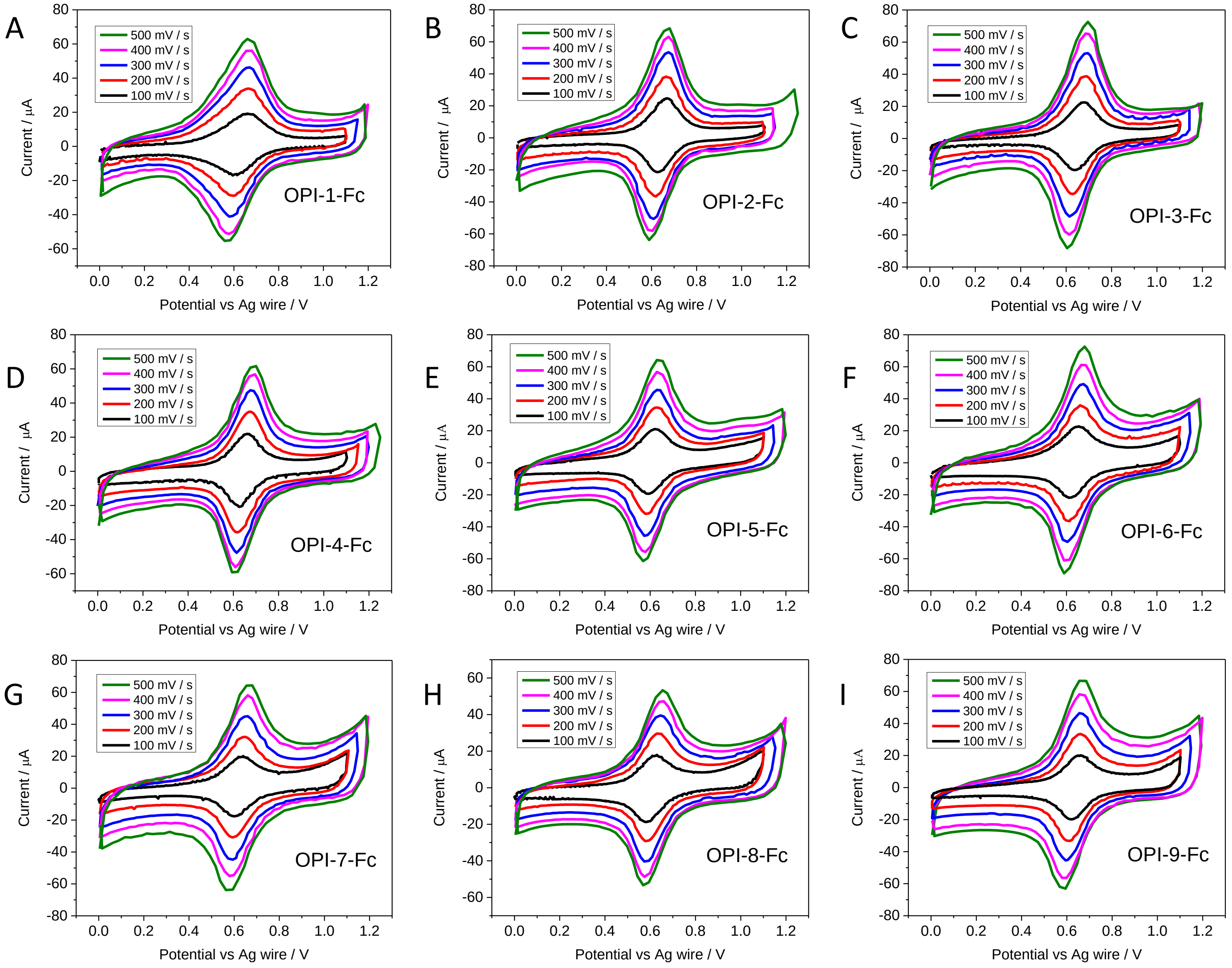

Figure 4.5 CV of ferrocene capped OPI wires at 100, 200, 300, 400, and 500 mV/s. A) OPI-1-Fc B) OPI-2-Fc C) OPI-3-Fc D) OPI-4-Fc E) OPI-5-Fc F) OPI-6-Fc G) OPI-7-Fc H) OPI-8-Fc and I) OPI-9-Fc. The electrolyte was 0.1 M $[Bu_4N^+][PF_6^-]$ in acetonitrile. The reference and counter electrodes were Ag and Pt, respectively. The sweep rate and redox peaks are linearly proportionality as expected for surface confined species. Au geometrical area: 0.64 cm^2. Average Coverage of Fc for all wires: 1.97±0.24 molecules / nm^2.

The surface coverage, N_s (molecules/cm^2), for Fc centers was calculated according to equation 4.1,

$$N_s = \frac{Q}{n\,F\,A} \tag{4.1}$$

where Q is the charge injected into the SAM, n is the number of electrons involved in the transfer process (1), F is the Faraday constant, and A is the surface area of the monolayers examined (0.64 cm^2).

The surface coverage results are plotted in Figure 4.6. The standard deviations derive from data sets of 60 sweeps for OPI-3-Fc to OPI-9-Fc, and 30 sweeps for OPI-1-Fc and OPI-2-Fc. On average, the surface coverage for ferrocene capped wires was 1.97 ± 0.24 molecules/nm^2. This value compares favorably with coverages obtained for ferrocene terminated alkyl thiol SAMs on Au (typically 2.28 - 2.71 molecules/nm^2).[34,35]

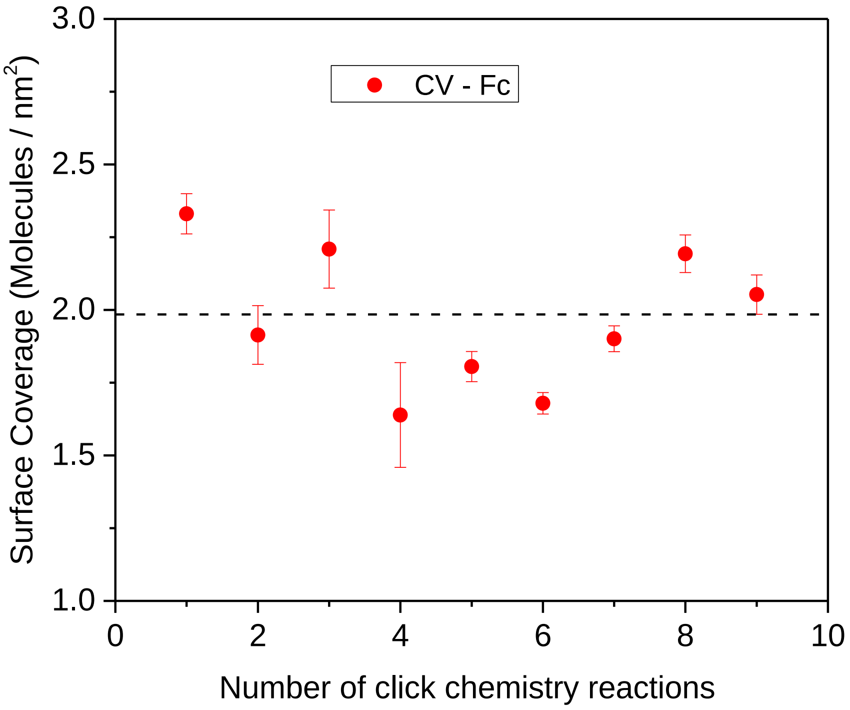

Figure 4.6 CV surface coverage results of OPI-Fc wires.

Wire surface coverage by RBS. RBS is a nondestructive ion beam analysis technique that is used to measure elemental composition, and in suitable situations, its depth dependence. (Here we integrate signals from all depths of the thin organic films.) A beam of high energy ${}_{2}^{4}He^{2+}$ ions impinges the sample and the backscattered ion count versus energy spectrum is used to determine elemental composition. The elemental surface coverage, N_s (atoms/cm^2), can also be determined by the following formula[36]:

$$N_s = A \cos\theta / [\ (\frac{d\sigma}{d\Omega})\ \Omega\ Q] \tag{4.2}$$

where, A is the total number of ions detected, and θ is the tilt angle of the sample relative to the ion beam (75°), $\frac{d\sigma}{d\Omega}$ is the differential scattering cross section per unit angle (1.48×10^{-25} cm^2/sr (S), and 3.99×10^{-25} cm^2/sr (Fe)), Ω is the detector solid angle (3.6×10^{-3} sr), and Q is the total number of incident ions (3.0×10^{14}). There are only a few papers that report the use of RBS as a quantitative tool for organic monolayers.[37–39]

Figure 4.7b displays the RBS spectrum for OPI-9-Fc on thin Au (20 nm). The Au thickness was kept to 20 nm (not thicker) so that the Fe peak was clearly resolved from the broader Au peak. Clear signals were detected for S and Fe, as expected; a magnified view of the S and Fe region is shown in Figure 4.7c. Spectra were acquired with the incident beam impinging at an angle of 75° with respect to the sample normal, with an energy of 3.0 MeV, and a backscattering angle of 165°. Tilting increases the energy loss of ${}_{2}^{4}He^{2+}$ ions that backscatter from finite depth in the sample,[36] in our case resulting in separation of the S signal from two distinct depth locations.

To illustrate this point, the magnified spectra of OPI-3-Fc, OPI-4-Fc, OPI-5-Fc, OPI-6-Fc, and OPI-7-Fc are shown in Figure 4.7c. Three distinct peaks lie between the Si

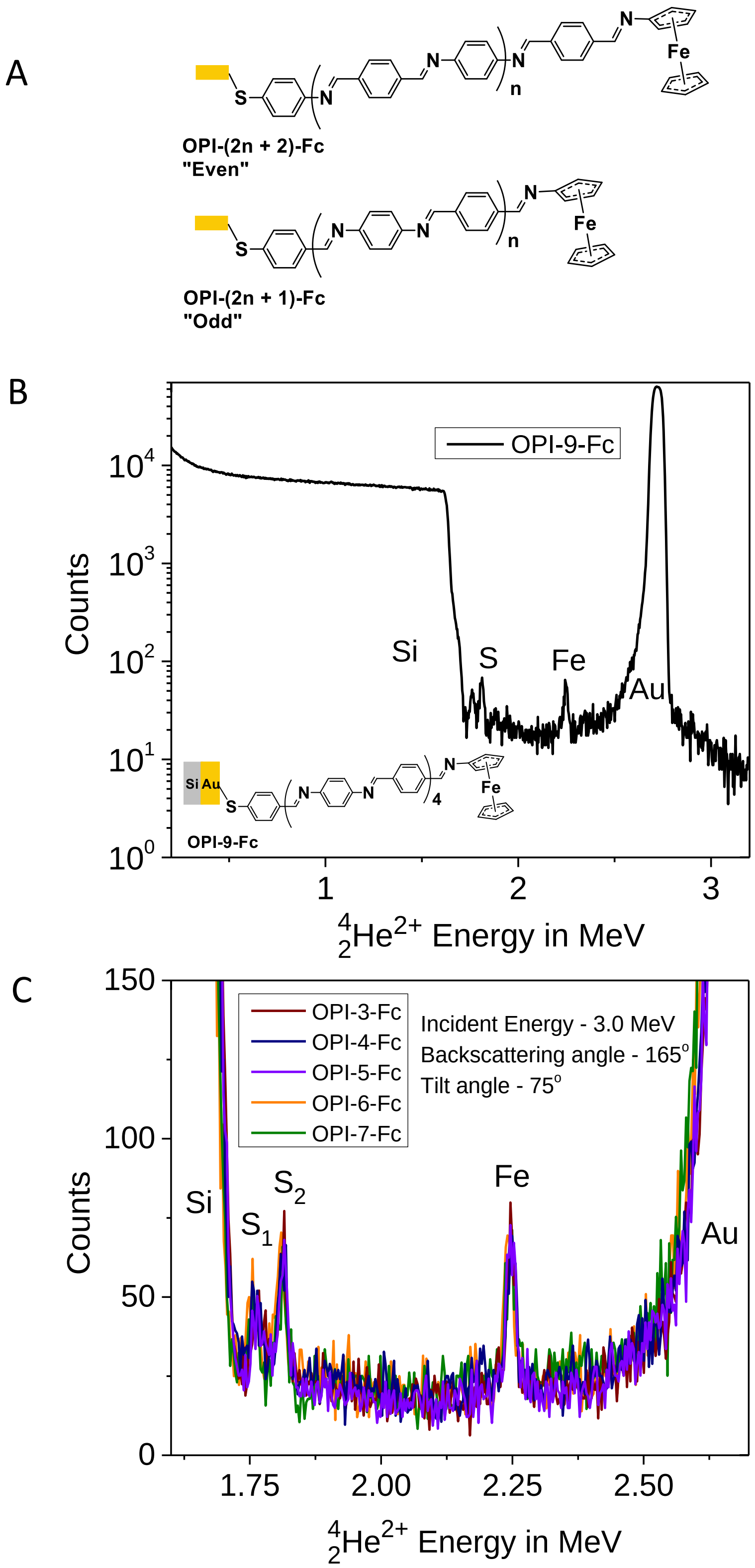

Figure 4.7 (A) Molecular structure for ferrocene (Fc) terminated OPI wires. (B) RBS spectrum of OPI-9-Fc on 20 nm Au film coated on Si without adhesion layer. The S and Fe peaks are separated from Si and Au signals. (C) RBS spectra of OPI-3-Fc, OPI-4-Fc, OPI-5-Fc, OPI-6-Fc, and OPI-7-Fc showing the S and Fe peaks. The spectral heights were normalized to the Si signal intensity.

and Au signals, which are assigned to two S peaks and one Fe peak. Simulation of RBS spectra with QUARK freeware indicated only the higher-energy sulfur peak, S_2, when the presence of S was modeled only at the film/Au interface. The lower-energy sulfur peak, S_1, could be simulated by incorporating roughly a monolayer of S at the Au/Si interface. Control spectra taken at other tilt angles and other beam energies were consistent with this assignment. No other simulated elemental assignments could reproduce the spectral peak locations.

The presence of “deep sulfur (S_1)” implicit in the preceding spectral analysis suggests diffusion of the 4-ATP or 4-FTP molecules to the Au/Si interface via the Au grain boundaries during the first chemisorption step. To test our hypothesis, we prepared 20-nm and 40-nm Au substrates and flame-annealed them before adsorption of 4-ATP. The purpose of annealing was to increase the grain size of the Au and reduce the total number of grain boundaries. If the 4-ATP or 4-FTP molecules diffused via grain boundaries, then reducing the number of grain boundaries should reduce the number of molecules reaching the Au-Si interface. The results shown in Figure 4.8 were consistent with our hypothesis: only one S (S_2) peak was detected. Furthermore, the un-annealed 40-nm Au substrate also showed no S_1 peaks, supporting our conclusion because thicker Au layers present a greater diffusion barrier. However, we decided to collect the final RBS spectra (Figure 4.7) using 20-nm un-annealed Au films because annealing results in greater tailing of the Au peak edge toward the Fe peak due to an increase in Au surface roughness (grain coarsening). In order to rule out any Fe contamination of the thermally evaporated Au film from the deposition chamber or Au nuggets, the RBS spectrum of OPI-5 (with no ferrocene) was collected. Figure 4.9 shows that no Fe peaks.

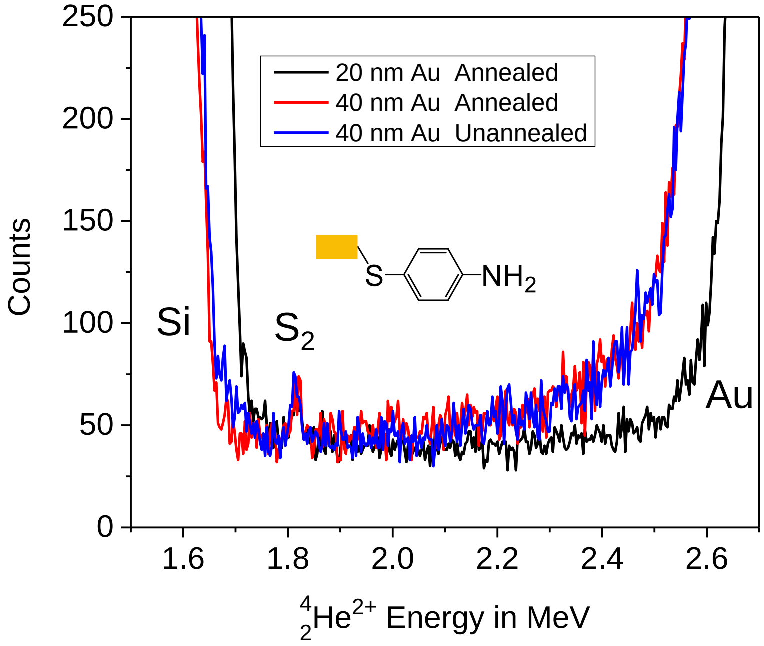

Figure 4.8 RBS spectra of 4-ATP on annealed & unannealed Au 20 nm and 40 nm substrates on Si. The disappearance of S_1 peak supports our hypothesis that it originated from diffusion of 4-ATP into Au-Si interface via grain boundaries.

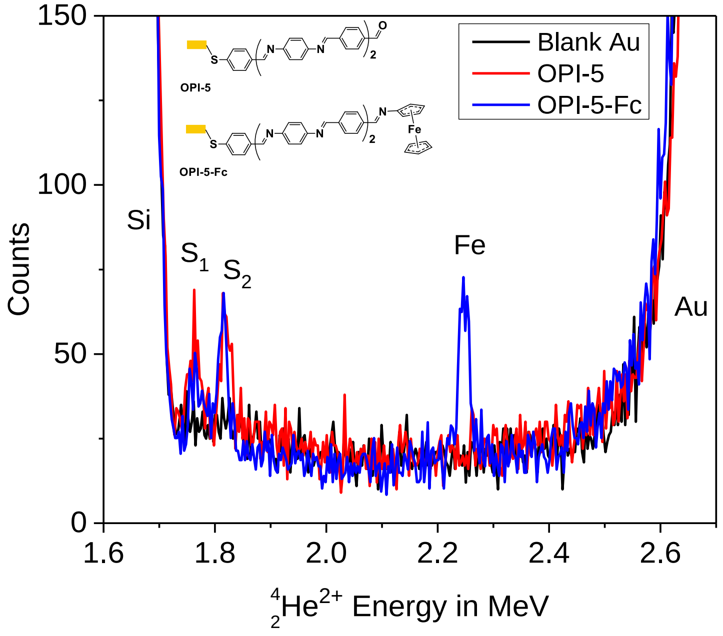

Figure 4.9 RBS spectra of OPI-5, OPI-5-Fc, and blank Au substrate. The spectra of blank Au and OPI-5 indicated that Fe peaks were detected only from Fc capped wires, and could not be due to impurities from the substrate.

The surface coverages of OPI-Fc wires were calculated according to equation 4.2. The areas under the S_2 and Fe peaks were integrated to yield the total number of backscattered ions from the S and Fe units. The differential scattering cross sections were calculated from Marion and Young's equation.[36] For each sample, two distinct locations were analyzed, and the results are plotted in Figure 4.10. On average, we obtained surface coverage values of 1.9 ± 0.1, and 3.6 ± 0.1 molecules/nm^2 for Fe and S, respectively.

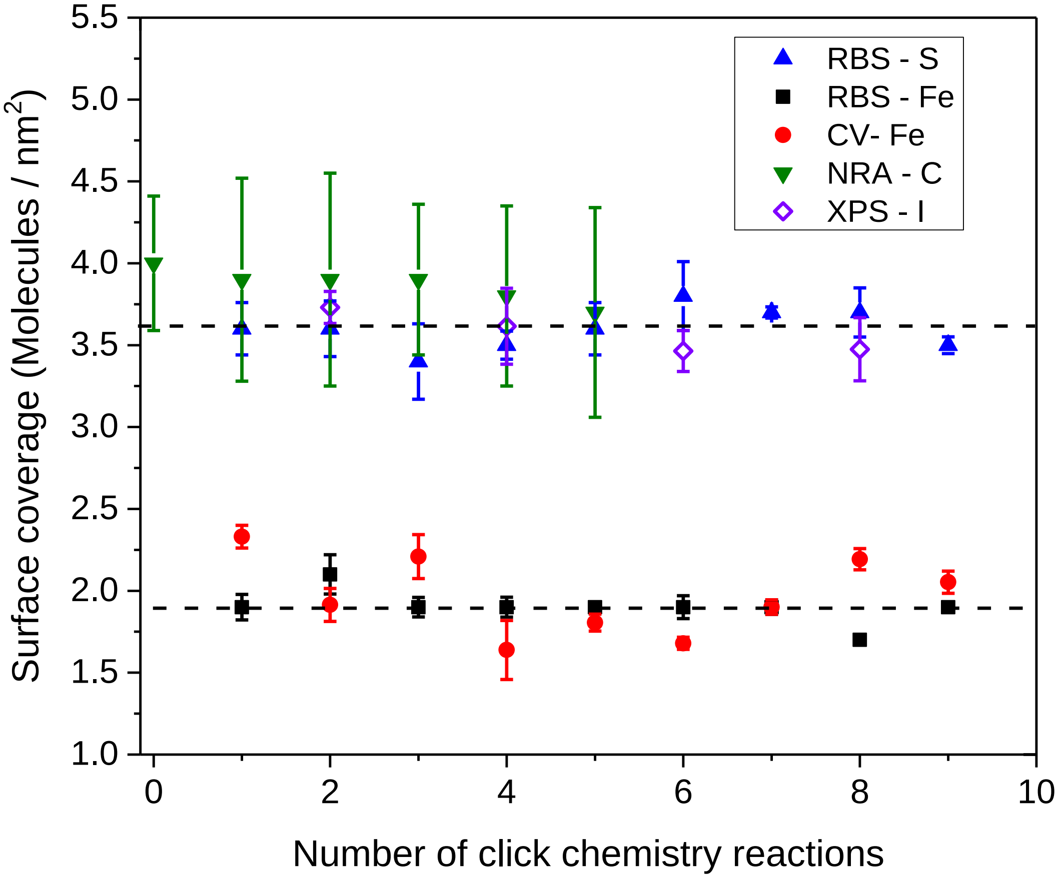

Figure 4.10 Surface coverage results obtained by RBS, CV, NRA and XPS as a function of number of click chemistry reactions (wire length). Blue triangles and black squares correspond to coverage values of S and Fe, respectively from RBS, and red circles correspond to coverage value of Fe from CV. Inverted green triangles correspond to surface coverage of C atoms from NRA divided by the anticipated number of C atoms / wire, and violet diamonds correspond to surface coverage of I atoms from XPS. Error bars represent one standard deviation.

Our results indicate that on average only 52% (1.9 / 3.6) of the wires were capped with ferrocene. This was also confirmed by the IR spectra in Figure 4.11, which showed unreacted carbonyl peaks after the capping reaction with aminoferrocene. In fact, the ratio of the carbonyl peak area of OPI-3-Fc to OPI-3 gave a value of 38% indicating that only 62% of OPI-3 wires were capped with ferrocene.

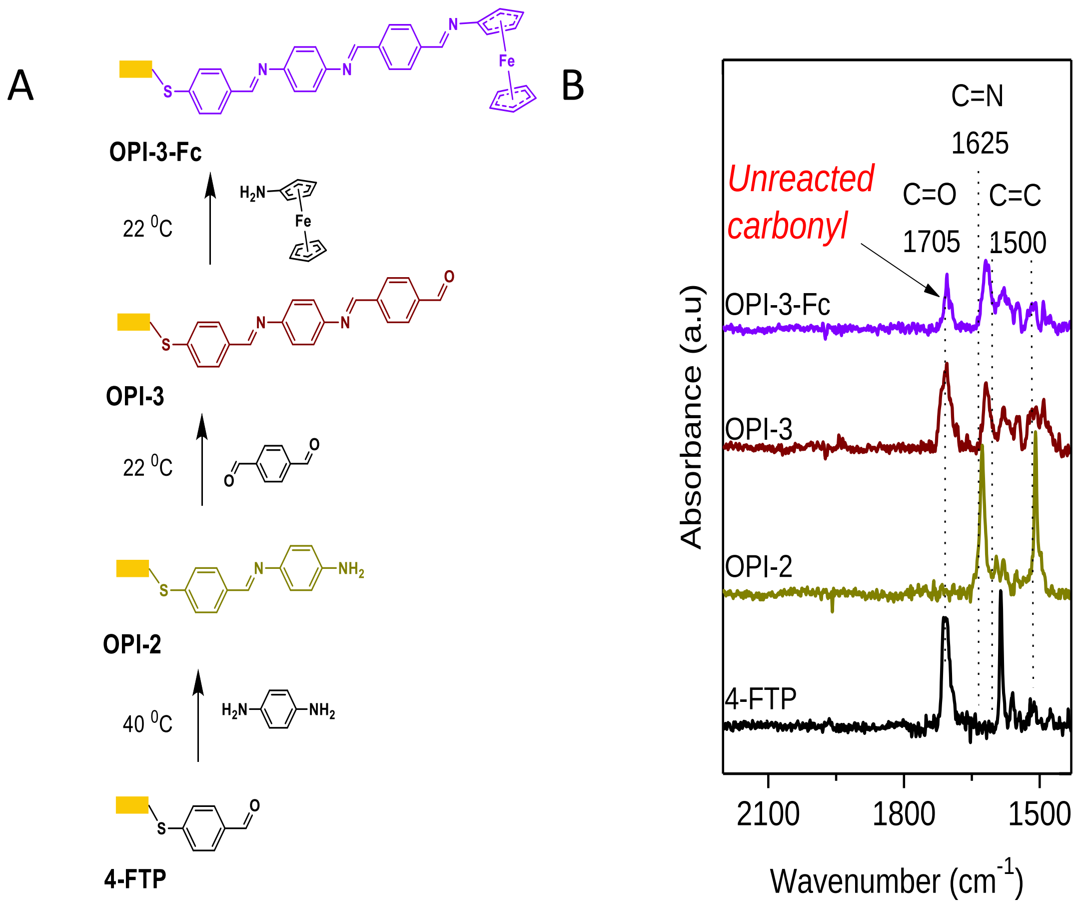

Figure 4.11 (A) Molecular structure and step-wise growth of OPI-3-Fc wire starting from 4-FTP. (B) The corresponding RAIRS spectra on the right. The residual carbonyl peak at 1705 cm^{-1} for reaction of OPI-3-Fc with aminoferrocene indicated an incomplete reaction. The ratio of carbonyl peak area of OPI-3-Fc to OPI-3 was 38%. Therefore, only 62% of carbonyl units of OPI-3 reacted with aminoferrocene whereas RBS result was 52%.

To further investigate if this was due to reaction kinetics or steric effects, the RBS spectrum of 6-(ferrocenyl)hexanethiol (Figure 4.12) was compared to OPI-Fc wires. The surface coverage values for 6-(ferrocenyl)hexanethiol were 2.1 and 2.1 molecules/nm^2 for S and Fe, respectively, very similar to the ferrocene coverage values obtained by both CV and RBS for OPI-Fc wires. We believe that it is not energetically favorable to pack more than 2 ferrocene molecules per nm^2 and that steric effects were likely the reason that aminoferrocene did not react completely with the carbonyl units on the OPI wires. Collectively, the RBS data give us a quantitative coverage measurement that is consistent with the cyclic voltammetry results. Figure 4.10 suggests that the wire coverage is ~ 3.6 OPI wires/nm^2.

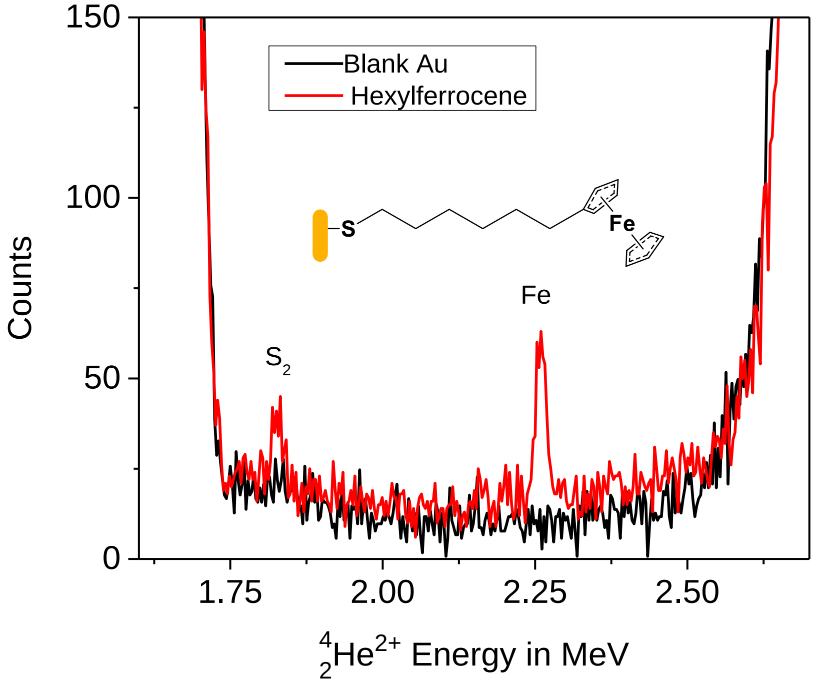

Figure 4.12 RBS spectra of 6-(ferrocenyl)hexanethiol and blank Au substrate. The surface coverage values of S and Fe were 2.1 and 2.1 molecules / nm^2, respectively. This result indicated that steric effects prevent packing more than 2 molecules / nm^2.

Wire surface coverage by NRA. Our ion beam analysis instrument at Minnesota also provides for quantitative nuclear reaction analysis (NRA) of low atomic mass elements, such as C, that are difficult to detect with RBS because their signal lies spectrally atop the much stronger substrate signal (Rutherford backscattering peak counts being proportional to atomic number squared), and with its correspondingly substantial noise. In NRA, an incident ${}_{2}^{4}He^{2+}$ ion may initiate a nuclear reaction by penetrating a target nucleus if it has enough energy to overcome the Coulomb barrier, forming an intermediate excited nuclear state that immediately decays back to the ground state by emission of a particle in the case of *prompt* reactions. (Some nuclear reactions generate more slowly decaying radioactive states, on the scale of minutes to hours, but we are not accessing such reactions in the present work.) This non-Rutherford scattering process can result in a distinct enhancement of the signal (peak intensity) of target nuclei because the quantum mechanics for activation of such nuclear states produces a scattering cross section that is much greater than that of Rutherford (classical Columbic) scattering. For ${}_{1}^{1}H^{+}$ and ${}_{2}^{4}He^{2+}$ projectiles with incident energies up to at most a few MeV (as are accessible with small accelerators in materials characterization facilities), there are only a few elements such as C, N, and O with analytically useful nuclear cross sections.[40] Thus, NRA cannot be used for the detection of arbitrary elements; rather, here we have exploited the known reaction of ${}_{6}^{12}C$ with ${}_{2}^{4}He^{2+}$ at 4.289 MeV to measure carbon coverage.

When the energy of the incident α particles is increased to 4.289 MeV, nuclear reaction between ${}_{6}^{12}C$ and ${}_{2}^{4}He^{2+}$ forms an unstable intermediate ${}_{8}^{16}O^{2+}$ that immediately decays back to ${}_{6}^{12}C$ and ${}_{2}^{4}He^{2+}$as shown in equation 4.3 (with the energetics of scattering, and thus spectral peak position, being identical to that of the Rutherford case). As with conventional RBS, the emitted ${}^{4}_{2}He^{2+}$ particles can then be counted to yield the surface coverage of C atoms following calibration to the enhanced nuclear scattering cross section. To our knowledge, this is the first work that has utilized NRA as a characterization tool for SAMs.

$$ {}^{12}_{6}\mathrm{C} + {}^{4}_{2}\mathrm{He}^{2+}(4.289\ \mathrm{MeV}) \rightarrow {}^{16}_{8}\mathrm{O}^{2+} \rightarrow {}^{12}_{6}\mathrm{C} + {}^{4}_{2}\mathrm{He}^{2+}\ (1.022\ \mathrm{MeV}) \qquad (4.3) $$

The OPI wires for NRA were synthesized starting from a SAM of 4-ATP followed by alternate addition of terephthalaldehyde or 1,4-benzenediamine in the usual manner. In order to reduce channeling in the substrate (as happens for the case of an untilted Si(100) substrate, reducing its signal) and thereby retain the utility of substrate-signal intensity for spectral normalization, mica substrates with 5 nm Cr and 50 nm Au (deposited by thermal evaporation) were employed. As shown in Figure 4.13a, wires with even numbers of phenyl rings (OPI-2, OPI-4, and OPI-6) were capped with benzaldehyde, and wires with odd numbers of phenyl rings (OPI-3 and OPI-5) were capped with 1,4-benzenediamine. The NRA C spectra in Figure 4.13b show a linear relationship between the intensity of carbon counts and total number of repeat units, i.e., each stepwise addition resulted in an increase in the integrated number of ${}^{4}_{2}He^{2+}$ ions scattered from ${}^{12}_{6}C$ nuclei, as expected. The surface coverage was calculated from equation 4.2 (similar to RBS of OPI-Fc wires), and the nuclear scattering cross section was interpolated from a table by Feng, et al[29] ($5.195 \pm 0.103 \times 10^{-25}$ cm^2/sr). The total number of incident particles was 1.5×10^{14}. The C surface coverage values are shown in Figure 4.13c for the first 6 repeat units (2 scans per sample). In order to correct for

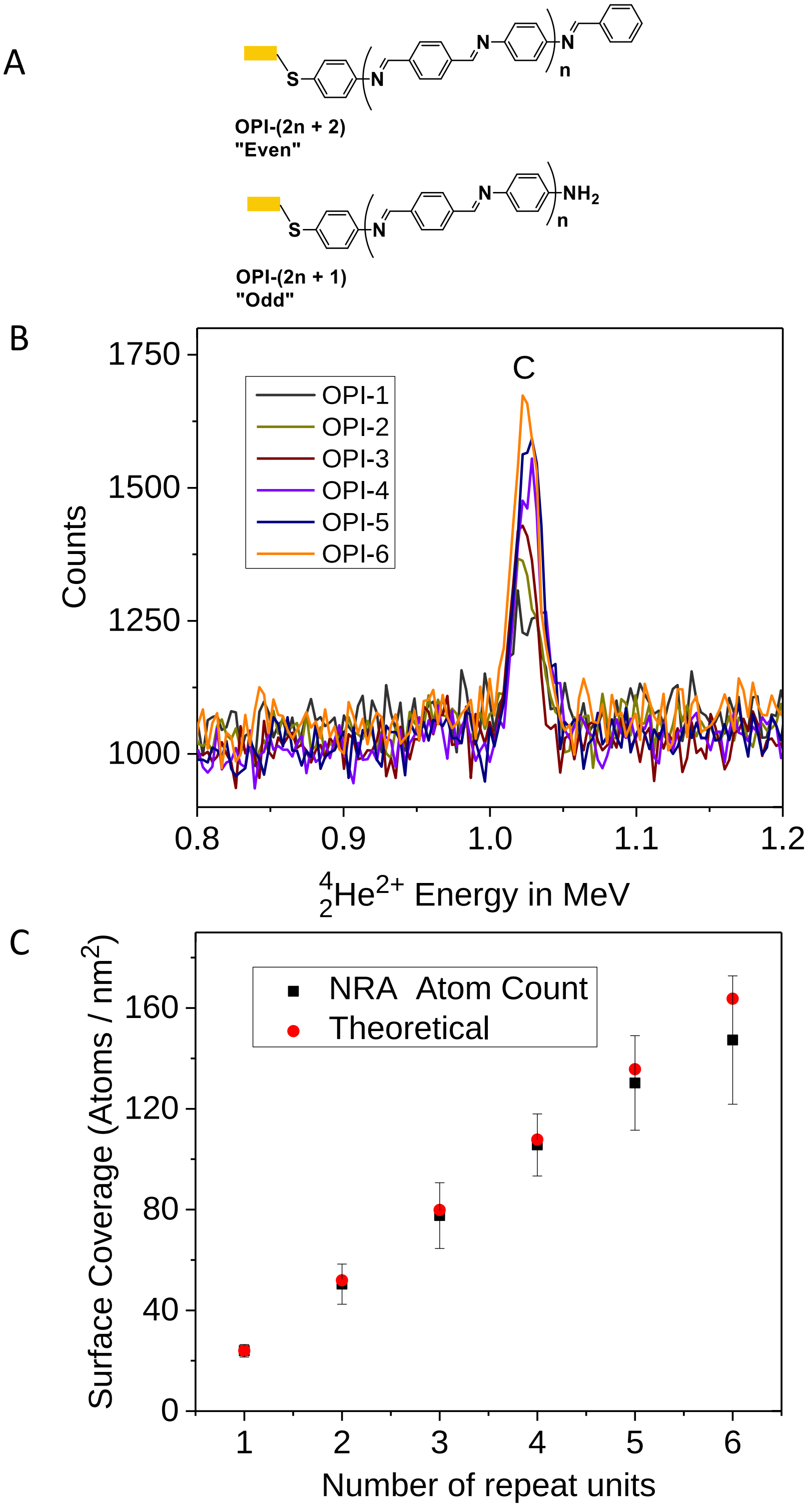

Figure 4.13 (A) Molecular structure of OPI wires capped with benzaldehyde (even positions), and uncapped (odd positions) for NRA. (B) NRA C spectra of OPI-1, OPI-2, OPI-4, OPI-5, and OPI-6 wires. Each stepwise addition resulted in an increase of the C peak intensity. The spectral heights were normalized to the substrate signal. (C) Surface coverage values for C atoms (black squares) as a function of number of repeat units. The error bars represent one standard deviation.

adventitious adsorbed hydrocarbons from the chamber, the y-intercept from a linear fit of raw peak area vs repeat units was subtracted.

The approximate linear growth in C concentration is excellent evidence that the wire synthesis proceeds as outlined in Figure 4.2 and our previous papers,[5,6] and it is consistent with the thickness data in Figure 4.3. The molecule count, as shown in Figure 4.10, was obtained by dividing the atom count by the expected number of carbon atoms per chain. On average, we obtained a surface coverage value of 3.9 ± 0.1 molecules/nm^2 for C, which is in excellent agreement with values obtained for S using RBS, Figure 4.10.

Wire surface coverage by XPS. The availability of para-halogenated anilines or benzaldehydes from commercial sources makes these species ideal tags to investigate OPI wire synthesis by XPS. Among all of the halogenated anilines or benzaldehydes, I is the best XPS tag because it has the highest photoemission cross-section (8.39×10^{-23} m^2) followed by Br (1.35×10^{-23} m^2), F (6.36×10^{-24} m^2), and Cl (5.86×10^{-24} m^2), respectively.[41] Thus, spectra with good signal-to-noise ratio could be obtained in 30 min acquisition times for I tags verses 240 min for Cl tags. For F-labeled monomers, coverage was anomalously low presumably because the electron withdrawing F-substituent decreased the reactivity of 4-fluoroaniline with the formyl units (more information available in the additional work section).

OPI wires were capped with I as shown in Figure 4.14a by reacting the aldehyde termini with 4-iodoaniline. The spectra in Figure 4.14b and 4.15 show photoemission counts for I 3d peaks and the two pairs of peaks correspond to different chemical states of I. To rule out any contribution from charging effects on the substrate, the spectrum for OPI-3-I was collected by applying an electron neutralizer. The results shown in Figures

4.16a and 4.16b indicate that both peaks were present up to neutralizer energies of 10 eV, and thus they likely represent two different chemical states. Iodine is known to bind to coinage metals such as Cu, Ag, and Au.[42]

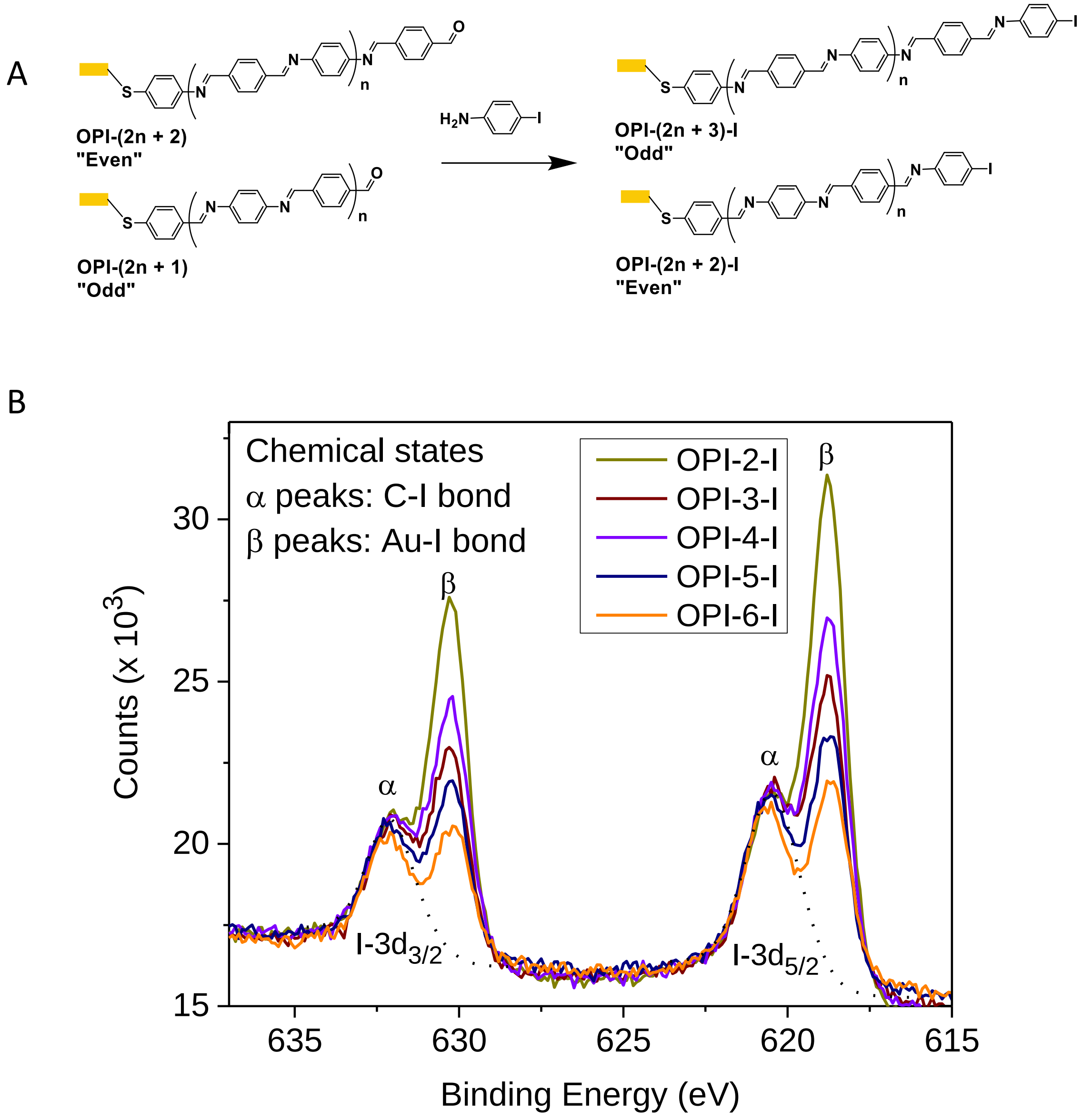

Figure 4.14 (A) Molecular structure for aldehyde terminated wires before (left) and after capping with 4-iodoaniline (right) (B) XPS high resolution spectra of I 3d for OPI-2-I, OPI-3-I, OPI-4-I, OPI-5-I, and OPI-6-I. The two pairs of peaks are from different chemical states of I. The α peaks are from C-I bonds, while the β peaks are from Au-I bonds.

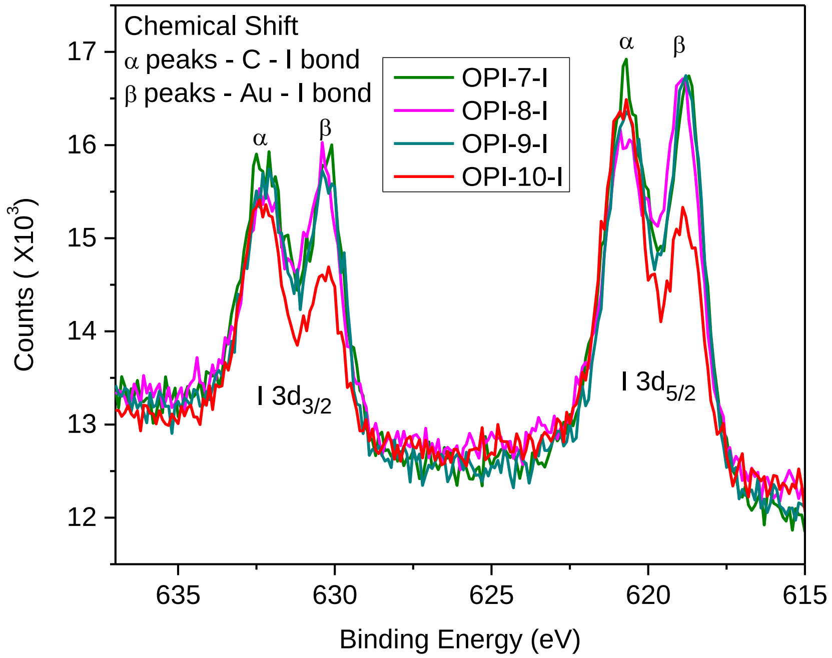

Figure 4.15 XPS high resolution spectra of I 3d for OPI-7-I, OPI-8-I, OPI-9-I, and OPI-10-I. The two pairs of peaks are from different chemical states of I. The α peaks are from C-I bonds, while the β peaks are from Au-I bonds.

To determine which pairs of peaks are from the iodophenylene units (wires) versus Au-I bonds, a blank Au substrate was inserted into a 20 mM solution of 4-iodobenzaldehyde. The spectrum in Figure 4.17a clearly indicated that β peaks were only present for the blank Au substrate, whereas α peaks observed for OPI samples correspond to C-I bonds, which are the peaks of interest for calculating surface coverage.

The high resolution XPS spectra in Figures 4.14 and 4.15 were acquired at three different locations for each sample, and the average of I-3d$_{5/2}$ and I-3d$_{3/2}$ normalized peak areas were used for calculating the extent of reaction. All data were fit by using a combination of Lorentzian and Gaussian peak shapes such that spin orbit coupling rule was obeyed. In order to check the degradation of the sample to prolonged X-ray beam

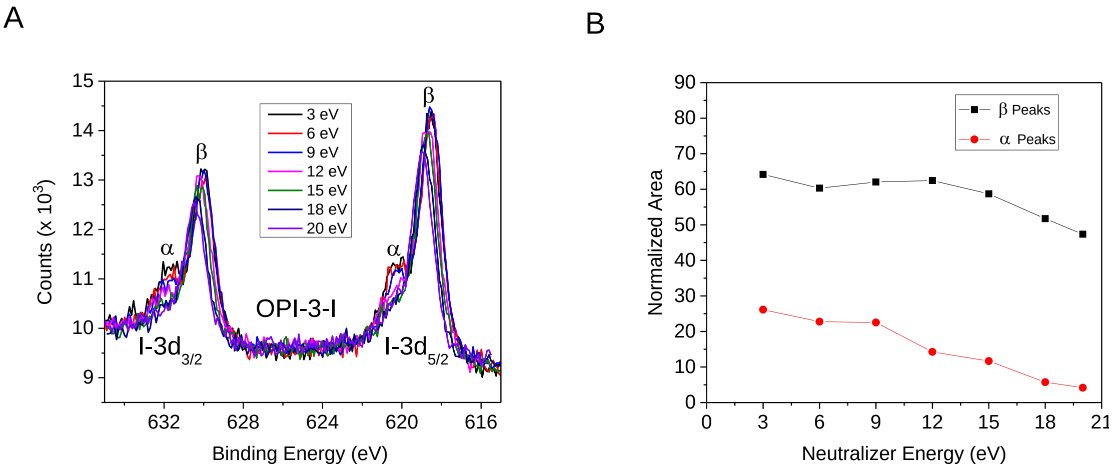

Figure 4.16 XPS spectra of I 3d peaks collected at various neutralizer energy to check whether the α peaks are due to charging effect or chemical states. (B) Sum of α and β peaks verses the applied neutralizer energy. The presences of both peaks suggest two chemical states of I.

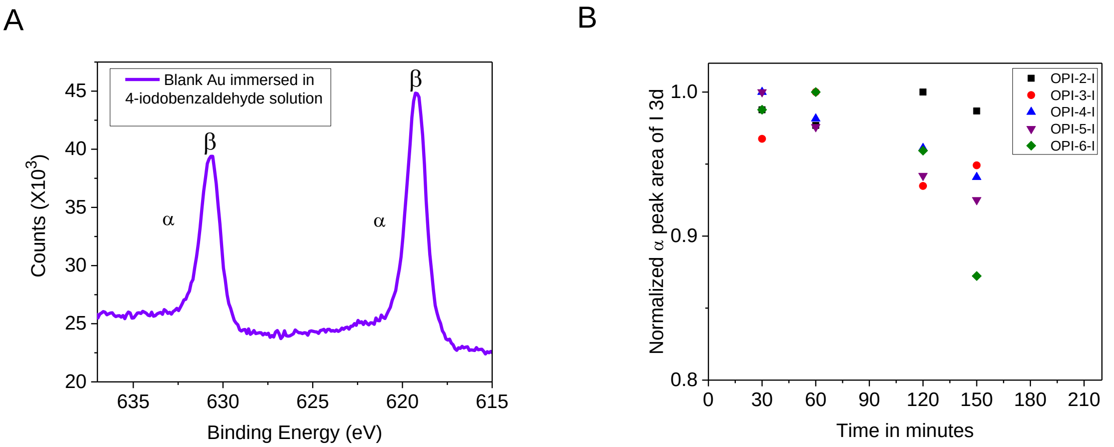

Figure 4.17 (A) XPS spectra of blank Au substrate immersed into 20 mM solution of 4-iodobenzaldehyde. The β peaks are clearly present (Au-I bonds); whereas, α peaks (C-I bonds) are absent. (B) X-ray exposure and degradation study of α-I peaks of OPI-2-I, OPI-3-I, OPI-4-I, OPI-5-I, and OPI-6-I. The normalized peak intensities are plotted on the y-axis verse the exposure time in minutes on the x-axis. The data for each sample was collected at the same location, and the results indicated that OPI-I wires were not degraded by prolonged exposure to x-ray beam.

exposures, a series of high resolution spectra for I terminated wires were collected at the same position for up to 2.5 h. The results displayed in Figure 4.17b indicate that alpha peaks were stable to the X-ray beam up to 2 h, and dropped only by 10% in absolute area afterwards. Figure 4.18 displays the normalized peak areas for the α-I peaks as a function of repeat units. On average, within error, there is not much variation in the peak area of the α-I as a function of the number of repeat units. Thus, this is consistent with near quantitative stepwise reaction.

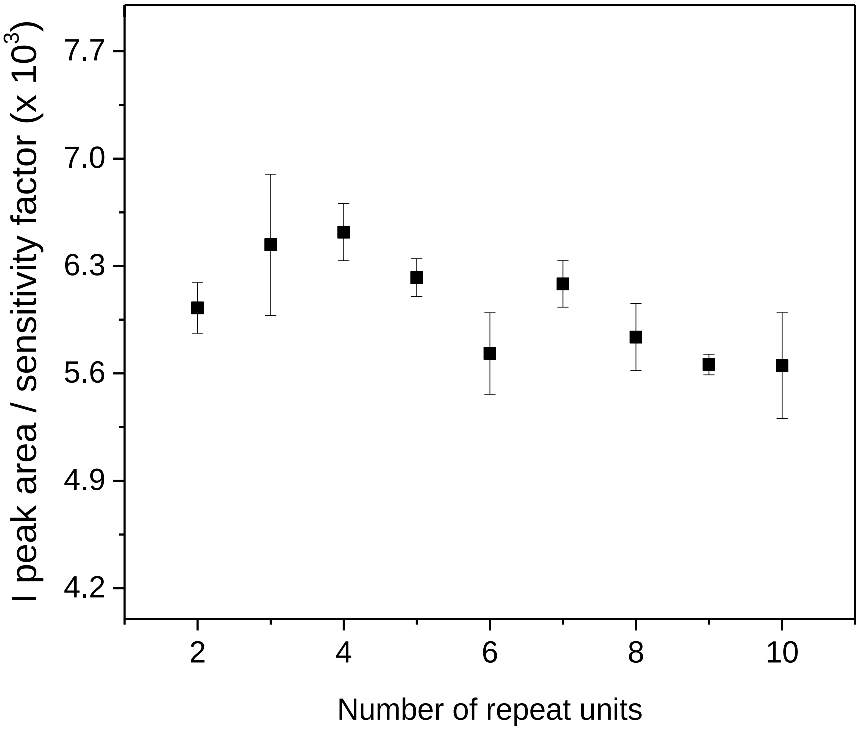

Figure 4.18 Average of sensitivity factor corrected XPS peak areas of I 3d$_{3/2}$ and I 3d$_{5/2}$ as a function of repeat unit.

Surface coverage via XPS. The surface coverage was derived from a set of formalisms[28,43], which are as follows:

7. X-ray reflection, attenuation and refraction are negligible.
8. The surface of the sample is flat and amorphous.
9. The composition of the sample is uniform over the thickness range analyzed.
10. The sample area irradiated by the X-ray is larger than the analyzed area (A_0).
11. Elastic scattering of the photoelectrons are negligible.
12. Photoelectrons are attenuated exponentially as they travel towards the detector in the sample (Beer's law).

Under the above assumptions, the detected photoelectron current emitted at a depth dz from an element i, and core level j is[28] (For example, Au 4f photoelectrons):

$$dI_{ij} = F_x T(KE)\left(\frac{d\sigma}{d\Omega}\right)_{ij} \Delta\Omega D f_{ij} M_i(z)\frac{A_o}{\cos\theta} e^{\frac{-z}{\lambda_i \cos\theta}} dz \qquad (4.4)$$

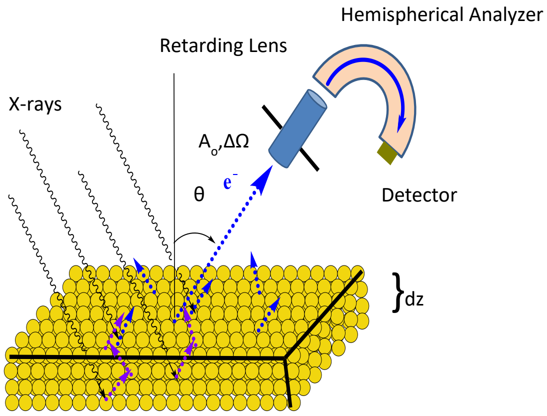

where, Fx is the x-ray flux, T(KE) is the transmission function of the analyzer, which depends on the electron energy, $\left(\frac{d\sigma}{d\Omega}\right)_{ij}$ is the differential photoionization cross section from core level j, *ΔΩ* is the analyzer solid angle, D is the detector efficiency, f_{ij} is the fraction of photoelectrons that appear in the main peak for core level j, $M_i(z)$ is the number of analyzed atoms per unit volume, $\frac{A_o}{\cos\theta}$ is the sample area viewed by the analyzer, $e^{\frac{-z}{\lambda\cos\theta}}$ is Beer's exponential attenuation factor, and λ is the inelastic mean free path. Upon integrating the above equation for a homogenous sample (i.e M(z) is independent of z),

$$I_{ij} = F_x T(KE)\left(\frac{d\sigma}{d\Omega}\right)_{ij} \Delta\Omega \frac{M_i A_o}{\cos\theta} D f_{ij} \int_0^{\infty} e^{\frac{-z}{\lambda_i \cos\theta}} dz$$

$$I_{ij} = F_x T(KE)\left(\frac{d\sigma}{d\Omega}\right)_{ij} \Delta\Omega \frac{M_i A_o}{\cos\theta} \mathrm{D}\, f_{ij} \lambda_i \cos\theta$$

$$I_{ij} = F_x T(KE)\left(\frac{d\sigma}{d\Omega}\right)_{ij} \Delta\Omega M_i A_o \lambda_i D f_{ij} \tag{4.5}$$

The detected photoelectron current emitted from terminal atoms confined in 2D space (such as the red atoms shown in the scheme) can be derived in a similar approach with the assumption that Beer's exponential factor is equal to 1. This assumption applies only for the terminal atoms because the photoemitted electrons travel towards the analyzer without any or very little exponential scattering.

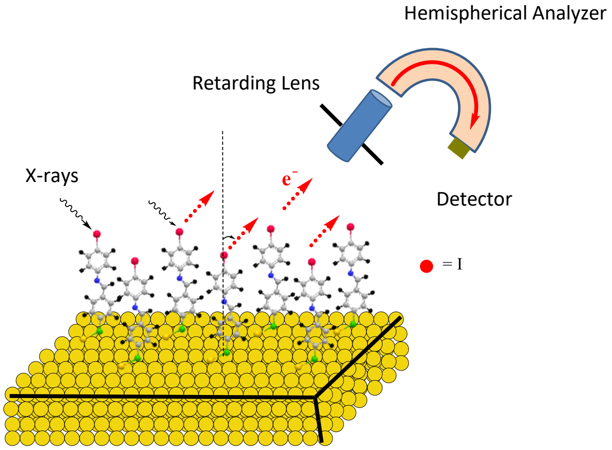

$$I_{ij} = F_x T(KE)\left(\frac{d\sigma}{d\Omega}\right)_{ij} \Delta\Omega \frac{A_o}{\cos\theta} f_{ij} N_s D \tag{4.6}$$

where N$_s$ is the surface coverage (molecules per unit area). In order to correct for x-ray flux flucttutation, and detector efficency which may change from spectrum to spectrum, a bare Au wafer was used as a standard.

The surface coverage of I terminated OPI wires was calculated from the ratio of equation 6 and 5, after normalizing to scan time (t) as follows,

$$\frac{\Gamma_{I3d_{5/2}} t_{Au4p_{3/2}}}{\Gamma_{Au4p_{3/2}} t_{I3d_{5/2}}} = \frac{F_x T(KE)_{I3d_{5/2}} \left(\frac{d\sigma}{d\Omega}\right)_{I3d_{5/2}} \Delta\Omega f_I D \frac{A_o N_{s(I_{3d_{5/2}})}}{\cos\theta}}{F_x T(KE)_{Au4p_{3/2}} \left(\frac{d\sigma}{d\Omega}\right)_{Au4p_{3/2}} \Delta\Omega \rho_{Au} f_{Au} A_o \lambda_{Au} D} \tag{4.7}$$

where, $I_{I3d_{5/2}} = \frac{\Gamma_{I3d_{5/2}}}{t_{I3d_{5/2}}}$, $\mathrm{I}_{Au4p_{3/2}} = \frac{\Gamma_{Au4p_{3/2}}}{t_{Au4p_{3/2}}}$, $\Gamma_{Au4p_{3/2}}$ is the area under Au 4p$_{3/2}$ peak, and $\Gamma_{I3d_{5/2}}$ is the area under I 3d$_{5/2}$ peak.

Upon solving for $N_{s(I_{3d_{5/2}})}$,

$$N_{s(I_{3d_{5/2}})} = \frac{\Gamma_{I3d_{5/2}} T(KE)_{Au4p_{3/2}} \left(\frac{d\sigma}{d\Omega}\right)_{Au4p_{3/2}} \rho_{Au} f_{Au} \lambda_{Au} t_{Au4p_{3/2}} \cos\theta}{\Gamma_{Au4p_{3/2}} T(KE)_{I3d_{5/2}} f_I \left(\frac{d\sigma}{d\Omega}\right)_{I3d_{5/2}} t_{I3d_{5/2}}} \tag{4.8}$$

The differential cross-section can be approximated as follows:[4]

$$\left(\frac{d\sigma}{d\Omega}\right)_{Au4p_{3/2}} = \sigma_{Au4p_{3/2}} Q_{Au4p_{3/2}} \left[\frac{1-\left[\beta_{eff(Au4p_{3/2})}(3\cos^2\psi-1)\big/4\right]}{4\pi}\right] = \sigma_{Au4p_{3/2}} Q_{Au4p_{3/2}} L_{Au4p_{3/2}}$$

where σ is Scofield's scattering cross section[41], Q is a correction factor for elastic scattering[28], L is a function of β (the angular asymmetry factor which describes the anisotropy of photoemission[28,44]), and ψ (angle between the x-ray and photoelectron trajectory, 71°). For I photoelectrons, the effects of elastic scattering were ignored.

At low resolution (typically used in survey scans), the transmission function can be assumed to be constant for photoelectrons of similar kinetic energy, Au $4p_{3/2}$ (K.E = 940 eV) and I $3d_{5/2}$ (K.E = 866 eV). This approximation does not hold for high resolution spectra, where the transmission function is not linearly proportional to the kinetic energy. Thus, we were not able to convert the peak area values to surface coverages for the high resolution spectra (Figures 4.14 and 4.15).

$$N_{s(I3d_{5/2})} = \frac{\Gamma_{I3d_{5/2}} \sigma_{Au4p_{3/2}} Q_{Au4p_{3/2}} L_{Au4p_{3/2}} \rho_{Au} \lambda_{Au} \, \mathrm{t}_{Au4p_{3/2}} \cos\theta}{\Gamma_{4p_{3/2}} \sigma_{I3d_{5/2}} L_{I3d_{5/2}} t_{I3d_{5/2}}} \tag{4.9}$$

The α-I $3d_{5/2}$ surface coverage values obtained from low resolution scans of OPI-3-I, OPI-5-I, OPI-7-I, and OPI-9-I are shown in Figure 4.10. At ~ 3.57 I tags/nm^2, they are in good agreement with the results obtained by RBS, CV, and NRA. The following values were used for calculating the surface coverage of I; σ (Au $4p_{3/2}$) = 8.01×10^{-24} m^2 and σ (I $3d_{5/2}$) = 2.70×10^{-23} m^2,[41] $Q_{Au} = 0.92$,[28] $L_{Au}= 0.0913$,[44] $\rho_{Au} = 59.04$ atoms / nm^3, $\lambda_{Au} = 2.23$ nm,[28,45] $\theta = 35°$, $L_I= 0.0954$,[44] and $f_{Au} = f_I = 0.84$[46]. The low resolution spectra of Au $4p_{3/2}$ and I 3d peaks are shown in Figure 4.19. On average, we obtained surface coverage value of 3.57 ± 0.13 I tags / nm^2, which is in excellent agreement with the results obtained by RBS, NRA, and CV.

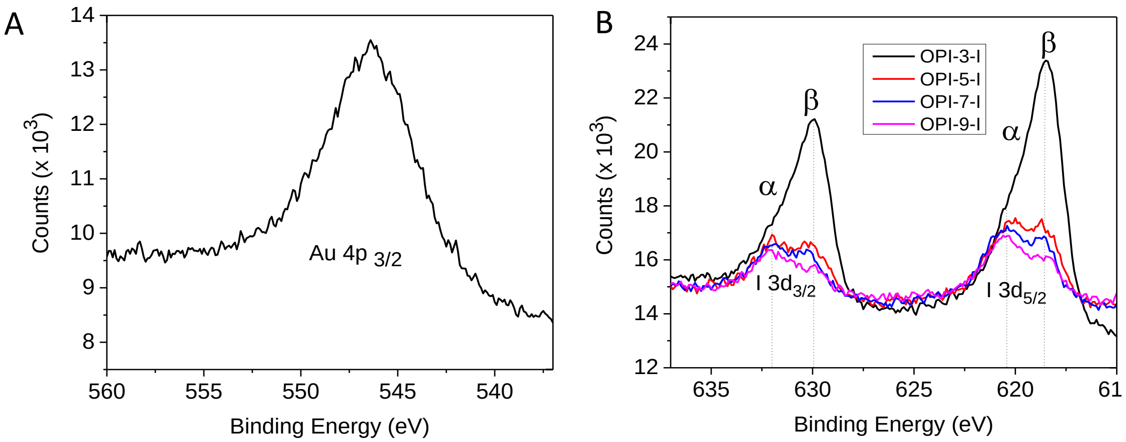

Figure 4.19 Low resolution XPS spectra of bare Au $4p_{3/2}$ (A) and I 3d of OPI-3-I, OPI-5-I, OPI-7-I, and OPI-9-I (B).

Reaction yield per synthesis step. A central goal of our work is to determine the reaction yield for the surface click reactions, Figure 4.20. This was achieved by taking the ratio of consecutive average surface coverage values obtained by RBS, CV, and NRA, carbonyl peak area from IR, and iodine peak area from XPS, according to equation 4.10 below:

$$\text{Extent of reaction} = \frac{\text{Signal due to (OPI)}_{\text{n}}}{\text{Signal due to (OPI)}_{\text{n-1}}} \qquad (4.10)$$

For example, to calculate the extent of reaction for the 5th step by XPS, the I peak area ratio of OPI-5-I (20.0×10^3) to OPI-4-I (19.1×10^3) from Figure 4.18 was evaluated (96%). The extent of reaction measured by each method, as an average of the first 9 surface reactions yields a value of 98 ± 7.9% by FTIR, 99 ± 6.6% by RBS, 99 ± 16% by CV, 99 ± 5.8% by XPS, and 98 ± 2.4% by NRA. It is evident that these yields are remarkably similar across the 5 different techniques and the 5 different tags. Averaging across all techniques, we estimated the extent of reaction yield to be 99% per step.

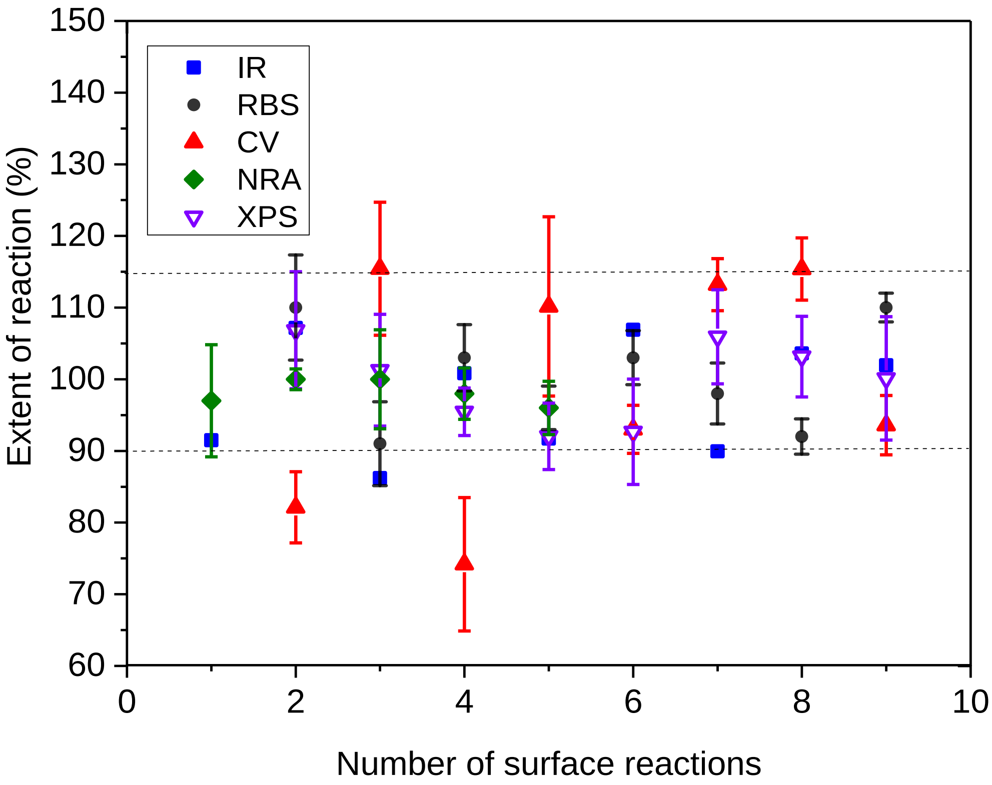

Figure 4.20 Extent of reaction of OPI wires as a function of number of surface reactions. The results for CV, RBS & NRA were obtained from surface coverage values (Figure 4) whereas IR & XPS results were obtained from peak areas associated with carbonyl and iodine units, respectively.

The scatter evident in Figure 4.20 deserves some discussion. Fundamentally, quantitative surface analysis is challenging because of the low number of molecules / atoms per unit area. For example, typical XPS uncertainties for atomic concentrations are on the order of 5-10%. One can see that if reaction yields are near quantitative, then uncertainties can lead to reaction yield estimates for a single step greater than 100%. This might be better understood by inspection of the NRA data in Figure 4.13c. The quality of these data is quite high, but if it were worse, and there were more vertical scatter for each experimental point, then ratioing coverages for consecutive steps (eg. coverage after 4 reactions divided by coverage after 3 reactions) could easily give an apparent yield greater than 100%. The actual NRA estimate of extent of reaction in Figure 4.13 is reasonably tight across consecutive surface reactions. These are our highest quality data. In connection with Figure 4.20, it should be clear that we are not claiming intentionally that the reaction yield is ever over 100%. The percentages in Figure 4.20 represent the uncertainty of the measurement and the combination of errors when employing equation 10. In a sense, Figure 4.10 is more meaningful than Figure 4.20. Figure 4.10 shows that within experimental error, the coverage of tag elements is unchanged for consecutive reactions.

It is also evident from Figure 4.20 that the extent of reaction varies as much as 40% for CV, and approximately 10 – 20% for other methods. This could be due to both large scan size for CV (10 × greater than RBS and XPS), which makes it more prone to defects on Au, and contributions from the onset of an irreversible redox process in the OPI wires around 0.7 V. Importantly, the chain length distribution can be calculated from the extent of reaction of each reaction step. Given the average yield per step of 99%, the chain length distribution is as shown in Figure 4.21b after 9 click reactions. That is, for 10 repeat units, 91% of the chains will have the expected length. On the other hand, if the extent of reaction for each step proceeded to 90% completion, the chain length distribution for the longest wire decreases significantly to the point that only 38% of the wires contain the wire length of interest after 9 surface reactions as shown in Figure 4.20a. This is important information for ongoing molecular electronics experiments that employ these wires.

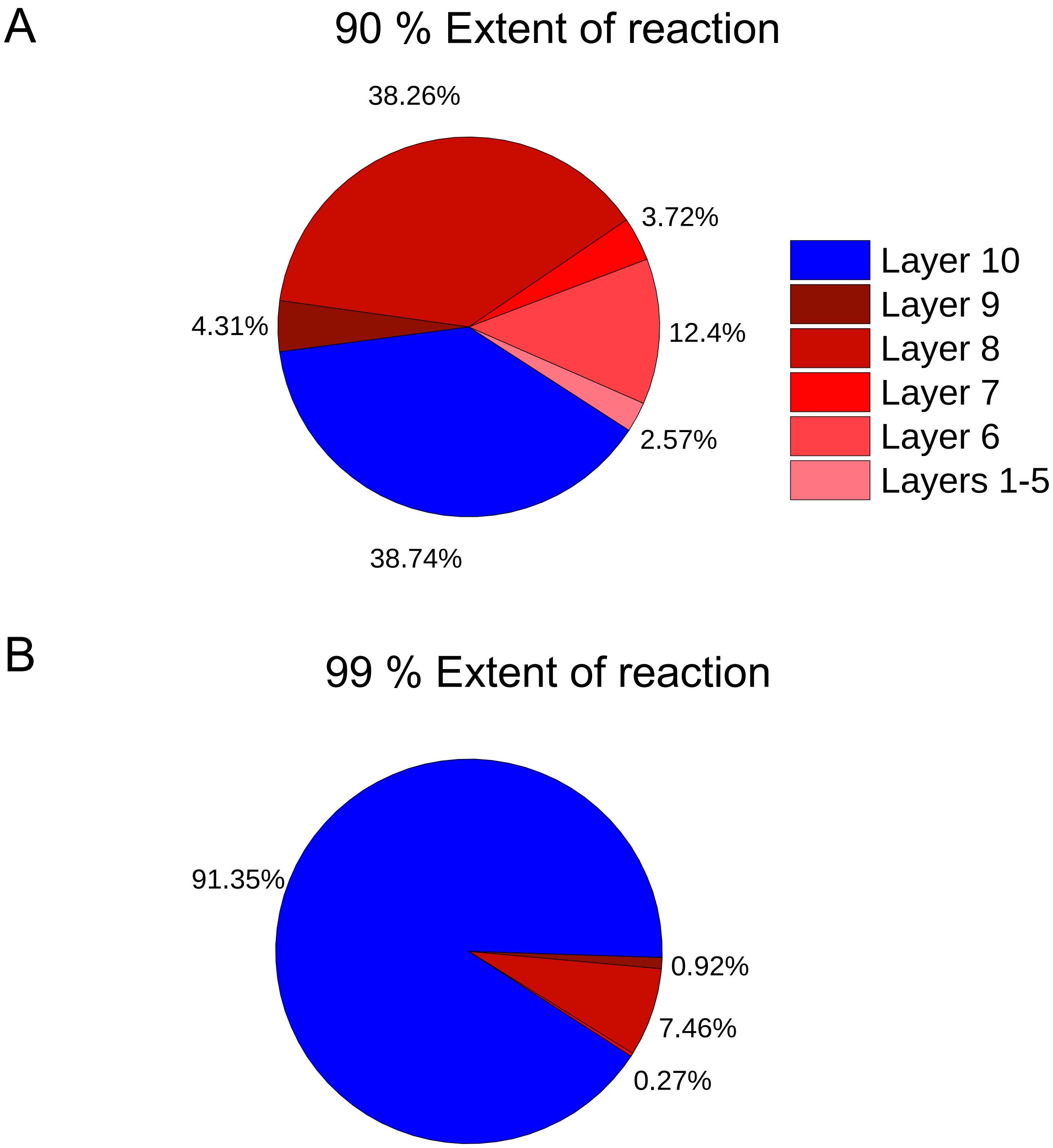

Figure 4.21 Pie chart of chain length distribution as a function of the total number of repeat units (layers) after 9 Schiff base reactions for 90% (A) and 99% (B) extent of reaction for each stepwise reaction. $x_i(p) = p^{i-1}$, where p is extent of reaction and x_i is the mole fraction of the longest wire (chain length of interest).

4.5 Conclusion

We have systematically measured the coverage and surface reaction yield for a set of π-conjugated molecular wires ranging in length between 0.6 and 5.5 nm. The OPI wires were grown from SAMs of 4-aminothiophenol or 4-formylthiophenol, and reacted stepwise with alternate addition of terephthalaldehyde (22 °C) or 1,4-benzenediamine (40 °C). Surface analysis by 6 different techniques – SE, CV, IR, RBS, NRA, and XPS demonstrates that the surface reaction yields via imine click chemistry are high, approximately 99%. The high yields and correspondingly high surface coverages of π-conjugated molecular wires (3.5 molecules/nm^2) bode well for continued use of these systems in ongoing molecular electronics experiments. Additionally, these OPI wires serve as an excellent platform for quantitative comparison of different surface analytical techniques and in particular for demonstrating the effective use of NRA for SAM characterization for the first time. Future work will focus on the synthesis of OPI wires with a broad spectrum of backbone architectures to enhance electronic functionality.

4.6 Additional Attempts on Measuring Reaction Yield of OPI Wires

Initially, all of the wire growth steps were conducted at room temperature as outlined in previous papers because residual aldehyde peaks were not observed with the Nicolet Series II Magna-IR System 750 IR spectrometer. In fall 2013, our characterization facility purchased a new Nicolet iS50 spectrometer, which had a much better sensitivity. Consequently, measurements with this new IR bench revealed that room temperature reaction of 1,4-phenylenediamine with carbonyl terminated wires resulted in an incomplete reaction as shown in Figure 4.1. However, a considerable amount of synthesis and characterization was already done on measuring the reaction yield of un-optimized OPI wires on template stripped Au, which will be the focus of this section.

XPS of halogen incorporated OPI wires. Our initial approach to calculate the extent of reaction was to incorporate halogen atoms along the wire backbone as shown below.

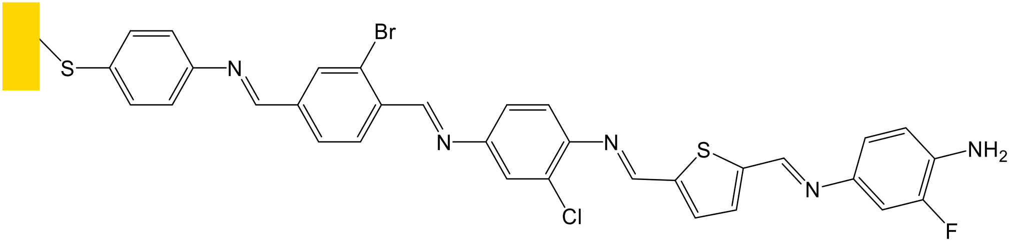

Figure 4.22 Molecular structure of halogen incorporated OPI wire

In order to grow the above molecular wire, the monomers shown in Schemes 4.2 and 4.3 were synthesized using procedures reported in literature. All starting materials were bought from Sigma-Aldrich Chemicals (2-Bromo-1,4-dimethylbenzene (99%), 2-Chloro-4-nitroaniline (99%), and 2-Fluoro-4-nitroaniline (95%)) and used as purchased.

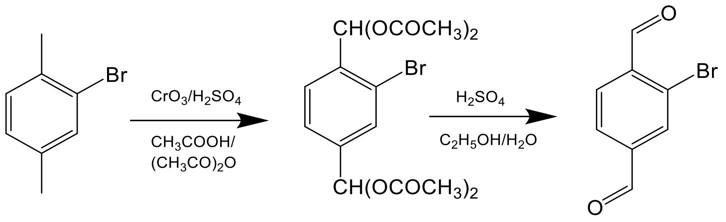

Scheme 4.2 Synthesis of 2-bromoterpethaladehyde

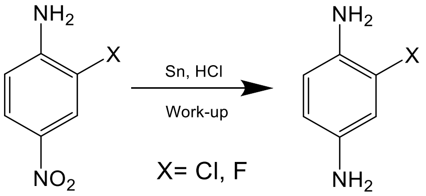

Scheme 4.3 Synthesis route of 2-chlorophenylenediamine and 2-fluorophenylenediamine

Freshly evaporated Au substrates were immersed into 1 mM 4-aminothiophenol (4-ATP) in absolute ethanol. After 24 h, the SAM-coated Au substrates were removed from the thiophenol solution and rinsed thoroughly with absolute ethanol to remove physisorbed molecules before immersing them into a 20 mM solution of 2-bromoterephthalaldehyde in ethanol for 24 hours, followed by consecutive reaction with 2-chlorophenylenediamine, 2-5-thiophenedicarbaldehyde, and 2-fluorophenylenediamine in the usual manner at room temperature. Each growth step was monitored by RAIRS as shown in Figure 4.23b. The alternate appearance and disappearance of C=O bend peaks (1705 cm^{-1}) and NH_2 stretch peaks (3200-3600 cm^{-1}), and increase in the C=N stretch

(1625 cm^{-1}) and C=C bend modes (1500 cm^{-1}) are good indicators that the reaction proceeds similarly as outlined in the main text and Figure 4.23a.

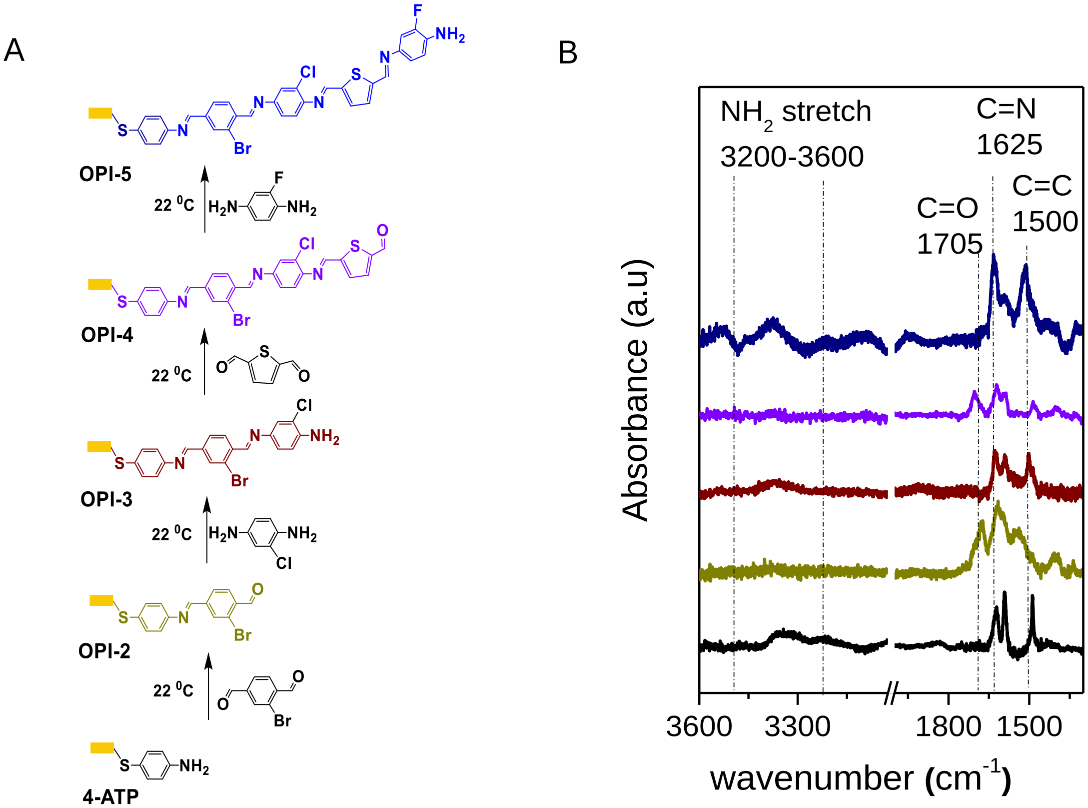

Figure 4.23 Molecular structures (left) and RAIRS spectra (right) for growth of halogen incorporated OPI wires. The vertical lines indicate the position of NH_2 stretch (3200-3600 cm^{-1}), C=O bend (1705 cm^{-1}) and C=N (1625 cm^{-1}).

Reaction yield for 2nd growth step of halogen incorporated wires.

To calculate the extent of reaction of reaction for the 2nd growth step, the photo-emitted electron counts of Br and Cl were compared. As shown in Figure 4.24, the XPS spectrum revealed well resolved Cl and Br peaks along with their respective spin-orbit coupling splitting. A computer program that uses shirely background subtraction was then used to calculate the peaks areas for quantitative analysis. The extent of reaction was calculated by taking the peak area ratio of Cl to Br according to equation 4.11:

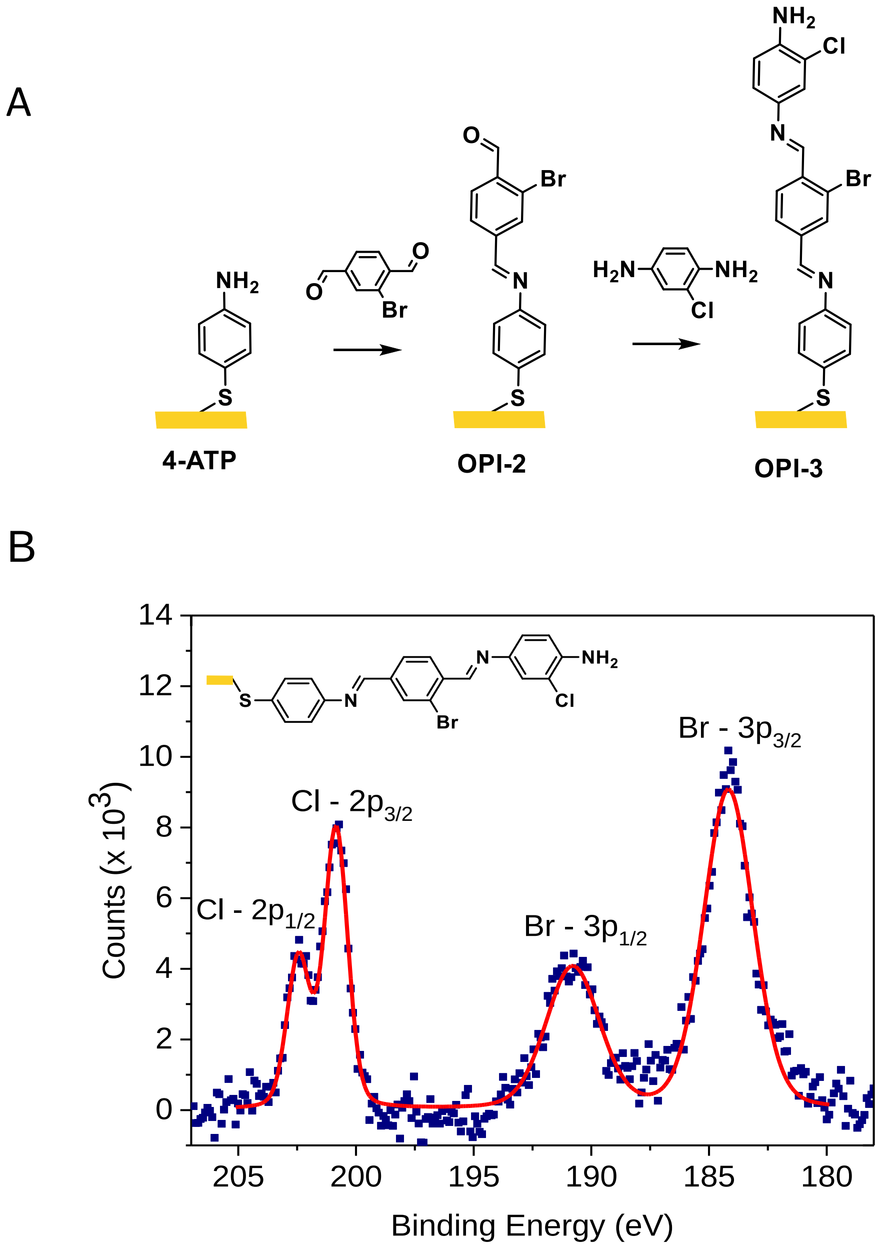

Figure 4.24 (A) Molecular structure and step-wise growth of halogen incorporated OPI wires. (B) XPS spectrum of OPI-3 with Cl and Br labeling units. The Br 3p and Cl 2p peaks were resolved clearly along with their respective spin-orbit coupling ratio.

$$\frac{x_{Cl}}{x_{Br}} = \frac{I_{Cl}\sigma_{Br}L_{Br}}{I_{Br}\sigma_{Cl}L_{Cl}} \tag{4.11}$$

where, I is the peak area, σ is the photoionization cross section[41], and L is the angular asymmetry factor[28,44] which describes the anisotropy of photoemission. We obtained an average value of 96.3 ± 6.08% for the extent of reaction of Cl to Br (2nd surface reaction). Even though this method is suitable for tagging each monomer units, it does not take in to account attenuation of the Br photoelectrons (Beer's law), and will result in over estimation of the extent of reaction. Furthermore, the value of the inelastic photoelectron mean free path (λ) for monolayer films is not necessarily similar to its value for bulk solids. Thus, capping wires with halogen termini was the ideal method to follow the reaction for each stepwise growth instead of incorporating them along the monomer units.

Reaction yield for 2nd, 3rd, and 4th growth steps of halogen capped wires.

The growth steps for the halogen capped wires were monitored by RAIRS as shown in Figures 4.25, 4.26 and 4.27. Unlike the RAIRS spectra in Figure 4.23 where each surface reaction was monitored by the alternate appearance and disappearance of aldehyde and amine peaks, the Cl terminated molecular wires were qualitatively characterized by the disappearance of the aldehyde or amine peak prior to addition of Cl terminated conjugated unit as shown in Figures 4.25 - 4.27.

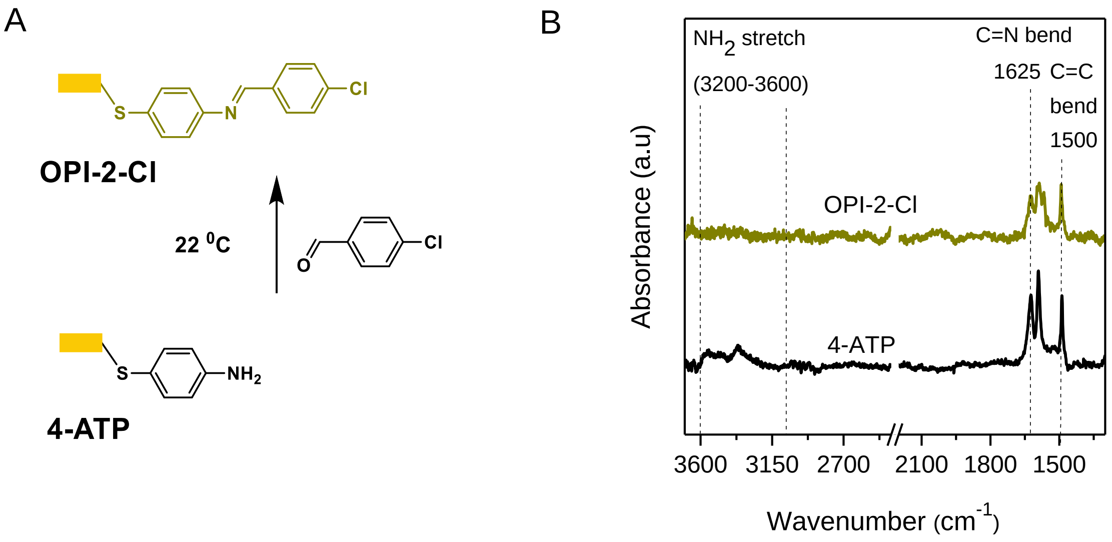

Figure 4.25 Molecular structures (left) and RAIRS spectra (right) for 4-ATP, and OPI-2-Cl wires. The vertical lines indicate the position of NH_2 stretch (3200-3600 cm^{-1}), and C=N (1625 cm^{-1}). Note the disappearance of the amine stretch in OPI-2-Cl.

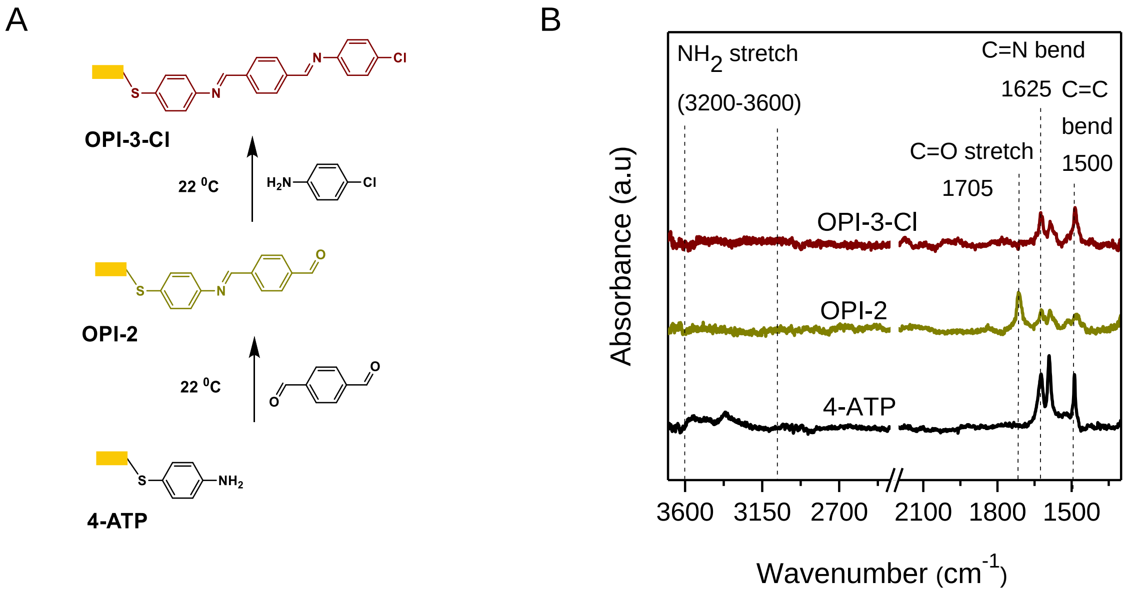

Figure 4.26 Molecular structures (left) and RAIRS spectra (right) for 4-ATP, OPI-2, and OPI-3-Cl wires. The vertical lines indicate the position of NH_2 stretch (3200-3600 cm^{-1}), C=O bend (1705 cm^{-1}) and C=N (1625 cm^{-1}). Note the disappearance of the aldehyde peak when 4-chloroaniline was reacted with OPI-2.

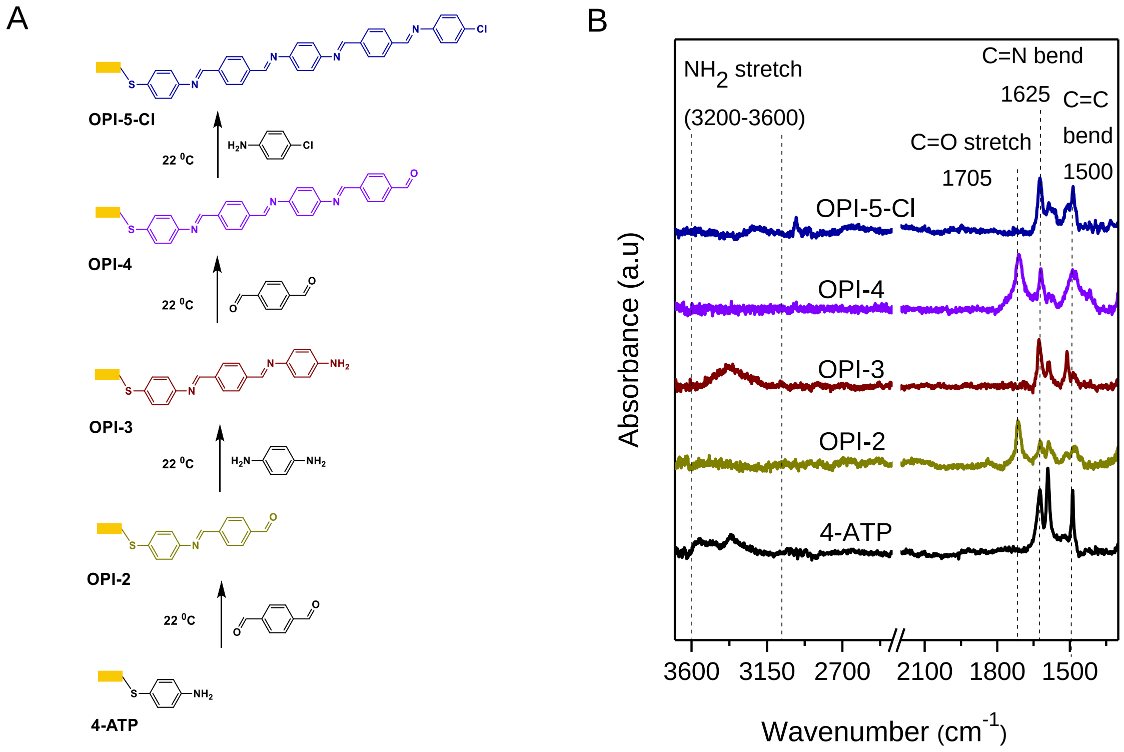

Figure 4.27 Molecular structures (left) and RAIRS spectra (right) for 4-ATP, OPI-2, OPI-3, OPI-4, OPI-5-Cl wires. The vertical lines indicate the position of NH_2 stretch (3200-3600 cm^{-1}), C=O bend (1705 cm^{-1}) and C=N (1625 cm^{-1}).

Ellipsometry was employed to determine the thickness of the wire films. As shown in Figure 4.28, the length of the wires increased with the number of repeat units. The estimated (theoretical) thickness was calculated by assuming perpendicular orientation and trans-configuration for each chain length. The index of refraction (n) and absorption coefficient (k) for ellipsometry were assumed to be 1.45 and 0, respectively, over the wavelength region 600-1000 nm. The ellipsometry data are reasonably well matched to theoretical expectations.

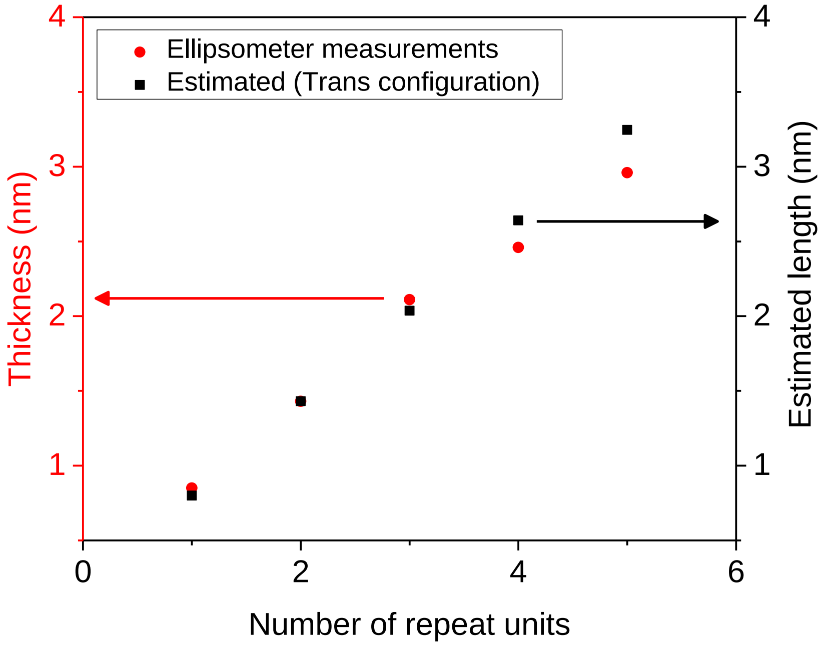

Figure 4.28 Measured and estimated thicknesses of OPI films as a function of number of repeat units. The estimated thicknesses were calculated using Cambridge Scientific ChemBio 3D, assuming trans configuration of the molecules oriented normal to the substrate; the Au-S bond length was taken to be 2.36 Å.[5,47]

Halogen capped wires have 2 major advantages verses halogen incorporated wires. They are;

1) Similar halogen atom can be used to cap wires at the desired growth step, i.e., no need to compare signals of Br and Cl. Instead Cl peaks can be compared to each other directly after normalizing to scan time.
2) Uncertainty regarding the attenuation of photoelectrons (Beer's law) can be eliminated because the photoelectrons from the halogen atom travel through vacuum only.

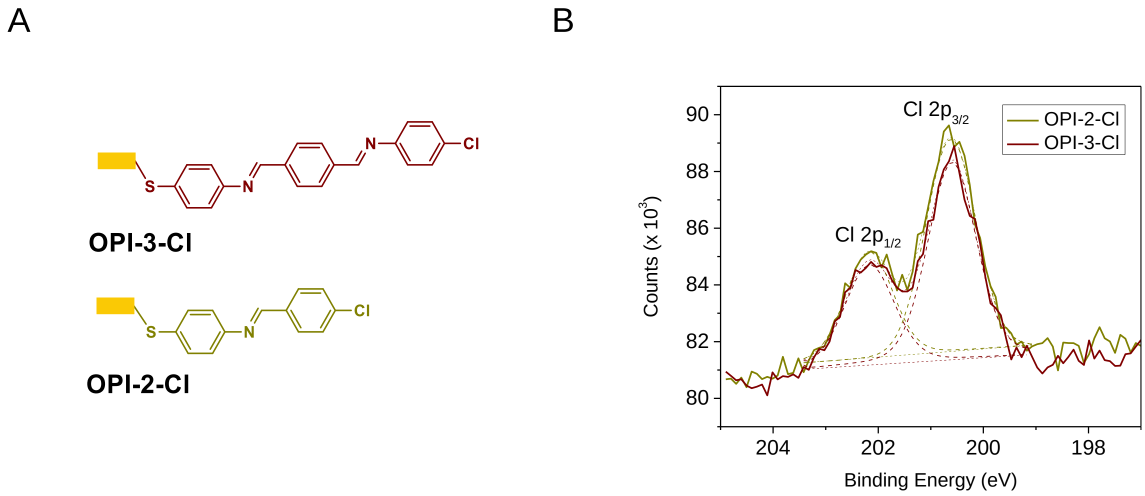

Figure 4.29 XPS spectra of Cl 2p for OPI-2 and OPI-3 (600 scans with resolution of 100 meV/step). Solid lines indicate collected data, while broken lines are the Gaussian fits.

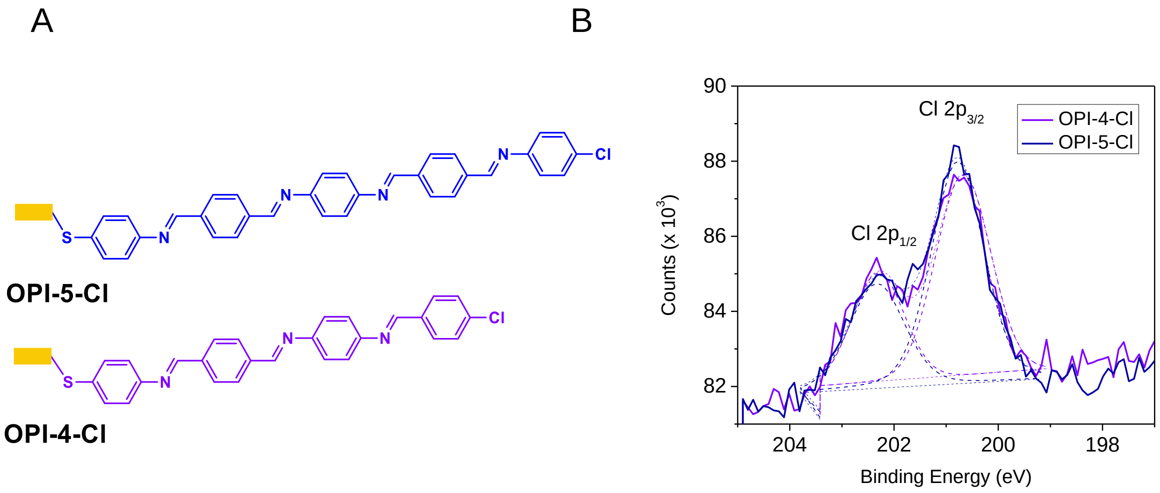

Figure 4.30 XPS spectra of Cl 2p for OPI-4-Cl and OPI-5-Cl. (600 scans with resolution of 100 meV/step). Solid lines indicate collected data, while broken lines are the Gaussian fits.

To calculate the extent of reaction, the XPS intensity of each Cl peak was compared to the corresponding previous layer. Cl was chosen because the scan window is half the size required for Br. Therefore, high resolution spectra can be obtained in a short amount of time. This method was used for the 2nd, 3rd and 4th extent of reaction. The spectra in Figure 24 shows the intensity count of Cl for OPI-2-Cl and OPI-3-Cl. 600 scans were taken for each spectrum at resolution of 100 meV/step. The extent of reaction was then calculated by comparing the intensity of the Gaussian fits for both Cl-2p-3 and Cl-2p-1.

Table 4.1 Peak areas of OPI-Cl wires.

Wire type	**BE**	**Peak Area**
OPI-2-Cl $2p_{3/2}$	200.62	90747.25
OPI-2-Cl $2p_{1/2}$	202.17	43847.34
OPI-3-Cl $2p_{3/2}$	200.69	88600.45
OPI-3-Cl $2p_{1/2}$	202.34	44291.73
OPI-4-Cl $2p_{3/2}$	200.77	76207.51
OPI-4-Cl $2p_{1/2}$	202.40	38976.72
OPI-5-Cl $2p_{3/2}$	200.78	79255.82
OPI-5-Cl $2p_{1/2}$	202.33	39353.82

The extent of reaction was calculated by equation 4.10. For example, to calculate the extent of reaction for the 2nd growth step of OPI-Cl wires, the peak area ratio of OPI-3-Cl to OPI-2-Cl was evaluated as shown below

$$E.O.R\ for\ 2nd\ growth\ step = \frac{Peak\ area\ of\ OPI-3-Cl\ 2p_{3/2}}{Peak\ area\ of\ OPI-2-Cl\ 2p_{3/2}} = \frac{88600.5}{90747.3} = 98\%$$

Similar analysis was performed for 3rd and 4th reaction step for both Cl $2p_{3/2}$ and Cl $2p_{1/2}$ peaks. The results are summarized below.

Table 4.2 Extent of reaction of OPI-Cl wires.

	Extent of reaction	
Growth step	$2p_{3/2}$	$2p_{1/2}$
2	0.98	1.01
3	0.86	0.88
4	1.04	1.01

Extent of reaction for the first click step

The first extent of reaction was calculated by using two methods:

1) By comparing the intensity of N 1s photoelectron peak and Br 3p peaks.

OPI wires with terminal N and Br were chosen to aviod any attenuation of signals through the sample. Thus, spectra of N 1s from 4-ATP and Br 3p from OPI-2Br were collected, and the respective intensities were computed by using the built in sensitivity factor of the instrument. This method yielded a high extent of reaction (99%) for the first click reaction. The N 1s spectra has a small shoulder peak due to charging effect which is caused by molecules that remained in excited ot charged state after photoemission. The two peaks were then tabulated as if they had originated from the same wires, and the following data was obtained:

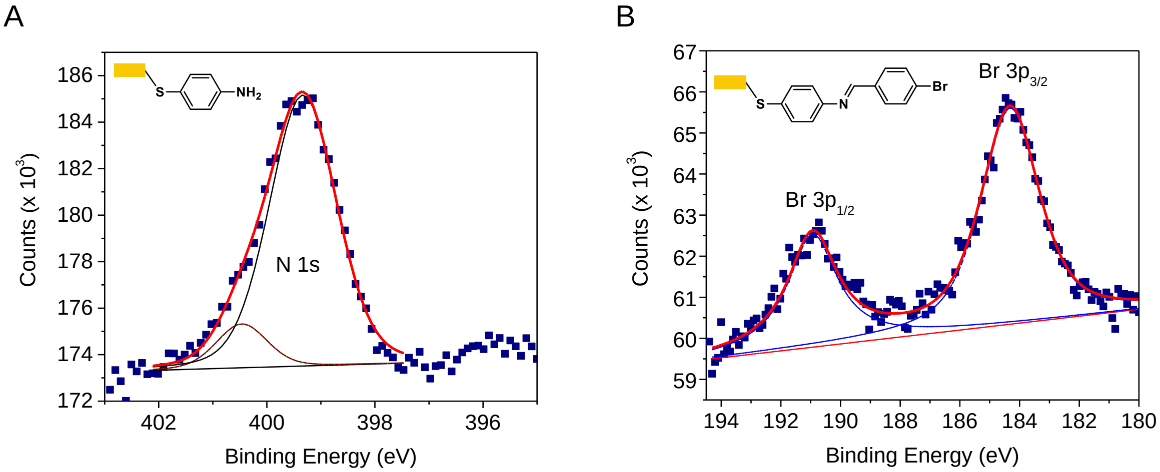

Figure 4.31 XPS spectra of N 1s for 4-ATP and Br 3p of OPI-2-Br.

Table 4.3 Normalized peak areas of N1s (4-ATP) and Br 3p (OPI-2-Br).

XPS Line	***Adj'ed Be***	***Sensitivity factor***	***Area***	***Norm Area***	***Atom %***
N 1s	399.066	1.8	203671.6	30.28	47.57
N 1s	400.495	1.8	11614.76	1.73	2.72
Br 3p1	190.92	1.72	76977.07	16.32	25.63
Br 3p3	184.336	3.31	139668.9	15.33	24.08

$$\frac{x_{Br}}{x_N} = \frac{49.81}{50.19} = 99\%$$

2) By comparing the intensities of 4-chlorothiophenol and 4-chlorobenzaldehyde

If method 1 was used to compute the Cl 2p peak areas of OPI-2-Cl instead of Br 3p of OPI-2-Br, the extent of reacction is approximately 66%. This is due to incorrect built in sensitivity factor of the XPS capture software, which computes an 'average cross section' for Cl 2p$_{3/2}$ and Cl 2p$_{1/2}$ orbitals instead of assigning separate values tabulated by Scoffield (most likely programming error). To circumvent this issue, the Cl 2p peaks of 4-chlorothiophenol were directly compared to OPI-2 Cl. This method assumed that the packing density (surface coverage) of 4-chlorothiohenol is similar to 4-ATP. The following two spectra were obtained respectively.

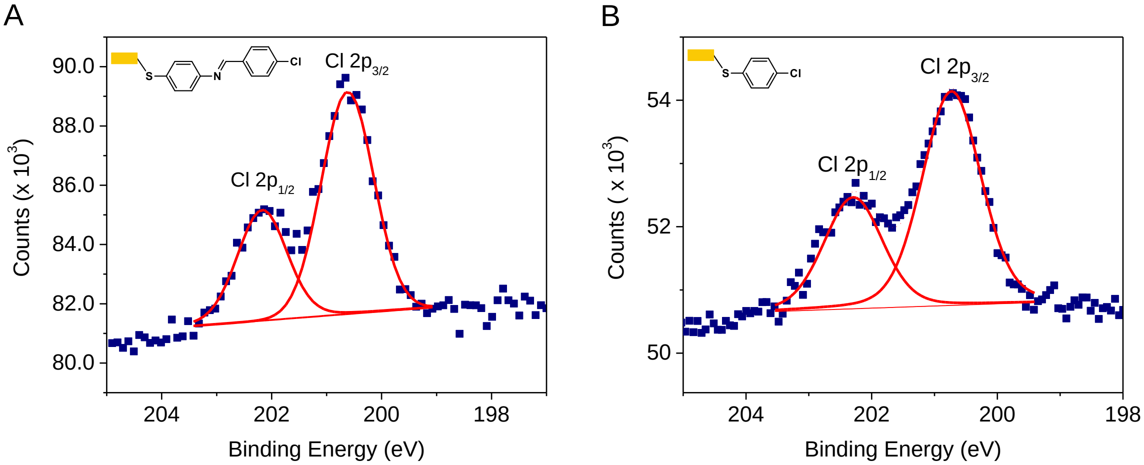

Figure 4.32 XPS spectra of Cl 2p for OPI-2-Cl (A) and 4-chlorothiophenol (B).

Table 4.4 Peak areas of 4-chlorothiophenol and OPI-2-Cl.

	Area	***Normalized Area***	***Atomic %***
4-Chlorothiophenol			
Cl 2p-3	103583	11.31	35.37
Cl 2p-1	51878	5.67	17.72
OPI-2-Cl			
Cl 2p-3	90747.25	10.11	31.63
Cl 2p-1	43847.34	4.89	15.28

$$\frac{x_{Cl(4-chlorobenzaldehyde)}}{x_{Cl(4-chlorothiophenol)}} = \frac{46.91}{53.09} = 88\%$$

Since this method assumes similar packing density, it is prone to errors than method 1. The average of the two methods was used for the first extent of reaction (93.5%).

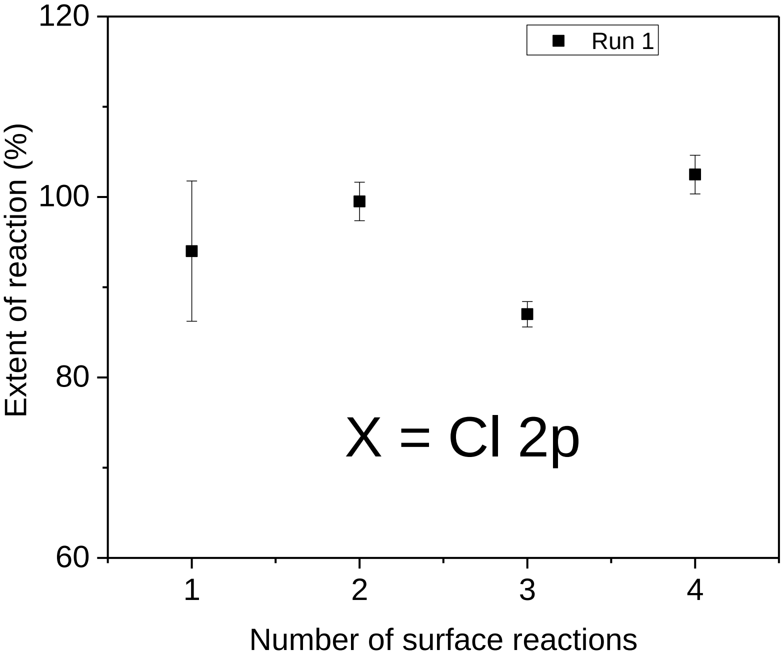

Figure 4.33 Extent of reaction for the first 4 surface reactions obtained from Cl terminated OPI wires. On average, the wires reacted to 90% completion.

Figure 4.33 displays the extent of reaction for the first 4 surface reactions obtained from Cl terminated OPI wires. It is clear that ratioing peak areas can easily give rise to extent of reaction greater than 100%. In connection with Figure 4.20, it should be clear that we are not claiming intentionally that the reaction yield is ever over 100%. The percentages in Figure 4.33 represent the uncertainty of the measurement and the combination of errors when employing equation 4.10.

We also performed similar measurements on I and F tagged OPI wires for the 2nd, 3rd, 4th, and 5th surface reaction. Here, we did not attempt to calculate the extent of reaction for the first surface reaction as outlined for OPI-Cl wire. Among all of the halogens, I is the best XPS tag because it has the highest scattering cross-section (8.39 × 10^{-23} m^2) followed by Br (1.35 × 10^{-23} m^2), F (6.36 × 10^{-24} m^2), and Cl (5.86 × 10^{-24} m^2), respectively.[41] Thus, spectra collection time was much shorter for F and I tagged wires. The spectra for OPI-F and OPI-I wires are displayed in Figure 4.34. The extent of reaction was calculated in a similar manner for OPI-Cl wires, and the results for 5 different runs for OPI-F and 3 different runs for OPI-I are displayed in Figures 4.34c and 4.34d, respectively. OPI-F wires were particularly problematic and showed variation in peak intensity from sample to sample presumably because the F-substituent altered its reactivity.

We speculate that the electronegativity of F significantly affects the reactivity of 4-fluoroaniline by withdrawing electron density from the lone pair of electrons on the amine (NH_2) unit. Since it is the lone pair of electrons that attack the carbonyl termini, and initiate the imine condensation reaction; any substituent that tends to interfere with the lone pairs will affect its reactivity. On the other hand, we think that the reactivity for 4-fluorobenaldehyde is unaffected in comparison to 4-fluoroanilne, because the F withdraws the lone electron pairs from the O of the carbonyl unit. As a result, the lone pair of N on the wire termini can easily attack the carbonyl groups. However, as we will show in chapter 7, the intensity of F signals depends on the electronic structure of the wires. This may lead to additional errors when calculating reaction yield (more later).

The extent of reaction for OPI-F, OPI-Cl, and OPI-I wires for the first 5 repeat units is shown in Figure 4.35. It is clear that F has the highest scatter than Cl and I. Averaging across all the data sets; we obtained an average extent of reaction of 98.8 ±

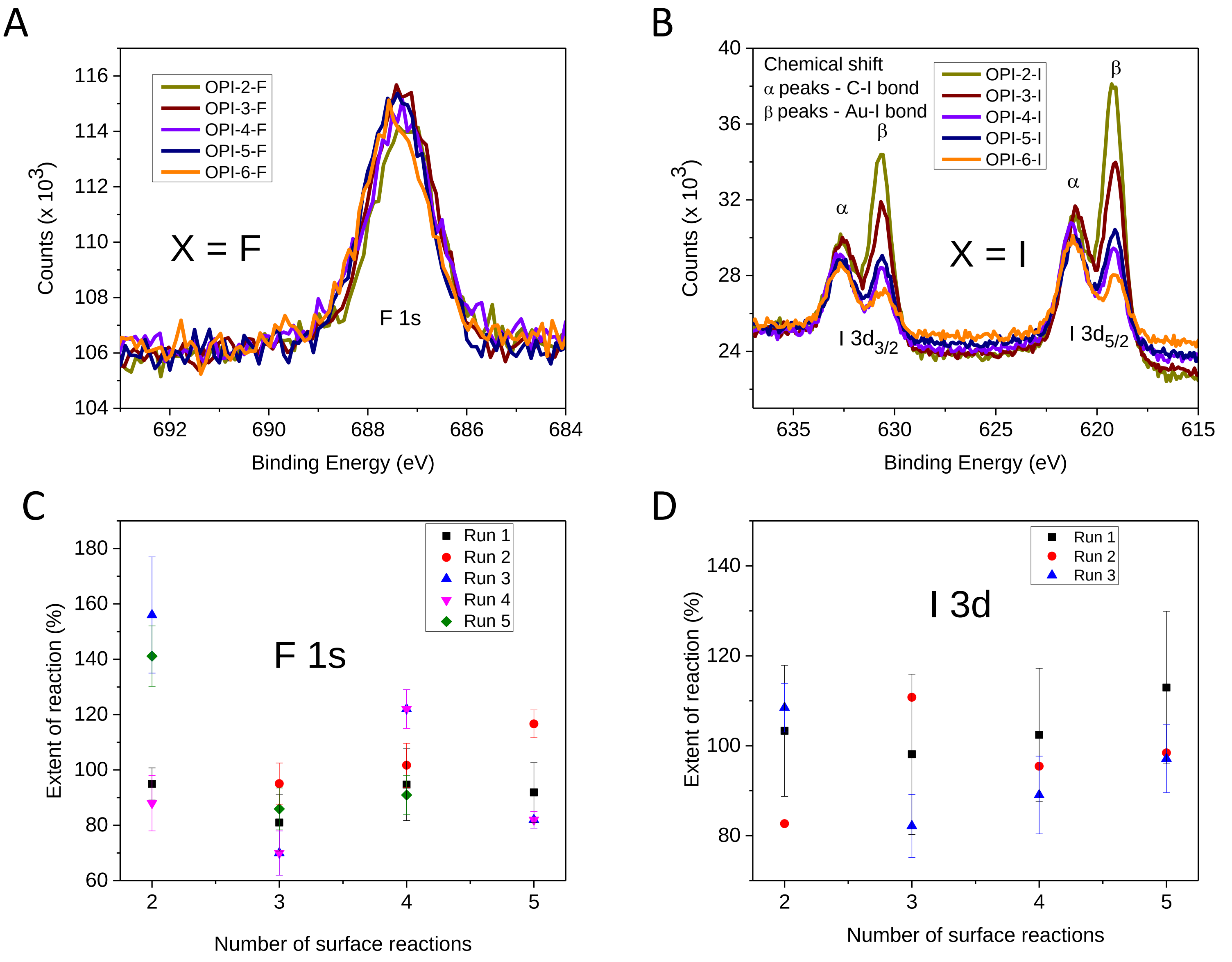

Figure 4.34 (A).Molecular structure for para-halogen terminated OPI wires. All wires were synthesized starting from SAM of 4-ATP. (B) XPS spectra of F terminated OPI wires. (C) XPS spectra of Cl terminated wires. (D) XPS spectra of I terminated wires.

18%. We note here that the reaction conditions are not optimized unlike the data sets in Figure 4.20

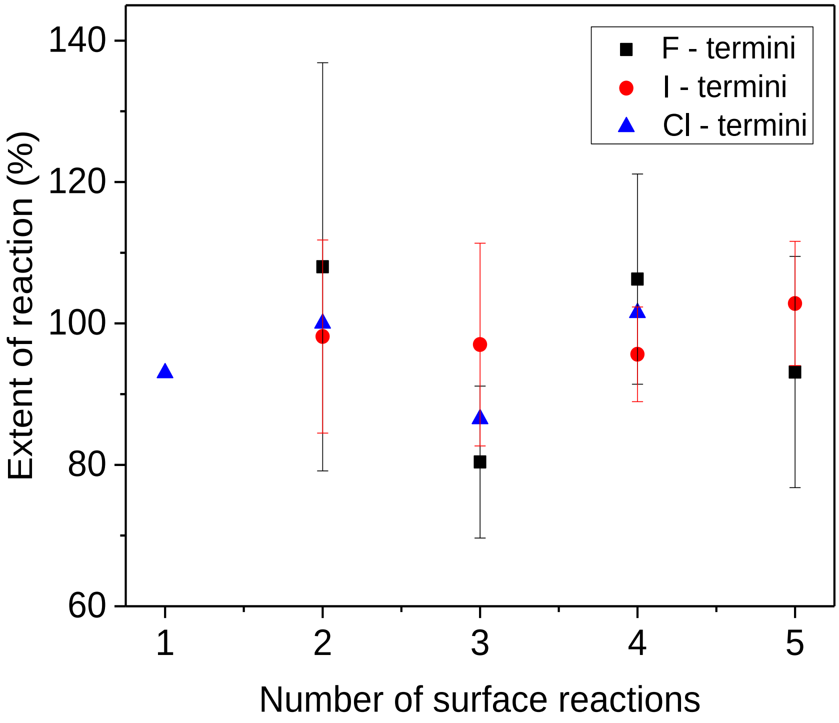

Figure 4.35 Extent of reaction of F, Cl, and I (alpha peaks) terminated OPI wires verses the total number of click chemistry reactions done on template stripped Au. F terminated wires have higher scattering due to high electronegativity of F which can potentially lead to low extent of reaction.

The extent of reaction for stepwise wire growth is extremely important since it establishes the limit on the length of the molecular wires. Figure 4.21a shows the chain length distribution for an average extent of reaction of 90%. It is clear that undesirable dispersities are present for un-optimized wires, whereas the 99% extent of reaction obtained by averaging across five different analytical tools gave much smaller distribution growth of OPI wires. A related area of interest is to investigate the extent of reaction for cycloaddition reaction, and other stepwise growth approaches via similar analytical techniques used in this chapter.

4.7 References

(1) Lin, W.; Lin, W.; Wong, G. K.; Marks, T. J. *J. Am. Chem. Soc.* **1996**, *118*, 8034.

(2) Yoon, M.-H.; Facchetti, A.; Marks, T. J. *Proc. Natl. Acad. Sci. U. S. A.* **2005**, *102*, 4678.

(3) DiBenedetto, S. A.; Facchetti, A.; Ratner, M. A.; Marks, T. J. *Adv. Mater.* **2009**, *21*, 1407.

(4) Tuccitto, N.; Ferri, V.; Cavazzini, M.; Quici, S.; Zhavnerko, G.; Licciardello, A.; Rampi, M. A. *Nat. Mater.* **2009**, *8*, 41.

(5) Choi, S. H.; Kim, B.; Frisbie, C. D. *Science* **2008**, *320*, 1482.

(6) Choi, S. H.; Frisbie, C. D. *J. Am. Chem. Soc.* **2010**, *132*, 16191.

(7) Luo, L.; Choi, S. H.; Frisbie, C. D. *Chem. Mater.* **2011**, *23*, 631.

(8) Luo, L.; Balhorn, L.; Vlaisavljevich, B.; Ma, D.; Gagliardi, L.; Frisbie, C. D. *J. Phys. Chem. C* **2014**, *118*, 26485.

(9) Luo, L.; Frisbie, C. D. *J. Am. Chem. Soc.* **2010**, *132*, 8854.

(10) Yuan, L.; Jiang, L.; Zhang, B.; Nijhuis, C. A. *Angew. Chemie - Int. Ed.* **2014**, *53*, 3377.

(11) Cabarcos, O. M.; Shaporenko, A.; Weidner, T.; Uppili, S.; Dake, L. S.; Zharnikov, M.; Allara, D. L. *J. Phys. Chem. C* **2008**, *112*, 10842.

(12) Bonifas, A. P.; McCreery, R. L. *Nano Lett.* **2011**, *11*, 4725.

(13) Sangeeth, C. S. S.; Wan, A.; Nijhuis, C. a. *J. Am. Chem. Soc.* **2014**, *136*, 11134.

(14) Lavi, A.; Cohen, H.; Bendikov, T.; Vilan, A.; Cahen, D. *Phys. Chem. Chem. Phys.* **2011**, *13*, 1293.

(15) Nijhuis, C. A.; Reus, W. F.; Whitesides, G. M. *J. Am. Chem. Soc.* **2009**, *131*, 17814.

(16) Lewis, P. A.; Inman, C. E.; Maya, F.; Tour, J. M.; Hutchison, J. E.; Weiss, P. S. *J. Am. Chem. Soc.* **2005**, *127*, 17421.

(17) Aradhya, S. V; Venkataraman, L. *Nat. Nanotechnol.* **2013**, *8*, 399.

(18) Vericat, C.; Vela, M. E.; Benitez, G.; Carro, P.; Salvarezza, R. C. *Chem. Soc. Rev.* **2010**, *39*, 1805.

(19) Hihath, J.; Tao, N. *Semicond. Sci. Technol.* **2014**, *29*, 054007.

(20) Heimel, G.; Zojer, E.; Romaner, L.; Brédas, J.-L.; Stellacci, F. *Nano Lett.* **2009**, *9*, 2559.

(21) Bergfield, J. P.; Ratner, M. A. *Phys. status solidi* **2013**, *250*, n/a.

(22) Rosink, J. J. W. M.; Blauw, M. A.; Geerligs, L. J.; van der Drift, E.; Rousseeuw, B. A. C.; Radelaar, S.; Sloof, W. G.; Fakkeldij, E. J. M. *Langmuir* **2000**, *16*, 4547.

(23) Alloway, D. M.; Hofmann, M.; Smith, D. L.; Gruhn, N. E.; Graham, A. L.; Colorado, R.; Wysocki, V. H.; Lee, T. R.; Lee, P. A.; Armstrong, N. R. *J. Phys. Chem. B* **2003**, *107*, 11690.

(24) Willicut, R. J.; McCarley, R. L. *Langmuir* **1995**, *11*, 296.

(25) Bâldea, I.; Xie, Z.; Frisbie, C. D. *Nanoscale* **2015**, *7*, 10465.

(26) Golchoubian, H.; Hosseinpoor, F. *Molecules* **2007**, *12*, 304.

(27) Norman Young, R.; Yves Gauthier, J.; Coombs, W. *Tetrahedron Lett.* **1984**, *25*, 1753.

(28) Powell, C. J.; Jablonski, a. *J. Electron Spectros. Relat. Phenomena* **2010**, *178-179*, 331.

(29) Feng, Y.; Zhou, Z.; Zhou, Y.; Zhao, G. *Nucl. Instruments Methods Phys. Res. Sect. B Beam Interact. with Mater. Atoms* **1994**, *86*, 225.

(30) Lin-Vien, D.; Colthup, N. B.; Fateley, W. G.; Grasselli, J. G. *The Handbook of Infrared and Raman Characteristic Frequencies of Organic Molecules*; Elsevier, 1991.

(31) Ledbetter, J. W. *J. Phys. Chem.* **1977**, *81*, 54.

(32) Smalley, J. F.; Sachs, S. B.; Chidsey, C. E. D.; Dudek, S. P.; Sikes, H. D.; Creager, S. E.; Yu, C. J.; Feldberg, S. W.; Newton, M. D. *J. Am. Chem. Soc.* **2004**, *126*, 14620.

(33) Sikes, H. D.; Smalley, J. F.; Dudek, S. P.; Cook, A. R.; Newton, M. D.; Chidsey, C. E.; Feldberg, S. W. *Science* **2001**, *291*, 1519.

(34) Valincius, G.; Niaura, G.; Kazakeviciene, B.; Talaikyte, Z.; Kazemekaite, M.; Butkus, E.; Razumas, V. *Langmuir* **2004**, *20*, 6631.

(35) Walczak, M. M.; Popenoe, D. D.; Deinhammer, R. S.; Lamp, B. D.; Chung, C.; Porter, M. D. *Langmuir* **1991**, *7*, 2687.

(36) Chu, W.-K.; Mayer, J. W.; Nicolet, M. *Backscattering Spectrometry*; Academic Press, INC: New York, 1978.

(37) Colvin, V. L.; Goldstein, A. N.; Alivisatos, A. P. *J. Am. Chem. Soc.* **1992**, *114*, 5221.

(38) Wohlfart, P.; Weiβ, J.; Käshammer, J.; Winter, C.; Scheumann, V.; Fischer, R. A.; Mittler-Neher, S. *Thin Solid Films* **1999**, *340*, 274.

(39) Beebe, J. M.; Engelkes, V. B.; Liu, J.; Gooding, J. J.; Eggers, P. K.; Jun, Y.; Zhu, X.; Paddon-Row, M. N.; Frisbie, C. D. *J. Phys. Chem. B* **2005**, *109*, 5207.

(40) *Surface and Thin Film Analysis: A Compendium of Principles, Instrumentation and Applications*; Bubert, H.; Jenett, H., Eds.; John Wiley & Sons: Dortmund, 2002.

(41) Scofield, J. H. *J. Electron Spectros. Relat. Phenomena* **1976**, *8*, 129.

(42) Berry, G. M.; Bravo, B. G.; Bothwell, M. E.; Cali, G. J.; Harris, J. E.; Mebrahtu, T.; Michelhaugh, S. L.; Rodriguez, J. F.; Soriaga, M. P. *Langmuir* **1989**, *5*, 707.

(43) Powell, C. J.; Werner, W. S. M.; Smekal, W. *Surf. Interface Anal.* **2011**, *43*, 1046.

(44) Reilman, R. F.; Msezane, A.; Manson, S. T. *J. Electron Spectros. Relat. Phenomena* **1976**, *8*, 389.

(45) Seah, M. P.; Gilmore, I. S. *Surf. Interface Anal.* **1998**, *26*, 908.

(46) Yarzhemsky, V. G.; Nefedov, V. I.; Trzhaskovskaya, M. B.; Band, I. M.; Szargan, R. *J. Electron Spectros. Relat. Phenomena* **2002**, *123*, 1.

(47) Tour, J. M.; Jones, L.; Pearson, D. L.; Lamba, J. J. S.; Burgin, T. P.; Whitesides, G. M.; Allara, D. L.; Parikh, A. N.; Atre, S. *J. Am. Chem. Soc.* **1995**, *117*, 9529.

5. Quantitative Surface Coverage Measurements of Self-Assembled Monolayers by Nuclear Reaction Analysis of Carbon-12

5.1 Abstract

We report surface coverage measurements by Rutherford backscattering spectrometry (RBS) of self-assembled monolayers (SAMs) of both alkyl thiols and oligophenylene thiols on Au-coated mica, Si, and pyrolytic graphite. The ^{12}C atom concentration was probed at 4.266 MeV $^{4}_{2}He^{2+}$ primary beam energy, which enhances the $^{4}_{2}He^{2+}$ scattering cross-section by exciting ^{12}C nuclear resonance states; this is a sub-mode of RBS commonly referred to as nuclear reaction analysis (NRA). The surface coverage of ^{12}C increased linearly with the number of ^{12}C atoms in each SAM. The consistency of the ^{12}C atom coverage values obtained by NRA was cross-checked by measuring the ^{32}S atom concentration by conventional RBS. From these data, we obtained an average coverage of 3.5 ± 0.2 molecules per nm^2 for both alkyl thiols and oligophenylene thiols on polycrystalline Au surfaces. The results show the utility of NRA for quantitative analysis of SAM coverage on Au.

5.2 Introduction

Molecular chemisorption via metal – thiol bonding is widely employed to form self-assembled monolayers (SAMs).[1–8] However, methods to measure the surface coverage of SAMs are limited. In their pioneering work, Ly et al., synthesized ^{35}S radiolabeled SAMs of octadecanethiol on Au and determined coverage via scintillation counting.[9] This method is not compatible with non-radiolabeled SAMs. Other methods to estimate coverage include in-plane X-ray diffraction,[10] helium diffraction,[11] scanning tunneling microscopy (STM),[12] atomic force microscopy (AFM),[13] X-ray photoelectron spectroscopy (XPS),[14–16] and cyclic voltammetry of redox tagged SAMs.[17–19] The diffraction and proximal probe techniques provide the crystalline unit cell structure for well-ordered SAMs, from which the large area coverage is then inferred. These analyses indicate that well-ordered alkyl thiol SAMs form epitaxial overlayers on Au (111) with the $\sqrt{3} \times \sqrt{3}\,R30°$ unit cell structure; the corresponding surface coverage on Au is thus 4.6 molecules / nm^2. Indeed this matches the reported coverage obtained by scintillation counting of radiolabeled SAMs on Au.[9] However, it is desirable to have methods for directly measuring molecular surface coverage of a variety of SAMs without the need for labeling or the need for crystalline order. Quantifying carbon content is especially attractive as the surface concentration of ^{12}C should be proportional to molecular weight and SAM thickness. In this context, XPS, already mentioned, has been a broadly adopted method in which molecular coverage is determined by comparison of sample C_{1s} and Au_{4f} peak signals to that of a well-known standard.[14–16] That is, in practice XPS is used to provide *relative* ^{12}C coverages for SAMs with respect to a reference.

Previously, we employed Rutherford backscattering spectrometry (RBS) to measure the surface coverage of π-conjugated oligophenylene imine (OPI) wires anchored to Au.[20] In that work, we demonstrated that carbon surface coverage can be determined directly by exciting nuclear resonance states via an RBS variant termed nuclear reaction analysis (NRA) using a ${}^{4}_{2}He^{2+}$ probe beam energy of 4.289 MeV. In NRA, an incident ${}^{4}_{2}He^{2+}$ ion initiates a nuclear reaction by penetrating a target nucleus if it has enough energy to overcome the Coulomb barrier, forming an intermediate excited nuclear state that promptly decays back to the ground state by emission of an α particle

$$ {}^{12}_{6}\mathrm{C} + {}^{4}_{2}\mathrm{He}^{2+}(4.266\ \mathrm{MeV}) \rightarrow [{}^{16}_{8}O^{2+}]^{*} \rightarrow {}^{12}_{6}\mathrm{C} + {}^{4}_{2}\mathrm{He}^{2+}(1.019\ \mathrm{MeV}) \qquad (5.1) $$

(${}^{4}_{2}He^{2+}$). Equation 5.1 describes the NRA process for detection of ^{12}C at a backscattering angle of 165°. This resonant scattering process results in a distinct enhancement of the ^{12}C peak intensity relative to classical (elastic) Rutherford scattering.

A potential advantage of RBS/NRA for organic thin film analysis is that it allows straight forward determination of *absolute* ^{12}C coverage (atoms/nm^2), as will be shown below. This is because the ^{12}C nuclear scattering cross-section is known very accurately[21] and further, the interaction of ${}^{4}_{2}He^{2+}$ particles with electrons in ultra-thin films is extremely weak, meaning every particle scattered in the direction of the detector is counted; there is essentially no signal attenuation with film thickness. By contrast, in XPS there is a Beer's Law attenuation of photoelectrons that somewhat complicates quantitative analysis because C atoms residing deeper in a film are not detected with the same efficiency as the ^{12}C atoms at the very surface.

Here we apply NRA for the first time for coverage measurements of conventional SAMs of alkyl thiols and oligophenylene thiols on Au. By tuning the incident beam energy from 4.289 MeV to 4.266 MeV, we achieved a two fold increase in the ^{12}C nuclear scattering cross section, thus increasing the sensitivity to ^{12}C atoms (Figure S1). Our results demonstrate that NRA is a powerful analytical tool for the surface science of ultra-thin organic films, in particular SAMs.

5.3 Experimental Methods

A MAS 1700 pelletron tandem ion accelerator (5SDH) equipped with a charge exchange RF plasma source (National Electrostatics Corporation, NEC: Middleton, WI) was used to generate a 4.266 MeV ${}_{2}^{4}He^{2+}$ beam with a current of 30-40 nA measured at the sample. ${}_{2}^{4}He^{2+}$ ions backscattered by nuclear collisions were counted by an Ortec silicon ion detector that was positioned at a scattering angle of 165° with respect to the incident beam and subtending a solid angle of 3.6 msr. Spectra consisting of counts versus backscattered ion energy were acquired with a multichannel analyzer controlled by NEC RC43 software. The projected beam cross section was approximately 2 × 2 mm (square). Visibly luminescent control samples of the same thickness were employed to precisely locate the beam position per sample goniometer coordinates. More precise quantitative comparisons between spectra (vertical scale) were achieved by normalizing to the signal intensity of the substrate. This treatment accounted for small variations in the accuracy of beam current integration (i.e., error in determination of the total number of incident ions, Q). Furthermore, the corrected spectra were simulated with SIMNRA software (Max Planck Institute) to check the accuracy of Q.

The substrates for NRA were prepared by thermal evaporation of 5 nm of Cr followed by 20 nm of Au in a home built thermal evaporator at a rate of approximately

0.5-1 Å/s and base pressure of $\leq 2 \times 10^{-6}$ Torr. Substrates were bare Si (100) wafer (Wafer Net), freshly cleaved AFM grade mica (Ted Pella), or pyrolytic graphite sheet (Digi-Key). The coated substrates were immediately transferred into a 1 mM fresh ethanol solution of 1-octanethiol (C8), 1-decanethiol (C10), 1-dodecanethiol (C12), 1-tetracedanethiol (C14), 1-hexadecanethiol (C16), or 1-octadecanethiol (C18). For oligophenylene thiols, the mica substrates were transferred into 1 mM of thiophenol (Ph-1), 0.05 mM of biphenyl-4-thiol (Ph-2), and 0.05 mM of 1,1',4,4"-terphenyl-4-thiol (Ph-3) in ethanol. All starting materials except C16 were purchased from Sigma Aldrich and used as received. C16 was purchased from TCI America.

5.4 Results and Discussion

Figures 5.1a and 5.1c display representative RBS spectra of alkyl thiol and oligophenylene thiol SAMs on Au-coated Si and mica substrates, respectively. The energy of the backscattered ions depends on the kinematic factor, as discussed in chapter 2. In general, heavy nuclei have higher kinematic factor than light nuclei, and thus the backscattered ${}^{4}_{2}He^{2+}$ projectiles have higher kinetic energy following backscattering from heavy elements. This is exemplified by the RBS spectrum on Au/Cr/mica (Figure 5.1c), which contains a succession of steps (elemental signal edges corresponding to scattering from the surface) for elements O to Fe in the mica. At 4.266 MeV, the primary beam energy is well into the nuclear reaction regime for Si and O.[22,23] The dip in Figure 5.1a near 1.5 MeV corresponds to the nuclear anti-resonance of ^{28}Si (Si^{AR}), whereas the peak near 2.2 MeV is due to nuclear resonance of ^{28}Si (Si^{R}) at shallower depth.[24] Figures 5.1b and 5.1d show the NRA spectra of ^{12}C spectral region for alkyl thiols on Au/Cr/Si

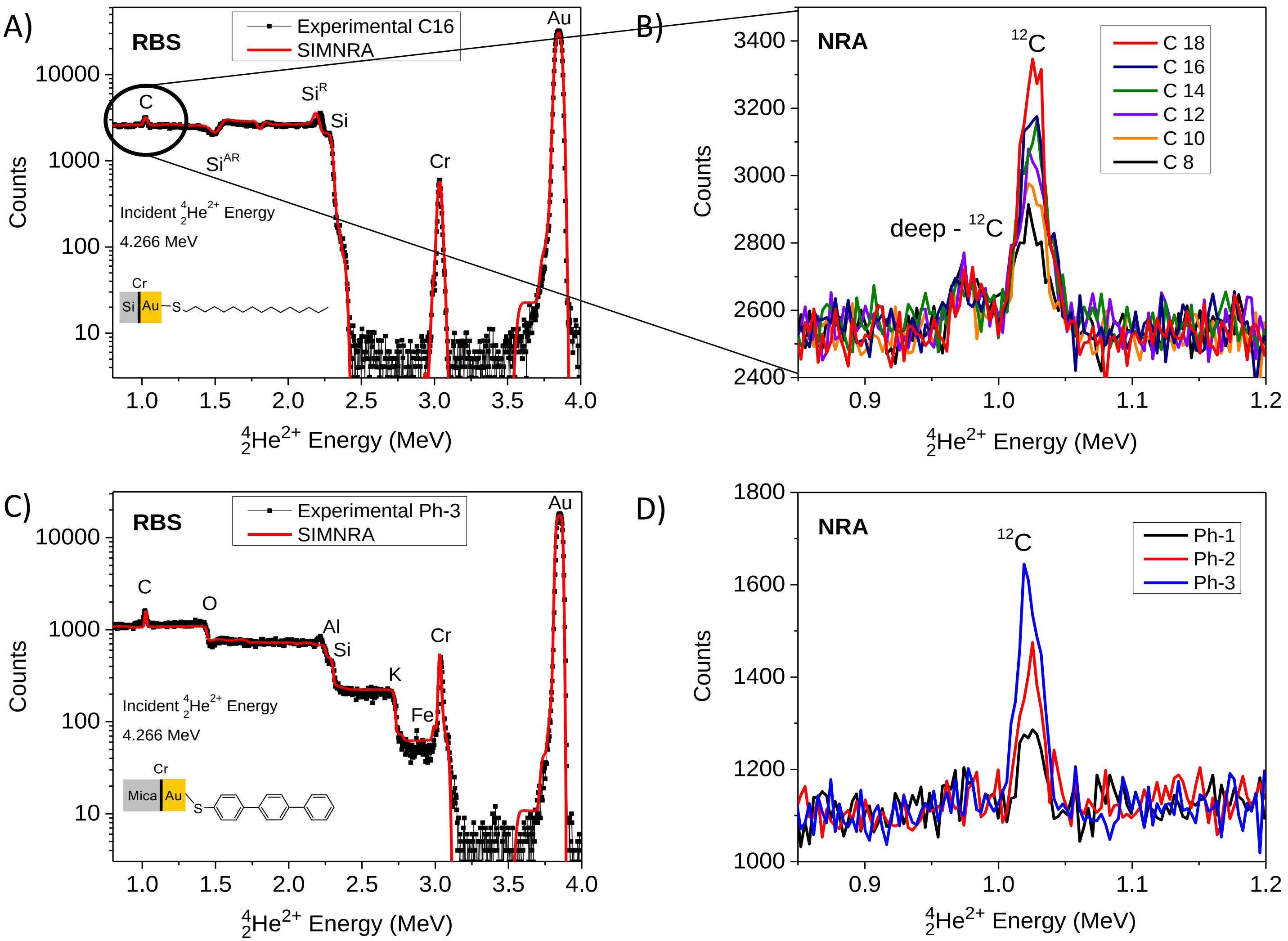

Figure 5.1 RBS & NRA spectra of alkyl and oligophenylene thiols on Au deposited on Si and mica substrates, respectively. A) RBS spectrum of C16 thiol on 50 nm Au / 5 nm Cr deposited on Si substrate. B) Corresponding NRA spectra of C8, C10, C12, C14, C16, and C18 thiols (35 min acquisition time per spectrum). C) RBS spectrum of terphenyl thiol on 50 nm Au / 5 nm Cr deposited on mica. D) Corresponding NRA spectra of phenyl (Ph-1), biphenyl (Ph-2), and terphenyl (Ph-3) thiols (25 min acquisition time per spectrum). Incident beam energy = 4.266 MeV.

and for oligophenylene thiols on Au/Cr/mica, respectively. The ^{12}C atom signal increases with the total number of ^{12}C atoms in the SAMs, as expected. For SAMs on Au/Cr/Si, spectra were collected at 3 different positions per sample, 25 µC at each location, and the total spectra were summed (Figures 5.1a and 5.1b). NRA of aryl thiols on mica were collected at 2 different positions, 44 µC each (Figure 5.1c and 5.1d). In the present work, we prevented $^4_2He^{2+}$ channeling in single-crystal Si by tilting the surface normal of the sample by 3° (θ) and rotating it around the beam per variable azimuthal angle (φ) during spectral acquisition.

The ^{12}C atom surface coverage (N_s) was calculated from the NRA data according to equation 5.2:

$$N_s = A \cos\theta \,/\, [\, (\frac{d\sigma}{d\Omega})\, \Omega\, Q] \qquad (5.2)$$

Here, A is the total number of ions detected in the ^{12}C atom peak, θ is the tilt angle of the sample normal relative to the ion beam (3°), $\frac{d\sigma}{d\Omega}$ is the differential scattering cross section per unit solid angle[21] (1.07×10^{-24} cm^2/sr for a backscattering angle of 165° and 4.266 MeV $^4_2He^{2+}$ beam energy), Ω is the detector solid angle (3.6×10^{-3} sr), and Q is the total number of incident ions (7.8×10^{13} for Si samples and 1.3×10^{14} for mica samples). The surface coverage values on Au obtained from Equation 5.2 are plotted in Figure 5.2. The coverage values increased with the total number of ^{12}C atoms as expected. It is noteworthy that consecutive steps of 2 ^{12}C atoms resulted in distinct increases of measured surface coverage, which clearly demonstrates that NRA is a sensitive quantitative tool capable of quantifying coverage of ultrathin organic films. The ^{12}C surface coverage values of oligophenylene thiols are also plotted in Figure 5.2 (black squares). As expected, the coverage increased with the number of ^{12}C atoms in the SAMs with similar slope as the alkyl thiol SAMs. In order to correct for adventitious adsorbed hydrocarbons, the y-intercept from a linear fit of raw peak area vs number of ^{12}C atoms was subtracted. Note that from the data, the y-intercepts for alkyl thiol and

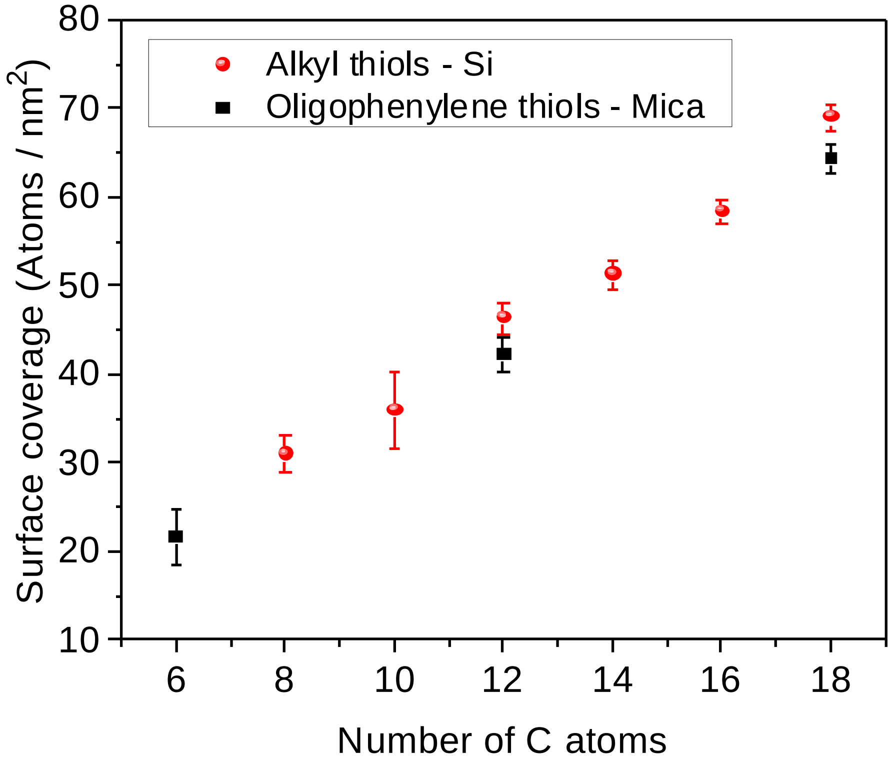

Figure 5.2 NRA-determined ^{12}C atomic surface coverage for alkyl (red circles) and oligophenylene (black squares) thiols on Au/Si, and Au/mica substrates, respectively. Coverage calculated for geometrical area. The error bars represent one standard deviation.

oligophenylene thiol SAMs were -1.6 ± 3.2 and -1.4 ± 1.3 atom/nm^2, respectively. Both values fall within the standard deviation of the data sets. NRA spectra of alkyl thiols were also collected on Au deposited on pyrolytic graphite sheet (PGS) substrates as shown in

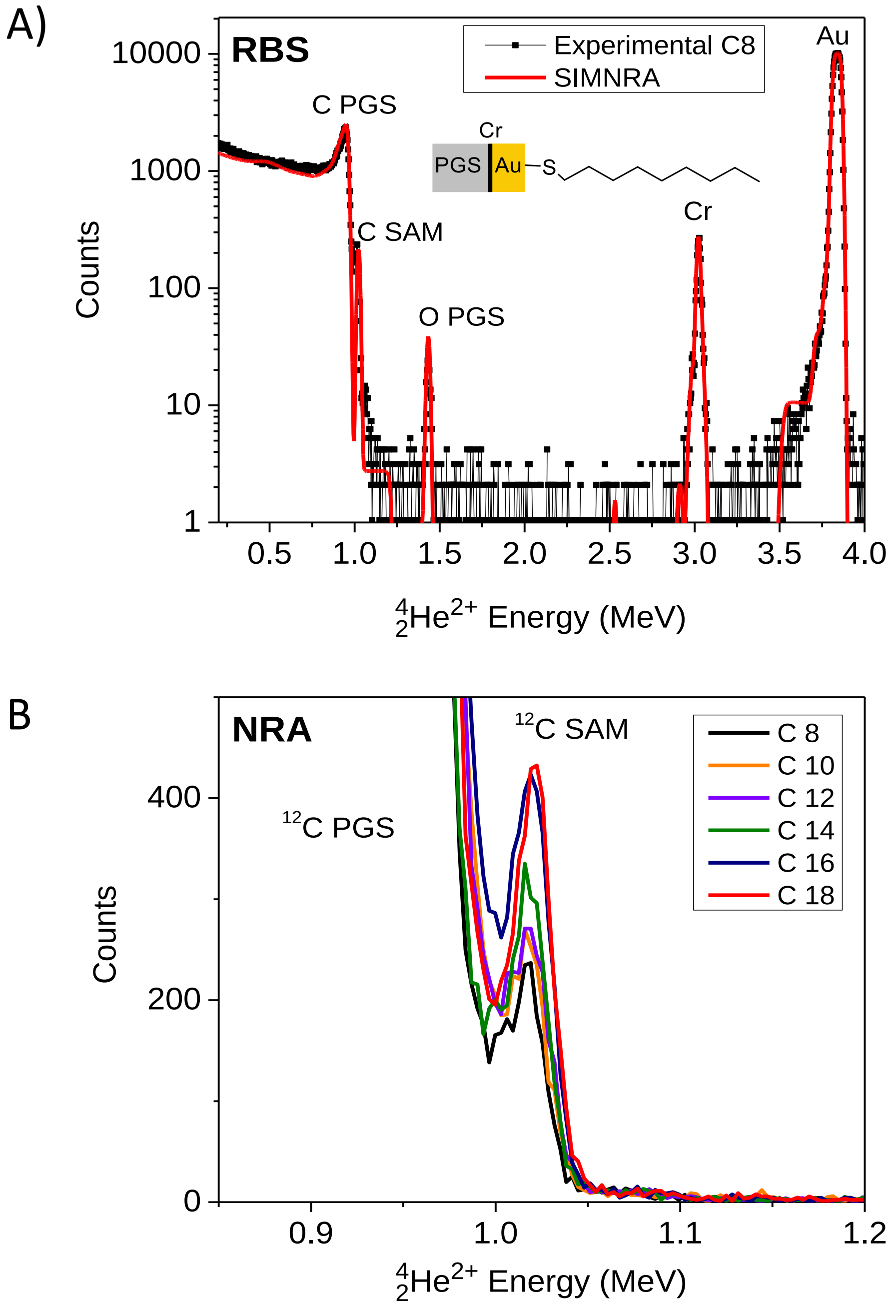

Figure 5.3 RBS & NRA spectra of alkyl thiols. A) RBS spectrum of C8 thiol on 50 nm Au / 5 nm Cr deposited on PGS (pyrolytic graphite sheet) substrate. B) Corresponding NRA spectra of C8, C10, C12, C14, C16, and C18 thiols (35 min acquisition time per spectrum).

Figure 5.3. PGS was the ideal substrate for NRA because the C signal did not lie atop of the substrate signal as in the Si and mica cases. Instead the substrate and thiol C peaks are located next to each other with a slight tailing of the PGS C peak towards the SAM C peak due to roughness of the PGS. This was corrected by a linear baseline subtraction method. Spectra were collected at 3 different positions, 25 µC at each location. The quality of alkyl thiol SAMs on the Au/Cr/PGS substrate was check with XPS. As shown in Figure 5.4, the survey spectra of C16 SAMs on Au/Cr/Si and Au/Cr/PGS substrates are similar.

Furthermore, the high resolution C 1s atom count for SAMs on PGS increased with chain length as shown in Figure 5.4. Collectively, the XPS data indicate that good quality monolayers were prepared on Au/Cr/PGS with reasonable surface coverages. The NRA C atom surface coverage was calculated according to equation 5.2, and the results are shown in Figure 5.6. Overall there is good agreement in the coverage values of alkyl thiols on Au/Cr/Si, Au/Cr/mica, and Au/Cr/PGS substrates.

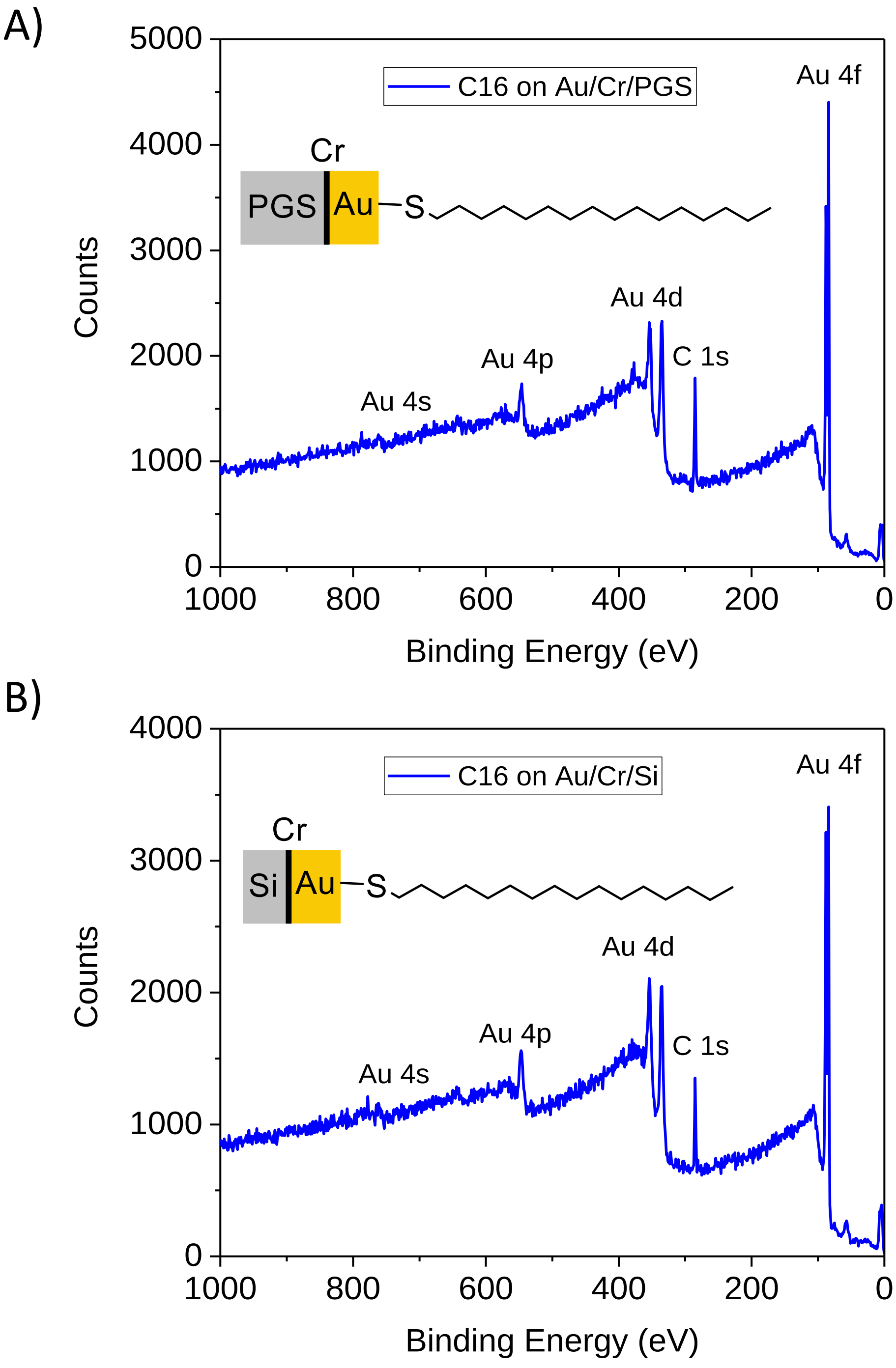

Figure 5.4 XPS survey spectrum of C16 on Au/Cr/PGS (A) and on Au/Cr/Si (B). The intensity of C1s to Au 4f suggests that good quality films were deposited on the PGS substrate.

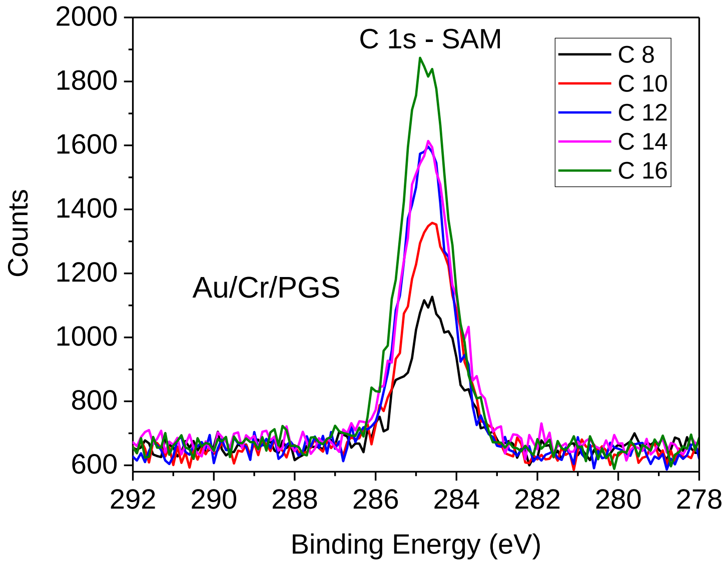

Figure 5.5 XPS C1s high resolution spectra of C8, C10, C12, C14, and C18 thiols on Au/Cr/PGS. As expected, the C 1s counts increased with the number of C in each

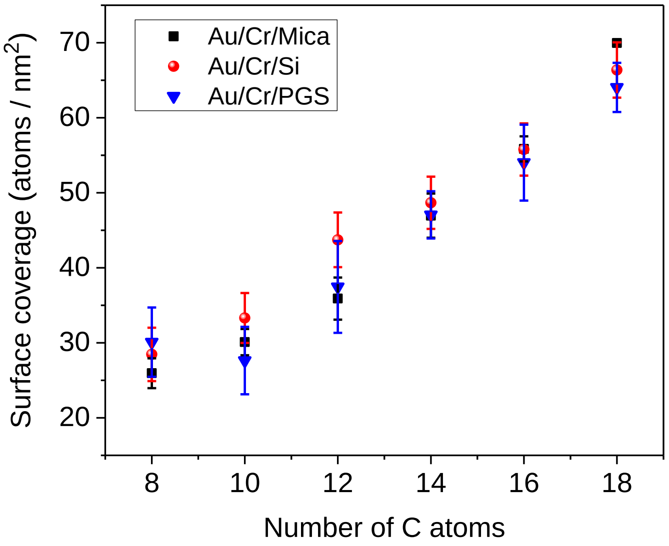

Figure 5.6 Surface coverage results of alkyl thiols on Au/Cr/Mica (black squares), Au/Cr/Si (red circles), and Au/Cr/PGS (blue triangles).Overall, there is good agreement of coverage values across the different substrates.

In order to check the consistency of our NRA ^{12}C atom surface coverage, conventional RBS of ^{32}S was employed as a second measure of molecular coverage. Depth resolution was improved by tilting the sample by 75° (sample normal with respect to beam) thereby elongating the analytical spot size to ~ 8 mm along one dimension. The samples for ^{32}S analysis were prepared by depositing 2 nm W followed by 20 nm Au on bare Si wafer using a CHA e-beam evaporator (SEC 600) at a rate of approximately 1 Å/s and base pressure of $\leq 2 \times 10^{-6}$ Torr. The RBS results near the ^{32}S region are shown in Figure 5.7 for both alkyl and oligophenylene SAMs, and indicate the presence of surface bound ^{32}S atoms at a backscattered ${}^{4}_{2}He^{2+}$ beam energy of 1.83 MeV (incident beam energy was 3.0 MeV). The elemental surface coverage, N_s (atoms/cm^2), was determined by equation 5.2 and the results are shown in Figure 5.8 (Here, $\theta = 75°$, $\frac{d\sigma}{d\Omega} = 1.48 \times 10^{-25}$ cm^2/sr for backscattering angle of 165° and 3.0 MeV ${}^{4}_{2}He^{2+}$ beam energy,[25] and $Q = 2.3 \times 10^{14}$).

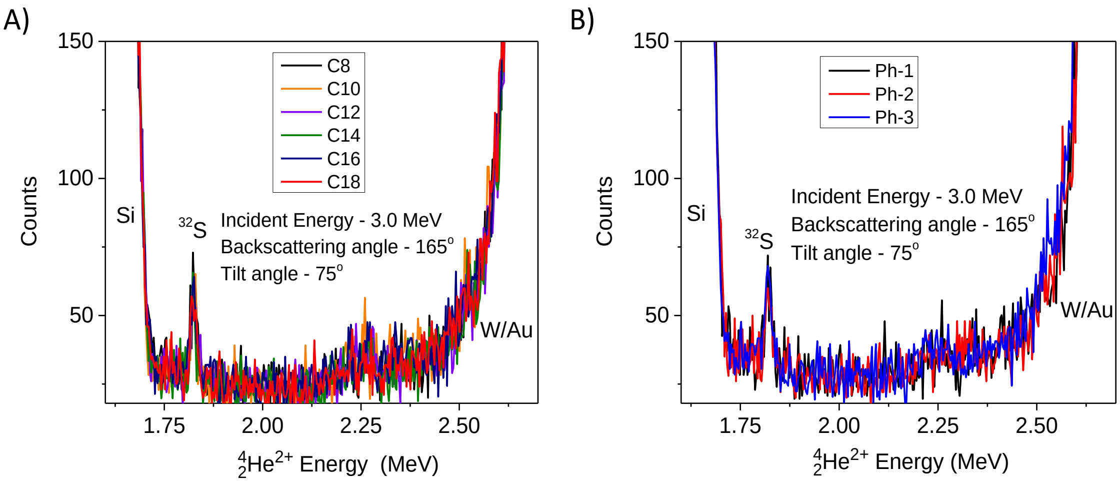

Figure 5.7 A) RBS spectra of alkyl thiols on Au (20 nm) / W (3 nm) on Si substrate. B) RBS spectra of oligophenylene thiols on Au (20 nm) / W (3 nm) on Si substrate. Incident beam energy = 3.0 MeV.

Previously, we demonstrated that tilted RBS of oligophenylene imine wires yielded two distinct S peaks due to diffusion of the chemisorbing molecules along the grain boundaries (deep vs surface S).[20] The presence of the W adhesion layer improves the quality of the Au film, and effectively reduces the spacing between the grains such that diffusion to the Si interface is hindered. However, this does not completely preclude the presence of a few molecules at the interface, which may be the source of the small bump on the left side of the ^{12}C peak, Figure 5.1b (“deep ^{12}C”). Since the deep ^{12}C is no longer at resonance, there are more deep ^{12}C atoms than the relative peak intensities suggest, see Figure 2.12. We note that the advantage of NRA relative to conventional RBS is that it makes detection of ^{12}C possible, whereas conventional RBS (1 – 4 MeV) does not produce a measurable ^{12}C signal due to the much stronger substrate signal, and low Rutherford (classical) scattering cross sections associated with light elements.

Figure 5.8 indicates the calculated SAM coverage in molecules/nm^2 from the ^{32}S and ^{12}C coverage for alkyl thiols and oligophenylene thiols on Au. The ^{12}C surface coverage values in Figure 5.2 (atoms per nm^2) were divided by the total number of ^{12}C atoms in the SAM to convert to molecular coverage. Overall, there was a good agreement in the molecular coverage values for both alkyl and oligophenylene SAMs obtained either from the ^{32}S or ^{12}C atomic coverages. On average, we obtained surface coverages of 3.4 ± 0.3, and 3.5 ± 0.3 molecules / nm^2, respectively, for alkyl SAMs on Au/W/Si and Au/Cr/Si substrates, and 3.5 ± 0.1 and 3.5 ± 0.2 molecules molecules/nm^2, for oligophenylene SAMs on Au/W/Si and Au/Cr/mica substrates, respectively.

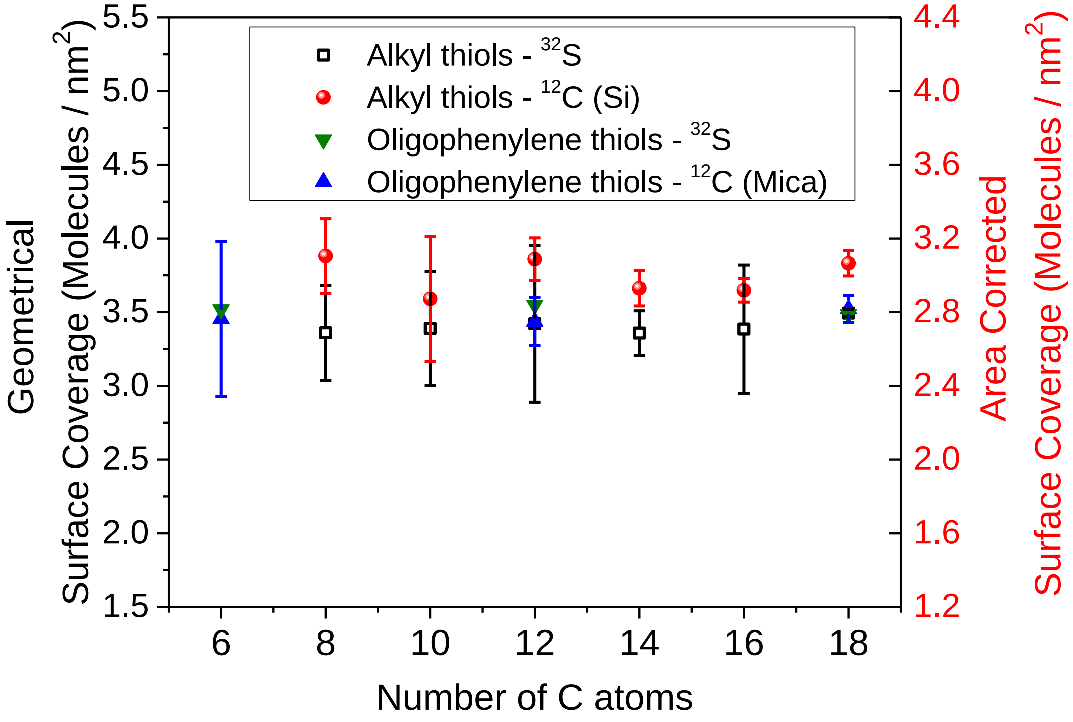

Figure 5.8 Molecular surface coverage obtained from ^{12}C (Figure 2) and ^{32}S (Figure 3) coverages for SAMs of alkyl and oligophenylene thiols. Coverage calculation was based on geometrical area (left axis) and true area (right). The error bars represent one standard deviation.

Of course, due to surface roughness, the areas of the Au substrates are larger than the geometrical area. Au/Cr/Si substrates were imaged with ultra-sharp (radius ~ 1 nm) AFM tips (Figure 5.9). These experiments indicated that the true area was ~ 25% greater than the geometrical area (based on a 250 nm x 250 nm scan). The area corrected molecular surface coverages are displayed on the right axis of Figure 4 (red labels). These corrected coverages are 36% lower than the ideal coverage on single crystal Au (111).[10–13] The difference is likely due to the polycrystalline Au surfaces used in our work, where the obtained coverage values are averaged over all of the crystal faces and grain sizes. Furthermore, disorder at grain boundaries may lead to unoptimized packing of the thiols.

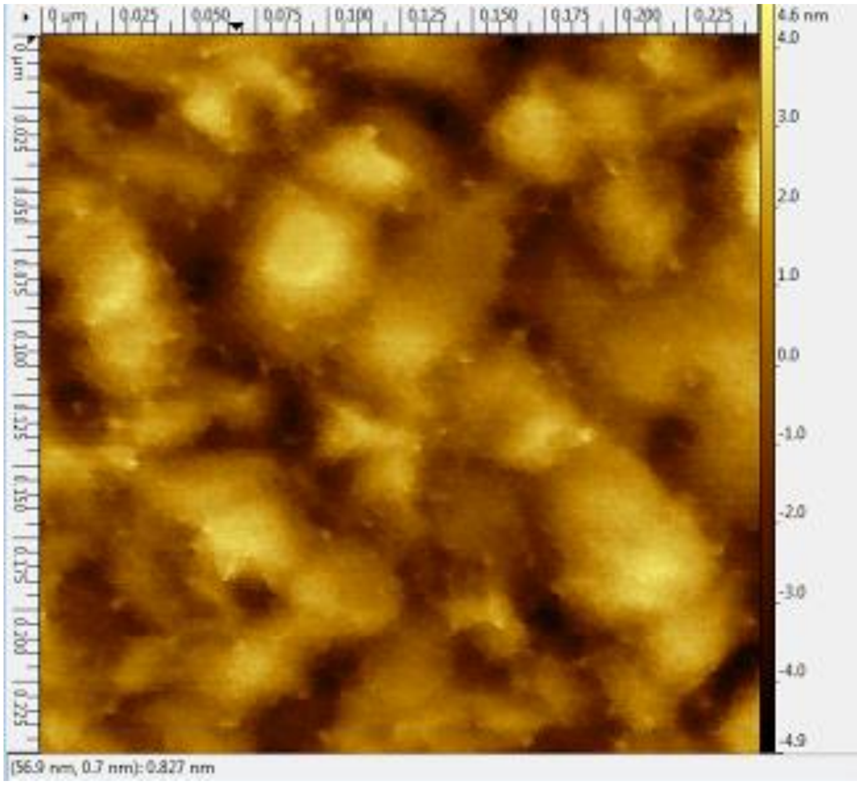

Figure 5.9 AFM image of bare Au on Au/Cr/Si substrate. Image based on 250 nm x 250 nm scan size. Excess area ~ 25%.

In conclusion, we have shown here the utility of NRA in determining quantitative surface coverages of standard alkyl and aromatic thiols on Au. The ability to measure ^{12}C atom concentration by NRA is an advantage for SAM surface science as ^{12}C is the most abundant element in such films and the need to incorporate specific radioactive or redox tags is obviated. It is likely that XPS will continue to be favored for SAM coverage measurements because of the far greater availability of XPS instruments relative to ion beam accelerators (though we note that most ion beam analysis tools are part of regional or national open access characterization facilities). However, NRA offers a complementary approach and it may have advantages with respect to XPS for quantitative (absolute) ^{12}C coverage determination. Further, as RBS is routinely carried out on insulators, ^{12}C analysis by NRA of organic films on insulating materials may be simpler than by XPS, which is quite sensitive to surface charging.[25,26] Such investigations will be the subject of future work.

5.5 References

(1) Love, J. C.; Estroff, L. A.; Kriebel, J. K.; Nuzzo, R. G.; Whitesides, G. M. *Chem. Rev.* **2005**, *105*, 1103.

(2) Bain, C. D.; Troughton, E. B.; Tao, Y. T.; Evall, J.; Whitesides, G. M.; Nuzzo, R. G. *J. Am. Chem. Soc.* **1989**, *111*, 321.

(3) Tour, J. M.; Jones, L.; Pearson, D. L.; Lamba, J. J. S.; Burgin, T. P.; Whitesides, G. M.; Allara, D. L.; Parikh, A. N.; Atre, S. *J. Am. Chem. Soc.* **1995**, *117*, 9529.

(4) Smalley, J. F.; Sachs, S. B.; Chidsey, C. E. D.; Dudek, S. P.; Sikes, H. D.; Creager, S. E.; Yu, C. J.; Feldberg, S. W.; Newton, M. D. *J. Am. Chem. Soc.* **2004**, *126*, 14620.

(5) Alloway, D. M.; Hofmann, M.; Smith, D. L.; Gruhn, N. E.; Graham, A. L.; Colorado, R.; Wysocki, V. H.; Lee, T. R.; Lee, P. A.; Armstrong, N. R. *J. Phys. Chem. B* **2003**, *107*, 11690.

(6) Abu-Husein, T.; Schuster, S.; Egger, D. A.; Kind, M.; Santowski, T.; Wiesner, A.; Chiechi, R.; Zojer, E.; Terfort, A.; Zharnikov, M. *Adv. Funct. Mater.* **2015**, *25*, 3943.

(7) Ulman, A. *Chem. Rev.* **1996**, *96*, 1533.

(8) Luo, L.; Choi, S. H.; Frisbie, C. D. *Chem. Mater.* **2011**, *23*, 631.

(9) Schlenoff, J. B.; Li, M.; Ly, H. *J. Am. Chem. Soc.* **1995**, *117*, 12528.

(10) Torrelles, X.; Barrena, E.; Munuera, C.; Rius, J.; Ferrer, S.; Ocal, C. *Langmuir* **2004**, *20*, 9396.

(11) Camillone, N.; Chidsey, C. E. D.; Eisenberger, P.; Fenter, P.; Li, J.; Liang, K. S.; Liu, G.-Y.; Scoles, G. *J. Chem. Phys.* **1993**, *99*, 744.

(12) Vericat, C.; Vela, M. E.; Corthey, G.; Pensa, E.; Cortés, E.; Fonticelli, M. H.; Ibañez, F.; Benitez, G. E.; Carro, P.; Salvarezza, R. C. *RSC Adv.* **2014**, *4*, 27730.

(13) Caldwell, W. B.; Campbell, D. J.; Chen, K.; Herr, B. R.; Mirkin, C. A.; Malik, A.; Durbin, M. K.; Dutta, P.; Huang, K. G. *J. Am. Chem. Soc.* **1995**, *117*, 6071.

(14) Park, J.-S.; Vo, A. N.; Barriet, D.; Shon, Y.-S.; Lee, T. R. *Langmuir* **2005**, *21*, 2902.

(15) Lee, S.; Shon, Y.-S.; Colorado, R.; Guenard, R. L.; Lee, T. R.; Perry, S. S. *Langmuir* **2000**, *16*, 2220.

(16) Rittikulsittichai, S.; Jamison, A. C.; Lee, T. R. *Langmuir* **2011**, *27*, 9920.

(17) Chidsey, C. E. D.; Bertozzi, C. R.; Putvinski, T. M.; Mujsce, A. M. *J. Am. Chem. Soc.* **1990**, *112*, 4301.

(18) Gardner, T. J.; Frisbie, C. D.; Wrighton, M. S. *J. Am. Chem. Soc.* **1995**, *117*, 6927.

(19) Creager, S.; Yu, C. J.; Bamdad, C.; O'Connor, S.; MacLean, T.; Lam, E.; Chong, Y.; Olsen, G. T.; Luo, J.; Gozin, M.; Kayyem, J. F. *J. Am. Chem. Soc.* **1999**, *121*, 1059.

(20) Demissie, A. T.; Haugstad, G.; Frisbie, C. D. *J. Am. Chem. Soc.* **2015**, *137*, 8819.

(21) Feng, Y.; Zhou, Z.; Zhou, Y.; Zhao, G. *Nucl. Instruments Methods Phys. Res. Sect. B Beam Interact. with Mater. Atoms* **1994**, *86*, 225.

(22) Cheng, H.; Shen, H.; Yang, F.; Tang, J. *Nucl. Instruments Methods Phys. Res. Sect. B Beam Interact. with Mater. Atoms* **1994**, *85*, 47.

(23) Leavitt, J. A.; McIntyre, L. C.; Ashbaugh, M. D.; Oder, J. G.; Lin, Z.; Dezfouly-Arjomandy, B. *Nucl. Instruments Methods Phys. Res. Sect. B Beam Interact. with Mater. Atoms* **1990**, *44*, 260.

(24) Leung. Ph.D. Thesis, University of Kentucky, 1972.

(25) Chu, W.-K.; Mayer, J. W.; Nicolet, M. *Backscattering Spectrometry*; Academic Press, INC: New York, 1978.

(26) Powell, C. J.; Jablonski, a. *J. Electron Spectros. Relat. Phenomena* **2010**, *178-179*, 331.

6. Comparison of DC and AC Transport in Oligophenylene Imine Molecular Wires across Two Junction Platforms: Eutectic Ga-In versus Conducting Probe Atomic Force Microscope Junctions

6.1 Abstract

We have utilized DC and AC transport measurements to measure the resistance and capacitance of thin films of conjugated oligophenylene imine (OPI) molecules ranging from 1.5 – 7.5 nm in length. These films were synthesized on Au surfaces utilizing the imine condensation click chemistry between terephthalaldehyde (benzene-1,4-dicarbaldehyde) and 1,4-benzenediamine. Near edge X-ray absorption fine structure (NEXAFS) spectroscopy yielded molecular tilt angles of 33° - 43°, consistent with a standing up phase. To probe DC and AC transport, we employed Au-S-OPI//GaO$_X$/EGaIn junctions having contact areas of 9.6×10^2 μm^2 (10^9 nm^2) and compared to previously reported DC results on the same OPI system obtained using Au-S-OPI//Au conducting probe atomic force microscopy (CP-AFM) junctions with 50 nm^2 areas. We found that intensive (i.e., area independent) observables agreed very well across the two junction platforms. Specifically, the EGaIn-based junctions showed: (i) a crossover from tunneling to hopping transport at molecular lengths near 4 nm; (ii) activated transport for wires >4 nm in length with an activation energy of 0.245 ± 0.008 eV for OPI-7; (iii) exponential dependence of conductance with molecular length in the

tunneling regime with a decay constant β of 2.84 ± 0.18 nm^{-1} and an apparent β of 1.01 ± 0.08 nm^{-1} in the hopping regime. These findings agree with prior CP-AFM results. However, even after attempts to normalize the resistances by the respective junction areas, the absolute resistances of Au-S-OPI//GaO_X/EGaIn junctions were approximately 100 times higher than for the corresponding CP-AFM junctions. This discrepancy is likely attributable to imperfect normalization due to Au surface roughness in the EGaIn junction and to differences in metal-molecule contact resistances between the two platforms. AC measurements on the EGaIn junctions were fit to an equivalent circuit model and yielded $\beta = 2.92 \pm 0.13$ nm^{-1} in the tunneling regime, $\beta = 1.01 \pm 0.08$ nm^{-1} in the hopping regime, and a previously unreported value of 4.3 ± 0.2 for the dielectric constant along the OPI wires. Overall, the agreement in the measured values across the EGaIn and CP-AFM platforms provides a good example of the reproducibility that can be obtained in molecular electronics using precision soft contact junction fabrication methods and well characterized π-conjugated molecular films.

6.2 Introduction

A long-standing goal in molecular electronics is to understand the influence of molecular structure on electrical conduction across metal-molecule-metal junctions.[1–14] Currently, there are a variety of testbeds for measuring electrical transport across molecules such as the break junction,[15,16] the conducting probe atomic force microscope,[17] the scanning tunneling microscope,[18] the eutectic gallium indium alloy (EGaIn) junction,[19–21] the Hg drop junction,[22,23] the conducting polymer junction,[24,25] the surface diffusion mediated junction,[26] and others. However, limited reproducibility of experimental results across different platforms remains a vexing issue that has several possible causes including different types of molecule-electrode contacts (e.g., metal type and chemisorbed vs physisorbed contacts), dissimilar ambient environments (e.g., air vs solvent vs vacuum), and widely varying effective electrical junction areas (i.e., the electrode areas in direct contact with molecules); see discussion below.[27–29] It is well-known that measured resistances per molecule can be about 8-9 orders of magnitude smaller in single and few molecule junctions (so-called small area junctions) than junctions consisting of large numbers of molecules (10^3 – 10^{12}) (large area junctions).[28,30] In an excellent review, Akkerman, et al. noticed that the resistance per molecule progressively decreases with decreasing junction area but a good explanation for this general observation across testbeds is lacking.[31] Therefore, a central question in molecular electronics is: How reproducible are the electrical characteristics for a given molecular architecture across different types of junctions?[29]

To identify and quantify the factors that cause large discrepancies between testbeds, our goal was to compare transport measurements on well characterized oligophenylene imine (OPI) wires 1.5 – 7.5 nm in length using two different junction platforms, namely large area junctions fabricated with the “EGaIn-technique” (EGaIn = eutectic indium gallium alloy, Figure 6.1a) and small area junctions fabricated with

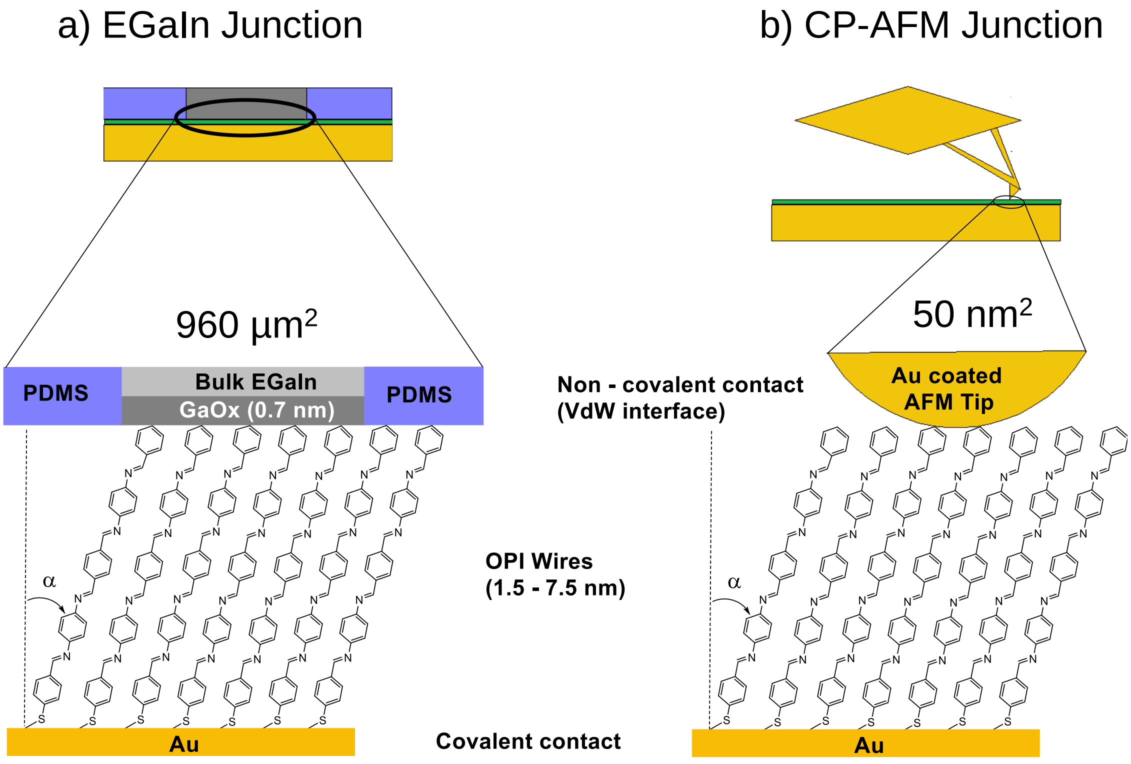

Figure 6.1. Schematic illustration of the OPI wire based junction. The OPI monolayers are attached to the Au via metal-thiolate bonds and form a van der Waals contact with the top electrode (not drawn to scale). a) The top-electrode is a non-Newtonian liquid metal stabilized in a through-hole in PDMS. EGaIn = eutectic alloy of Ga and In, GaO_x = native gallium oxide layer which is highly conductive and 0.7 nm thick, PDMS = polydimethylsiloxane.[38,44,70] b) The top electrode is Au coated AFM tip (~ 50 nm in thickness).[36,37,52] Tilt angle *α* is defined as the angle of the SAM with respect to the surface normal. The illustrations are not drawn to scale.

conducting probe atomic force microscope (CP-AFM, Figure 6.1b) top electrodes[32–34]. These two platforms have vastly different junction areas of approximately 9.6×10^2 μm^2 and 50 nm^2, respectively, and they also employ different metals (EGaIn/GaOx vs Au) for the top contact. Thus, these two junctions could be expected to yield very different results for OPI wires. On the contrary, however, we find that certain key measured values described below are identical within error. We note that the OPI system is a good test-case for platform comparison because different charge transport mechanisms are observable in this system. For example, previous CP-AFM results have shown that there is a clear change in transport mechanism from tunneling to thermally-assisted hopping as OPI wire length increases.[34–37] The crossover in transport mechanism manifests itself in both the length and temperature dependence of resistance, providing a rich data set for comparison between the two junction testbeds. Initial questions included whether the crossover from tunneling to hopping is observable in large area EGaIn junctions and whether the crossover length and temperature dependence (i.e., activation energy in the hopping regime) were the same as measured by small area CP-AFM based junctions.

In the new EGaIn based data reported here, a clear transition in transport mechanism is indeed observed near 4 nm in wire length, as has been reported previously using CP-AFM.[34–37] That is, for wires <4 nm, the conductance decreases exponentially with length with a decay constant β of 2.92 ± 0.13 nm^{-1} and for wires >4 nm the apparent decay constant β is 1.01 ± 0.08 nm^{-1}, similar to the values found by CP-AFM (i.e., 3.0 ± 0.08 nm^{-1} and 0.9 ± 0.07 nm^{-1},[37] respectively). Furthermore, for long wires, the transport is thermally activated, consistent with hopping; the activation energy of 0.245 ± 0.008 eV also agrees very well with previous CP- measurements (0.280 eV)[37]. From the general molecular electronics perspective it is gratifying that these two platforms, which differ by seven orders of magnitude in terms of the contact areas they provide, can achieve such similar results. Furthermore, the EGaIn results reported here represent the first time a clear crossover behavior from tunneling to hopping has been observed in a large area junction, providing confirmation of this important result. However, the absolute resistances of the OPI wires, normalized for effective electrical contact area, differ by two orders of magnitude between the two platforms. This is likely due to a combination of imperfect area normalization and differences in contact resistance, a point we will return to later.

Importantly, the EGaIn platform also allows AC impedance measurements on molecular junctions.[38,39] Thus, an additional goal of this work was to perform AC impedance measurements on OPI wires for the first time. These new data corroborate and extend the DC results. Specifically, a simple equivalent circuit consisting of a contact resistance R_C in series with a parallel combination of the OPI resistance (R_{OPI}) and capacitance (C_{OPI}) was sufficient to fit the Nyquist and Bode behavior. The R_{OPI} from AC measurements also showed a crossover from tunneling to hopping near 4 nm, similar to DC measurements. Furthermore, the dielectric constant of the OPI films normal to the substrate was extracted for the first time from C_{OPI} and the result agreed well with theoretical calculations of conjugated SAMs.[40] In general, the agreement obtained for OPI wires between the EGaIn and CP-AFM testbeds provides a good example of the consistency and reproducibility that can be obtained in current molecular electronics experiments based on well-characterized π-conjugated molecular films.

6.3 Experimental Methods

***Materials and Reagents*.** Au pellets were purchased from Mowrey Inc. (St. Paul, MN). Silicon wafers were purchased from Wafer Net (San Jose, CA). 4-aminothiophenol (4-ATP), terephthalaldehyde, 1,4-benzenediamine, and benzaldehyde were purchased from Sigma Aldrich (St. Louis, MO) and used as received. Absolute ethanol was purchased from Decon Labs (King of Prussia, PA), and dimethyl sulfoxide (DMSO) was purchased from Fisher Scientific (Waltham, MA). 4-formylthiophenol (4-FTP) was synthesized according to the literature.[41,42]

Synthesis of OPI wires. Au substrates were prepared by electron beam evaporation. 50 Å of Cr was first evaporated on bare Si wafer followed by 500 Å of Au using a CHA evaporator (SEC 600) at a rate of approximately 1 Å/s and base pressure $\leq 2 \times 10^{-6}$ Torr. The Au substrates were then immersed into purged solutions of 1 mM 4-ATP (absolute ethanol) or 4-FTP (DMSO). After 24 h, the SAM-coated Au substrates were removed from the thiophenol solution and rinsed thoroughly with absolute ethanol to remove physisorbed molecules before immersing them into Ar purged 20 mM solution in ethanol containing the next dialdehyde or diamine derivative depending on the wire design.

***Surface characterization* (RAIRS, XPS, UPS, and NEXAFS).** Reflection-absorption infrared spectra (RAIRS) were collected with a Nicolet iS50 spectrometer with a Harrick Seagull accessory for grazing angle specular reflectance measurements. The incident angle for the p-polarized IR beam was 84° from the surface normal. For each sample and background, an average of 300 scans at a resolution of 2 cm^{-1} were collected after 15 min of purging with dry air. The XPS, UPS and NEXAFS spectroscopy were performed at the SINS (Surface, Interface and Nanostructure Science) beamline of Singapore Synchrotron Light Source (SSLS).[43] We measured all the samples at room temperature in an ultrahigh vacuum (UHV) chamber with a base pressure of 1×10^{-10} mbar. A sputter-cleaned gold foil was in electrical contact with the samples to calibrate the photon energy with Au $4f_{7/2}$ core level peak at 84.0 eV. The photon energy resolution was 50 meV. We used the photon energy at 350 eV to probe the C 1*s* and S 2*p* states, and at 550 eV to probe the N 1*s* state. In UPS measurements, we used the photon energy at 60 eV and applied -10 V to the sample to overcome the work function of the analyzer. The UPS spectra were referenced to the Fermi edge of Au (Figure S3). All XPS and UPS spectra were normalized by their photon current recorded during the measurements. We carried out the angular-dependent NEXAFS spectra at C *K*-edge in the Auger electron yield mode with a Scienta R4000 electron energy analyzer. The synchrotron light was linearly *p*-polarized with the degree of 90% linear polarization and the photon energy resolution was 200 meV. We normalized the NEXAFS spectra to the incident photon flux, and then normalized to have the same absorption edge step height well above the absorption edge. Two incident angles (θ, the angle between the incident light and the sample surface), normal incidence ($\theta = 90°$) and grazing incidence ($\theta = 20°$), were used to record the NEXAFS spectra in order to calculate the tilt angle (α, the angle between the long axis of the molecular wire and the surface normal) of the OPI molecular wire (Please see detailed methods in Supporting Information page S7).

Junctions with GaO_X/EGaIn Top-Electrodes. The method to form electrical contacts has been reported elsewhere.[44] The GaO_X/EGaIn confined within a through-hole in the transparent rubber PDMS (polydimethylsiloxane) served as the top-electrode with a geometrical area 9.6×10^2 μm^2. We placed the top-electrode gently in contact with an Au bottom-electrode that supported the OPI wires for conducting the transport measurements. The *J*(V) measurements were carried out using Keithley 6430 source meter and data were acquired using LabView 2010.We measured the impedance of these junctions using an impedance analyzer (model Solartron 1260A with 1296A dielectric interface) in reference mode with a standard 10 pF capacitor as the external reference. Before we started the impedance measurements, we determined the *J*(V) characteristics of the devices and recorded the values of *J* over the range of biases of -0.50 to 0.50 V (one trace ≡ 0 V → 0.50 V → -0.50 V → 0 V) at intervals of 20 mV. The scan rate for the current voltage measurements were in the range 0.06 - 0.1 V/s. The temperature dependent *J*(V) measurements were performed in a probe station (Lakeshore CRX-VF) at a pressure of 3×10^{-5} bar.

6.4 Results and Discussion

Wire synthesis and characterization. Figure 6.2a shows the stepwise growth of OPI wires starting from a monolayer of 4-formylthiophenol (4-FTP); the stepwise growth from a SAM of 4-ATP is discussed in Chapter 4. This method facilitated high yield, sub-nanometer control of wire length along the sample normal as shown previously.[45] Figure 6.2b shows the wire capping step, i.e., amine terminated wires with even (4-FTP, Figure 6.2a) and odd (4-ATP) numbers of phenyl rings were reacted with benzaldehyde to obtain a consistent terminal group which facilitated reproducible electrical characterization. Figure 6.2c displays the reflection absorption infrared spectroscopy (RAIRS) spectra of capped OPI wires with odd numbers of phenyl units. The intensity of the C=N stretch peak (1625 cm^{-1}) and C=C stretch peak (1500 cm^{-1}) increased with the number of repeat units as expected. Figure 6.2d represents the normalized peak area of the imine stretch as a function of the total number of click steps, which increases approximately linearly.

Figure 6.3 shows the angle-dependent NEXAFS spectra of OPI-3, OPI-5, OPI-7, OPI-9, OPI-11, and the tilt angles (α; defined in Fig. 6.1). Two incident angles (θ = 90° and 20°) were used to probe the angle dependence of the resonance signal. We normalized all spectra with photon flux and then normalized to have the same absorption edge step height well above the absorption edge. We used the lowest resonance peak (π to π*) located at 284.9 eV to calculate the molecular tilt angle (α) of the molecular wire, which was defined as the angle between the molecular long axis and the surface normal. The values of α can be calculated by equation 6.1 as follows:[46]

$$I(\theta) = \frac{1}{3}AP\left[1 + \frac{1}{2}(3\cos^2\theta - 1)(3\sin^2\alpha - 1)\right] + \frac{1}{2}A(1 - P)\cos^2\alpha \qquad (6.1)$$

where A is the normalization factor. The values of α for all five molecules we measured are between 33° and 43°, which is in line with other reported values of α for SAMs or molecular wire systems on Au surfaces with up-standing phase.[47] Thus, the NEXAFS data reveal that the OPI molecular wires from n = 3 to 11, i.e., from short to long wire regimes, are tilted.

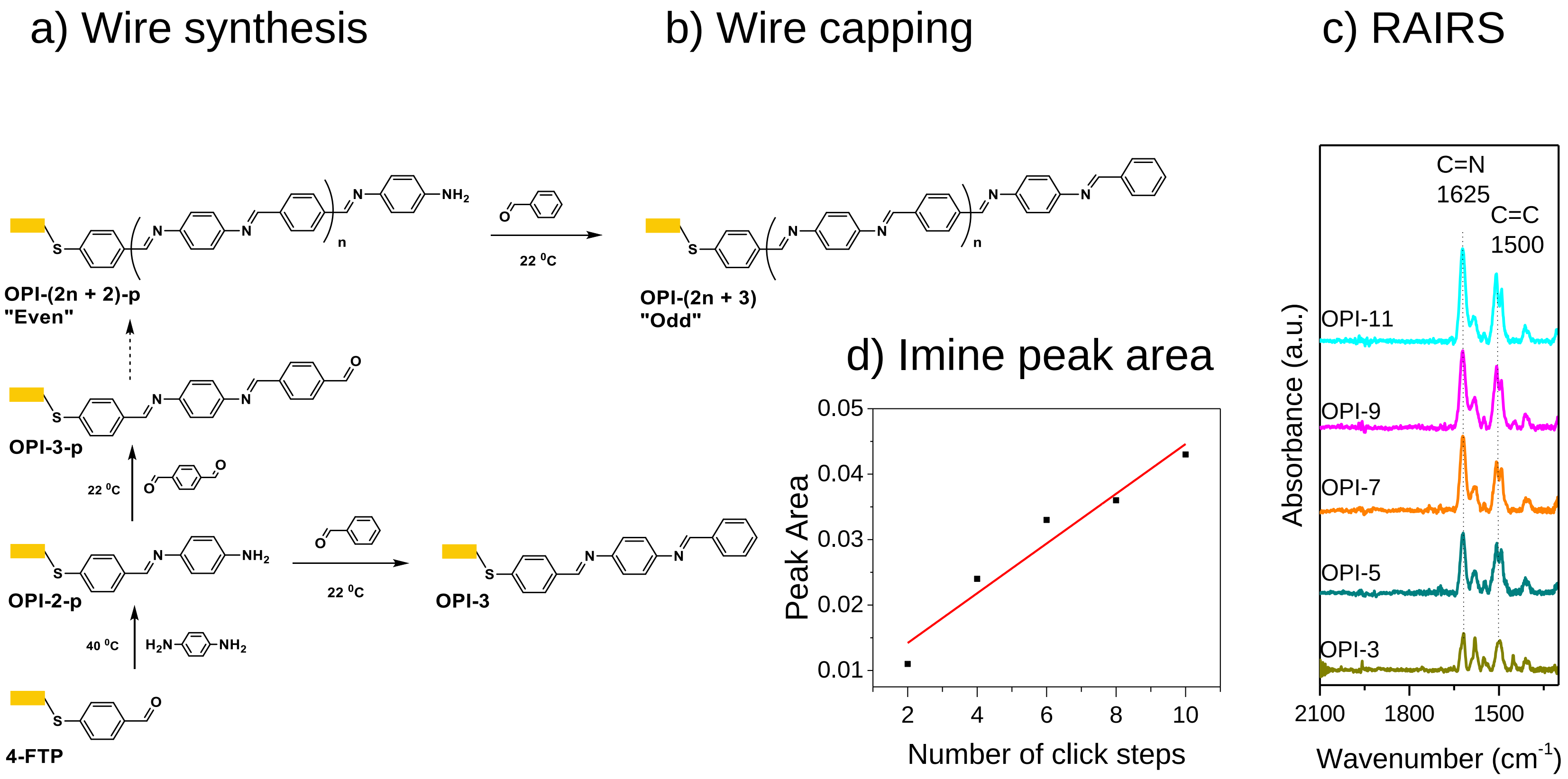

Figure 6.2 a) Molecular structure and stepwise wire growth of OPI wires starting from 4-FTP. b) Molecular structure of OPI wires capped with benzaldehyde, and the corresponding RAIRS spectra (c). (d) Normalized peak area of the C=N (1625 cm^{-1}) stretch mode as a function of the total number of click reactions.

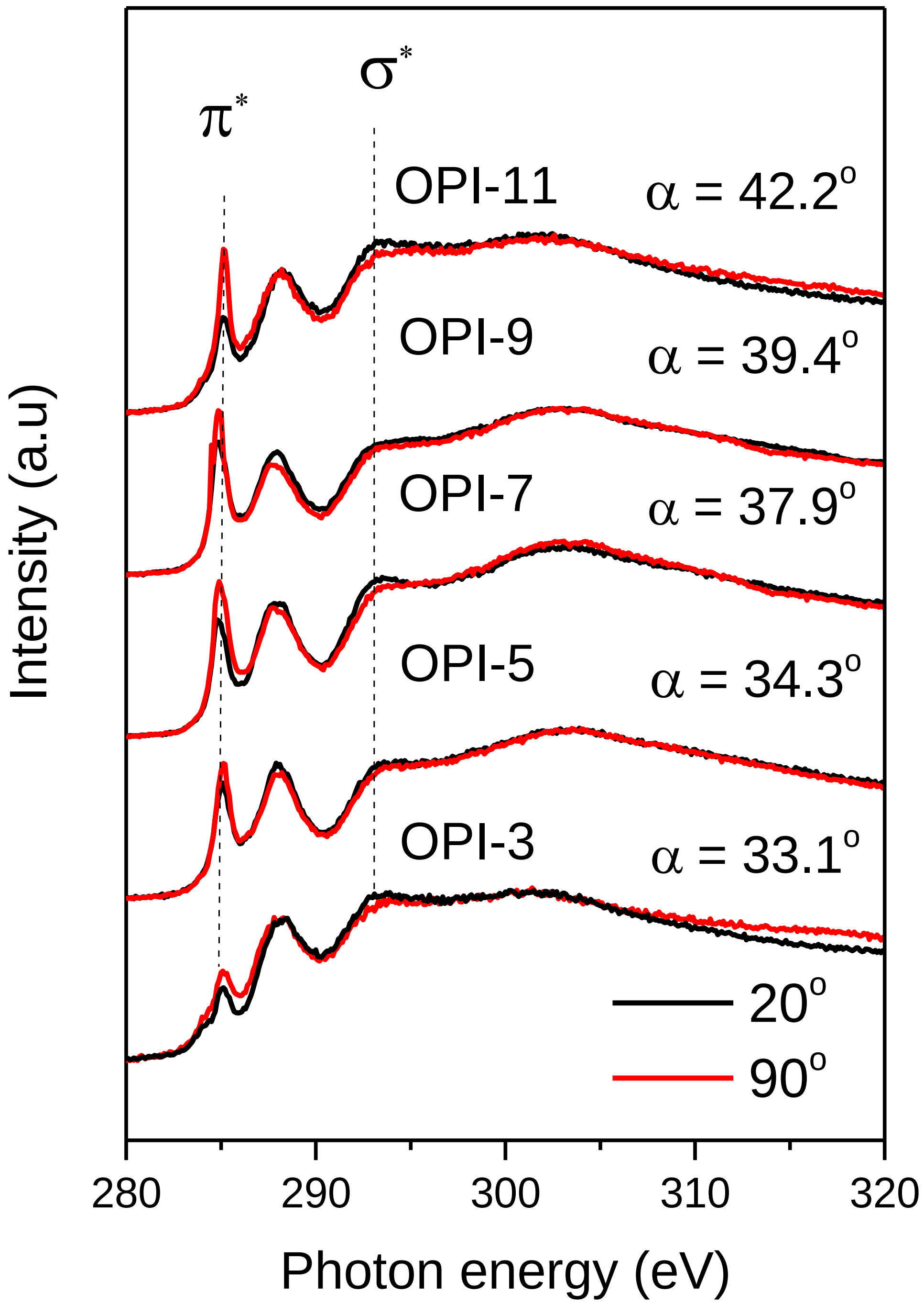

Figure 6.3 Angle dependent C K-edge NEXAFS spectra of OPI-3, OPI-5, OPI-7, OPI-9, and OPI-11. The black and red traces correspond to 20° and 90° incident angles respectively, measured from the sample surface. Data collected by Dr. Yuan, National University of Singapore.

DC characteristics. Figure 6.4a displays the *J(V)* characteristics of OPI wires measured with the EGaIn technique. The *J(V)* data are often interpreted using the general tunneling equation (eq 6.2) where β is the decay constant, d is the length of the OPI wire (in nm), and $J_0(V)$ is the hypothetical current through the junction for d = 0 nm.

$$J(V) = J_0(V)e^{-\beta d} \tag{6.2}$$

Eq. 6.2 implies that at a given bias, the current density (J) decreases with increasing d. Figure 6.4b shows the semilog plot of J at V = -0.5 V versus d revealing two distinct regimes of the exponential decay of J with a crossover near 4 nm. The error bars derive from 1 standard deviation for a total of 60 scans at 3 different sample locations. The change in the value of β indicates that the transport mechanisms in the short and long molecular wires are different. The red solid lines represent fits to eq 6.2. The short molecular wires (OPI 2 - OPI 5) yield $\beta = 2.84 \pm 0.18$ nm^{-1}, while the long molecular wires yield an apparent $\beta = 1.01 \pm 0.08$ nm^{-1} ('apparent' because tunneling does not occur in this regime; see below). The absence of hysteresis in the J(V) curves obtained from both platforms indicates that charging effects can be ignored. We wish to note that the role of defects in the EGaIn junctions have been studied in detail and can be ignored provided ultra-flat bottom-electrodes are used and the geometrical junction area is kept below 9.6×10^2 μm^2.[48,49]

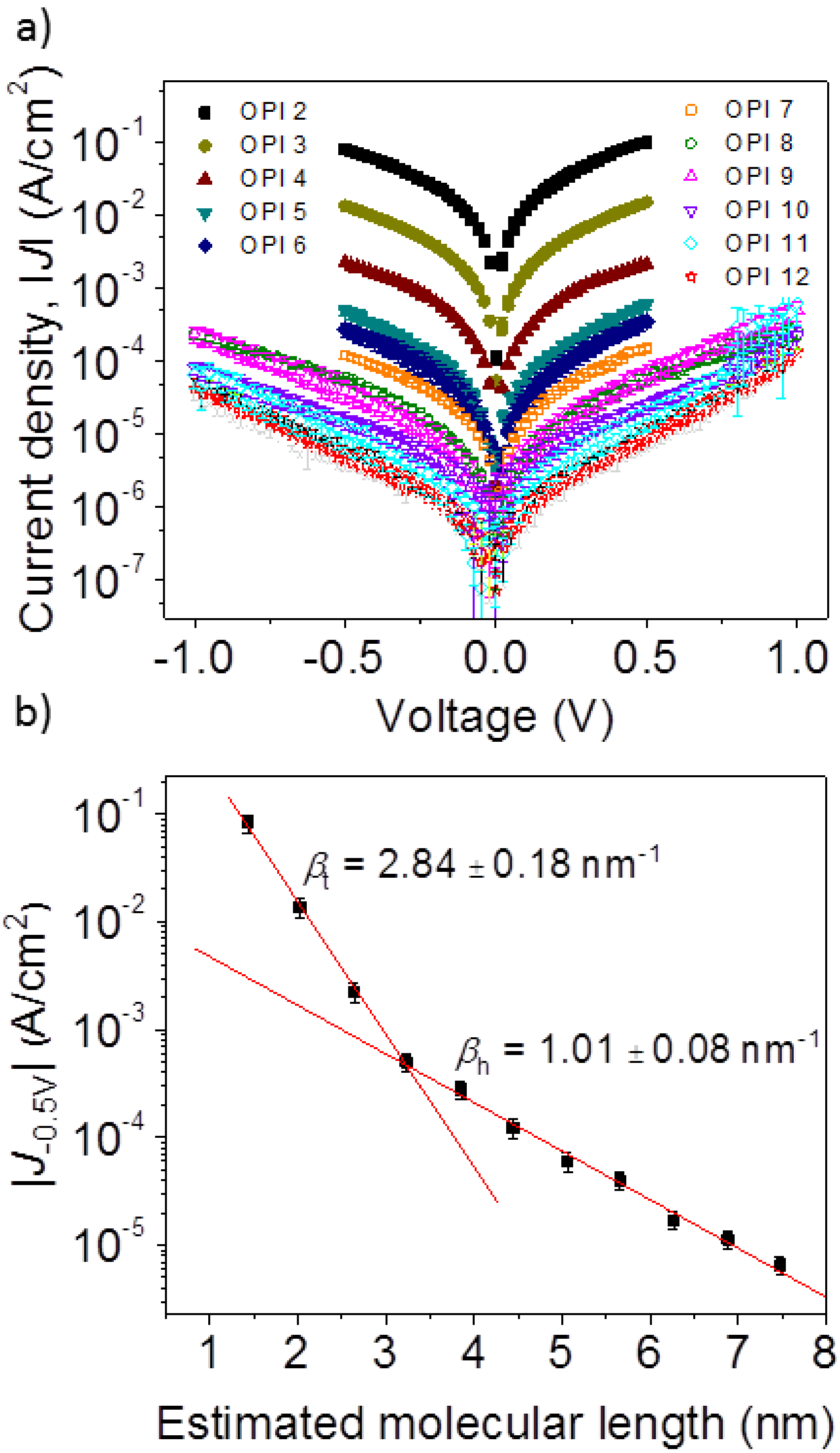

Figure 6.4 DC *J-V* measurements on EGaIn junctions. a) The average *J*(V) traces for the Au-OPI//GaO$_X$/EGaIn junctions for OPI wires of different lengths. b) *J* vs molecular length at *V* = -0.5 V. The red solid line represents fit to eq 6.2. Data collected by Dr. Sangeeth.

The value of β depends on various factors including the nature of the bonds in the molecular backbone, energy level alignment, and transport mechanism.[50,51] The β value of 2.84 ± 0.18 nm^{-1} is typically observed for aromatic monolayers in the tunneling regime, but the very low value of $\beta = 1.01 \pm 0.08$ nm^{-1} is characteristic for hopping (note that here we did not change the nature of the backbone of the SAM or the nature of the molecule - electrode interfaces). In hopping transport, charge is injected into the molecular backbone from one contact, and driven along to the other contact via the applied electric field. This regime has different temperature, bias, and length dependences than the tunneling regime.[36,37,52–56] Lateral or intermolecular charge transport can be ignored since the electric field is very large along the sample normal (approximately 2 MV / cm). Nevertheless, it is very clear that there is a change in the length dependence when wire length crosses over 3-4 nm.

To confirm the mechanism crossover, we performed temperature dependent *J(V)* measurements on short (OPI 4) and long (OPI 7) molecular wires. The *J(V,T)* data are shown in Figure 6.5. Junctions with the short molecular wire OPI 4 show temperature independent *J(V)* curves indicating that charge transport in these short wires is dominated by through bond tunneling. On the other hand, the temperature dependent *J(V)* curves for junctions with OPI 7 indicate that the long molecular wires display activated hopping transport. We determined the activation energy, E_a, by fitting the plot of ln J versus $1/T$ at $V = 0.6$ V (Figure 6.5d) to the Arrhenius equation (eq 6.3):

$$J(V,T) = J_0(V)\exp\left(\frac{-E_a}{k_B T}\right) \tag{6.3}$$

where k_B is the Boltzmann constant. For junctions with OPI 7 wires we found $E_a = 245 \pm 8$ meV.

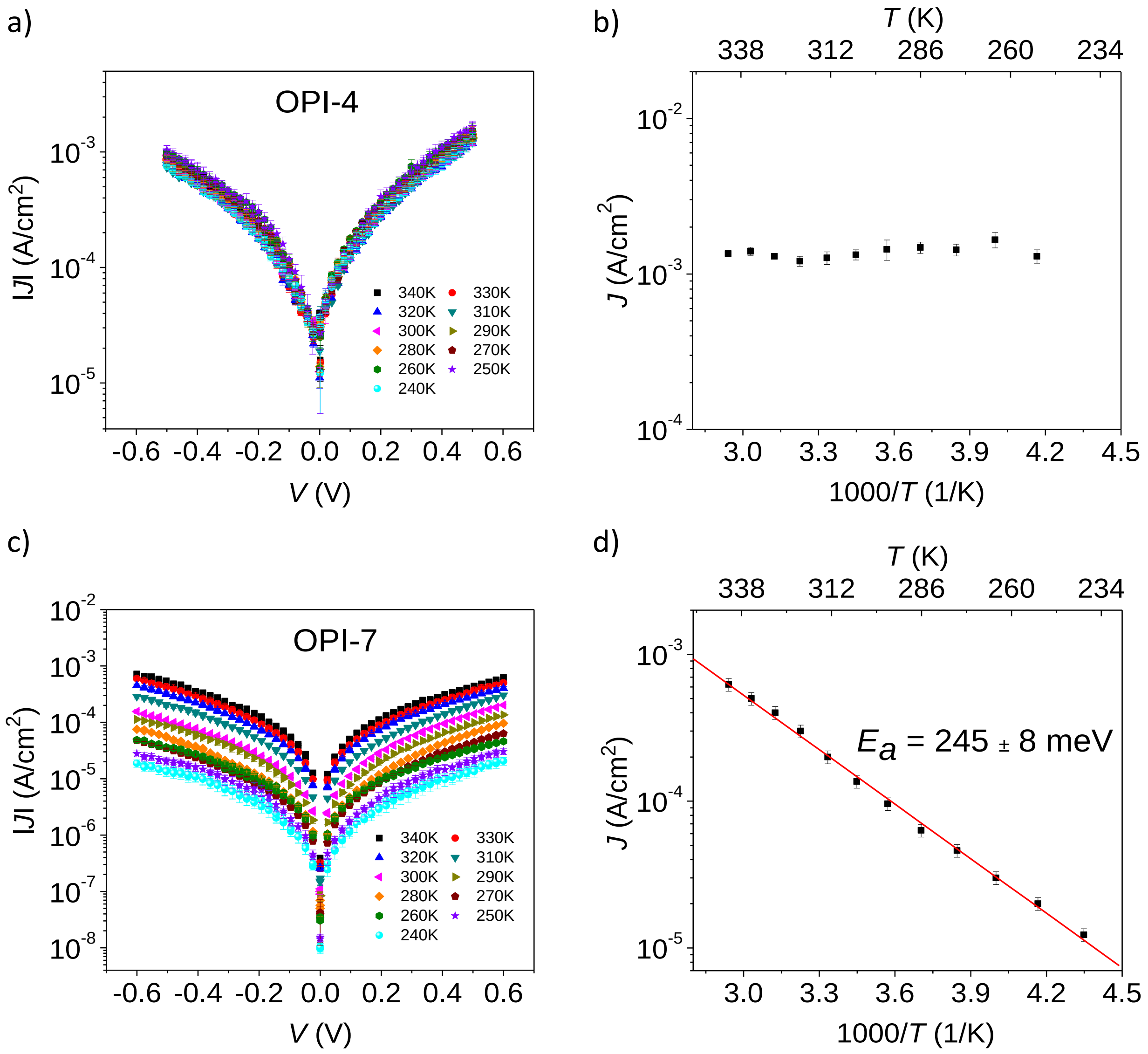

Figure 6.5 Variable temperature EGaIn DC bias measurements for (a) OPI-4 and (c) OPI-7 wires. The activation energy was calculated from the Arrhenius plot of ln *J*(T) verses (1/T). Error bars represent one standard deviation. Data collected by Dr. Sangeeth.

The origin of the activation energy, E_{a}, may be rationalized on the basis of the Marcus theory of electron transfer, which is expressed by eq 6.4:[57,58]

$$k_{ET} = \sqrt{\frac{\pi}{\hbar^2 k_B T \lambda}}\,\mathrm{H}^2 \exp\left(-\frac{\left(\lambda + \Delta G^0\right)^2}{4\lambda k_B T}\right) \tag{6.4}$$

where k_{ET} is the charge hopping rate, H is the effective Hamiltonian that couples initial and final states, $\Delta G°$ is the voltage-dependent thermodynamic driving force, λ is the reorganization energy and includes contributions from electronic and nuclear rearrangements, and T is the temperature. Thus, E_{a} can be expressed as $(\lambda_{total} + \Delta G°)^2/4\lambda_{total}$. The obtained value of 245 ± 8 meV for E_a is comparable to our previous result for OPI wires by CP-AFM,[37] and decreases with applied bias as shown in Figure 6.6. This decrease is likely due to the increase in $|\Delta G°|$ with applied V. Our previous work on oligonapthalenefluoroeneimine (ONI) wires[34] and oligo-tetrathiafulvalene-pyromelliticdiimide-imine (OTPI) wires[35] has shown that E_a is influenced by molecular conformation (e.g., planarity), and the HOMO-LUMO gap (extent of delocalization). For OPI wires, the ultraviolet (UV) visible absorption spectra indicate that conjugation does not extend over the entire wire, i.e., the optical band gap does not reduce beyond OPI-3,[37] consistent with the picture that the charge makes multiple hops along each chain. E_a may depend on torsional motions within the OPI wires that transiently couple conjugated sub-units along the chain.[52] Indeed 245 meV corresponds very well to the typical torsional vibrations in conjugated molecules. If ΔG° is estimated to be around -25 meV (for low bias), then the solution to $Ea = (\lambda_{total} + \Delta G°)^2/4\lambda_{total}$ yields total reorganization energy of ~ 1.1 eV. Detailed analysis of E_a is, however, not our principal focus here.

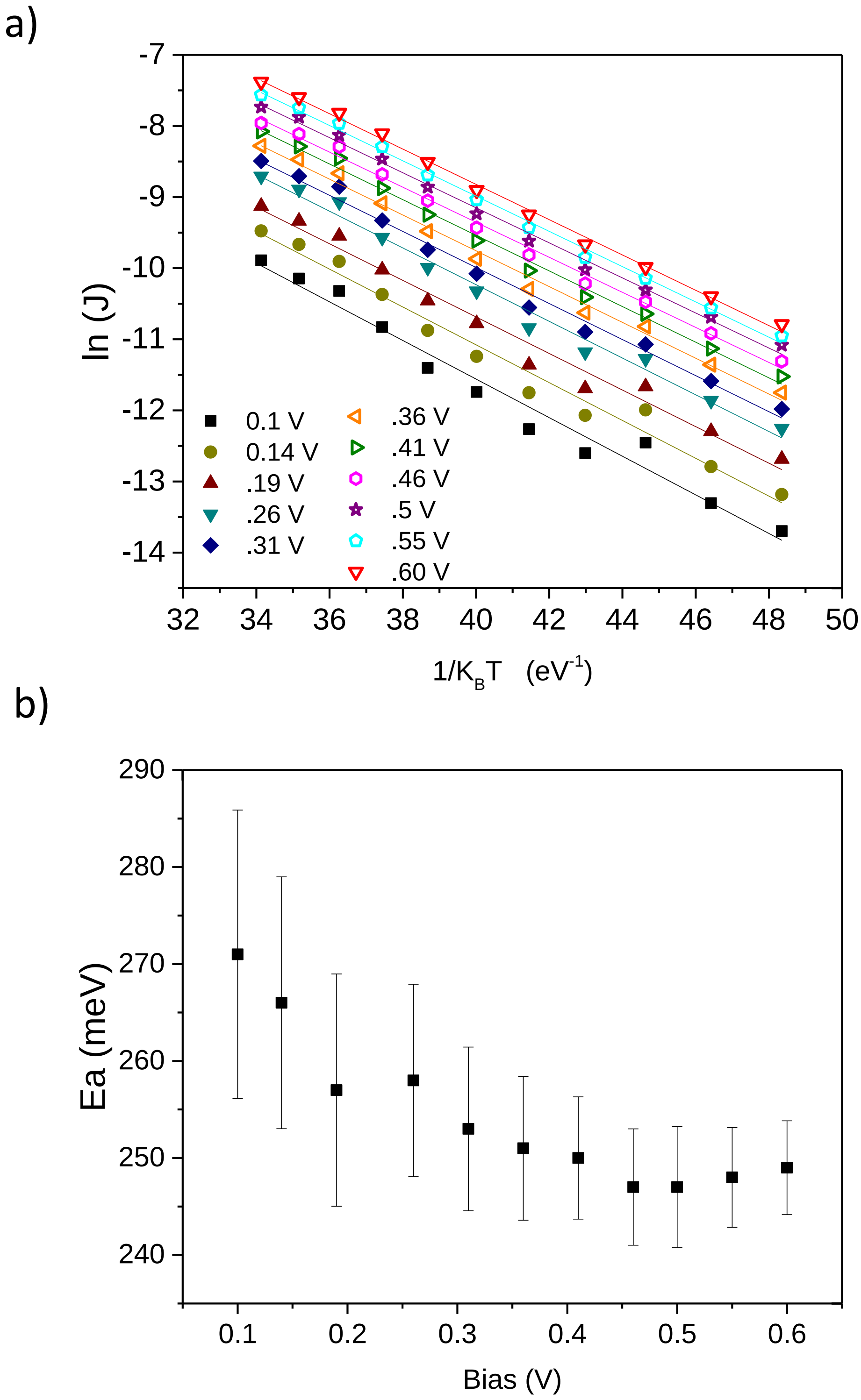

Figure 6.6 a) Semi log plot of current density (J) versus inverse temperature for different applied bias. b) The obtained values of activation energy from linear fit to equation 6.3 as function of applied bias. Data collected by Dr. Sangeeth.

AC characteristics. An important advantage of the EGaIn molecular junction verses other platforms is that it can be employed easily to measure AC transport by impedance spectroscopy.[38,39,59] The complex impedance Z is more general than resistance since it contains amplitude and phase information.[60] Figure 6.7a shows the frequency dependence of the modulus of the complex impedance ($|Z|$) for different molecular wires (OPI-2 to OPI-12) formed on Au. The Nyquist plots (Figure 6.8) show only one semicircle which indicates the presence of one capacitor (C_{OPI}) in the equivalent circuit. The modulus $|Z|$ increases over four orders of magnitude as the estimated molecular length changes from 1.5 nm (OPI 2) to 7.5 nm (OPI 12). The frequency dependence of $|Z|$ is nearly constant at low frequencies (dominated by the resistance of the molecular wire), but decreases with increasing frequency as the capacitive reactance ($X_{\mathrm{c}}=1/\omega^n C_{\mathrm{OPI}}$) decreases with frequency ω.[38,39]

To fit the impedance data we used an equivalent circuit consisting of a contact resistance R_{C} in series with a parallel combination of a constant phase element (CPE) and R_{OPI}. The CPE is modeled by an additional exponential empirical constant (n) on the reactance equation that is often used to account for non-ideal capacitance due to defects in the semiconductor material (e.g., grain boundaries and surface roughness). For $n = 1$ the CPE is the same as an ideal capacitor. Table 6.1 shows that $n = 0.99 - 0.994$ for the short wires but then monotonically decreases to 0.975 for the long wires. In this study, we used e-beam deposited Au films that generate relatively small grains with deep grain boundaries, compared with smooth surfaces, i.e., template-stripped Au substrates (more later). Thus, there are defects in the wires caused by the topography of the Au films resulting in n values slightly lower than 1. The small decrease in the value of n as a

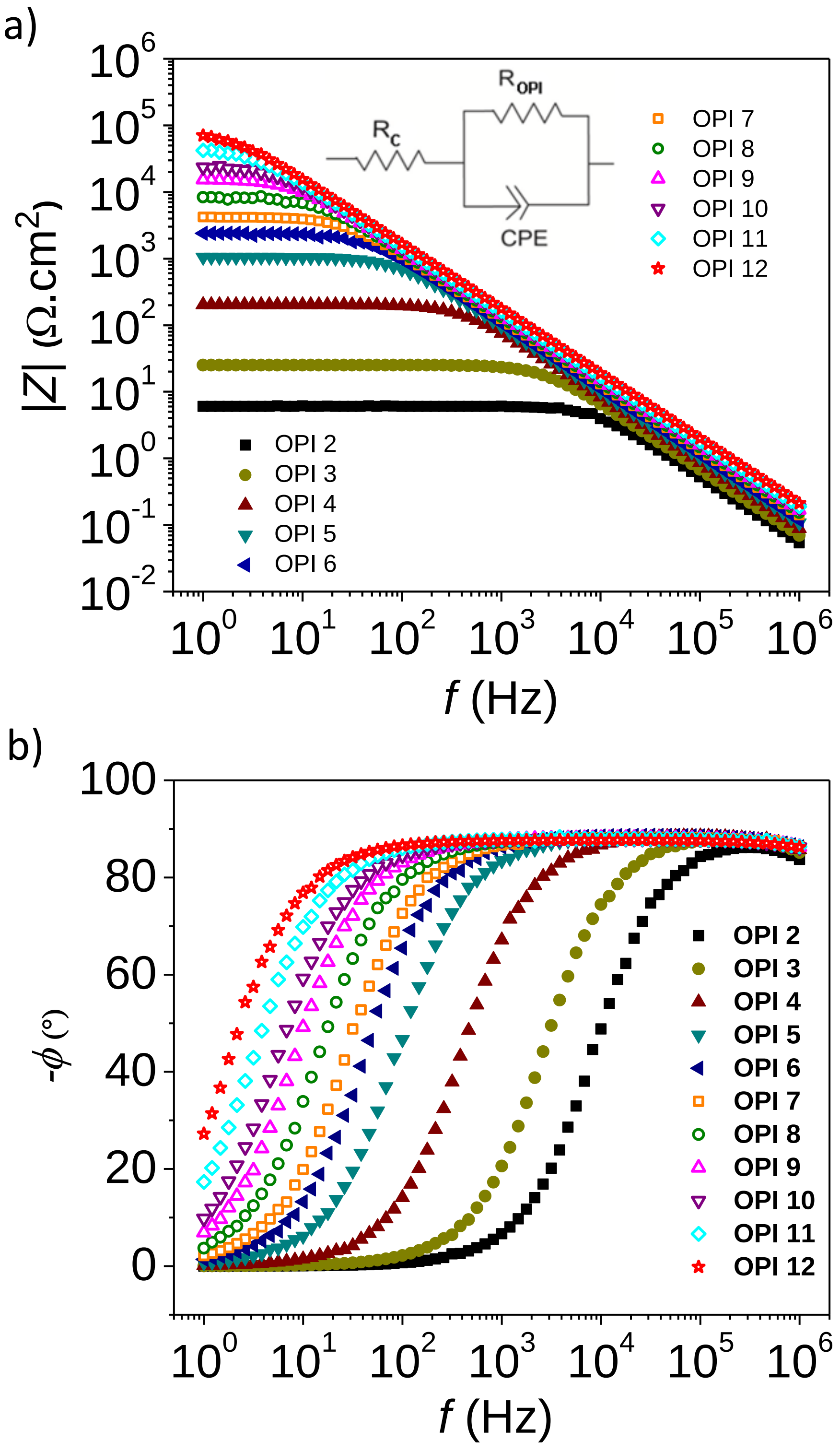

Figure 6.7 EGaIn AC Impedance measurements. a) Frequency dependence of |*Z*| for different OPI wire length. b) The phase angle vs. frequency plots. Data collected by Dr. Sangeeth.

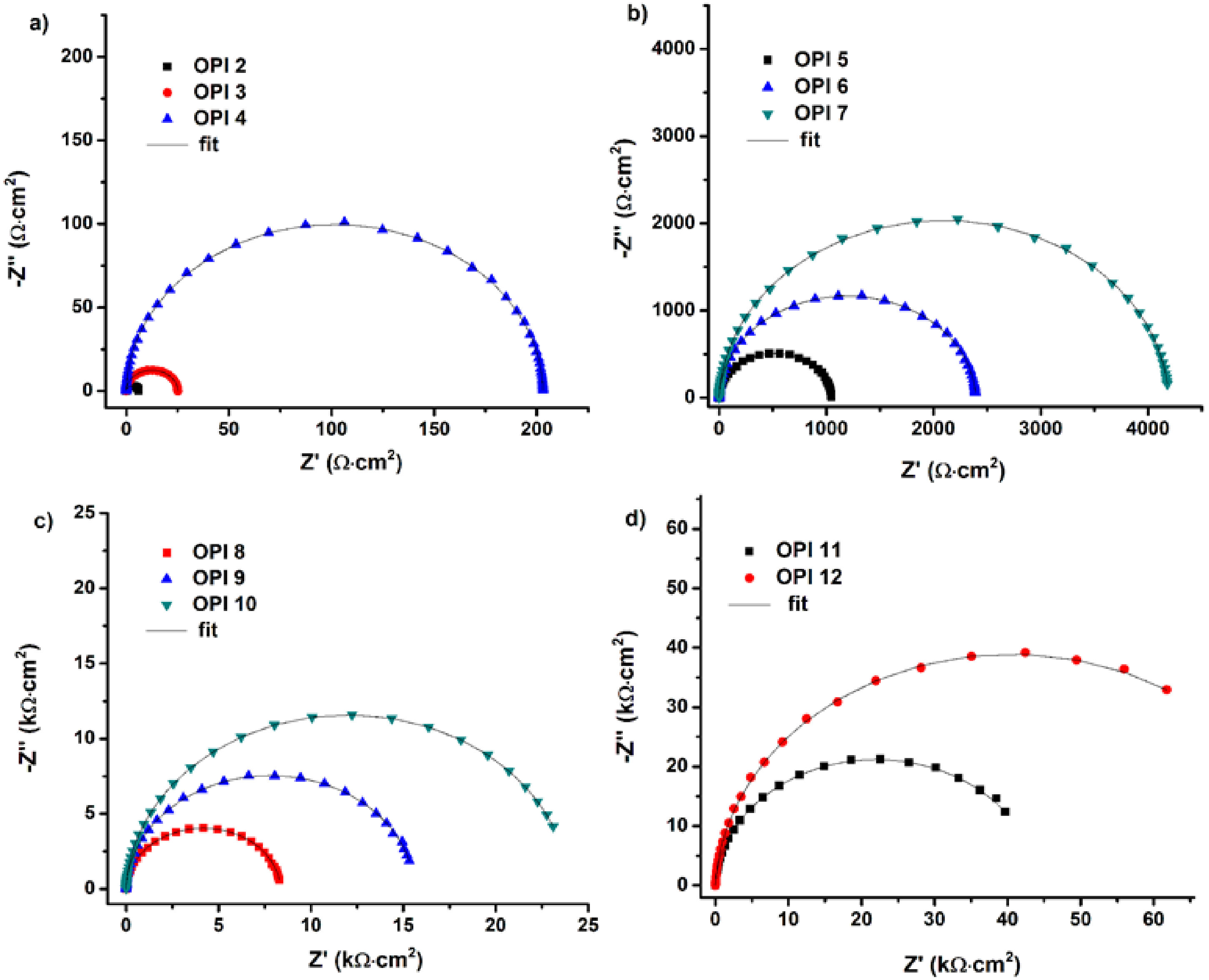

Figure 6.8 Nyquist plots of OPI wires. Data collected by Dr. Sangeeth.

function of wire length is likely caused by a small increase in the number of defects with wire length. Importantly, the plateau value at low frequency in Figure 6a is equal to the sum of R_C and R_{OPI}.

Figure 6.7b shows the phase ϕ against the frequency. The phase increases to 90° as the frequency increases and high frequency impedance is dominated by the capacitance (for capacitors ϕ is 90° while for ideal resistors ϕ is 0°). From Figures 6.7a and 6.7b it is therefore clear that up to a roll-off frequency associated with the kinks in the $|Z|$ vs ω and the ϕ vs ω curves, the wires exhibit resistive behavior. For frequencies higher than the roll-off ω, the response becomes increasingly capacitive. We were able to fit the Figure 6.7a behavior to equation 6.5 based on the equivalent circuit described above.

$$Z = R_{\mathrm{C}} + \frac{R_{OPI}}{1 + R_{OPI}^2 \omega^{2n} C_{OPI}^2} - j\left(\frac{\omega^n C_{OPI} R_{OPI}^2}{1 + R_{OPI}^2 \omega^{2n} C_{OPI}^2}\right) \tag{6.5}$$

The values of R_{OPI}, C_{OPI}, and n for each wire obtained from the fit are summarized in Table 6.1. Near a molecular length of 4 nm the OPI wires show a transition in the slope. Modifying eq 6.2, we can relate d to R_{OPI} where $R_{\mathrm{OPI,0}}$ is the pre-exponential factor.

Figure 6.9a displays the molecular length dependence of R_{OPI} obtained by impedance measurements. Clearly short OPI wires show a different trend compared to the long molecular wires. Near a molecular length of 4 nm the OPI wires show a transition in the slope. Modifying eq 6.2, we can relate d to R_{OPI} where $R_{\mathrm{OPI,0}}$ is the pre-exponential factor.

$$R_{\mathrm{OPI}} = R_{\mathrm{OPI,0}} e^{\beta d} \tag{6.6}$$

Table 6.1: Equivalent circuit parameters

Molecular wire	**R_{SAM} ($\times 10^{-5}$ MΩ.cm^2)**	**R_C ($\times 10^{-5}$ Ω.cm^2)**	**CPE C_{OPI} (pF)**	**CPE n**
OPI-2	0.6 ± 0.1	492 ± 59	32.6 ± 1.6	0.994
OPI-3	2.5 ± 0.4	506 ± 60	25.2 ± 1.3	0.994
OPI-4	20.1 ± 3.2	511 ± 61	21.1 ± 1.1	0.99
OPI-5	104 ± 17	488 ± 62	18.5 ± 0.9	0.986
OPI-6	239 ± 38	523 ± 50	16.7 ± 0.8	0.987
OPI-7	419 ± 67	508 ± 60	14.9 ± 0.7	0.983
OPI-8	835 ± 131	532 ± 60	14.2 ± 0.7	0.98
OPI-9	1561 ± 250	555 ± 67	12.9 ± 0.7	0.98
OPI-10	2392 ± 382	563 ± 71	12.5 ± 0.6	0.978
OPI-11	4379 ± 701	548 ± 63	11.9 ± 0.5	0.978
OPI-12	8018 ± 1282	567 ± 68	11.2 ± 0.5	0.975

Fitting the data in Fig. 6.9a to eq 6.6 the short molecular wires (OPI 2- OPI 5) yield $\beta = 2.92 \pm 0.13$ nm^{-1}, while the long molecular wires yield an apparent $\beta = 0.99 \pm 0.11$ nm^{-1}. These β values are close to the values estimated using the DC *J(V)* data (Figure 6.4) indicating the consistency in our transport measurements. Figure 6.9b shows the variation of contact resistance with molecular length. The contact resistance is likely dominated by the molecular wire//GaO$_X$ interface which is of van der Waals type. The molecular length independent R_C indicates that the van der Waals type interface is similar for all the molecules as observed for other molecular systems with GaO$_X$/EGaIn as top contact.[38,39]

C_{OPI} is plotted as a function of 1/*d* in Figure 6.9c and it follows a straight line fit given by the parallel plate capacitance relation (eq 6.7)

$$C_{\mathrm{OPI}} = \varepsilon_0 \varepsilon_{\mathrm{r,OPI}}\ A_{\mathrm{geo}} \Big/ d \tag{6.7}$$

where ε_0 is the permittivity of the free space, $\varepsilon_{\mathrm{r,OPI}}$ is the dielectric constant of the wires and A_{geo} is the geometrical area of the electrode. Fitting C_{OPI} values to eq 6.7 gave a value of $\varepsilon_{\mathrm{r,OPI}}$ of 4.3 ± 0.2. This parallel capacitance model holds for our system because the separation between the plates (length of OPI films) is much smaller than the contact area. The error bars were tabulated using non-linear least square method from a total of 15 scans at 3 different sample locations.

Recently, Ratner, et al. used first principle calculations to show that the dielectric constant is strongly influenced by the SAM properties such as polarizability, surface coverage, tilt angle, and configuration.[40] Our obtained $\varepsilon_{\mathrm{r,OPI}}$ value of 4.3 is approximately 17 - 20% different than the calculated ε_{r} values of conjugated polyyne SAMs. Even though our OPI wires contain more polarizable repeat units than polyyne SAMs, the non-

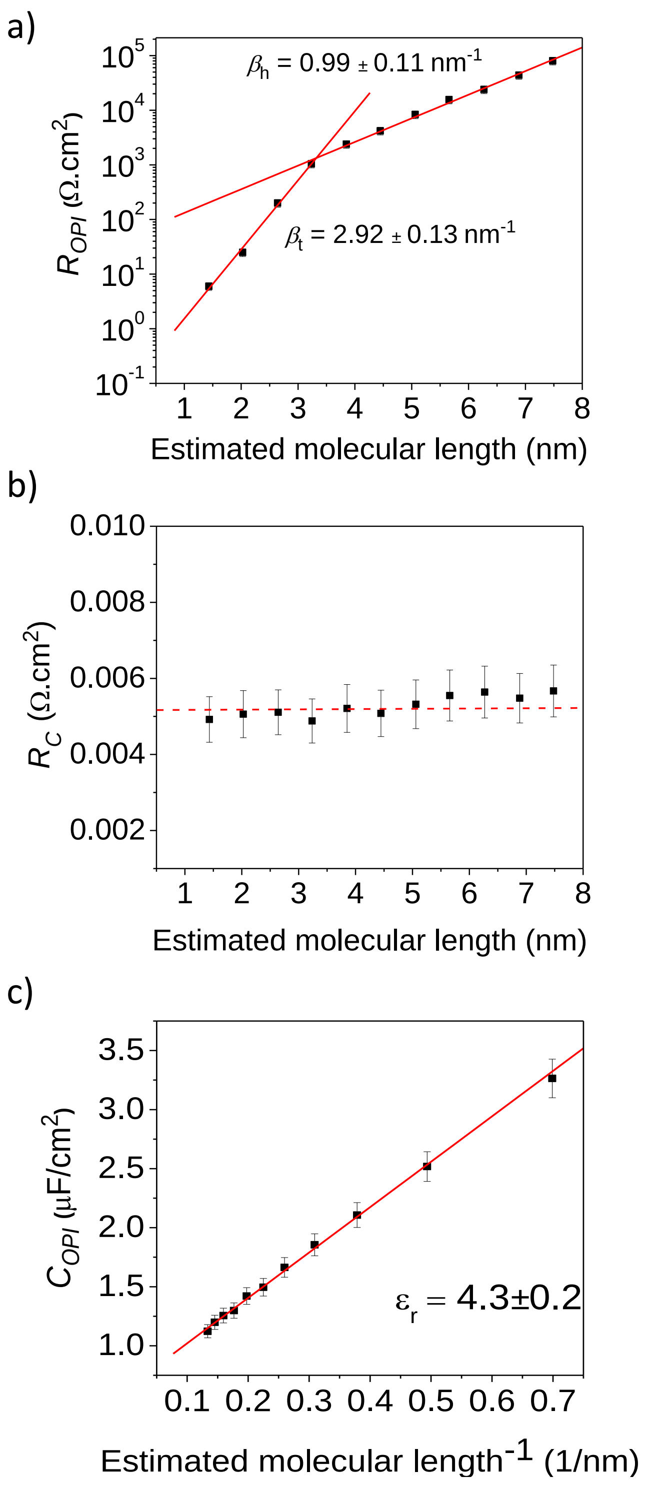

Figure 6.9 EGaIn AC impedance results. a) Resistance of the molecular wires (R_{OPI}) vs length. Red solid lines are fits to eq 6.6. b) The contact resistance (R_C) as a function of wire length. The red dashed line is a guide to the eye. c) Capacitance of the molecular wires (C_{OPI}) vs inverse length. The red solid line represents the fit to parallel plate capacitance relation (eq 6.7). Data collected by Dr. Sangeeth.

zero dihedral and tilt angles of the OPI wires disrupt molecular planarity and suppress electron cloud polarizability by the electric field, which presumably results in lower $\varepsilon_{r,OPI}$ values.

Comparison of EGaIn and CP-AFM Measurements. When comparing molecular electronics testbeds, it is important to identify quantities that are intensive, i.e., independent of the junction area, versus extensive, i.e., dependent on junction area. Considerable uncertainties in junction areas can make comparison of extensive quantities difficult. However, intensive quantities should be directly comparable.

Measured intensive quantities. The area independent transport characteristics such as β, crossover length, hopping decay slope, and E_a are summarized in Table 6.2 for both CP-AFM and EGaIn junctions. There is remarkable agreement between the intensive transport characteristics of EGaIn and CP-AFM junctions. The β values for instance agree within 10%, the crossover lengths are identical, and the activation energies agree within 13%. Collectively, these results indicate exceptional reproducibility in these key area-independent transport parameters across two very different platforms for charge transport.

Table 6.2. Comparison of intensive (area independent) transport characteristics of CP-AFM and EGaIn junctions.

Junction Platform	$\boldsymbol{\beta_{Tunneling}}$ **(nm^{-1})**	**Crossover length (nm)**	**Activation Energy (meV)**	$\boldsymbol{\beta_{Hopping}}$ **(nm^{-1})**
CP-AFM[37]	3.0 ± 0.08	4	280	0.9 ± 0.07
DC EGaIn	2.84 ± 0.18	4	245 ± 8	1.01 ± 0.08

AC EGaIn	2.92 ± 0.13	4	NA	0.99 ± 0.11

Measured extensive quantities. On the other hand, it is far more challenging to compare absolute resistance values for the two junctions as resistance depends on the number of molecules in active electrical contact. Further, the geometrical contact areas for the EGaIn and CP-AFM junctions differ by a factor of ~10^7. Computational work by Landau, et al. has shown that for junctions with tens of molecules, the conductance should scale linearly with the number of contacted molecules.[61] Thus, the total resistance can be described by eq 6.8:

$$1/R_{\mathrm{OPI}} = 1/r + 1/r + 1/r..... = n_{mol}/r = \Gamma_{OPI} A/r \tag{6.8}$$

where, r is the resistance per molecule, and n_{mol} is the number of molecules in the junction, which is determined by the surface coverage ($\mathit{\Gamma}_{OPI}$) and junction area (A). The surface coverage for OPI wires on Au was found previously to be 3.5 molecules/nm^2.[45] Note that this coverage value is the same for both the EGaIn and CP-AFM platforms as both used OPI wires grown on Au prepared by the same method. Using this coverage value, the total number of molecules within the CP-AFM junction is approximately 200, and 3×10^9 for the EGaIn junction based on the geometrical contact areas.

Figure 6.10 displays the estimated single molecule resistances r as a function of d for CP-AFM junctions along with the measured AC and DC r values for the EGaIn junctions. The initial values (black squares vs blue triangles) differ by colossal 6-7 orders of magnitude. The relevant sources of discrepancies between the two testbeds are discussed below.

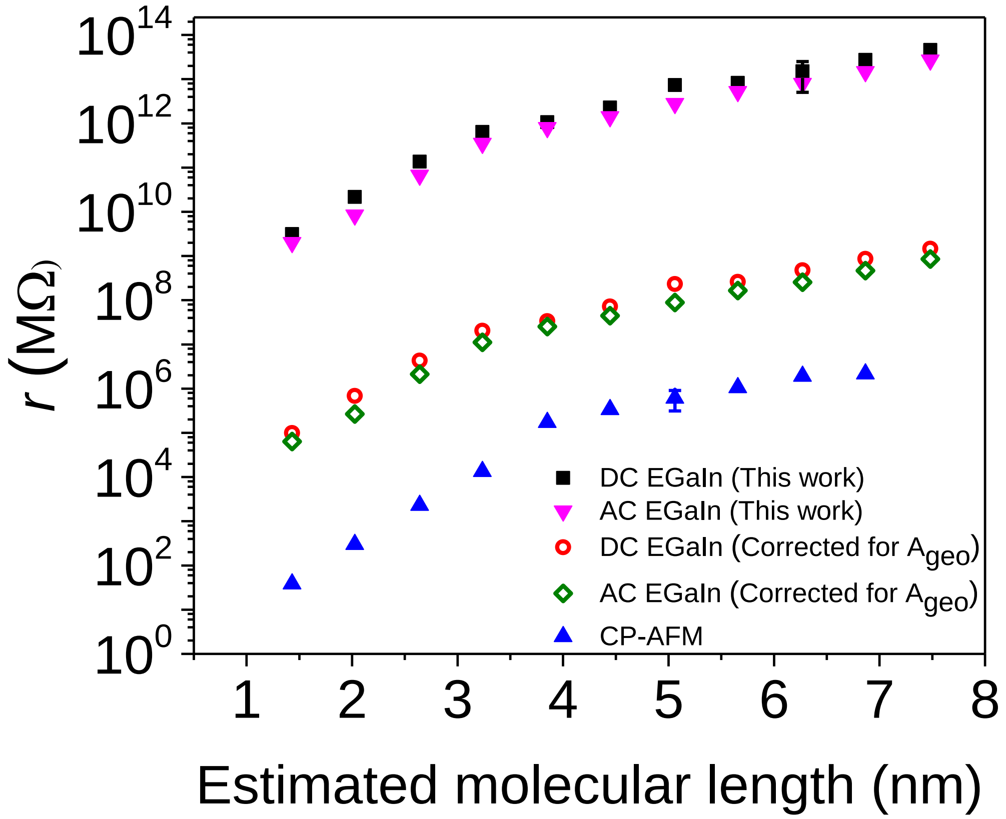

Figure 6.10 A semilog plot of resistance per molecule versus molecular length for OPI wires obtained from CP-AFM[37] and EGaIn test beds. Representative error bars are shown on select points.

Correcting for the effective EGaIn electrode contact area. Akkerman, et al. summarized in a review that the observed resistance per molecule increases with increasing geometrical area of the junctions.[28] In other words, the observed resistances per molecule in large area SAM based junctions are 7 orders of magnitude larger than those values obtained from single molecule experiments.[28] Whitesides, et al. postulated that one of the "culprits" for this large discrepancy could be the difference between effective electrical contact area (area of the electrode in direct contact with molecules) and the geometrical contact area.[62,63] Their results showed that the effective contact area of the EGaIn top contact is approximately 10^{-4} times smaller than the geometrical contact area for alkyl thiol SAMs on a template-stripped Ag substrate.[62] In that work, a correction factor of 10^{-3} was reported to account for the surface roughness of the EGaIn/GaO$_x$ top-contact and an additional roughness factor of 10^{-1} was included for the template stripped bottom-contact.

Correcting for the Au substrate roughness. In this study, the relatively large roughness associated with thermally deposited Au (not template-stripped) further reduces the total number of contacted molecules. The correction factor for the bottom Au electrode was calculated using a similar method outlined by Whitesides, et al. based on a high resolution STM image of the Au electrode.[62] The STM image pixel count within the first 2 Å from the top most average plane of the image in Figure 6.11 was calculated, and this resulted in an additional roughness correction factor of $10^{-1.5}$. This correction, combined with the factor of 10^{-3} mentioned above for the EGaIn electrode, gives a combined area correction factor of $10^{-4.5}$. The red and green data points in Figure 6.10 show the r vs d behavior after correcting by this factor. It is clear that there is still a large difference between the EGaIn and CP-AFM values of r of approximately a factor of 10^2.

Role of contact resistance and electrode work function. Importantly, based on the red and blue data points in Figure 6.10, we estimate that the contact resistances *per molecule* for DC EGaIn and CP-AFM junctions are approximately 500 MΩ and 1 MΩ, respectively, a substantial difference. These contact resistances (at d = 0 nm) were extrapolated from linear fits of the semi-log plots of r vs d in the tunneling regimes (red and blue symbols in Figure 6.10). It is well known that contact resistances are strongly influenced by the work function of the electrodes and nature of contact (physisorbed vs chemisorbed).[50,64–68] For example, we have previously reported that contact resistance for SAMs of alkyl

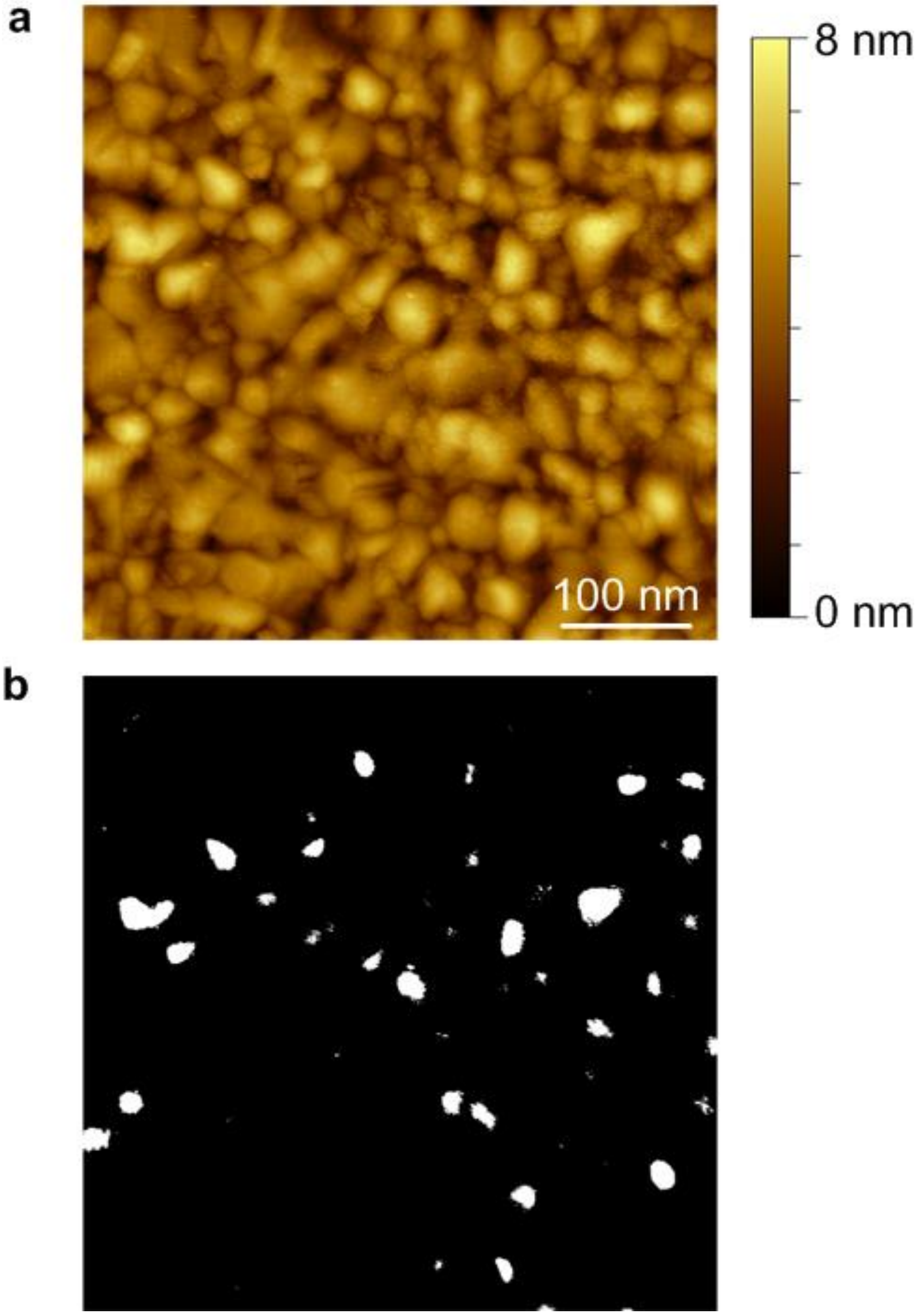

Figure 6.11 (a) Scanning tunneling microscopy image of a typical Au substrate. (b) Surface area available for contact (white area) estimated via digital analysis of the STM image in (a). The contact area (3.1%) was estimated as the number of pixels within 2 Å from the top-most average plane of the image in (a). STM image collected by Mr. Wang.

thiols decreased by 2 orders of magnitude with increasing work function of the metal contacts.[65] That is, contact effects can result in orders of magnitude changes in absolute resistance; the effects are comparable to the corrections for effective contact area. It is not surprising that the contact resistance is substantially higher for EGaIn versus CP-AFM junctions given the presence of the GaO_x interlayer and the lower work function of EGaIn versus Au top contact (4.2 eV vs 5.1 eV). In EGaIn junctions, the native 0.7 nm thick layer of GaOx acts as a protective barrier that prevents the bulk EGaIn from alloying with the bottom-electrode. It has been shown that resistance of GaOx is about 100 times more than that of bulk EGaIn. For these reasons we believe that the difference in the observed values of *r* between the CP-AFM and EGaIn junctions of two orders of magnitude (after correction for effective electrical contact area) is caused by contact resistance between the SAM//top-electrode.

6.5 Conclusion

DC and AC electrical characterization have been measured for a set of systematically synthesized conjugated oligophenyleneimine wires varying between 1.5 and 7.5 nm in molecular length via the EGaIn top contact approach. The EGaIn junction affords access to both AC measurements and high precision variable temperature measurements which are critical for understanding transport mechanisms. The DC bias J-V results indicated a clear crossover from tunneling to hopping transport near 4 nm. Thus this crossover was confirmed in a large area junction previously observed only in CP-AFM based junctions. Variable temperature measurements indicated thermally activated transport for long wires with activation energy of 0.245 ± 0.008 eV in line with previously reported CP-AFM data. AC impedance spectroscopy measurements were utilized to calculate the wire resistance, wire capacitance, and for the first time, the dielectric constant of the wires. The AC results also indicated a similar crossover from tunneling to hopping transport near 4 nm with a decay constant β of 2.92 ± 0.13 nm^{-1} in the tunneling regime, and 1.01 ± 0.08 nm^{-1} in the hopping regime. Our results show excellent overall agreement between EGaIn and CP-AFM junctions for the measured intensive (area independent) quantities such as the length decay constant, crossover length, and activation energy. Based on these results, we conclude the differences in absolute resistance per molecule (extensive, area dependent quantity) in our large and small area junctions reflect correction factors for effective contact area due to roughness and contact resistance due to differences in the work function of the electrodes. Future work will exploit the impedance spectroscopy and variable temperature approaches afforded by the EGaIn junctions to examine the connection between wire architecture and transport in the hopping regime.

Studies that compare charge transport characteristics for a given molecular structure to gauge reproducibility across different testbeds are rare, though there are prior examples. For example, Chiechi et al. found good agreement between EGaIn and CP-AFM junctions based on monolayers of photosystem I.[69] However, due to the lack of cross testbed studies, a general explanation for the large observed discrepancy in absolute resistances per molecule is lacking.[29] In agreement with Whitesides et al.,[62] our results indicate that the surface roughness of the electrodes can account for five orders of magnitude of spread in the data. We believe in our case that the molecule—electrode contact resistances account for 2 orders of magnitude difference in absolute values of r.

More studies are needed to confirm whether effective contact areas and contact resistances can in general account for the large spread of r values across other small and large area junctions.

6.6 References

(1) Perrin, M. L.; Verzijl, C. J. O.; Martin, C. A.; Shaikh, A. J.; Eelkema, R.; van Esch, J. H.; van Ruitenbeek, J. M.; Thijssen, J. M.; van der Zant, H. S. J.; Dulić, D. *Nat. Nanotechnol.* **2013**, *8*, 282.

(2) Wang, L.; Rangger, G. M.; Romaner, L.; Heimel, G.; BucÌŒko, T.; Ma, Z.; Li, Q.; Shuai, Z.; Zojer, E. *Adv. Funct. Mater.* **2009**, *19*, 3766.

(3) Bâldea, I.; Xie, Z.; Frisbie, C. D. *Nanoscale* **2015**, *7*, 10465.

(4) Heimel, G.; Brédas, J.-L. *Nat. Nanotechnol.* **2013**, *8*, 230.

(5) Capozzi, B.; Xia, J.; Adak, O.; Dell, E. J.; Liu, Z.-F.; Taylor, J. C.; Neaton, J. B.; Campos, L. M.; Venkataraman, L. *Nat. Nanotechnol.* **2015**, *10*, 522.

(6) Heimel, G.; Rissner, F.; Zojer, E. *Adv. Mater.* **2010**, *22*, 2494.

(7) Egger, D. A.; Rissner, F.; Zojer, E.; Heimel, G. *Adv. Mater.* **2012**, *24*, 4403.

(8) Abu-Husein, T.; Schuster, S.; Egger, D. A.; Kind, M.; Santowski, T.; Wiesner, A.; Chiechi, R.; Zojer, E.; Terfort, A.; Zharnikov, M. *Adv. Funct. Mater.* **2015**, *25*, 3943.

(9) Toledano, T.; Sazan, H.; Mukhopadhyay, S.; Alon, H.; Lerman, K.; Bendikov, T.; Major, D. T.; Sukenik, C. N.; Vilan, A.; Cahen, D. *Langmuir* **2014**, *30*, 13596.

(10) Fereiro, J. A.; Kondratenko, M.; Bergren, A. J.; McCreery, R. L. *J. Am. Chem. Soc.* **2015**, *137*, 1296.

(11) Motiei, L.; Lahav, M.; Gulino, A.; Iron, M. A.; van der Boom, M. E. *J. Phys. Chem. B* **2010**, *114*, 14283.

(12) Sikes, H. D.; Smalley, J. F.; Dudek, S. P.; Cook, A. R.; Newton, M. D.; Chidsey, C. E.; Feldberg, S. W. *Science* **2001**, *291*, 1519.

(13) Tuccitto, N.; Ferri, V.; Cavazzini, M.; Quici, S.; Zhavnerko, G.; Licciardello, A.; Rampi, M. A. *Nat. Mater.* **2009**, *8*, 41.

(14) Sakamoto, R.; Wu, K.-H.; Matsuoka, R.; Maeda, H.; Nishihara, H. *Chem. Soc. Rev.* **2015**, *44*, 7698.

(15) Perrin, M. L.; Frisenda, R.; Koole, M.; Seldenthuis, J. S.; Gil, J. A. C.; Valkenier, H.; Hummelen, J. C.; Renaud, N.; Grozema, F. C.; Thijssen, J. M.; Dulić, D.; van der Zant, H. S. J. *Nat. Nanotechnol.* **2014**, *9*, 830.

(16) Hines, T.; Diez-Perez, I.; Hihath, J.; Liu, H.; Wang, Z. S.; Zhao, J.; Zhou, G.; Müllen, K.; Tao, N. *J. Am. Chem. Soc.* **2010**, *132*, 11658.

(17) Wold, D. J.; Frisbie, C. D. *J. Am. Chem. Soc.* **2000**, *122*, 2970.

(18) Lauhon, L. J.; Ho, W. *Phys. Rev. Lett.* **2000**, *85*, 4566.

(19) Nijhuis, C. A.; Reus, W. F.; Whitesides, G. M. *J. Am. Chem. Soc.* **2009**, *131*, 17814.

(20) Nijhuis, C. A.; Reus, W. F.; Barber, J. R.; Whitesides, G. M. *J. Phys. Chem. C* **2012**, *116*, 14139.

(21) Chiechi, R. C.; Weiss, E. A.; Dickey, M. D.; Whitesides, G. M. *Angew. Chem. Int. Ed. Engl.* **2008**, *47*, 142.

(22) Yaffe, O.; Ely, T.; Har-Lavan, R.; Egger, D. A.; Johnston, S.; Cohen, H.; Kronik, L.; Vilan, A.; Cahen, D. *J. Phys. Chem. C. Nanomater. Interfaces* **2013**, *117*, 22351.

(23) Tran, E.; Rampi, M. A.; Whitesides, G. M. *Angew. Chem. Int. Ed. Engl.* **2004**, *43*, 3835.

(24) Akkerman, H. B.; Blom, P. W. M.; de Leeuw, D. M.; de Boer, B. *Nature* **2006**, *441*, 69.

(25) Neuhausen, A. B.; Hosseini, A.; Sulpizio, J. A.; Chidsey, C. E. D.; Goldhaber-Gordon, D. *ACS Nano* **2012**, *6*, 9920.

(26) Bonifas, A. P.; McCreery, R. L. *Nat. Nanotechnol.* **2010**, *5*, 612.

(27) Salomon, A.; Cahen, D.; Lindsay, S.; Tomfohr, J.; Engelkes, V. B.; Frisbie, C. D. *Adv. Mater.* **2003**, *15*, 1881.

(28) Akkerman, H. B.; de Boer, B. *J. Phys. Condens. Matter* **2008**, *20*, 013001.

(29) McCreery, R. L.; Bergren, A. J. *Adv. Mater.* **2009**, *21*, 4303.

(30) Milani, F.; Grave, C.; Ferri, V.; Samorì, P.; Rampi, M. A. *Chemphyschem* **2007**, *8*, 515.

(31) Bergren, A. J.; Harris, K. D.; Deng, F.; McCreery, R. L. *J. Phys. Condens. Matter* **2008**, *20*, 374117.

(32) Wold, D. J.; Frisbie, C. D. *J. Am. Chem. Soc.* **2001**, *123*, 5549.

(33) Engelkes, V. B.; Beebe, J. M.; Frisbie, C. D. *J. Phys. Chem. B* **2005**, *109*, 16801.

(34) Choi, S. H.; Risko, C.; Delgado, M. C. R.; Kim, B.; Brédas, J.-L.; Frisbie, C. D. *J. Am. Chem. Soc.* **2010**, *132*, 4358.

(35) Choi, S. H.; Frisbie, C. D. *J. Am. Chem. Soc.* **2010**, *132*, 16191.

(36) Luo, L.; Balhorn, L.; Vlaisavljevich, B.; Ma, D.; Gagliardi, L.; Frisbie, C. D. *J. Phys. Chem. C* **2014**, *118*, 26485.

(37) Choi, S. H.; Kim, B.; Frisbie, C. D. *Science* **2008**, *320*, 1482.

(38) Sangeeth, C. S. S.; Wan, A.; Nijhuis, C. a. *J. Am. Chem. Soc.* **2014**, *136*, 11134.

(39) Sangeeth, C. S.; Wan, A.; Nijhuis, C. A. *Nanoscale* **2015**, *7*, 12061.

(40) Heitzer, H. M.; Marks, T. J.; Ratner, M. A. *ACS Nano* **2014**, *8*, 12587.

(41) Golchoubian, H.; Hosseinpoor, F. *Molecules* **2007**, *12*, 304.

(42) Norman Young, R.; Yves Gauthier, J.; Coombs, W. *Tetrahedron Lett.* **1984**, *25*, 1753.

(43) Yu, X.; Wilhelmi, O.; Moser, H. O.; Vidyaraj, S. V.; Gao, X.; Wee, A. T. S.; Nyunt, T.; Qian, H.; Zheng, H. *J. Electron Spectros. Relat. Phenomena* **2005**, *144-147*, 1031.

(44) Wan, A.; Jiang, L.; Sangeeth, C. S. S.; Nijhuis, C. A. *Adv. Funct. Mater.* **2014**, *24*, 4442.

(45) Demissie, A. T.; Haugstad, G.; Frisbie, C. D. *J. Am. Chem. Soc.* **2015**, *137*, 8819.

(46) Stöhr, J. *NEXAFS Spectroscopy*; Springer Science & Business Media, 1992.

(47) Love, J. C.; Estroff, L. A.; Kriebel, J. K.; Nuzzo, R. G.; Whitesides, G. M. *Chem. Rev.* **2005**, *105*, 1103.

(48) Yuan, L.; Jiang, L.; Zhang, B.; Nijhuis, C. A. *Angew. Chem. Int. Ed. Engl.* **2014**, *53*, 3377.

(49) Jiang, L.; Sangeeth, C. S. S.; Wan, A.; Vilan, A.; Nijhuis, C. A. *J. Phys. Chem. C* **2015**, *119*, 960.

(50) Kim, B.; Choi, S. H.; Zhu, X.-Y.; Frisbie, C. D. *J. Am. Chem. Soc.* **2011**, *133*, 19864.

(51) Beebe, J. M.; Engelkes, V. B.; Liu, J.; Gooding, J. J.; Eggers, P. K.; Jun, Y.; Zhu, X.; Paddon-Row, M. N.; Frisbie, C. D. *J. Phys. Chem. B* **2005**, *109*, 5207.

(52) Smith, C. E.; Odoh, S. O.; Ghosh, S.; Gagliardi, L.; Cramer, C. J.; Frisbie, C. D. *J. Am. Chem. Soc.* **2015**, *137*, 15732.

(53) Goldsmith, R. H.; Sinks, L. E.; Kelley, R. F.; Betzen, L. J.; Liu, W.; Weiss, E. A.; Ratner, M. A.; Wasielewski, M. R. *Proc. Natl. Acad. Sci. U. S. A.* **2005**, *102*, 3540.

(54) Luo, L.; Choi, S. H.; Frisbie, C. D. *Chem. Mater.* **2011**, *23*, 631.

(55) Segal, D.; Nitzan, A.; Davis, W. B.; Wasielewski, M. R.; Ratner, M. A. *J. Phys. Chem. B* **2000**, *104*, 3817.

(56) Taherinia, D.; Smith, C. E.; Ghosh, S.; Odoh, S. O.; Balhorn, L.; Gagliardi, L.; Cramer, C. J.; Frisbie, C. D. *ACS Nano* **2016**.

(57) *Charge and Exciton Transport through Molecular Wires*; Siebbeles, L. D. .; Grozeman, F. C., Eds.; John Wiley & Sons, 2011.

(58) Marcus, R. A. *J. Chem. Phys.* **1965**, *43*, 679.

(59) Wang, D.; Fracasso, D.; Nurbawono, A.; Annadata, H. V; Sangeeth, C. S. S.; Yuan, L.; Nijhuis, C. A. *Adv. Mater.* **2015**, n/a.

(60) *Impedance Spectroscopy: Theory, Experiment, and Applications*; Barsoukvo, E.; Macdonald, J. R., Eds.; John Wiley & Sons, 2005.

(61) Landau, A.; Kronik, L.; Nitzan, A. *J.Comput. Theor. Nanosci* **2008**, *5*, 534.

(62) Simeone, F. C.; Yoon, H. J.; Thuo, M. M.; Barber, J. R.; Smith, B.; Whitesides, G. M. *J. Am. Chem. Soc.* **2013**, *135*, 18131.

(63) Holm, R. *Electric Contacts: Theory and Application*; Springer Berlin Heidelberg,

1999; Vol. 1.

(64) Beebe, J. M.; Engelkes, V. B.; Miller, L. L.; Frisbie, C. D. *J. Am. Chem. Soc.* **2002**, *124*, 11268.

(65) Engelkes, V. B.; Beebe, J. M.; Frisbie, C. D. *J. Am. Chem. Soc.* **2004**, *126*, 14287.

(66) Kim, B.; Beebe, J. M.; Jun, Y.; Zhu, X. Y.; Frisbie, G. D. *J. Am. Chem. Soc.* **2006**, *128*, 4970.

(67) Huang, M.-J.; Hsu, L.-Y.; Fu, M.-D.; Chuang, S.-T.; Tien, F.-W.; Chen, C.-H. *J. Am. Chem. Soc.* **2014**, *136*, 1832.

(68) Kim, T.; Liu, Z.-F.; Lee, C.; Neaton, J. B.; Venkataraman, L. *Proc. Natl. Acad. Sci.* **2014**, *111*, 10928.

(69) Castañeda Ocampo, O. E.; Gordiichuk, P.; Catarci, S.; Gautier, D. A.; Herrmann, A.; Chiechi, R. C. *J. Am. Chem. Soc.* **2015**, *137*, 8419.

(70) Cademartiri, L.; Thuo, M. M.; Nijhuis, C. A.; Reus, W. F.; Tricard, S.; Barber, J. R.; Sodhi, R. N. S.; Brodersen, P.; Kim, C.; Chiechi, R. C.; Whitesides, G. M. *J. Phys. Chem. C* **2012**, *116*, 10848.

7. X-ray Photoelectron Spectroscopy of Perfluorinated Oligophenylene Imine Molecular Wires – A Novel Method to Investigate Charge Transport of Thin Films

7.1 Abstract

We report the systematic electronic and surface characterization of anisotropic, π-conjugated oligophenyleneimine (OPI) films synthesized using aryl step-wise imine condensation. Film synthesis began with a self-assembled monolayer (SAM) of 4-formylthiophenol or 4-aminothiophenol on Au, followed by repetitive, alternate addition of terephthalaldehyde (benzene-1,4-dicarbaldehyde) or 1,4-Benzenediamine to form π-conjugated films ranging from 0.6 – 5 nm in thickness. By systematically capping the OPI films with pentafluoro termini, we were able to measure and compare the photo-emitted F 1s core state electrons by X-ray photoelectron spectroscopy (XPS). Our results show that the F 1s counts are sensitive to the position of the pentafluoro termini. Furthermore, the slope of peak area vs molecular length dropped sharply for short wires than for long wires. Nuclear reaction analysis was employed to calculate the surface coverage of carbon atoms, and the results agreed with OPI wires of corresponding length. To further investigate the role of molecular structure on the observed F 1s counts, conjugation blocking alkyl chains were inserted at different positions along the wire backbone. The results indicate that conjugation blocking units significantly impact the intensity of F 1s counts. Overall, we obtained good correlation between the wire structure and its corresponding effects on the magnitude of F 1s peak counts. We propose a model

based on radiative or auger emission of frontier orbital electrons coupled with transport of charges from substrate to wire as a possible core state relaxation mechanism. Although density functional theory (DFT) calculations are required to support the observed characteristics and proposed model, the results so far point to a new ultra-high vacuum method of studying charge transport.

7.2 Introduction

The fundamental investigation of charge transport in ultrathin organic films and molecules is an important research topic in molecular electronics.[1–16] There are dozens of techniques to study charge transport through molecular wires. They can generally be classified into 3 categories[17]: molecular junctions, photo-induced electron transfer (ET), and theoretical Landauer modeling. In molecular junctions, a single molecule or array of molecules are connected between two metal electrodes and their charge transport characteristics are studied by either direct current (DC) or alternating current (AC) measurements. In solution ET experiments, charge transfer is induced by photo excitation of an electron from HOMO to LUMO level, and the resulting charge separation and recombination rates are measured by transient absorption and fluorescence spectroscopy.[18–20] A better picture of charge transport gained through both molecular junction and solution ET experiments will help us to understand charge transport in biological systems, and to design devices for improved performance.

A relatively new approach for measuring charge transport rates in organic thin films is known as core-hole clock spectroscopy[21–23] – a method based on resonant auger Raman spectroscopy. In normal auger spectroscopy, auger electrons with constant kinetic energy (independent of the excitation photon energy) are emitted when excitation is made far from the absorption threshold. However, in auger resonant spectroscopy, the energy of the exciting photon approaches the core level threshold, and excites the core state electron into unoccupied orbitals. The excited electron now strongly interacts with other electrons in the system such that the process of excitation and decay cannot be treated as independent process. Instead, the exited electron can be classified into 2 categories based on whether it participates in the non-radiative decay process (participator type), or remain localized in the orbital (spectator type).[23] In both spectator and participator decay type; the kinetic energy of the auger electron is dependent on the incident photon energy. If there is charge transfer to the substrate during the life time of the core state, normal auger electrons with constant kinetic energy (photon energy independent) are detected. From the peak intensities of the different decay process, it is possible to estimate the charge transfer time in relation to the life time of the core. Zharnikov et al., used core hole clock spectroscopy to measure core-hole lifetime from N 1s core states of alkyl thiol self-assembled monolayers (SAMs) with nitrile (-C≡N) terminal units.[23] They measured decay constant of 0.93 Å per methylene unit, similar to electrical conductance measurements.[23]

In this chapter, we present preliminary results on perfluorinated oligophenylene imine (OPI) wires, which point to a potential new ultra-high vacuum method of measuring charge transport by x-ray photoelectron spectroscopy (XPS). Our motivation for this work was based on observation of film thickness measurements of OPI wires by XPS, which resulted in very small thickness change beyond 3 nm (near the tunneling to hopping transition length). Initial questions include: What is responsible for such low thickness values for long wires? How does a photo emitted core state relax back to the ground state? Are all the C 1s core electrons participating in photoelectron emission process? Our methodology to systematically investigate these issues is to tag terminal phenyl ring by other atoms with comparable number of electrons (size). Our stepwise approach of synthesizing OPI wires facilitates tagging the end unit with halogens or ferrocene as discussed Chapter 4. Among the halogens, we decided to tag the phenyl termini with F because it has comparable number of electrons to C ($Z = 9$ for F vs $Z = 6$ for C). In the additional work section in chapter 4, we noted that F terminated wires were problematic and caused variation from different experimental runs. The variation was caused by unoptimized reaction conditions employed for wire growth. For example, when carbonyl terminated wires were reacted with 4-fluoroaniline, the F atom withdrew electron density from the N lone pairs due to the high electronegativity of the F atom, and resulted in low reaction yield because it reduced the rate at which the lone electron pairs on the N atom attack the carbonyl units. Here, we optimized wire growth, and used pentafluorobenzaldehyde as the capping ligand with 5 F atoms to prevent problems associated with reduced extent of reaction, and to minimize the scan time required to get a good signal to nose ratio verses a F atom.

Indeed, our results show that the total F 1s photoelectron counts depends on the wire length. As wire length increases, the peak area dropped sharply for short wires than the long wires. The peak area vs estimated molecular length plot revealed a strikingly similar crossover behavior like molecular junction conductance measurements. The surface coverage of OPI-F5 (OPI wires capped with perfluoro termini) wires was measured with nuclear reaction analysis, and the results agreed with OPI wires with similar number of C atoms. The influence of chemical shifts, and charging effects were cross checked by synthesizing wires on native SiO_2. The results revealed that the crossover behavior was primarily due to electronic structure of the wires. We propose a model to describe the observed characteristics of OPI-F5 wires based on either auger or radiative decay followed by charge transport through frontier orbitals. To further investigate the electronic structure of the wires on the intensity of F 1s, we inserted conjugation breaking units at different positions. Overall, we found a strong correlation between the F 1s peak area, and the position and number of conjugation breaking units. Our results indicate that XPS can be a useful tool to understand structure-property relationships in molecular wires.

7.3 Experimental Methods

Materials. Au nuggets were purchased from Mowery Inc. (St. Paul, MN). Silicon wafers were purchased from Wafer Net (San Jose, CA). Aminoferrocene was purchased from TCI America (Portland, OR). Tetrabutylammonium hexafluorophosphate, 4-aminothiophenol (4-ATP), 1,4-benzenediamine, 1,4-diaminobutane, pentafluorothiophenol and terephthalaldehyde were purchased from Sigma Aldrich (St. Louis, MO). Absolute ethanol was purchased from Decon Labs (King of Prussia, PA), acetonitrile was purchased from ACROS Organics (Geel, Belgium). 4-formylthiophenol (4-FTP) was purchased from Biogene Organics (The Woodlands, TX).

Wire Growth and Characterization. Au substrates were prepared by conventional thermal evaporation. For thermal evaporation, 50 Å of Cr was first evaporated on bare Si wafer or mica as an adhesion layer followed by 700 Å of Au in a home-built evaporator at a rate of approximately 1-2 Å/s and base pressure $\leq 2 \times 10^{-6}$ Torr.

The Au substrates were then immersed into 1 mM 4-ATP (absolute ethanol) or 4-FTP (acetonitrile). After 24 h, the SAM-coated Au substrates were removed from the thiophenol solution and rinsed thoroughly with absolute ethanol to remove physisorbed molecules before immersing them into a 20 mM solution containing the next dialdehyde or diamine derivative depending on the wire design. Thus, the lengths of the wires were precisely controlled by alternate addition of the amine and aldehyde derivatives. In order to optimize wire growth, aldehyde-terminated wires were reacted at 40 ± 2 °C with 1,4-benzenediamine for 24 h, and amine-terminated wires were reacted at room temperature (22 °C) with terephthalaldehyde for 24 h. OPI wires were kept in absolute ethanol before any surface characterization. Upon removal, the samples were rinsed again with absolute ethanol, and blown dry with N_2 or Ar. The ferrocene capping reaction was carried out in a glove box with < 0.1 ppm O_2 because aminoferrocene decomposes in air. The aldehyde-terminated wires were reacted with 2 mM aminoferrocene in absolute ethanol for a period of 24 h at 40 ± 2 °C. The samples were then rinsed, dried and transferred to a clean centrifuge tube that contained absolute ethanol before taking them out of the glove box for further rinsing (ethanol) and characterization.

Reflection-absorption infrared spectra (RAIRS) were collected with a Nicolet iS50 spectrometer with a Harrick Seagull accessory for grazing angle specular reflectance measurements. The incident angle for the p-polarized IR beam was 84° from the surface normal. For each sample and background, an average of 300 scans at a resolution of 2 cm^{-1} were collected after 15 min of purging with dry air.

Ellipsometry measurements were accomplished on a variable angle spectroscopic ellipsometer (J.A. Woolam Co., Inc). The change in polarization angles (ψ and Δ) were measured as a function of wavelength (λ) over 600-1000 nm at incident angles of 55°, 65° and 75°. To obtain accurate measurements, the background for each sample was measured before any wire growth to fit for Cr and Au thickness. Measurements for the polarization angles were performed again after completion of wire growth at the same position and incident angles as the background. The new ψ and Δ values along with the measured background thickness were used to fit for thickness of the monolayers for fixed values of the indices of refraction (n=1.45) and absorption coefficient (k=0). From prior UV-visible spectroscopy work, the absorption coefficient for OPI wires was estimated to be approximately zero over the wavelength range of 600-1000 nm.[24]

XPS spectra were collected by an SSX-100-XPS system (Surface Science), which is equipped with a monochromatic Al K_α X-ray source (1486.3 eV), at a base pressure of $\leq 10^{-9}$ Torr. The Al X-ray anode was operated at 200 W, the illuminated spot size on the sample was 0.64 mm^2, and a hemi-spherical analyzer (at a 35° take-off angle with respect to the sample normal) with constant pass energy was used to guide the photo-emitted electrons towards the detector. The pass energy for survey scans was 150 eV, and 50 eV for high resolution scans. For each high resolution scan, the binding energy was referenced to Au $4f_{7/2}$ (84.0 eV). The areas under the peaks of interest were fit using the Shirley background subtraction method, which removes the contribution of inelastically scattered electrons from the main peak.[25]

Cyclic voltammetry (CV) measurements were undertaken to measure the surface coverage of redox-capped wires. A three-necked cylindrical electrochemical cell with a hole in the bottom was employed. An O-ring was placed between the bottom of the cell (0.9 cm in diameter), and the monolayer coated Au substrate, which acted as the working electrode. The cell was then filled with 0.1 M $[Bu_4N^+][PF_6^-]$ (tetrabutylammonium hexafluorophosphate) in extra dry acetonitrile (< 10 ppm H_2O). A Pt wire was employed as the counter electrode, and Ag wire as the quasi-reference electrode. The cell was purged with either N_2 or Ar gas prior to and during electrochemical measurements. For each monolayer, the scans were recorded at sweep rates of 100 – 500 mV/s, and the voltammograms were reproducible and stable to electrochemical cycling up to 1.2 V vs Ag wire.

A MAS 1700 pelletron tandem ion accelerator (5SDH) equipped with a charge exchange RF plasma source (National Electrostatics Corporation, NEC: Middleton, WI) was used to generate a 4.266 MeV ${}^4_2He^{2+}$ beam with a current of 30-40 nA measured at the sample. ${}^4_2He^{2+}$ ions backscattered by nuclear collisions were counted by an Ortec silicon ion detector that was positioned at a scattering angle of 165° with respect to the incident beam and subtending a solid angle of 3.6 msr. Spectra consisting of counts versus backscattered ion energy were acquired with a multichannel analyzer controlled by NEC RC43 software. The projected beam cross section was approximately 2 × 2 mm (square). Visibly luminescent control samples of the same thickness were employed to precisely locate the beam position per sample goniometer coordinates. More precise quantitative comparisons between spectra (vertical scale) were achieved by normalizing to the signal intensity of the substrate. This treatment accounted for small variations in the accuracy of beam current integration (i.e., error in determination of the total number of incident ions, Q). Furthermore, the corrected spectra were simulated with SIMNRA software (Max Planck Institute for plasma physics) to check the accuracy of Q.

7.4 Results and Discussion

Self-assembled monolayers (SAMs) of pentafluorothiophenol were prepared by immersing freshly prepared Au wafers into a 1mM pentafluorothiophenol solution in DMSO for 24h. For the purpose of consistency, we will label these SAMs as OP-1F5. Oligophenyleneimine (OPI) wires were prepared on Au surfaces by imine condensation click chemistry with alternate addition of terephthalaldehyde and 1,4-benzenediamine as outlined in chapter 4. In the notation OPI-X-Y, X represents the number of phenylene rings, and Y represents either a halogen or ferrocene capping unit (if present). OPI wires were synthesized from SAMs of 4-ATP and 4-FTP. A representative wire growth for OPI-8F5 is shown in Figure 7.1. Wires capped with amine units appear at odd positions (OPI-3, OPI-5, OPI-7, and OPI-9) for wires grown from 4-ATP (Figure 7.1), and even positions (OPI-2, OPI-4, OPI-6, OPI-8, and OPI-10) for wires grown from 4-FTP (not shown). The alternate appearance and disappearance of carbonyl stretch peaks[26] (1705 cm^{-1}) suggests an extent of reaction near completion for each step. The intensity of the imine stretch[26,27] (C=N, 1625 cm^{-1}) and benzene ring stretch mode[26] (C=C, 1500 cm^{-1}) increased with the number of repeat units, as expected.

Amine terminated OPI wires were capped with pentafluorobenzaldehyde at the desired length as shown in Figure 7.2a. The XPS F 1s counts from the pentafluorophenyl termini were monitored for wires ranging from OP-1-F5 to OPI-7F5 (F5 stands for the 5 F atoms on the pentafluoro unit). Contrary to Cl, Br, and I terminated wires discussed in chapter 4, the F 1s peak counts decreased as a function of wire length. This was a completely unexpected result. Figure 7.2b shows that the peak area drops sharply for short wires, than the long wires. That is, the slope of F 1s peak area vs wire length was

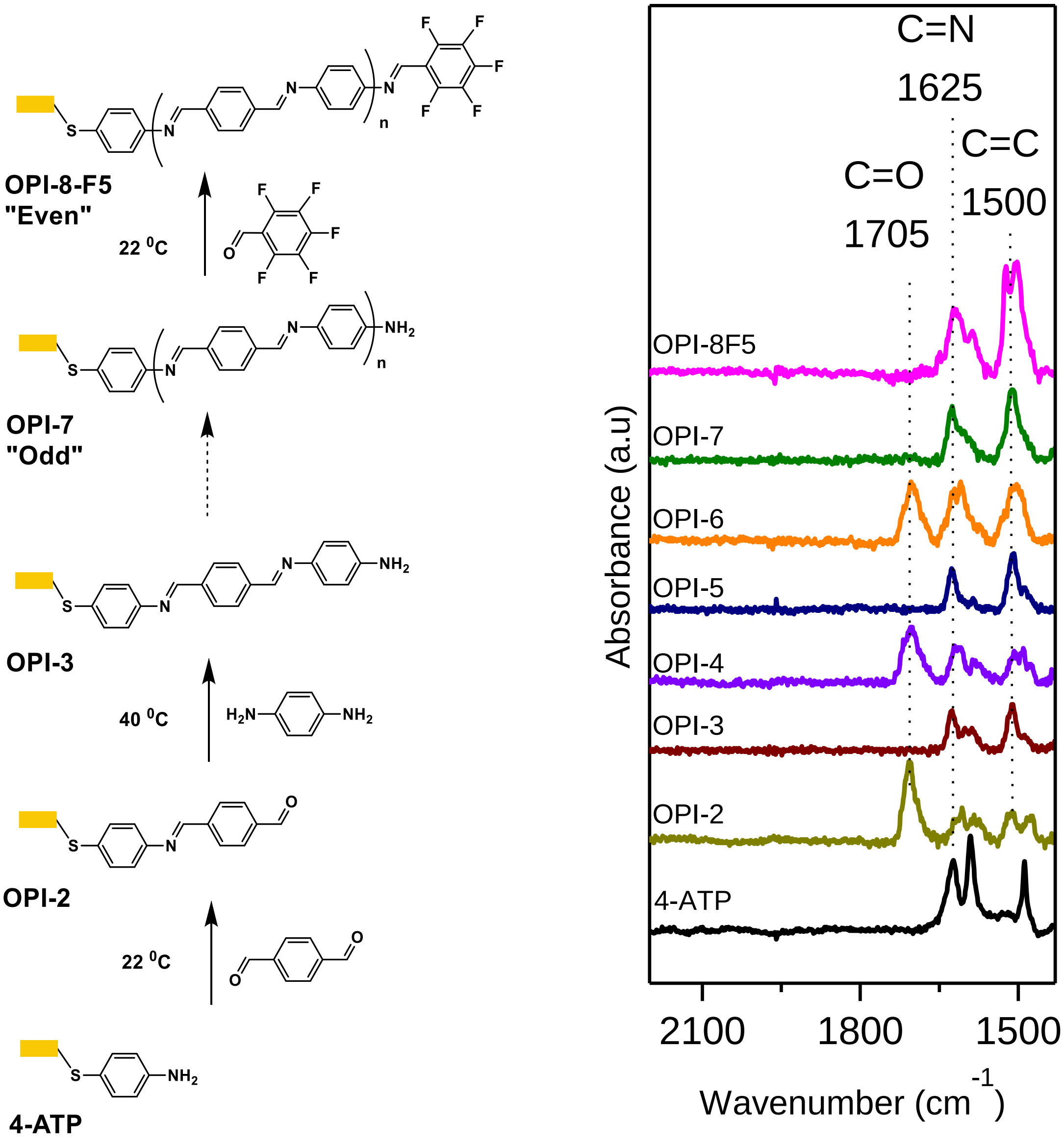

Figure 7.1 (A) Molecular structure and step-wise growth of OPI-8 F5 wire starting from 4-ATP and corresponding RAIRS spectra (right) showing the alternate appearance and disappearance of aldehyde peaks. The aldehyde peaks appear for even numbers of phenyl rings except for perfluoro capped wire (OPI-8F5).

greater for wires ranging from 0.6 – 3 nm than for long wires ranging from 3-5 nm in length. At a first glance, the peak area reflects the electron transport from the Au to the perfluoro unit (similar to the charge transport characteristics discussed in chapter 6). To rule out any contribution from coverage or extent of reaction from the growth steps prior to capping with perfluoro termini, NRA experiments were performed on OPI-2F5, OPI-4F5 and OPI-6F5, and the results were compared to OPI-2, OPI-4, and OPI-6. Figure 7.3b displays the obtained NRA C atom spectra of OPI-F5 wires grown on Au/Cr/mica substrate. The C atom peak counts increased with an increase in the total number of C atoms in the wires, as expected. The surface coverage was calculated according to equation 7.1:

$$N_s = A \cos\theta \, / \, \left(\frac{d\sigma}{d\Omega}\right) \Omega \, Q \tag{7.1}$$

where, A is the total number of ions detected, θ is the tilt angle of the sample relative to the ion beam (0°), dσ/dΩ is the nuclear scattering cross section per unit angle, and interpolated from a table by Feng, et al.,[28] ($5.195 \pm 0.103 \times 10^{-25}$ cm^2/sr for backscattering angle of 165° and 4.266 MeV beam energy), and Q is the total number of incident particles was 1.6×10^{14}. The C surface coverage values are displayed in Figure 7.3c along with OPI with similar number of C atoms. Since the coverage values for both OPI and OPI-F5 wires were almost identical, the NRA experiment confirmed that neither surface coverage nor extent of the wire was responsible for the observed trend in the F 1s peaks. Furthermore, if the extent of reaction was incomplete, it should have resulted in uniform slope for peak area vs wire length (i.e., the change in slope should not be observed).

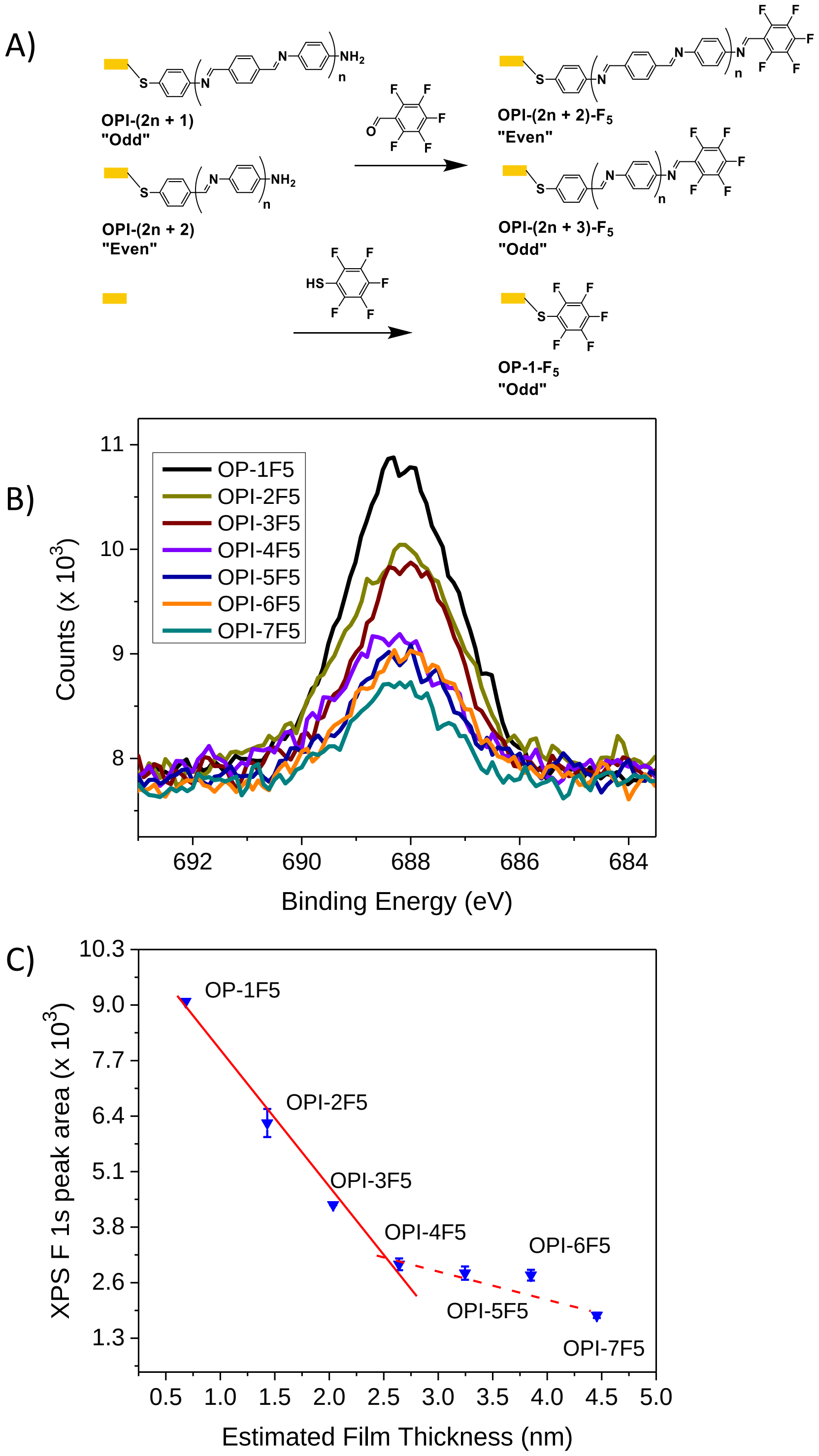

Figure 7.2 (A) Molecular structure for amine terminated wires (left) on Au before and after capping with pentafluoro benzaldehyde (right), and chemisorption of pentafluorothiophenol on bare Au (OP-1F5). (B) XPS spectrum of F1s for OP-F5, OPI-2F5 – OPI-7F5 wires on Au. (C) XPS F1s peak area verses estimated thickness of OPI-wires. The solid and broken red lines indicated two different slopes for short, and long wires respectively.

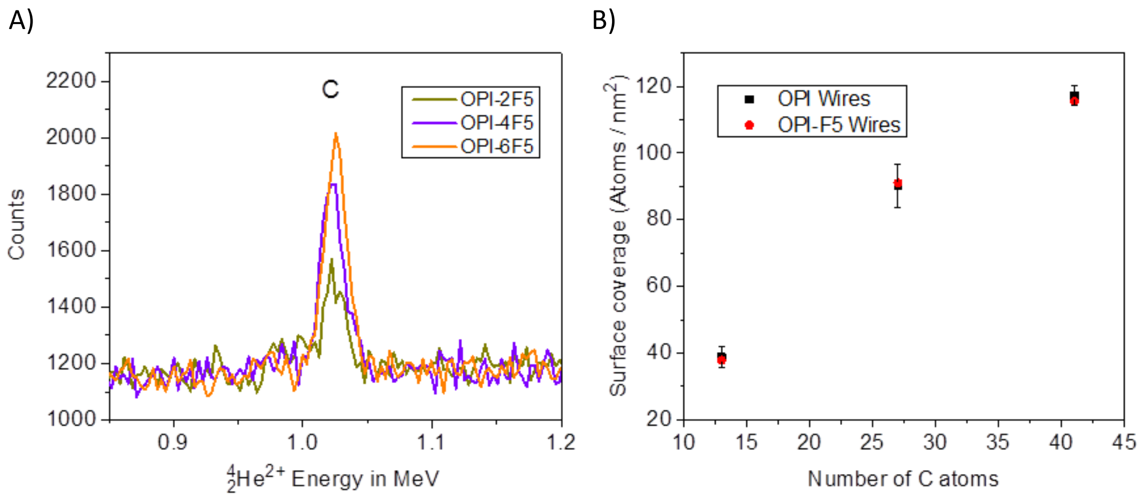

Figure 7.3 (A) Molecular structure of pentafluoro capped wires. (B) NRA C spectra of OPI-2F5, OPI-4F5, and OPI-6F5 wires on Au/Cr/mica substrates. Each step-wise addition resulted in an increase of the C peak intensity. The spectral heights were normalized to the substrate signal. (C) Surface coverage values for C atoms as a function of number of repeat units for OPI wires (black squares) and OPI-F5 wires (red circles).

A possible explanation for the observed transition in the slope could be related to the transport mechanisms that returns a photo-excited F atom back to the ground state before the next photoemission process. If an electron from F 1s atom is photo-emitted, the F 1s core state electron will not undergo a secondary photoemission before it acquires an extra electron and returns to the ground state. If secondary photoemission from F^+ atom was to take place, the binding energy of the 1s electron will be higher than F^0 atom due to electrostatic attraction between the F core nuclei and the 1s core electron, i.e. a chemical shift should be observed. The absence of any features of chemical shift in Figure 7.2b suggests that F atom must return to the ground state before consecutive photoemissions. Furthermore, conductive substrates such as Au have large amount of reservoir electrons that would prevent buildup of charges. For insulating substrates and powder samples, it is very common to apply charge neutralizer to compensate for buildup of positive charges on the surface (we did not use any neutralizer).

To further rule out any charging effect and chemical shift on Au, we synthesized wires on native SiO_2/Si substrate and monitored the F 1s peak intensity. Here, the growth procedure began by adsorption of a monolayer of (3-Aminopropyl)trimethoxysilane from 10^{-4} M solution of (3-Aminopropyl)trimethoxysilane in toluene for a period of 24 h under an inert atmosphere. The amino terminated monolayers on SiO_2/Si are now used as platforms to grow wires in the usual manner as shown in Figure 7.4a. The XPS spectra of F 1s are displayed in Figure 7.5b for OPI-1F5 to OPI-9F5 wires. As expected, there are

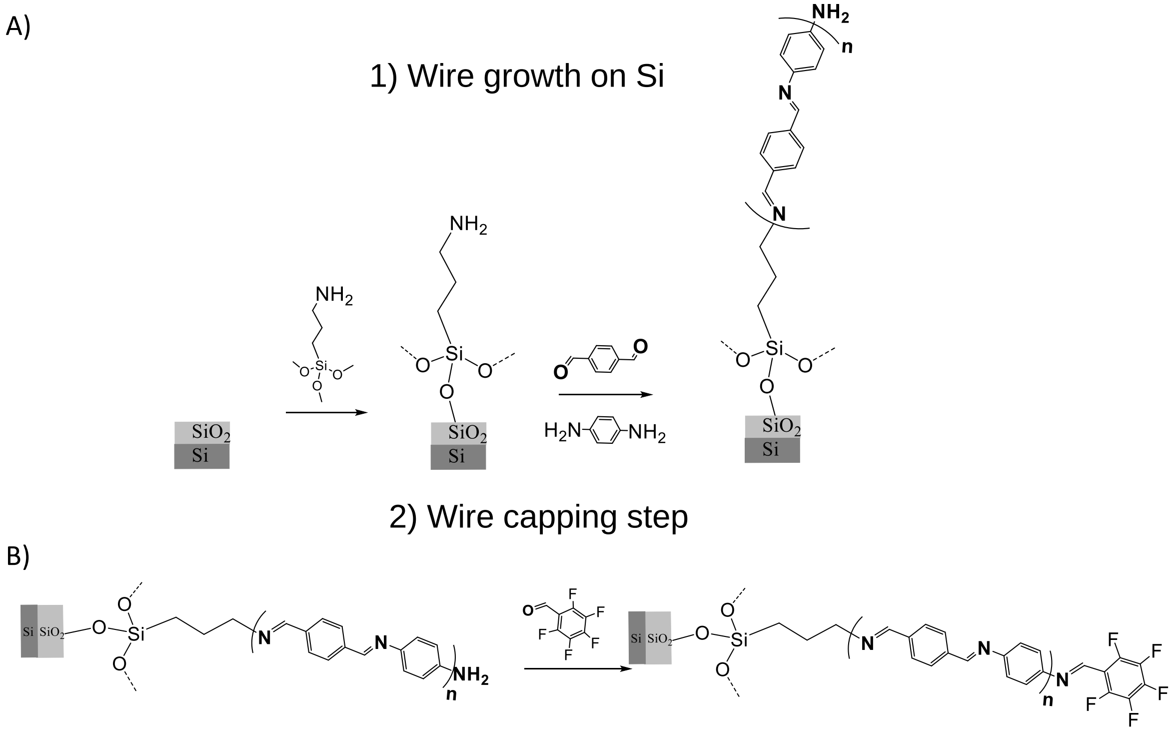

Figure 7.4 (A) Self-assembly of (3-Aminopropyl)trimethoxysilane on bare SiO_2 (native oxide) followed by Schiff base growth of OPI wires starting from free standing amines from the SAMs. (B) Molecular structure for amine terminated wires (left) on SiO_2 before and after capping with pentafluoro benzaldehyde (right).

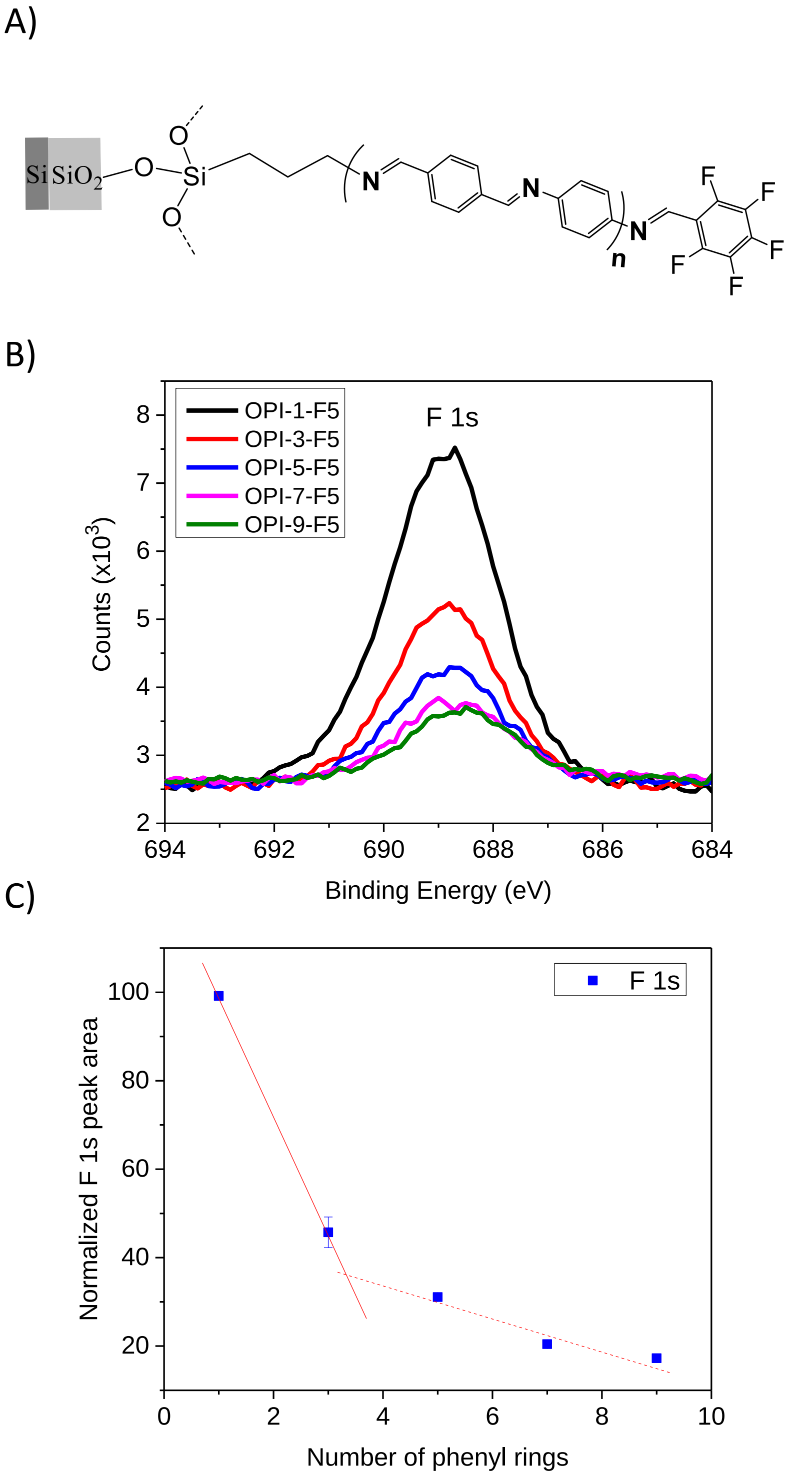

Figure 7.5 (A) Molecular structure of perfluorinated wires on native SiO_2/Si (B) XPS spectra of F1s for OPI-1F5, OPI-3F5, OPI-5F5, OPI-7F5, and OPI-9F5 on SiO_2/Si. (C) XPS F1s peak area verses estimated thickness of OPI-wires. The solid and broken red lines indicated two different slopes for short and long wires, respectively.

no shoulders or broadening of the F 1s peaks which otherwise would indicate buildup of charges. Furthermore, Figure 7.5c shows two distinct cross over for the slope of the F 1s peak area verses total number of phenyl rings, similar to OPI wires on Au. Figure 7.6b displays the XPS spectra of N 1s peaks of OPI wires on SiO_2/Si substrate. Here, two different chemical states are observed; one for neutral N and another for positively charged N. SAMs of (3-Aminopropyl)trimethoxysilane are known to form multilayers due to hydrogen bonding and polymerization between the NH_2 and Si-OH groups during self-assembly.[29] The peak at 400 eV is assigned to free or neutral N 1s, while the peak at 402 eV is assigned to N^+ 1s from multilayers. The imine N 1s (400 eV) peak counts increased with an increase in total number of click reactions. Figure 7.6c displays the normalized peak area of N 1s as function of the number of phenyl rings (stepwise reactions). The linear increase in the intensity of imine N 1s verses repeat units demonstrates that wire growth from free standing amine proceeded to completion as outlined in Chapter 4. In addition, the increase in N1s peak intensity reveals that coverage cannot explain the observed crossover for F 1s peaks.

Therefore, central questions here are: what are the processes that return a photo excited atom back to the ground state? How does it depend on temperature? What is the impact of conjugation breaking unit? The answers to the above question clearly depend on detailed study of charge transport as discussed in Chapter 6. However, charge transport experiments in molecular junctions experiments where electrons or holes either tunnel or hop along the molecular backbone under bias (electric field) are fundamentally different than the transport of charges that return photoemitted (excited) atom to ground state. Here, there is no applied bias, and the total number of atoms that undergo

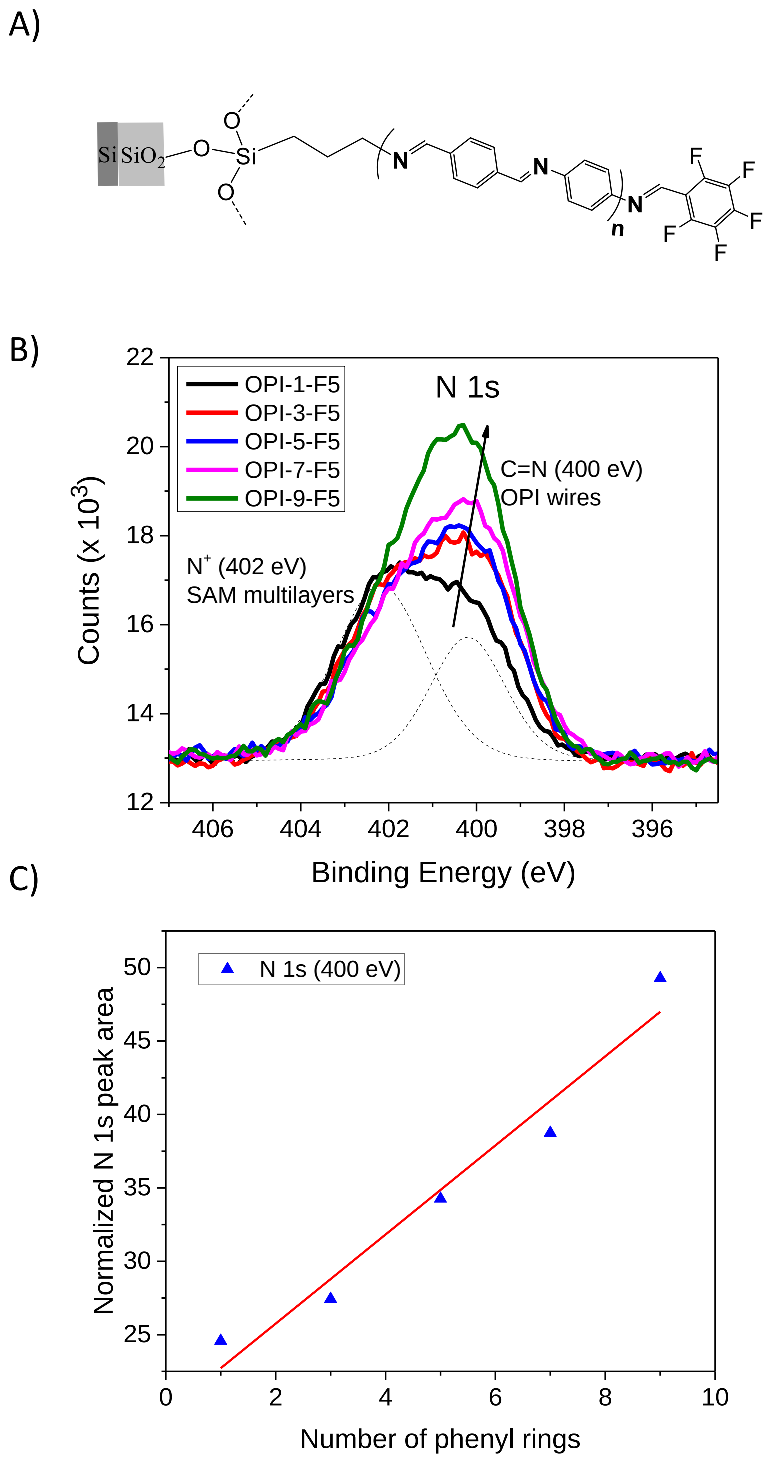

Figure 7.6 (A) Molecular structure of perfluorinated wires on native SiO_2/Si (B) XPS spectrum of N1s for OPI-1F5, OPI-3F5, OPI-5F5, OPI-7F5, and OPI-9F5 wires on SiO_2/Si. (C) XPS N1s peak area verses number of phenyl rings. The linear increase in N 1s (400 eV) is a good indication that the reaction proceeds in a quantitative manner as outlined.

photoemission simultaneously with in the x-ray beam spot size is unknown. Thus, the dynamic processes involved in the transport of charges in XPS cannot solely be explained in terms of the transport of charges through the frontier orbitals in molecular junctions.

We hypothesize that a combination of X-ray or auger emission processes coupled with transport of charges from the Au electrode through the molecular bridges are responsible for the core-state relaxation, as shown in Figure 7.7. The first step involves the photoelectron emission, where the x-ray knocks out the F 1s core state electron. The second step involves transfer of an electron from higher energy states (2p) to the core F 1s either by emission of X-rays or auger process. The last step (step 3) is transport of carriers through the wires to replenish HOMO electrons that participated in step 2. We speculate that tunneling and hopping transport mechanisms could be responsible for charge transport in step 3. This is supported by Figure 7.2c, which display the peak area of F 1s counts verses estimated film thickness, and clearly shows two different slopes similar to the direct current (DC) and alternating current (AC) measurements by conducting probe atomic force microscopy (CP-AFM) and eutectic gallium indium mixture (EGaIn) molecular junction testbeds, respectively in Chapter 6. In addition, variable temperature charge transport measurements are important to differentiate between tunneling and hopping transport. Therefore, we performed variable temperature XPS measurements on OPI-2F5 (short), OPI-5F5 (intermediate), and OPI-7F5 (long) wires. The results are shown in Figure 7.8, and clearly indicate the F 1s peak area did not change as a function of temperature ranging from 18°C - 83°C, regardless of wire length. Thus, we believe that tunneling is the dominant transport mechanism in which charges travel from the Au fermi level to the HOMO orbital in step 3.

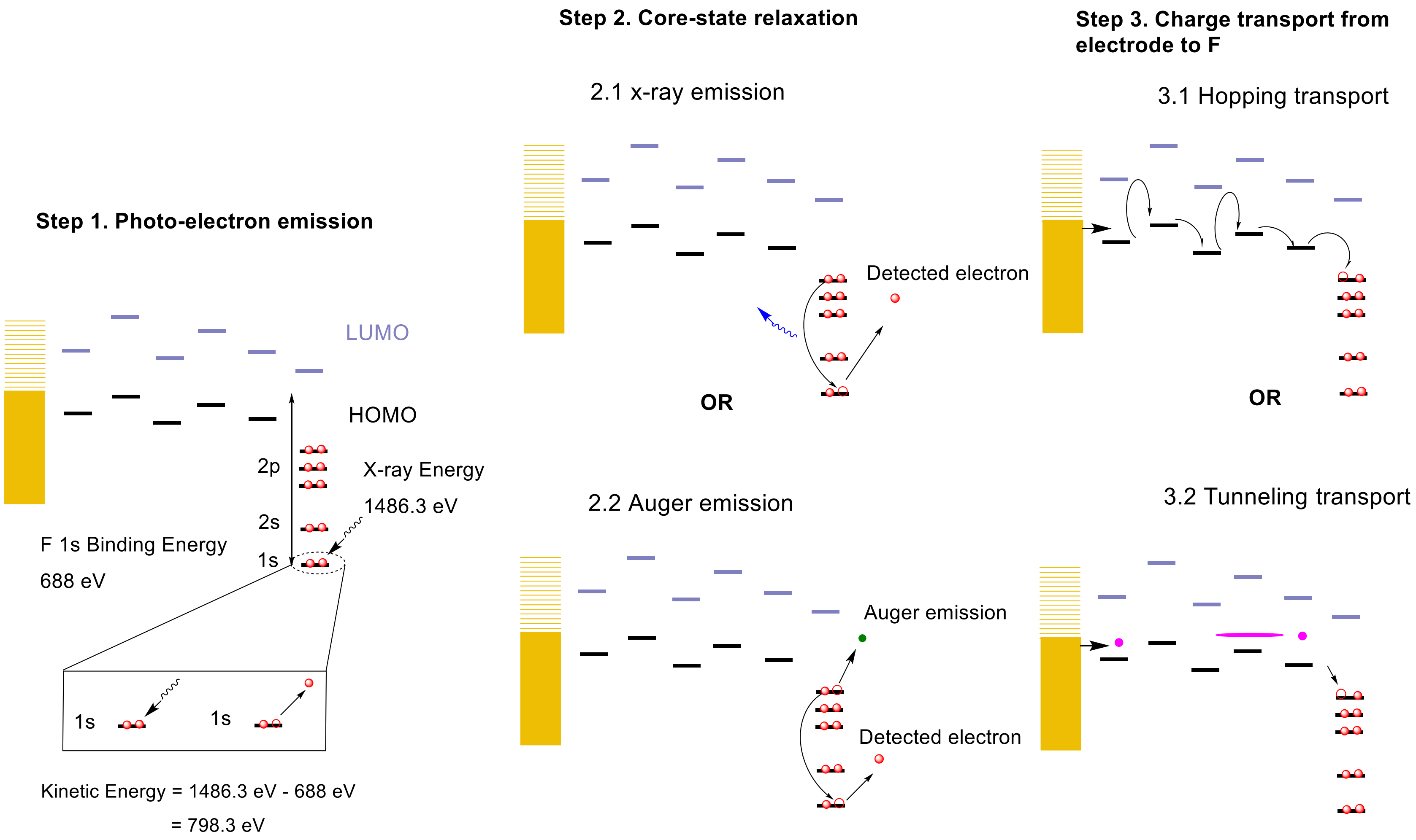

Figure 7.7 Suggested core-state relaxation mechanisms. Step 1 – Photoemission of F 1s by x-ray photon. Step 2 – Core state relaxation by either x-ray emission or auger emission of valence electrons to core state. Step 3 – Charge transport from Au electrode to F 1s valence level either by tunneling or hopping.

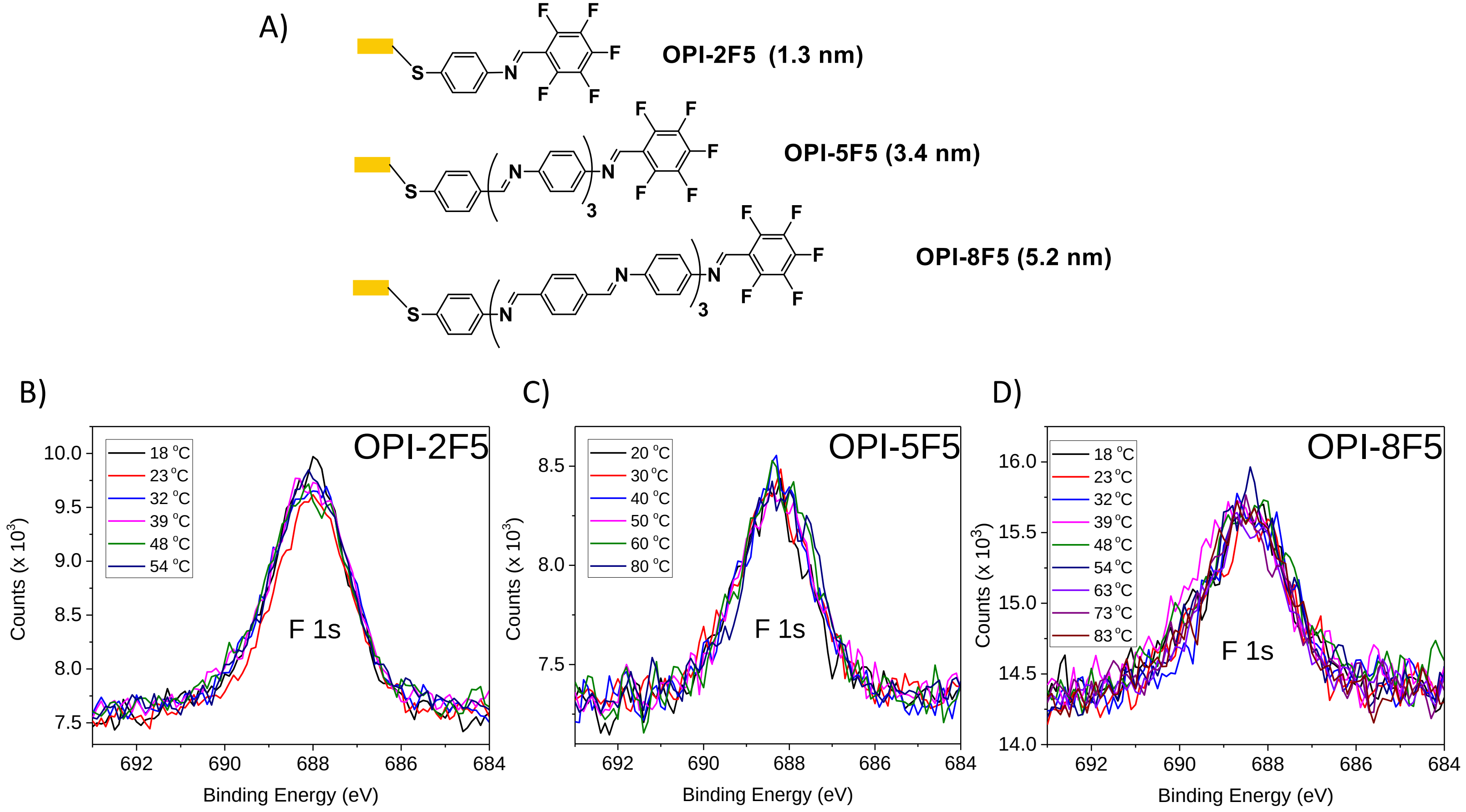

Figure 7.8 A) Molecular structure and estimated thickness of OPI-2F5, OPI-5F5, and OPI-8F5. Variable temperature XPS spectra for OPI-2F5 (B), OPI-5F5 (C), and OPI-8F5 (D).

Long range tunneling is not an uncommon phenomenon. C.A. Nijhuis and co-workers recently reported transition from coherent tunneling to sequential tunneling across ferretin based junctions via temperature and iron loading experiments.[30] They observed transition from coherent to temperature independent sequential tunneling, and each regime had its own decay constant. Similarly, McCreery and co-workers reported two transitions for conjugated oligothiophene molecular wires, from coherent to sequential tunneling at ~ 8 nm, and from temperature independent sequential tunneling to thermally activated hopping at ~ 16 nm.[31]

If transport of charges through HOMO orbitals are responsible for the change in slope in Figures 7.2c and 7.5c, then disruption of the conjugation along the wire backbone should impact F 1s peak counts. The conjugation broken (CB) OPI wires were synthesized by reacting aldehyde termini of OPI wires with 1,4-diaminobutane instead of 1,4-phenylenediamine along each possible sites. For example, during the stepwise synthesis of OPI-8F5, it has reacted with 1,4-phenylenediamine at 3 different sites (3,5, and 7) as shown in Figure 7.1. Thus, there are a total of 7 (2^3-1) different combinations of placing the conjugation breaking unit along the wire back bone.

Conjugation broken OPI-5F5 wires. In the notation OPI-XF5-CB-Z, X represents the total number of repeat units (phenyl and alkyl chains) per molecule, whereas Z represents the position of conjugation breaking unit(s). OPI-5F5 CB wires were synthesized starting from monolayer of 4-FTP followed by consecutive stepwise reaction with 1,4-benzenediamine or 1,4-diaminobutane, and terephthalaldehyde. The amine termini on OPI-4 were then capped with perfluorobenzaldehyde. Once the 1,4-diaminobutane is incorporated along the wires, all other subsequent reactions were carried out at 42°C. Figure 7.9 shows the molecular structure of conjugation broken OPI-5F5 wires. There are a total of 3 different combinations for placing the conjugation breaking unit not including the fully conjugated wire shown in Figure 7.9a, two different possibilities for inserting a single block, and only one possibility for inserting 2 blocks. The XPS spectra of F 1 are displayed in Figure 7.9b. The peak area of F 1s decreased sharply with the insertion of the conjugation blocking unit (Figure 7.9c). Furthermore, the

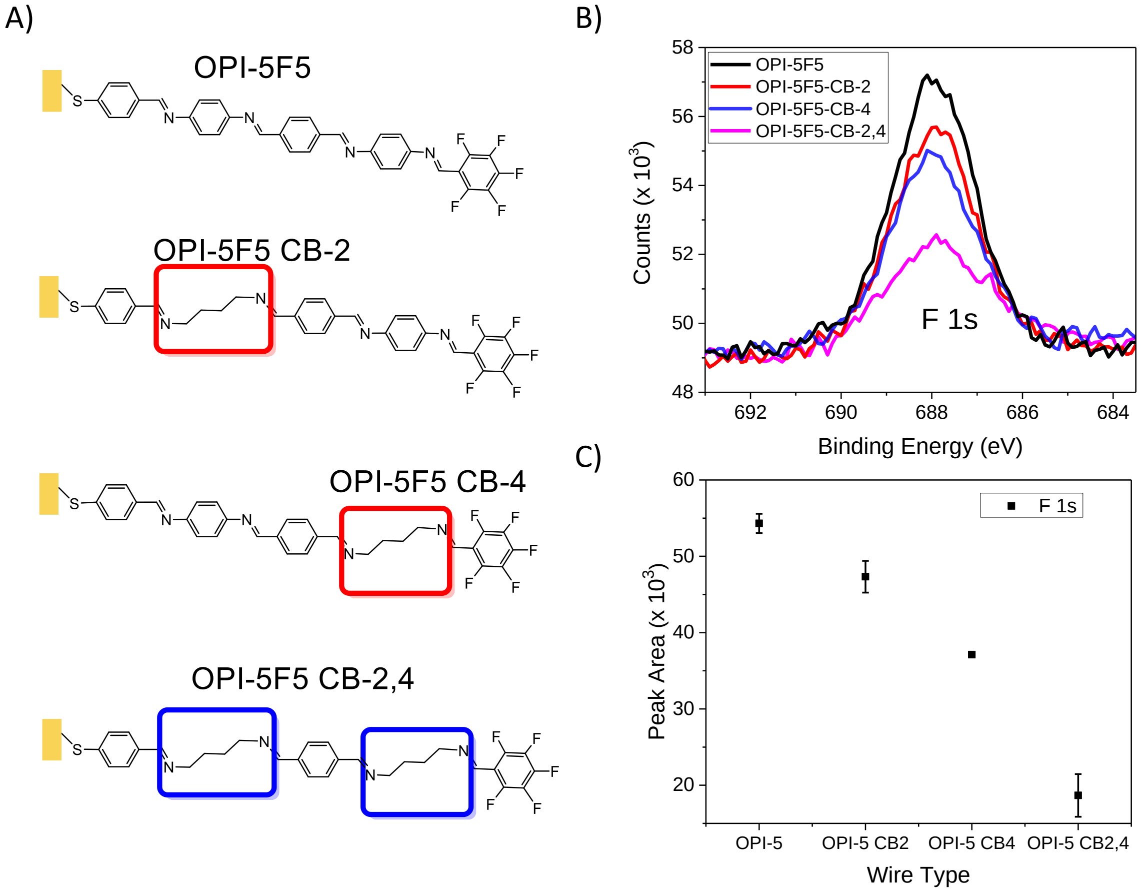

Figure 7.9 A) Molecular structures of OPI-5F5 and conjugation broken OPI-5F5 wires. The conjugation breaking is inserted in the 2^{nd} position for OPI-5F5-CB-2 wire, 4^{th} position for OPI-5F5-CB-4, and both 2^{nd} and 4^{th} positions for OPI-5F5-CB-2,4. B) XPS spectra of OPI-5F5 and CB-OPI-5F5 wires. C) XPS F 1s peak areas of OPI-5F5 and OPI-5F5 CB wires.

decrease in peak area depends on the position of the blocking group. That is, when the blocking unit was placed further from the perfluoro termini (OPI-5-F5-CB-2), the F 1s peak area was higher than OPI-5F5-CB-4, which had the blocking unit right before the perfluoro termini. As expected, the F 1s counts were significantly lower for OPI-5-F5-CB-2,4 wires since the conjugation was disrupted at both 2nd and 4th positions.

Conjugation broken OPI-6F5 wires. OPI-6F5 CB wires were synthesized starting from monolayer of 4-ATP followed by consecutive stepwise reaction with terephthalaldehyde, 1,4-benzenediamine or 1,4-diaminobutane. The amine termini on OPI-5 were then capped with perfluorobenzaldehyde. Once the 1,4-diaminobutane is incorporated along the wires, all other subsequent reactions were carried out at 42°C. Figure 7.10 shows the molecular structure of conjugation broken OPI-6F5 wires. There are a total of 3 different combinations for placing the conjugation breaking unit not including the fully conjugated wire shown in Figure 7.10a, two different possibilities for inserting a single block (Figure 7.10b and 7.10c), and only one possibility for inserting 2 blocks (Figure 7.10d). The XPS spectra of F 1s and C 1s are displayed in Figure 7.11a and 7.11b, respectively. The peak area of F 1s decreased sharply with the insertion of the conjugation blocking unit (Figure 7.11c). Furthermore, the decrease in peak area depends on the position of the blocking group. That is, when the blocking unit was placed away from the perfluoro termini (OPI-6-F5-CB-3), the total number of photo emitted F 1s counts was higher than OPI-6F5-CB-5, which had the blocking unit right before the perfluoro termini. As expected, the F 1s counts were much smaller for OPI-6-F5-CB-3,5 since the conjugation was disrupted at the 3rd and 5th positions. The relative constant intensity of C 1s peak area in Figure 7.11b suggests that the surface coverage is almost identical. Since the C 1s emitted from C atoms close to the Au surface are exponentially attenuated (Beer's law), they cannot be used to measured absolute coverages. Instead, only qualitative information is obtained from the C 1s XPS spectra. To further investigate the impact of 3 conjugation breaking units, we synthesized OPI-8F5 CB wire.

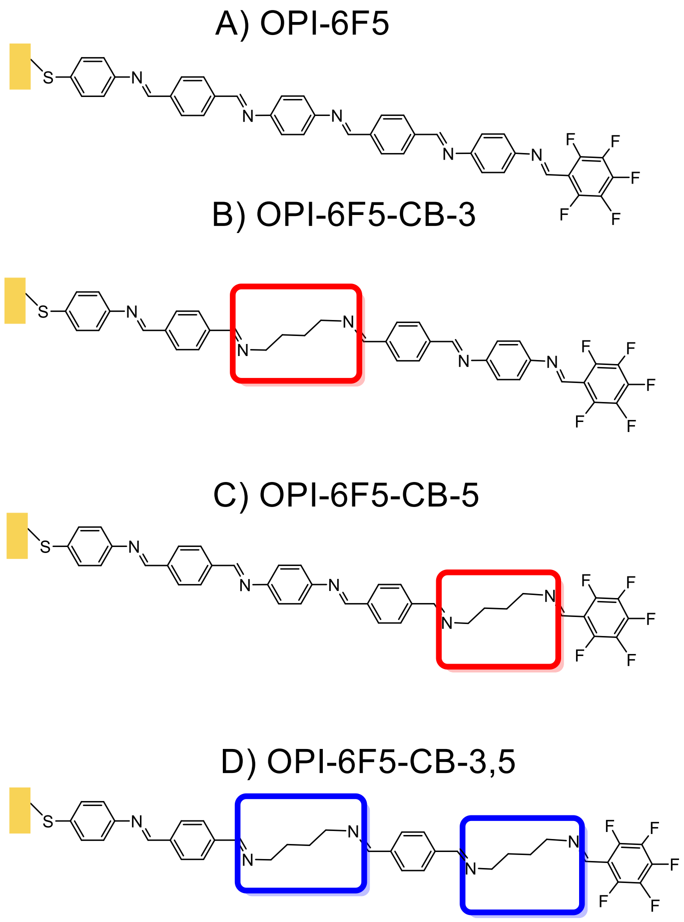
A) OPI-6F5

B) OPI-6F5-CB-3

C) OPI-6F5-CB-5

D) OPI-6F5-CB-3,5

Figure 7.10 Molecular structures of OPI-6F5 and conjugation broken OPI-6F5 wires. The conjugation breaking is inserted in the 3rd position for OPI-6F5-CB-3 wire (b), 5th position for OPI-6F5-CB-5 (c), and both 3rd and 5th position for OPI-6F5-CB-3,5 (d).

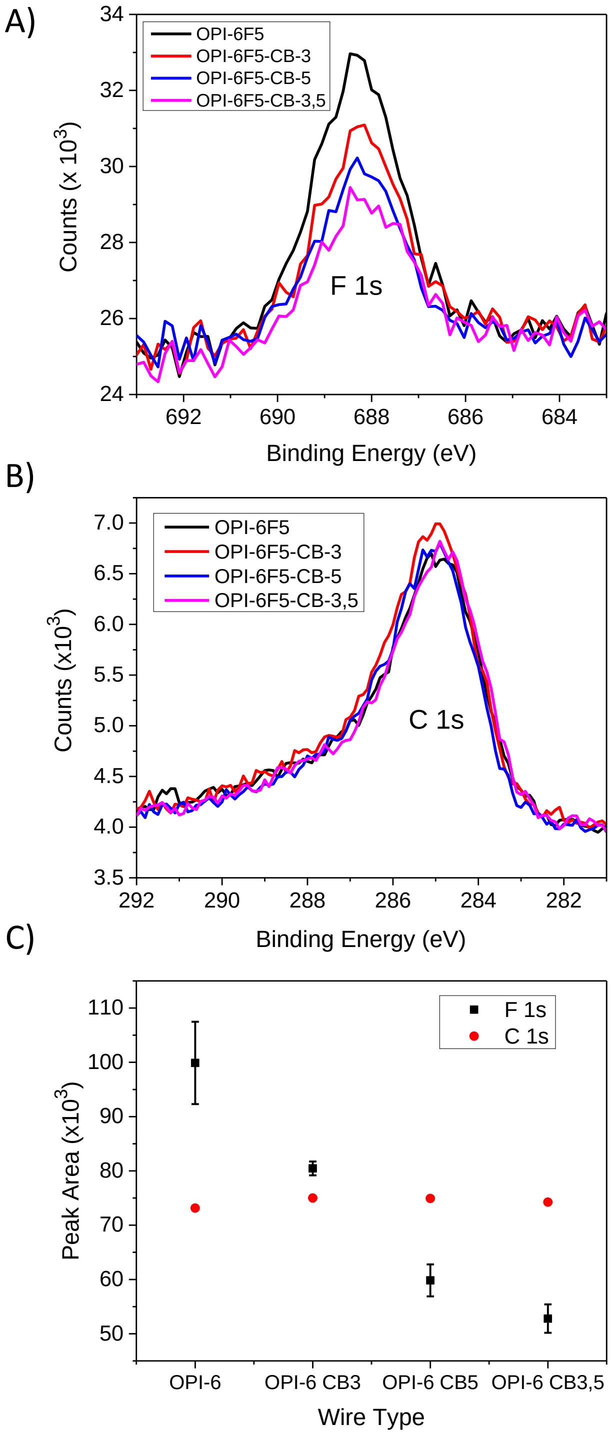

Figure 7.11 (A) XPS spectra of F1s for OPF6, OPI-6F5-CB-3, OPI-6F5-CB-5, and OPI-6F5-CB-3,5 wires, and corresponding XPS C 1s spectra on Au. (C) XPS F1s and C1s peak area for OPI-6 and OPI-6 CB wires. The peak areas decreased with an increase in the number of conjugation blocking units.

Conjugation broken OPI-8F5 wires. OPI-8F5 CB wires were synthesized starting from monolayer of 4-ATP followed by consecutive stepwise reaction with terephthalaldehyde, 1,4-benzenediamine or 1,4-diaminobutane, and capped with perfluorobenzaldehyde after 6 stepwise reactions. Figure 7.12 shows the molecular structure of conjugation broken OPI-6F5 wires. There are a total of 7 different combinations for placing the conjugation breaking unit not including the fully conjugated wire in Figure 7.12a, three different combinations for inserting a single block (Figures 7.12b-d), three different combinations for inserting double blocks (Figures 7.12e-g), and only one combination for inserting triple blocks (Figure 7.12h). The XPS spectra of F 1s are displayed in Figure 7.13. We obtained similar results to OPI-5F5 CB and OPI-6F5 CB wires. The peak area of F 1s decreased with an increase in the number of conjugation blocking units (Figure 7.13b). Furthermore, the decrease in peak area was more pronounced when the conjugation blocking units were placed right next to the perfluoro termini. Here, it is interesting to note that OPI-8F5-CB-3,5 wire with two blocks had higher F 1s count than OPI-8F5-CB-7 wire with a single block. Collectively, the CB OPI-5F5, CB OPI-6F5 and CB OPI-8F5 data sets reveal that the proposed mechanism in Figure 7.7 could be responsible for explaining the decreasing trend in peak area, assuming that coverage is similar.

The surface coverages of CB OPI-8F5 wires were determined by NRA and CV. As shown in Figure 7.14a, aldehyde-terminated OPI-X-CB-Z wires were reacted with aminoferrocene to yield OPI-X-Fc-CB-Z wires at 40°C. Figures 7.14b, 7.14c, and 7.14d display the CV spectra of OPI-4-Fc-CB-3, OPI-6-Fc-CB-3,5, and OPI-8-Fc-CB-3,5,7 wires, respectively. For each monolayer, CVs were recorded at sweep rates of 100, 200,

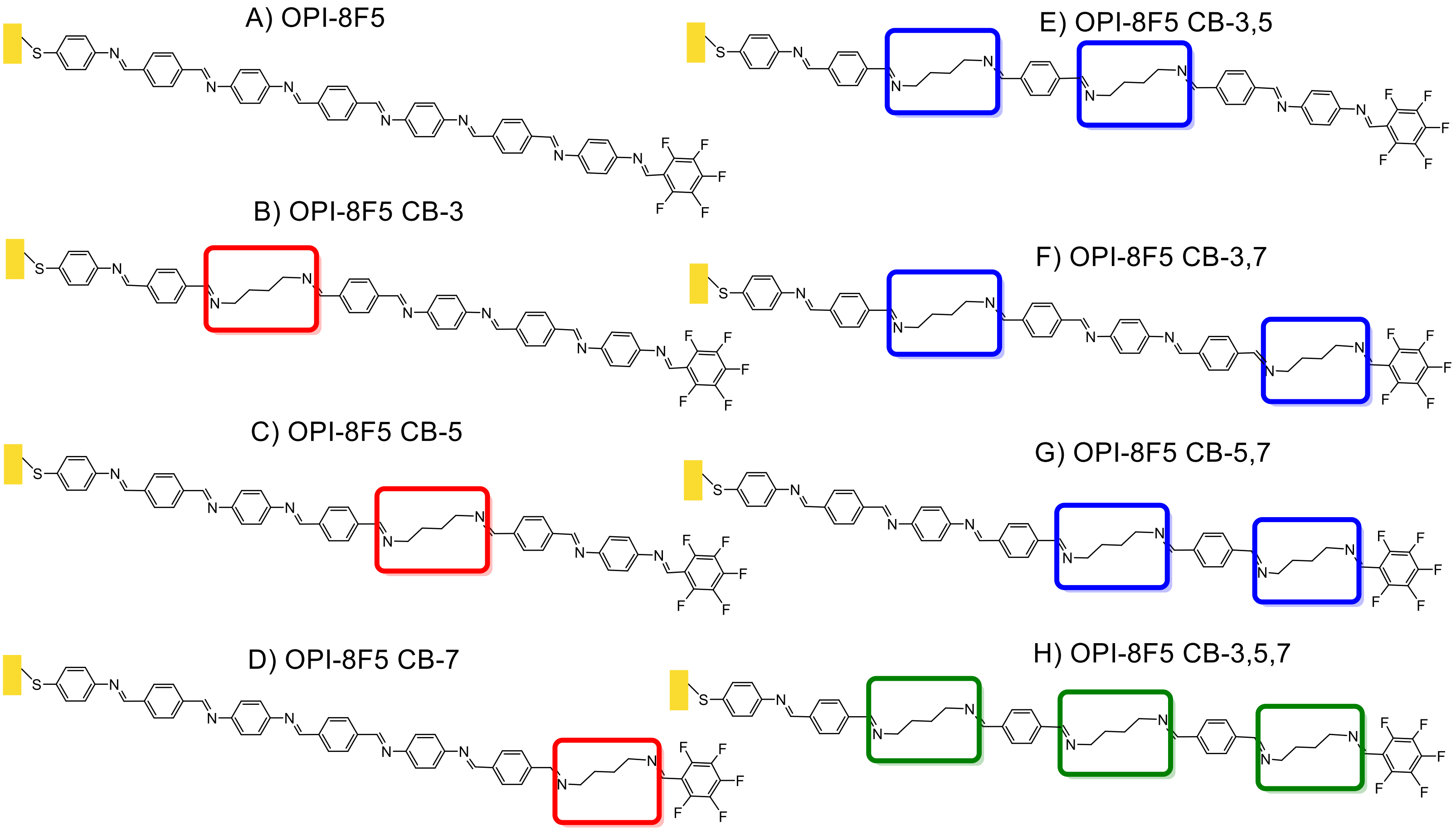

Figure 7.12 Molecular structures of OPI-8F5 and conjugation broken OPI-8F5 wires. The conjugation breaking unit is inserted in the 3rd position for OPI-8F5-CB-3 wire (b), 5th position for OPI-8F5-CB-5 (c), 7th position for OPI-8F5-CB-7 (d), 3rd and 5th position for OPI-8F5-CB-3,5 (e), 3rd and 7th position for OPI-8F5-CB-3,7 (f), 5th and 7th position for OPI-8F5-CB-5,7 (g), and 3rd, 5th, and 7th position for OPI-8F5-CB-3,5,7 (h).

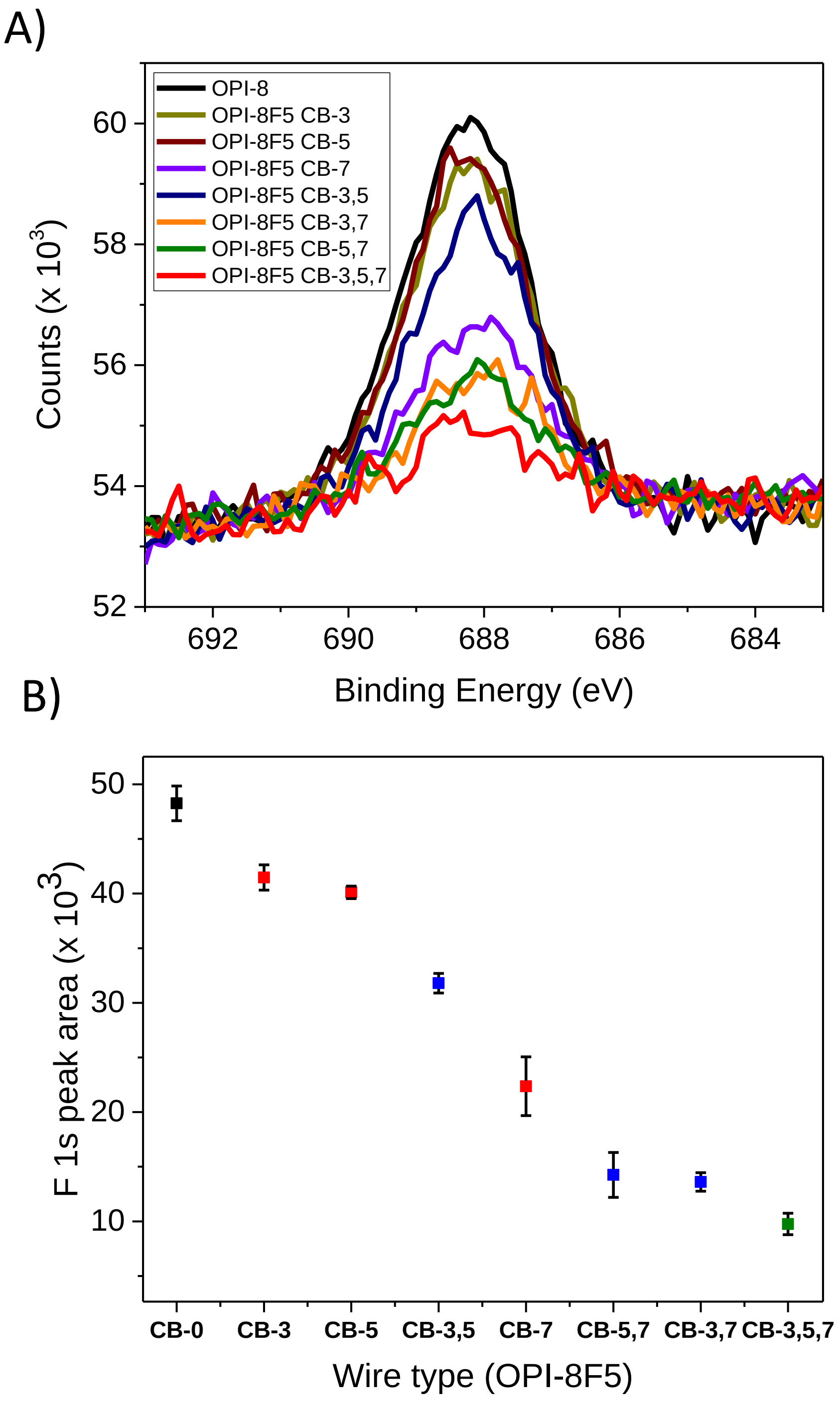

Figure 7.13 (A) XPS spectra of OPI-8F5 and OPI-8F5 CB wires. (B) XPS peak areas of (A) OPI-8F5 (black square), and OPI-8F5 CB wires with 1 blocking unit (red squares), 2 blocking units (blue squares), and 3 blocking units (green square). As the number of conjugation blocking units increase, the peak areas decreased.

300, 400, and 500 mV/s; and displayed reversible redox peaks characteristic of surface confined ferrocene. The surface coverage, N_s (molecules/cm^2), for Fc centers was calculated according to equation 7.2,

$$N_s = \frac{Q}{nFA} \tag{7.2}$$

where Q is the charge injected into the SAM, n is the number of electrons involved in the transfer process , F is the Faraday constant (96,487.0 C mol^{-1}), and A is the surface area of the monolayers examined (0.64 cm^2). The total charge injected (Q) was calculated by integrating the current versus time plot, and the total number of electrons (n) transferred during the redox step was taken to be 1. The surface coverage results are plotted in Figure 7.15b (black squares). On average, the surface coverages for ferrocene capped CB OPI wires were 1.5 ± 0.02, 1.7 ± 0.03, and 1.6 ± 0.03 molecules / nm^2 for OPI-4-Fc-CB-3, OPI-6-Fc-CB-3,5, and OPI-8-Fc-CB-3,5,7, respectively.

NRA of OPI-8F5 CB wires was utilized as second measure of coverage. Here, the C atom concentration was probed at 4.266 MeV ${}^{4}_{2}He^{2+}$ primary beam energy, which enhances the ${}^{4}_{2}He^{2+}$ scattering cross-section by exciting C nuclear resonance states. NRA was limited to mica substrates in our previous work and Figure 7.3, because they do not exhibit *channeling* whereas single crystal silicon substrates do. Channeling arises due to gentle, small-angle glancing collisions of ${}^{4}_{2}He^{2+}$ along rows or planes of crystal nuclei, which thereby steers the incident beam and reduces the back-scattered yield to variable degree. Here, we prevented channeling in single-crystal Si by tilting the surface normal of the sample by 3° (θ) and rotating it around the beam per variable azimuthal angle (φ) during spectral acquisition. Furthermore, the samples for NRA and XPS were cut from the same Au wafer after completion of wire growth.

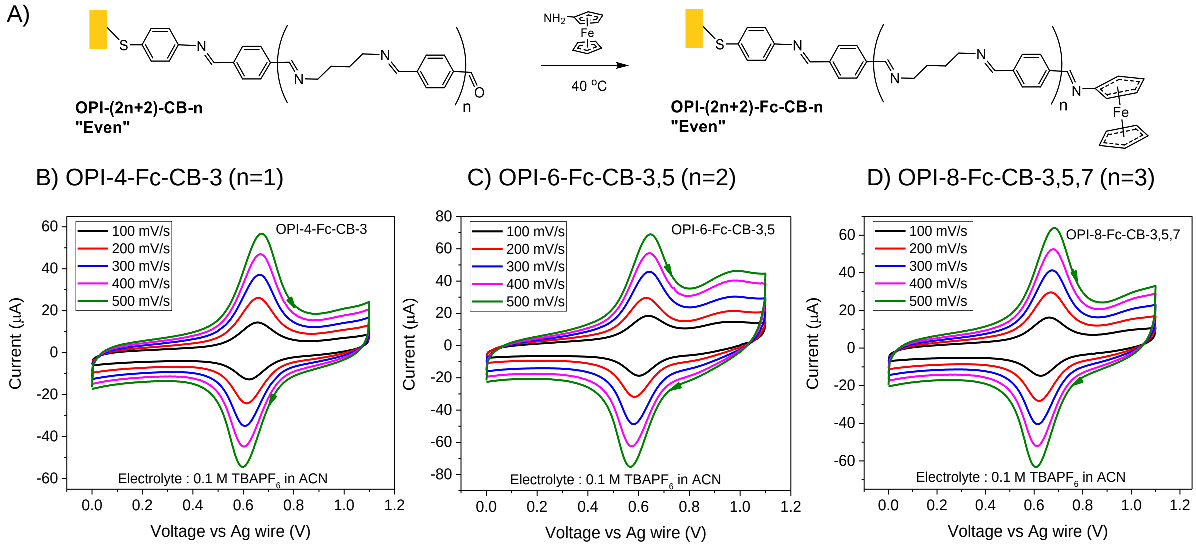

Figure 7.14 (A) Molecular structure for aldehyde terminated OPI CB wires (left) on Au before and after capping with aminoferrocene (right). Cyclic Voltammetry of OPI-4-Fc-CB-3 (B), OPI-6-Fc-CB-3,5 (C), and OPI-8-Fc-CB-3,5,7 (D) at different sweep rates. The electrolyte was 0.1 M [Bu$_4$N$^+$][PF$_6^-$] in acetonitrile. The reference and counter electrodes were Ag and Pt wires, respectively. The peak currents and sweep rates are linearly proportional, as expected, for surface confined species. Au geometrical area: 0.64 cm^2.

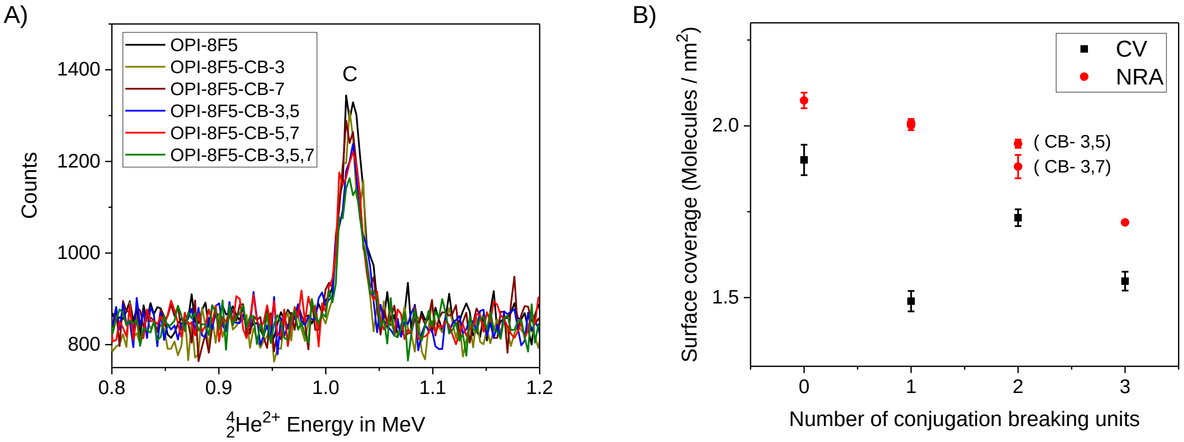

Figure 7.15 (A) NRA C spectra of OPI-8F5, OPI-8F5-CB-3, OPI-8F5-CB-7, OPI-8F5-CB-3,5, OPI-8F5-CB-5,7, and OPI-8F5-CB-3,5,7. The spectral heights were normalized to the Si signal. (B) Surface coverage values of C atoms from NRA spectra in A (red circles) and surface coverage values from CV (black squares, Figure 7.12).

Figure 7.15 displays the obtained C atom NRA spectra for OPI-8-F5, OPI-8-F5-CB-3, OPI-8-F5-CB-5, OPI-8-F5-CB-3,5, OPI-8-F5-CB-5,7, and OPI-8-F5-CB-3,5,7 wires. The surface coverages were calculated according to equation 7.1. We obtained coverage values of 2.02 ± 0.03, 2.0 ± 0.01, 2.01 ± 0.01, 1.95 ± 0.01, 1.88 ± 0.03, and 1.72 ± 0.02 molecules / nm^2, respectively. The coverage values are approximately 40% lower than typical coverages for OPI wires (3.5 molecules / nm^2). Future work will address this discrepancy from previously reported values. Collectively, the NRA and CV data suggest that surface coverage only changes by 15% across the different CB OPI-8F5 wires, and cannot account for the observed behavior.

Conjugation broken OPI-7F5 wires. OPI-7F5 CB wires were synthesized starting from monolayer of 4-FTP followed by consecutive stepwise reaction with 1,4-benzenediamine or 1,4-diaminobutane, and terephthalaldehyde. The amine termini were then capped with perfluorobenzaldehyde after 5 stepwise reactions. Figure 7.16 shows the molecular structure of conjugation broken OPI-7F5 wires. There are a total of 8 different combinations for placing the conjugation breaking unit (similar to OPI-8F5); one with no conjugation breaking units as shown in Figure 7.16a, three different possibilities for inserting a single block (Figures 7.16b-d), three different possibilities for inserting double blocks (Figures 7.16e-g), and only one possibility for inserting triple blocks (Figure 7.16h).

The XPS spectra of OPI-7F5 CB wires are displayed in Figure 7.17. As expected, the F 1s peak areas decreased with an increase in the number of conjugation disruption units. When the conjugation breaking units were placed next to the perfluoro termini, they had a pronounced decrease in F 1s peak area. It is worth noting that OPI-7F5 CB-7 wire has higher peak area than OPI-7F5-CB-2,4, OPI-7F5-CB-2,6, and OPI-7F5-4,6 wires (unlike OPI-8F5-CB-7 and OPI-8-F5-CB-3,5 wires discussed in the previous section). The surface coverage of CB OPI-7F5 and OPI-X-Fc CB wires were evaluated by NRA and CV, respectively. As shown in Figure 7.18a, aldehyde-terminated OPI-X-CB wires were reacted with aminoferrocene to yield OPI-X-Fc-CB wires. Figures 7.18b, 7.18c, and 7.18d show the CV spectra of OPI-3-Fc-CB-2, OPI-5-Fc-CB-2,4, and OPI-7-Fc-CB-2,4,6 wires. For each monolayer, CVs were recorded at sweep rates of 100, 200, 300, 400, and 500 mV/s; and displayed reversible redox peaks characteristic of surface confined ferrocene. The redox peak potentials did not change as function of conjugation disruption units, presumably due to an extremely fast charge transfer rates. The surface coverage, Ns (molecules/cm^2), for Fc centers was calculated according to equation 7.2. The surface coverage results are plotted in Figure 7.19b (black squares). On average, the surface coverages for ferrocene capped CB OPI wires were 1.35 ± 0.1, 1.04 ± 0.07, and 0.58 ± 0.05 molecules / nm^2 for OPI-3-Fc-CB-2, OPI-5-Fc-CB-2,4, and OPI-7-Fc-CB-2,4,6, respectively. Inspection of the redox peak current also reveals the decreasing trend in surface coverage of wires.

NRA of OPI-7F5 CB wires was utilized as second measure of coverage. Here, the C atom concentration was probed at 4.266 MeV ${}^{4}_{2}He^{2+}$ primary beam energy by tilting the surface normal of the sample by 3° (θ) and rotating it around the beam per variable azimuthal angle (φ) during spectral acquisition. Figure 7.19a displays the obtained C atom NRA spectra for OPI-7-F5, OPI-7-F5-CB-4, OPI-7-F5-CB-6, OPI-7-F5-CB-2,4, OPI-7-F5-CB-4,6, and OPI-7-F5-CB-2,4,6 wires. We obtained molecular coverage values of 3.41 ± 0.13, 2.42 ± 0.09, 2.76 ± 0.18, 2.32 ± 0.12, 2.94 ± 0.11, and 1.31 ± 0.18

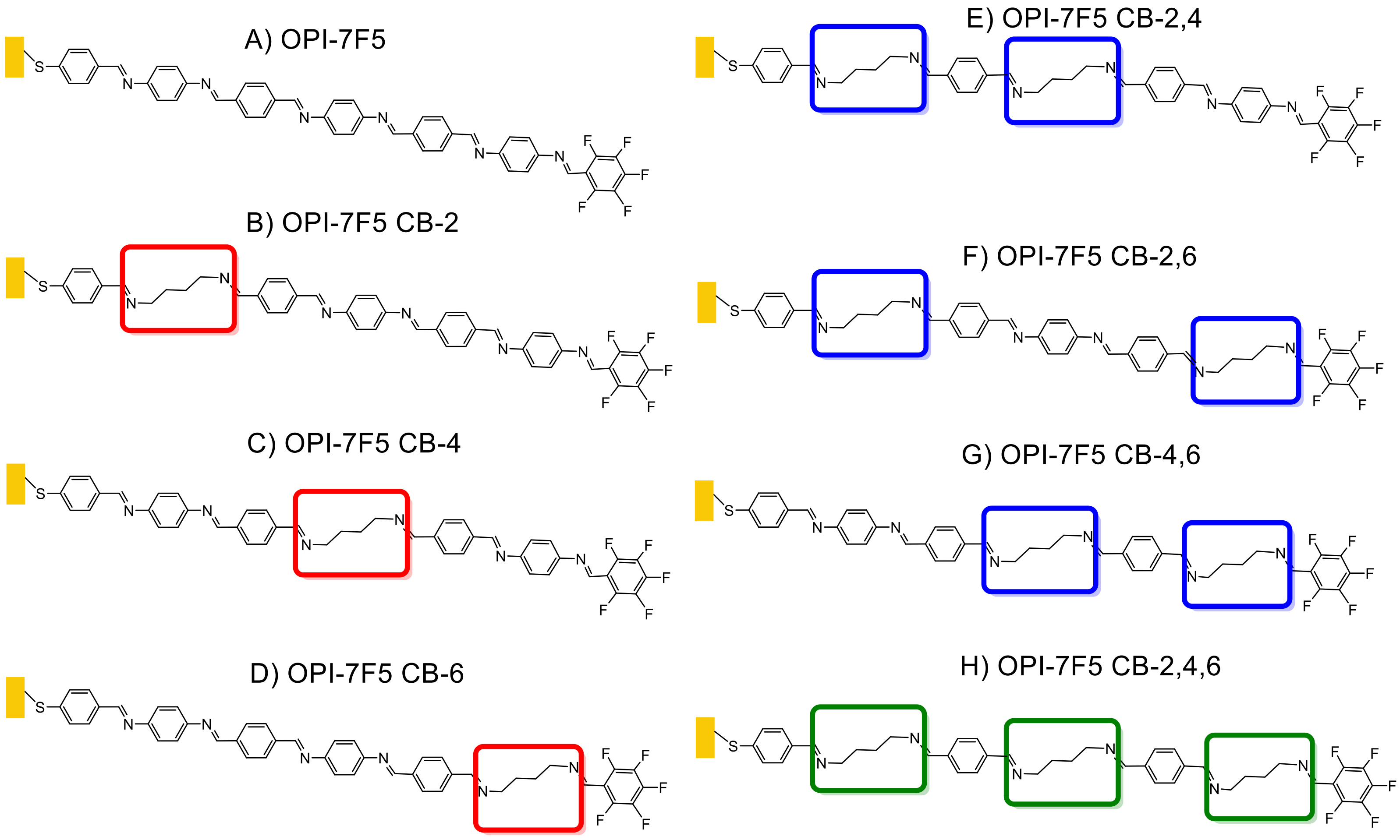

Figure 7.16 Molecular structures of OPI-7F5 and conjugation broken OPI-8F5 wires. The conjugation breaking is inserted in the 2nd position for OPI-7F5-CB-2 wire (b), 4th position for OPI-7F5-CB-4 (c), 6th position for OPI-7F5-CB-6 (d), 2nd and 4th position for OPI-7F5-CB-2,4 (e), 2nd and 6th position for OPI-7F5-CB-2,6 (f), 4th and 6th position for OPI-7F5-CB-4,6 (g), and 2nd, 4th, and 6th position for OPI-7F5-CB-2,4,6 (h).

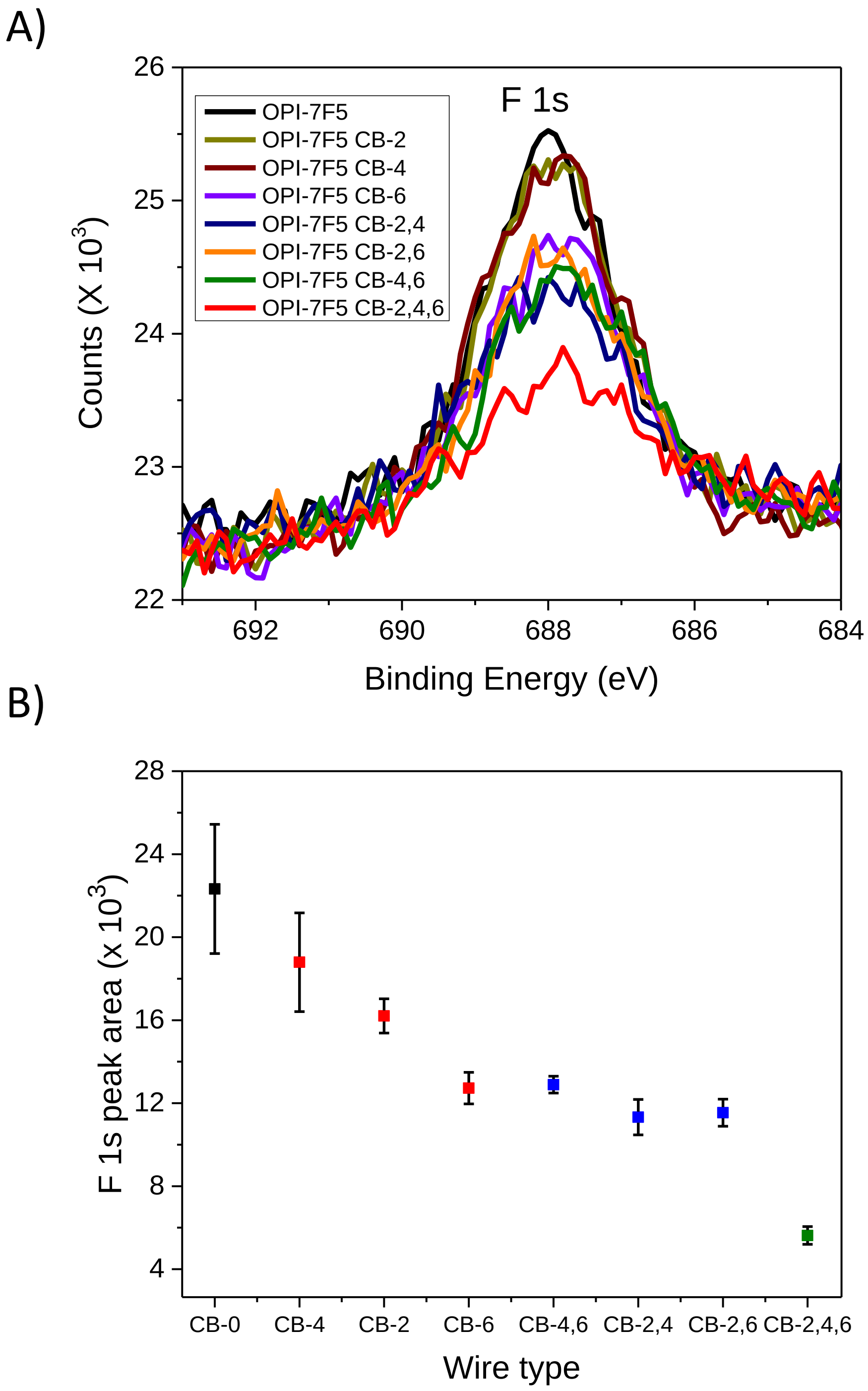

Figure 7.17 (A) XPS spectra of OPI-7F5 and OPI-7F5 CB wires. (B) XPS peak areas of (A) OPI-7F5 (black square), and OPI-7F5 CB with 1 blocking unit (red square), 2 blocking units (blue squares), and 3 blocking units (green square). As the number of conjugation blocking units increase, the peak areas decreased.

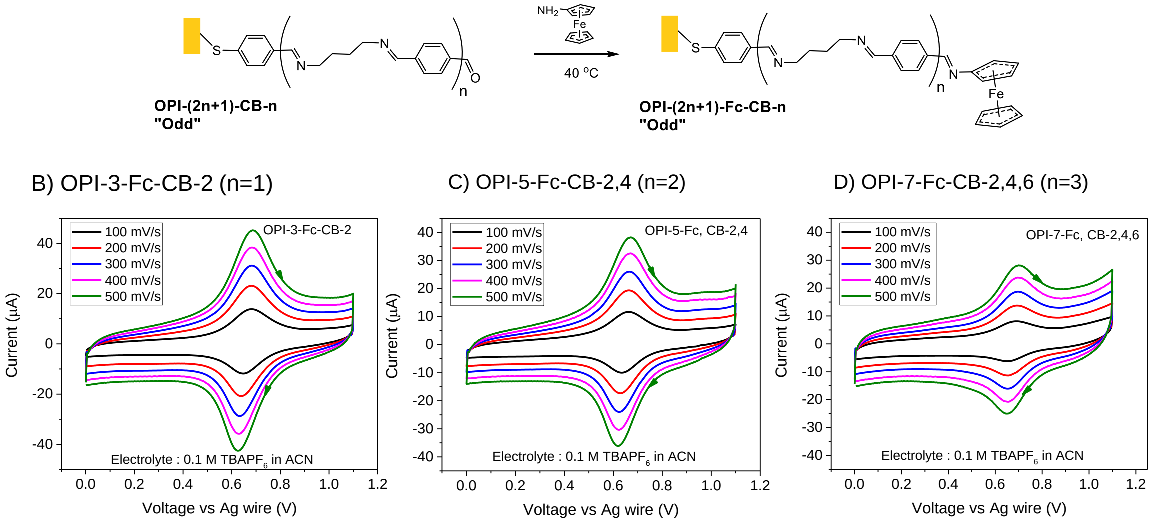

Figure 7.18 (A) Molecular structure for aldehyde terminated OPI-(2n+1)-CB-n wires (left) on Au before and after capping with aminoferrocene (right). Cyclic Voltammetry of OPI-3-Fc-CB-2 (B), OPI-5-Fc-CB-2,4 (C), and OPI-7-Fc-CB-2,4,6 (D) at different sweep rates. The electrolyte was 0.1 M $[Bu_4N^+][PF_6^-]$ in acetonitrile. The reference and counter electrodes were Ag and Pt wires, respectively. The peak currents and sweep rates are linearly proportional, as expected, for surface confined species. Au geometrical area: 0.64 cm^2.

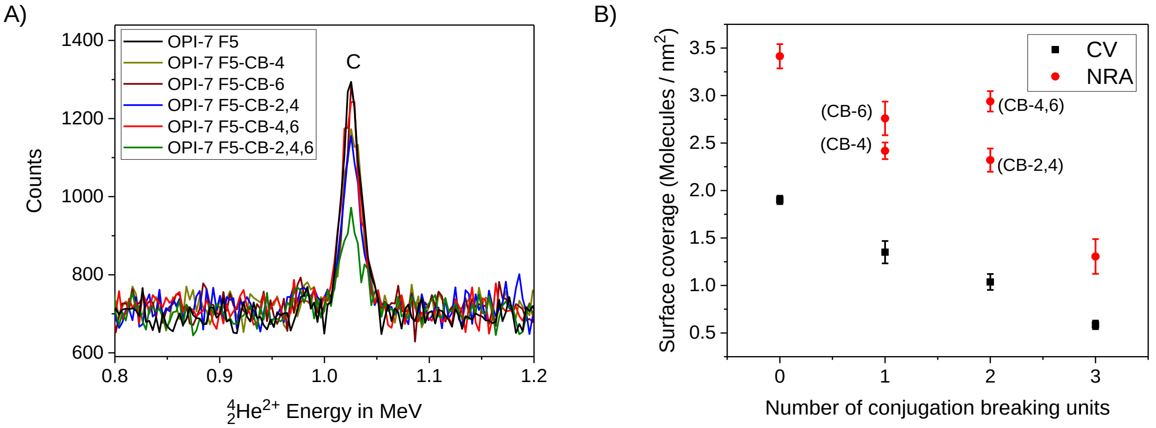

Figure 7.19 (A) NRA C spectra of OPI-7F5, OPI-7F5-CB-4, OPI-7F5-CB-6, OPI-7F5-CB-2,4, OPI-7F5-CB-4,6, and OPI-7F5-CB-2,4,6. The spectral heights were normalized to the Si signal. (B) Surface coverage values of C atoms from NRA spectra in A (red circles) and surface coverage values from CV (black squares, Figure 7.18).

molecules / nm^2, respectively. Both NRA and CV measurements reveal that the surface coverage decreases with an increase in the number of conjugation breaking units. The C-C σ-bonds in 1,4-diaminobutane (CB) units are free to rotate, with the results that it can adopt huge number of possible confirmations. This in turn can disrupt wire growth along the sample normal, and result in high tilt angles. Therefore, ellipsometry measurements were conducted on selected OPI-7F5 and OPI-7F5 CB wires, and OPI-8F5 and OPI-8F5 CB wires. The results are displayed in Table 7.1.

Table 7.1. Ellipsometry thickness values of OPI-7F5 CB and OPI-8F5 CB wires.

OPI-7F5 CB wires	**Measured Thickness (nm)**	**OPI-8F5 CB wires**	**Measured Thickness (nm)**
OPI-7F5	3.75 ± 0.29	OPI-8F5	4.18 ± 0.36
OPI-7F5-CB-4	3.22 ± 0.18	OPI-8F5-CB-3	3.83 ± 0.41
OPI-7F5-CB-6	3.02 ± 0.29	OPI-8F5-CB-7	3.81 ± 0.48
OPI-7F5-CB-4,6	2.46 ± 0.19	OPI-8F5-CB-5,7	3.65 ± 0.51
OPI-7F5-CB-2,4	1.18 ± 0.25	OPI-8F5-CB-3,5	3.26 ± 0.42
OPI-7F5-CB-2,4,6	0.53 ± 0.21	OPI-8F5-CB-3,5,7	3.05 ± 0.49

The ellipsometry values in Table 7.1 indicate that OPI-7F5 CB wires are tilted, whereas OPI-8F5 CB wires are standing up. Furthermore, the data supports that placing the conjugation breaking unit closer to Au surface results in a lower film thickness or large tilt angle. Thus, the surface coverage and ellipsometry measurements for OPI-8F5 and OPI-8F5 CB wires indicate that extent of reaction cannot account for the observed trend between the F 1s peak counts and number of conjugation disruption units. On the other hand, the ellipsometry measurements show that increasing the number of conjugation breaking units in OPI-7F5 CB wires resulted in an increase of the tilt angle. Furthermore, the nearly identical F 1s peak areas of OPI-7F5-CB-6, OPI-7F5-CB-2,4, OPI-7F5-CB-2,6, and OPI-7F5-CB-4,6 wires rules out extent of reaction as a possible cause of this discrepancy, because wires with two conjugation blocking units did not have lower peak area than OPI-7-CB-6 wires with one conjugation blocking unit. Thus, the conjugation breaking experiments revealed that the structure-property relationship of perfluorinated wires is due to final state core hole relaxation processes outlined in Figure 7.7.

Recently, Taherinia et al., performed DFT calculations and variable temperature CP-AFM measurements on OPI-6, OPI-6-CB-3, OPI-6-CB-5, and OPI-6-CB-3,5 wires.[32] The DFT calculation revealed that the activation energy for polaron hopping transport increased when conjugation blocking unit were inserted, and its corresponding value was also dependent on the position of the conjugation blocking unit. On the other hand, their experimental activation energy values via CP-AFM showed the opposite trend, i.e., the activation energy decreased with an increase of the conjugation disruption units.[32] Based on careful analysis of the transition states involve in charge transport at zero bias, the authors concluded that a combination of polaron tunneling and over-barrier polaron hopping is responsible for charge transport in OPI-6 CB wires.[32] Polaron hopping involves simultaneous change of nuclear configuration and electron localization. If we consider the magnitude of F 1s peak area analogous to the CP-AFM resistance measurements of Taherinia et al.,'s work[32]; the observed trend in OPI-F5 CB wires is in good agreement with the reported decreases in resistance values for OPI-6 CB wires. Future work will address these issues by performing DFT calculations on OPI-F5 and OPI-F5 CB wires to confirm the minimum energy and transition state for tunneling transport.

7.5 Conclusion

We have systematically examined the connection between electronic structure and x-ray photoelectron emission counts of F 1s for a set of π-conjugated molecular wires ranging in length between 0.6 and 4.5 nm. The OPI wires were grown from SAMs of 4-aminothiophenol or 4-formylthiophenol, and reacted step-wise with alternate addition of terephthalaldehyde (22 °C) or 1,4-Benzenediamine (40 °C). The perfluoro termini (cap) were introduced by reacting amine terminated wires with pentafluorobenzaldehyde. The XPS F 1s peak area from the pentafluoro termini decreased with wire length. The slope of peak area verses estimated thickness was large for short wires than long wires. A crossover in slope was observed near 3 nm. NRA experiments revealed that the surface coverages for the wires are similar, and do not account for the obtained XPS results. To rule out surface charging or chemical shifts, OPI wires were synthesized on native SiO_2/Si substrate starting from SAMs of (3-Aminopropyl)trimethoxysilane, and the results indicated no such effects. To further investigate the role of molecular structure on the observed F 1s counts, conjugation blocking alkyl chains were inserted at different positions along the wire backbone. The results show that conjugation blocking units significantly impact the intensity of F 1s counts. Overall, we obtained good correlation between the wire structure and its corresponding effects on the intensity of F 1s counts. When the conjugation breaking units were placed very close to the Au substrate, the XPS F 1s peak counts of CB OPI-75 wires were higher than their conjugated counterpart (OPI-7F5). We speculate that film thickness and polaron formation energy could account for this behavior. Future work will address these issues along with core hole clock spectroscopy to measure the lifetime of core states, and to develop this novel technique for calculating decay constants.

7.6 References

(1) Yuan, L.; Jiang, L.; Zhang, B.; Nijhuis, C. A. *Angew. Chemie - Int. Ed.* **2014**, *53*, 3377.

(2) Cabarcos, O. M.; Shaporenko, A.; Weidner, T.; Uppili, S.; Dake, L. S.; Zharnikov, M.; Allara, D. L. *J. Phys. Chem. C* **2008**, *112*, 10842.

(3) Bonifas, A. P.; McCreery, R. L. *Nano Lett.* **2011**, *11*, 4725.

(4) Sangeeth, C. S. S.; Wan, A.; Nijhuis, C. a. *J. Am. Chem. Soc.* **2014**, *136*, 11134.

(5) Lavi, A.; Cohen, H.; Bendikov, T.; Vilan, A.; Cahen, D. *Phys. Chem. Chem. Phys.* **2011**, *13*, 1293.

(6) Nijhuis, C. A.; Reus, W. F.; Whitesides, G. M. *J. Am. Chem. Soc.* **2009**, *131*, 17814.

(7) Lewis, P. A.; Inman, C. E.; Maya, F.; Tour, J. M.; Hutchison, J. E.; Weiss, P. S. *J. Am. Chem. Soc.* **2005**, *127*, 17421.

(8) Aradhya, S. V; Venkataraman, L. *Nat. Nanotechnol.* **2013**, *8*, 399.

(9) Vericat, C.; Vela, M. E.; Benitez, G.; Carro, P.; Salvarezza, R. C. *Chem. Soc. Rev.* **2010**, *39*, 1805.

(10) Hihath, J.; Tao, N. *Semicond. Sci. Technol.* **2014**, *29*, 054007.

(11) Heimel, G.; Zojer, E.; Romaner, L.; Brédas, J.-L.; Stellacci, F. *Nano Lett.* **2009**, *9*, 2559.

(12) Bergfield, J. P.; Ratner, M. A. *Phys. status solidi* **2013**, *250*, n/a.

(13) Rosink, J. J. W. M.; Blauw, M. A.; Geerligs, L. J.; van der Drift, E.; Rousseeuw, B. A. C.; Radelaar, S.; Sloof, W. G.; Fakkeldij, E. J. M. *Langmuir* **2000**, *16*, 4547.

(14) Alloway, D. M.; Hofmann, M.; Smith, D. L.; Gruhn, N. E.; Graham, A. L.; Colorado, R.; Wysocki, V. H.; Lee, T. R.; Lee, P. A.; Armstrong, N. R. *J. Phys. Chem. B* **2003**, *107*, 11690.

(15) Willicut, R. J.; McCarley, R. L. *Langmuir* **1995**, *11*, 296.

(16) Bâldea, I.; Xie, Z.; Frisbie, C. D. *Nanoscale* **2015**, *7*, 10465.

(17) *Charge and Exciton Transport through Molecular Wires*; John Wiley & Sons, 2011.

(18) Eng, M. P.; Albinsson, B. *Angew. Chem. Int. Ed. Engl.* **2006**, *45*, 5626.

(19) Segawa, H.; Takehara, C.; Honda, K.; Shimidzu, T.; Asahi, T.; Mataga, N. *J. Phys. Chem.* **1992**, *96*, 503.

(20) Segal, D.; Nitzan, A.; Davis, W. B.; Wasielewski, M. R.; Ratner, M. A. *J. Phys. Chem. B* **2000**, *104*, 3817.

(21) Wang, L.; Chen, W.; Huang, C.; Chen, Z.-K.; Wee, A. T. S. *J. Phys. Chem. B* **2006**, *110*, 674.

(22) Cao, L.; Yang, M.; Yuan, L.; Nerngchamnong, N.; Feng, Y.-P.; Wee, A. T. S.; Qi, D.-C.; Nijhuis, C. A. *J. Phys. Condens. Matter* **2016**, *28*, 094006.

(23) Kao, P.; Neppl, S.; Feulner, P.; Allara, D. L.; Zharnikov, M. *J. Phys. Chem. C* **2010**, *114*, 13766.

(24) Choi, S. H.; Kim, B.; Frisbie, C. D. *Science* **2008**, *320*, 1482.

(25) Powell, C. J.; Jablonski, a. *J. Electron Spectros. Relat. Phenomena* **2010**, *178-179*, 331.

(26) Lin-Vien, D.; Colthup, N. B.; Fateley, W. G.; Grasselli, J. G. *The Handbook of Infrared and Raman Characteristic Frequencies of Organic Molecules*; Elsevier, 1991.

(27) Ledbetter, J. W. *J. Phys. Chem.* **1977**, *81*, 54.

(28) Feng, Y.; Zhou, Z.; Zhou, Y.; Zhao, G. *Nucl. Instruments Methods Phys. Res. Sect. B Beam Interact. with Mater. Atoms* **1994**, *86*, 225.

(29) Vandenberg, E. T.; Bertilsson, L.; Liedberg, B.; Uvdal, K.; Erlandsson, R.; Elwing, H.; Lundström, I. *J. Colloid Interface Sci.* **1991**, *147*, 103.

(30) Kumar, K. S.; Pasula, R. R.; Lim, S.; Nijhuis, C. A. *Adv. Mater.* **2016**, *28*, 1900.

(31) Yan, H.; Bergren, A. J.; McCreery, R.; Della Rocca, M. L.; Martin, P.; Lafarge, P.; Lacroix, J. C. *Proc. Natl. Acad. Sci. U. S. A.* **2013**, *110*, 5326.

(32) Taherinia, D.; Smith, C. E.; Ghosh, S.; Odoh, S. O.; Balhorn, L.; Gagliardi, L.; Cramer, C. J.; Frisbie, C. D. *ACS Nano* **2016**.

8. Outlook: Probing Highly Conductive Wires and Metal Complex Wires

Recent success in structure and electrical characterization of ultrathin organic films opens the door to explore the role of molecular structure on charge transport. As explained in the introduction, a better picture of conduction gained through molecular junction experiments will aid in design of π conjugated polymers for improved device performance such as solar cells, thin film transistor and diodes. In the final part of this thesis, we will explore new insights on: (i) role of anchoring of groups on conductance, (ii) role of conjugation length, (iii) synthesis of metal bis complex wires, and (iv) synthesis of donor-block-acceptor wires.

8.1) Role of anchoring group

A variety of molecular junction experiments utilize thiol SAMs because they have been extensively studied and are easy to synthesize.[1–3] However, other functional groups such as isocyanides, amines, carbamates, and thioacetates have been used to form well-ordered SAMs.[1] Tao et al., investigated the effects of anchoring groups on charge transport for a variety of alkyl chains and their results showed that conductance values were strongly affected by the type of anchoring group used.[4] That is, the strength of electronic coupling at the metal - anchoring group interface strongly impacts charge transport. Recently, Venkataraman, et al synthesized highly conductive conjugated molecules with conductance values approaching quantum unit of conductance (Go) per molecule.[5] These molecules were terminated with trimethylstannylmethyl ($SnMe_3$) groups that cleaved *in situ* and formed direct covalent Au-C contacts as shown in Figure

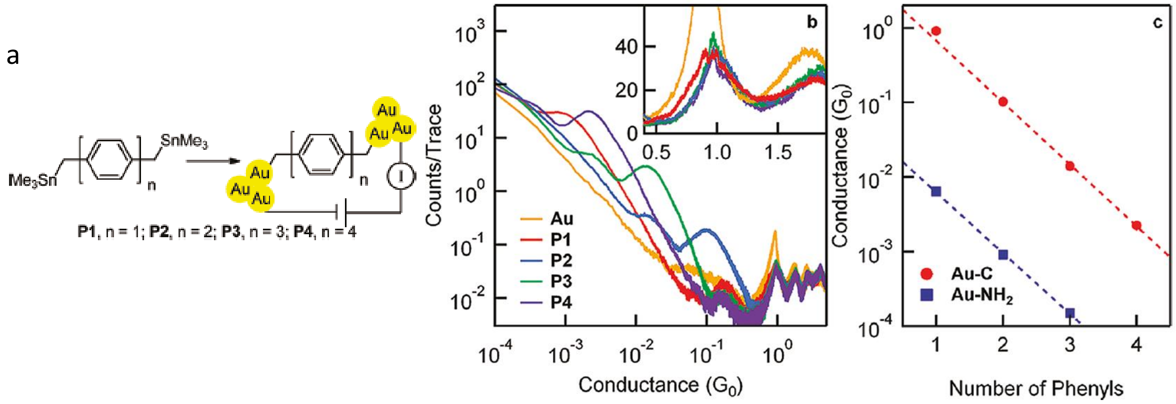

Figure 8.1 In situ formation of Au-C from $SnMe_3$ precursors. B) log-log plots of conductance histograms from over 1000 curves. The inset conductance peaks near Go for P1. C) Semi-log plots verses number of phenyl rings for Au-C interface vs Au-NH_2. Adapted from reference 5 with permission from the Journal of the American Chemical Society.

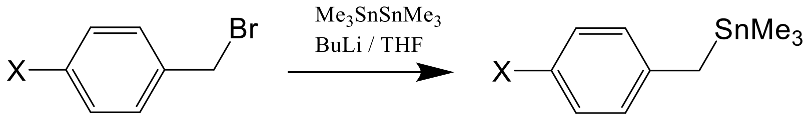

X = NH_2, C=O, N_3,C≡CH

Scheme 8.1 Synthesis of $SnMe_3$ precursors for growing wires. Modified from reference 5.

Step 1. Self-assembly

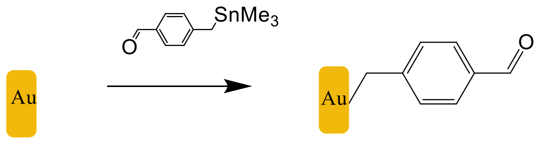

Step 2. Wire growth

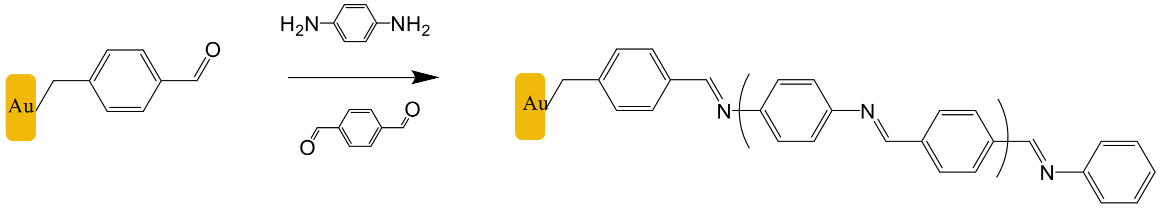

Figure 8.2 A) self-assembly of 4-formyltrimethylstannyl-benzene. B) Stepwise growth of OPI wires from in-situ cleaved stannyl precursors.

8.1. In contrast attempts to form direct Au-phenyl bond were not successful because it was much harder to cleave C-SnMe$_3$ with sp^2 C verses sp^3 C.[5] We propose to synthesize SnMe$_3$ phenyl molecules with functional group at the para position that can then be used to synthesize OPI wires as shown in Scheme 8.1 and Figure 8.2. We can then examine the impact of direct Au-C σ bond on decay length, tunneling to hopping crossover length, and activation energy.

An alternative strategy to form strong Au-C σ bonds is by chemisorption of alkynes (HC≡CR) on Au. Cyganik et al., prepared highly stable monolayers of n-alkynes formed on Au under an inert atmosphere.[6] Their combined spectroscopic and microscopic measurements showed that SAMs with similar coverage and orientation as alkanethiols were formed on Au (111).[6] We employed a similar approach to form SAMs of 4-ethynylbenzaldehyde on fresh Au film, and it indeed works. The RAIRS spectra reveals strong C=O (1705 cm^{-1}) and C=C (1500 cm^{-1}) stretch modes. The carbonyl units can then be used to synthesize wires as outlined in chapter 4. Alkyne SAMs are strongly coupled

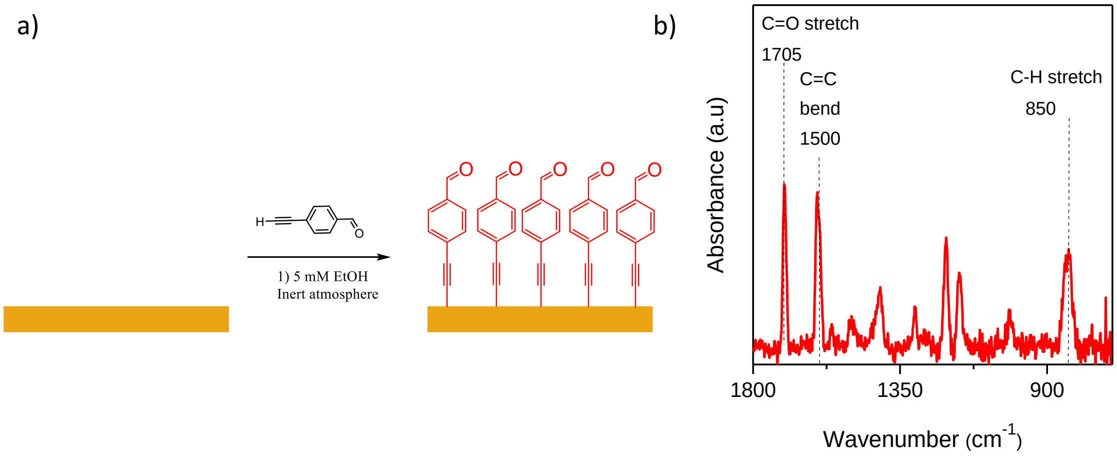

Figure 8.3 A) Self-assembly of 4-ethynylbenzaldehyde on Au. Corresponding RAIRS spectra for SAMs of A.

to π system since the Au is directly bonded to sp hybridized C atoms. Unlike Au-S bond which desorb at temperatures of 60°C or above, Au-C bond are thermally more stable. Thus, new chemistry that requires high temperature for growing wires in stepwise approach can be explored with alkyne chemisorbed SAMs.

8.2) Role of conjugation length

Prior UV-VIS measurements revealed that the conjugation length of OPI wires extended only to 3 repeat units due to steric hindrances along the oligoimine backbone.[7] As a result, the phenyl rings adopt a dihedral angle of 30° with respect to each other. A more coplanar configuration would release the ring strain, and result in more conductive wires. One strategy to minimize the dihedral angle is to utilize hydrogen bonding between the phenyl hydrogen and hydroxyl group. For example, a complex of Ru dye 3 (cis-Bis(isothiocyanato)bis(2,2′-bipyridyl-4,4′-dicarboxylato)ruthenium(II)) was used to

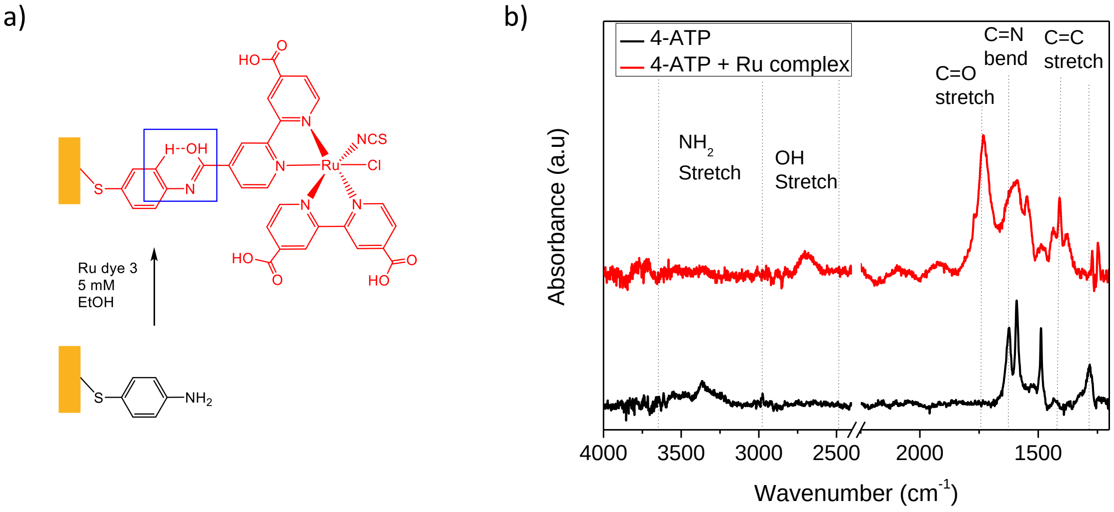

Figure 8.4 Stepwise growth of Ru dye 3 on SAMs of 4-ATP on Au. The hydrogen bonding interaction between OH and phenyl H forms a quasi-6 membered ring that releases ring strain. Corresponding RAIRS spectra of Ru Dye 3 (B).

interactions may be favorable enough to compensate for the steric strain associated with co-planar configurations. Incorporation of Ru complex may also lead to new I-V characteristics such as coulomb blockade. We have previously reported that SAMs of ruthenium(II) bis (σ-arylacetylide) complexes exhibited weak dependence of wire resistance on length, which was consistent with high degree of electronic communication (overlap) across the molecular backbone.[8] Furthermore, the low temperature conductance steps for SAMs with 3 Ru complexes agreed very well with the shape of the electrochemical oxidation waves.[8] Thus, future experiments will focus on the impacts of adding more Ru complexes via Schiff base chemistry. This also opens up the opportunity to vary the distance between the Ru complex centers, and investigate its effects on tunneling or hopping transport. We can also synthesize Ru complexes with carbonyl units in place of the carboxylic acids, and use it as a control for probing the effects ring strain (dihedral angle) on charge transport.

8.3) Synthesis of bis complex wires with Ru, Zn, Co, Ni, Cu and Fe centers

We can further explore the structure-property behavior of metal complexes by utilizing one of the most interesting and widely used ligand in supramolecular chemistry, the 2,2′:6′,2″- terpyridine ligand. For example, Schubert et al., synthesized terpyridine bis complexes with terminal alkyne functional groups, and employed cycloaddition reaction to covalently bond the alkyne unit with azide terminated SAMs on Si substrate.[9] Thus, we envision similar biscomplex synthesis methods to incorporate a variety of metal centers (Ru, Zn, Co, Ni, Cu and Fe) followed by cycloaddition reaction on to azide terminated wires on Au as shown in Schemes 8.2 and 8.3, and Figure 8.5. Thus, one can imagine a systematic study where the position of a single metal center is varied along the wire, and its influence of conductivity can be probed via CP-AFM. The alkyne terminal unit on the bis complexes can also be used to anchor the complexes directly on the Au surface as

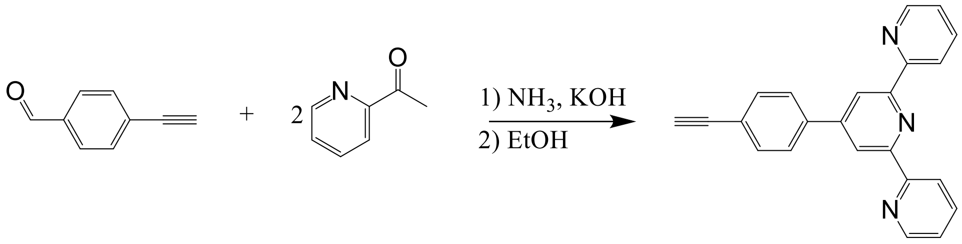

Scheme 8.2 Synthesis of 2,2′:6′,2″- terpyridine ligand. Adapted from reference 9.

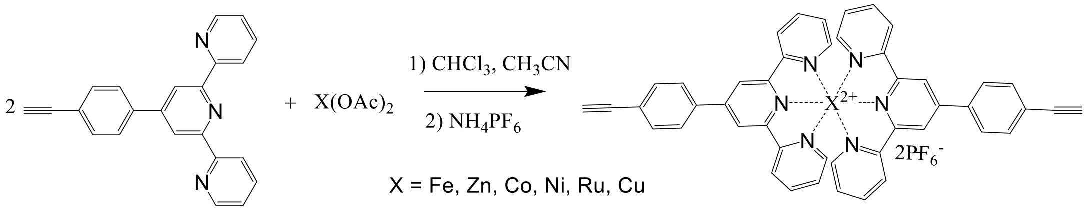

Scheme 8.3 Synthesis of terpyridine biscomplex ligand. Adapted from reference 9.

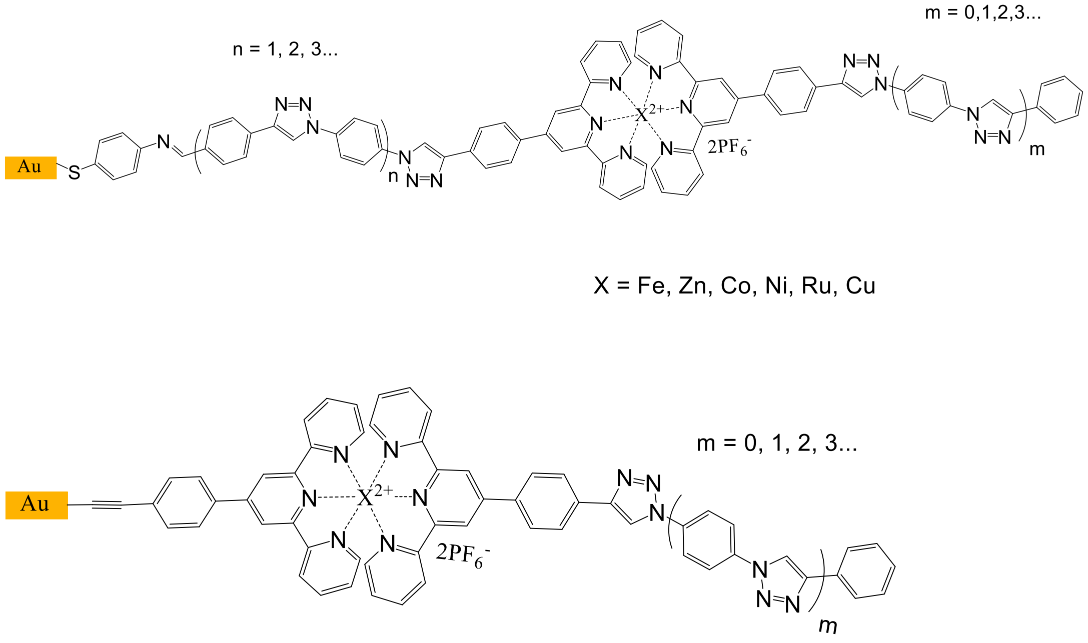

Figure 8.5 Proposed structure of metal containing wires.

Rampi et al., synthesized molecular wires by stepwise sequential coordination of metal ions of terpyridine based ligands as shown in Figure 8.6.[10] Among the metal centers, Co^{+2} was particularly interesting because it formed highly conductive wires up to 40 nm in length.[10] The high conductivity of metal complexed wires was attributed to the presence of d-orbitals that can be delocalized over the ligands. Since multiple charges can be accommodated by the redox sites, correlative effects such as charge-charge repulsion between two or more metal centers can be studied as function of distance between the metal centers as shown in Figure 8.7.[11] One can also explore the effects of 2 or more

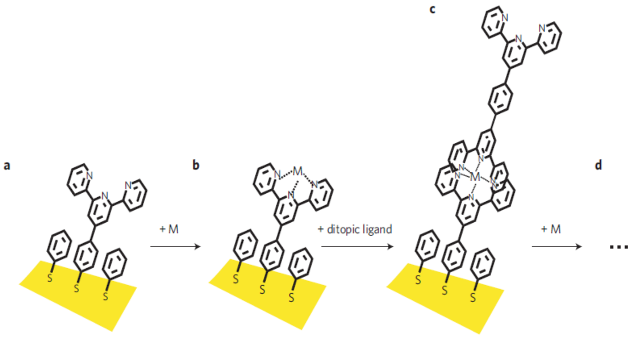

Figure 8.6 Stepwise assembly of metal center molecular wires in situ metal surfaces. a) Assembly on the Au surface. B) Coordination of the metal to the ligand. C) Coordination of the terpyridine ligand. D) Repeat of b and c. Adapted from reference 10 with permission from Nature Materials.

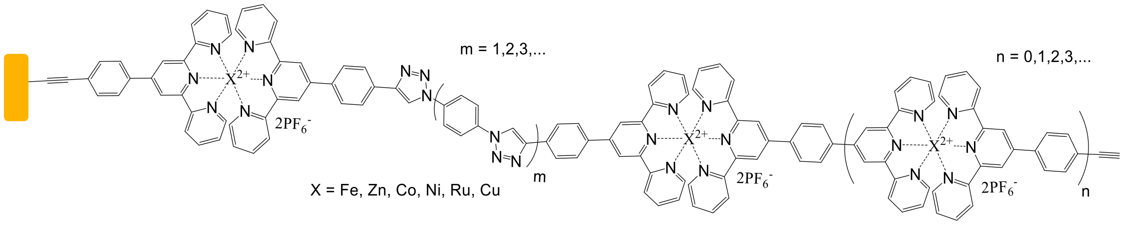

Figure 8.7 Proposed design of multiple metal containing molecular wires for studying charge-charge correlation. Note that the metal centers do not have to be similar. The first complex is directly chemisorbed, while the second and n metal centers are formed by cycloaddition of terpyridine ligand followed by in situ procedures employed by Rampi et al.

different types of metal ions incorporated in the same wire. Furthermore, ferromagnetic metals like Ni^{2+}, Co^{2+} and Fe^{2+} allow us to probe spin transport as function of ligand(s) position, applied bias, magnetic field strength, and temperature.

8.4) Synthesis of donor-block –acceptor wires

The diode or rectifier is a two terminal electronic component that facilitates current flow in one direction, and suppresses it on the other. In 1974, Aviram and Ratner proposed a rectifier based on a single organic molecule, which consisted of conjugated electron withdrawing and electron donating group linked by saturated σ – bond.[12] Similar to conventional pn diodes, the donor resembles the p-doped side while the acceptor resembles the n-doped side. The spacer or σ bond saturated linker is important to prevent overlap of donor and acceptor orbitals. In the Aviram-Ratner rectification model, the misalignment of the molecular orbitals of the donor and acceptor units is responsible for rectification.[12] As shown in Figure 8.8 for forward bias mode, if the electron affinities of the acceptors are high enough; electrons can be injected from the cathode into the

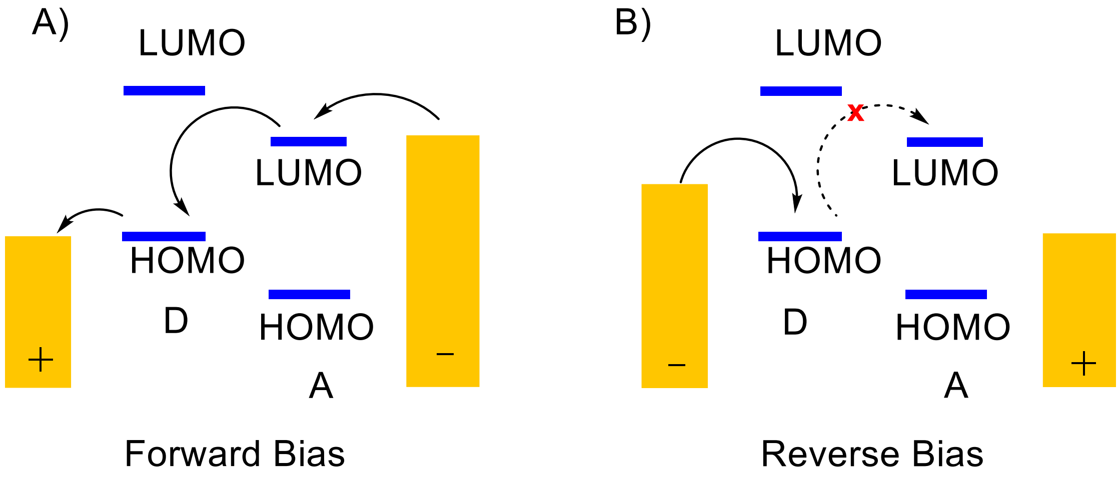

Figure 8.8 Aviram-Ratner rectification model.

acceptor LUMO level, fall downwards to HOMO of the donor, and then to the anode. On the other hand for the reverse bias, the electron encounters an energetically unfavorable uphill as it moves from the donor towards the acceptor. Thus, such asymmetric transport mechanism is responsible for rectification.

The metal complexes discussed in the previous section serve as excellent donors due to their d rich orbitals. Indeed, we speculate that a strong coupling of the donor molecules to the Au electrode through Au-C σ-bond could prevent fermi level pinning, that is commonly observed for thiols. In organic photovoltaic cells, fullerene and its derivatives are the most commonly used acceptor molecules due to their high electron affinity, and existence of low lying anion states that increase rate of charge separation.[13] As a result, we propose to incorporate fullerene molecules that are functionalized with either NH_2, C=O, and C≡C units as shown in Scheme 8.4.[14,15] The functionalized fullerene derivatives can then form covalent bond to the spacer either by imine condensation or triazole cycloaddition. Thus, such donor-block-acceptor systems open the door to explore the influence of the donor metal center, spacer length, spacer electronic structure (conjugated verses saturated systems), and temperature on rectification. The analytic techniques discussed in chapter 4 and 5 will be useful to characterize the surface coverage, and extent of reaction. In particular, the tilted RBS experiments will be useful to quantify the concentration of metal centers similar to ferrocene tagged OPI wires. Furthermore, cyclic voltammetry measurements can give more information on the total number of redox sites available, energy level, electrochemical band gap and surface coverage. Optical band gap can be calculated from UV-Vis measurements.

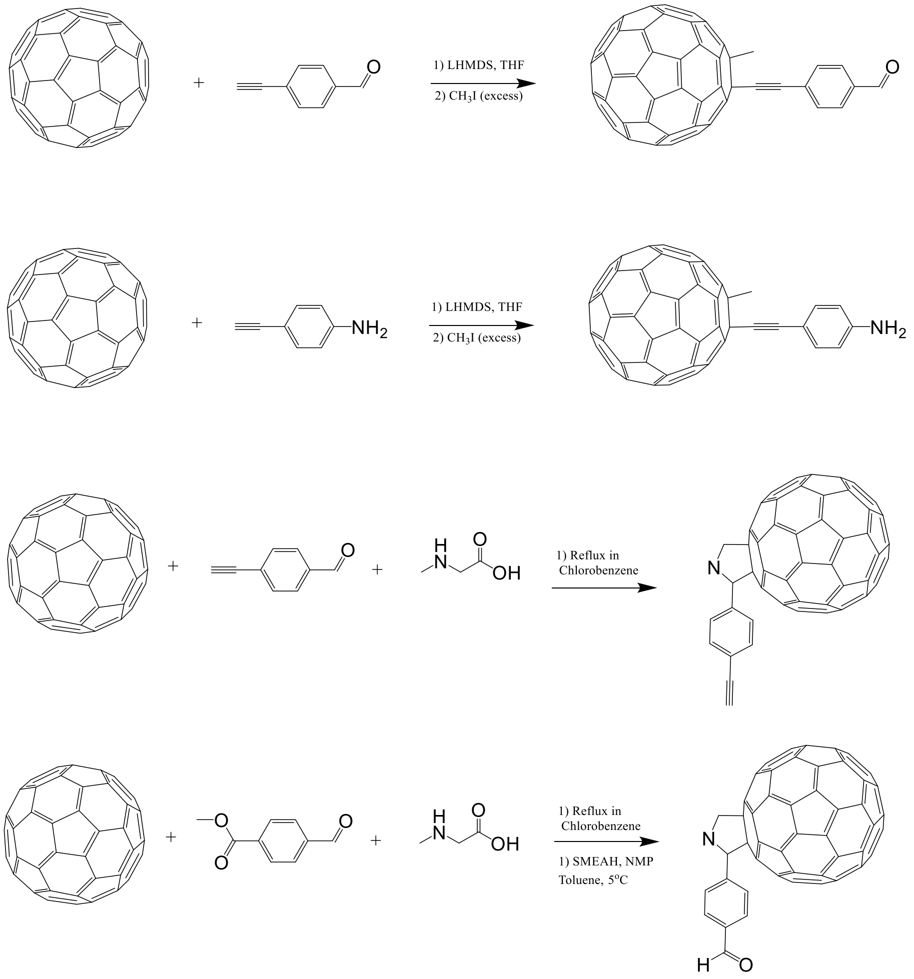

Scheme 8.4 Synthesis of functionalized fullerene for acceptor moieties. Adapted with modification from reference 14 and 15.

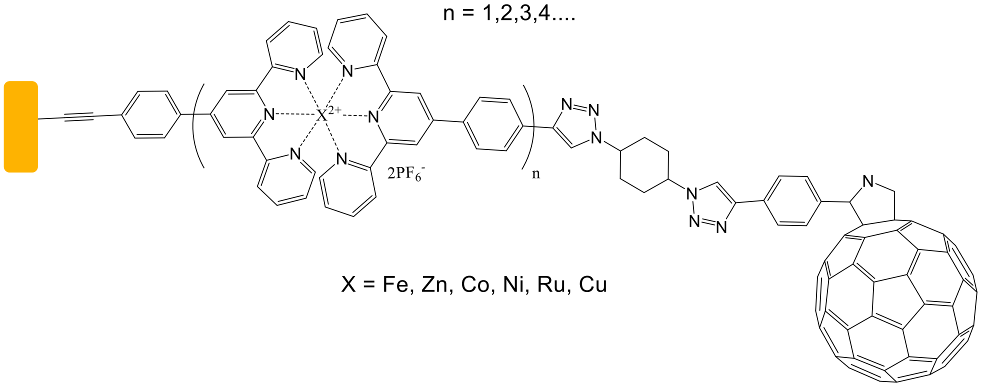

Figure 8.9 Proposed multiple donors – saturated block-acceptor wires.

.

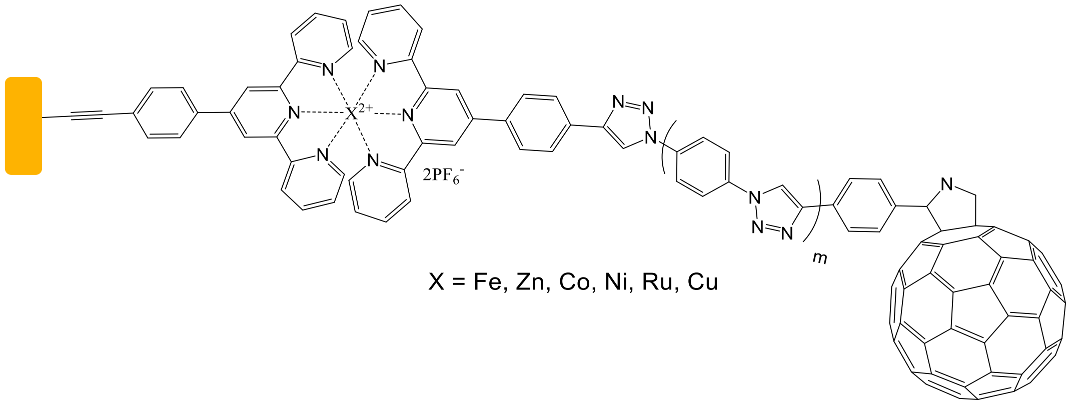

Figure 8.10 Proposed donor-acceptor wires separated by conjugated phenyl bridges.

8.5 References

(1) Love, J. C.; Estroff, L. a.; Kriebel, J. K.; Nuzzo, R. G.; Whitesides, G. M. Self-assembled monolayers of thiolates on metals as a form of nanotechnology. *Chemical Reviews*, 2005, *105*, 1103–1169.

(2) Vericat, C.; Vela, M. E.; Benitez, G.; Carro, P.; Salvarezza, R. C. *Chem. Soc. Rev.* **2010**, *39*, 1805.

(3) Ulman, A. *Chem. Rev.* **1996**, *96*, 1533.

(4) Chen, F.; Li, X.; Hihath, J.; Huang, Z.; Tao, N. *J. Am. Chem. Soc.* **2006**, *128*, 15874.

(5) Chen, W.; Widawsky, J. R.; Vázquez, H.; Schneebeli, S. T.; Hybertsen, M. S.; Breslow, R.; Venkataraman, L. *J. Am. Chem. Soc.* **2011**, *133*, 17160.

(6) Zaba, T.; Noworolska, A.; Bowers, C. M.; Breiten, B.; Whitesides, G. M.; Cyganik, P. *J. Am. Chem. Soc.* **2014**, *136*, 11918.

(7) Choi, S. H.; Kim, B.; Frisbie, C. D. *Science* **2008**, *320*, 1482.

(8) Kim, B.; Beebe, J. M.; Olivier, C.; Rigaut, S.; Touchard, D.; Kushmerick, J. G.; Zhu, X. Y.; Frisbie, C. D. *J. Phys. Chem. C* **2007**, *111*, 7521.

(9) Haensch, C.; Chiper, M.; Ulbricht, C.; Winter, A.; Hoeppener, S.; Schubert, U. S. *Langmuir* **2008**, *24*, 12981.

(10) Tuccitto, N.; Ferri, V.; Cavazzini, M.; Quici, S.; Zhavnerko, G.; Licciardello, A.; Rampi, M. A. *Nat. Mater*. **2009**, *8*, 41.

(11) *Charge and Exciton Transport through Molecular Wires*; Siebbeles, L. D. .; Grozeman, F. C., Eds.; John Wiley & Sons, 2011.

(12) Aviram, A.; Ratner, M. A. *Chem. Phys. Lett.* **1974**, *29*, 277.

(13) Thompson, B. C.; Fréchet, J. M. J. *Angew. Chem. Int. Ed. Engl.* **2008**, *47*, 58.

(14) Shirai, Y.; Cheng, L.; Chen, B.; Tour, J. M. *J. Am. Chem. Soc.* **2006**, *128*, 13479.

(15) Hau, S. K.; Cheng, Y.-J.; Yip, H.-L.; Zhang, Y.; Ma, H.; Jen, A. K.-Y. *ACS Appl. Mater. Interfaces* **2010**, *2*, 1892.

List of Publications

Book

T. Story and **A.T. Demissie**. Solutions Manual for Mathematical Modeling I and II: Kinetics, Thermodynamics, Statistical Mechanics, Quantum Mechanics, and Spectroscopy. Educational Publisher. Columbus. 2012. (http://www.amazon.com/Solutions-Manual-Mathematical-Modeling-II/dp/1622490312).

Papers

1. **A.T. Demissie**, G. Haugstad, C.D. Frisbie, "Growth of Thin, Anisotropic, π-Conjugated Molecular Films by Stepwise 'Click' Assembly of Molecular Building Blocks: Characterizing Reaction Yield, Surface Coverage, and Film Thickness vs. Addition Step Number" *Journal of the American Chemical Society* **2015**, *137* (27), 8819–8828. (http://pubs.acs.org/doi/abs/10.1021/jacs.5b04512)

2. S. Sangeeth, **A.T. Demissie**, Y. Li, C.D. Frisbie, C.A. Nijhuis. "Comparison of DC and AC Transport in 1.5-7.5 nm Oligophenylene Imine Molecular Wires across Two Junction Platforms: Eutectic Ga-In versus Conducting Probe Atomic Force Microscope Junctions" *Journal of the American Chemical Society* **2016**, 138 (23), 7305–7314. (http://pubs.acs.org/doi/abs/10.1021/jacs.6b02039) – Equal Contribution).

3. **A.T. Demissie**, G. Haugstad, C.D. Frisbie, "Quantitative Surface Coverage Measurements of Self-Assembled Monolayers by Nuclear Reaction Analysis of Carbon-12 " *Journal of Physical Chemistry Letters* **2016**, 7, pp 3477–3481. (http://pubsdc3.acs.org/doi/full/10.1021/acs.jpclett.6b01363)

4. **A. T. Demissie**, C.D. Frisbie, "X-ray Photoelectron Spectroscopy of Perfluorinated Oligophenylene Imine Molecular Wires – A Novel Method to Measure Charge Transport of Thin Films" (In preparation).

5. Z. Xie, I. Bâldea, **A.T. Demissie,** C.E. Smith, Y. Wu, G. Haugstad, C.D. Frisbie, "Achieving Remarkable Control on the Number of Molecules and Other Transport-Related Properties of Conducting Probe Atomic Force Microscopy (CP-AFM) Junctions Based on Oligophenylene Dithiols" (Will be shortly submitted to *Journal of the American Chemical Society*).

Copyright Permission Letters

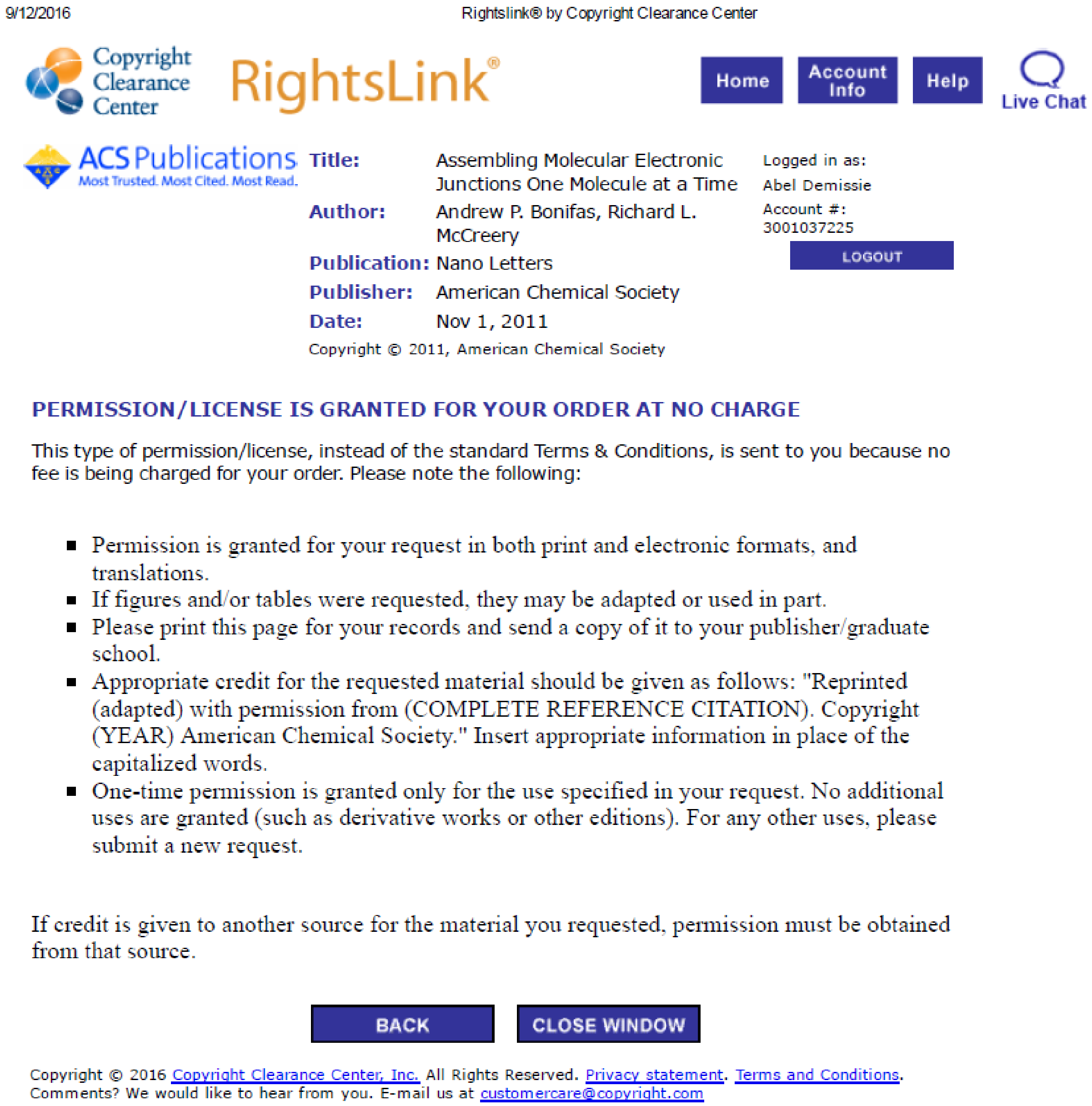

9/12/2016 Rightslink® by Copyright Clearance Center

Title: Assembling Molecular Electronic Junctions One Molecule at a Time

Author: Andrew P. Bonifas, Richard L. McCreery

Publication: Nano Letters

Publisher: American Chemical Society

Date: Nov 1, 2011

Copyright © 2011, American Chemical Society

Logged in as:
Abel Demissie
Account #:
3001037225

PERMISSION/LICENSE IS GRANTED FOR YOUR ORDER AT NO CHARGE

This type of permission/license, instead of the standard Terms & Conditions, is sent to you because no fee is being charged for your order. Please note the following:

- Permission is granted for your request in both print and electronic formats, and translations.
- If figures and/or tables were requested, they may be adapted or used in part.
- Please print this page for your records and send a copy of it to your publisher/graduate school.
- Appropriate credit for the requested material should be given as follows: "Reprinted (adapted) with permission from (COMPLETE REFERENCE CITATION). Copyright (YEAR) American Chemical Society." Insert appropriate information in place of the capitalized words.
- One-time permission is granted only for the use specified in your request. No additional uses are granted (such as derivative works or other editions). For any other uses, please submit a new request.

If credit is given to another source for the material you requested, permission must be obtained from that source.

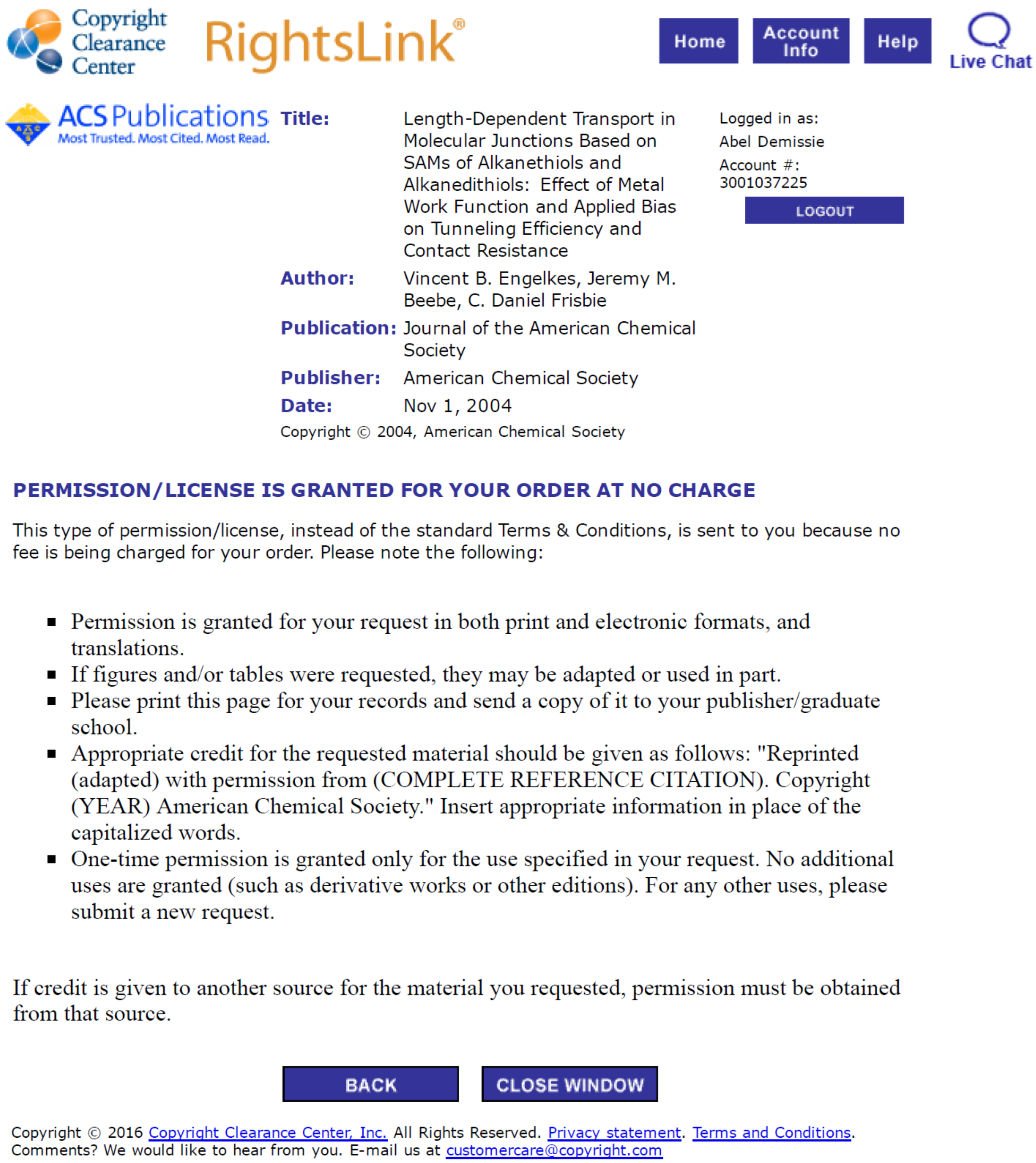

Title: Length-Dependent Transport in Molecular Junctions Based on SAMs of Alkanethiols and Alkanedithiols: Effect of Metal Work Function and Applied Bias on Tunneling Efficiency and Contact Resistance

Author: Vincent B. Engelkes, Jeremy M. Beebe, C. Daniel Frisbie

Publication: Journal of the American Chemical Society

Publisher: American Chemical Society

Date: Nov 1, 2004

Copyright © 2004, American Chemical Society

Logged in as:
Abel Demissie
Account #:
3001037225

PERMISSION/LICENSE IS GRANTED FOR YOUR ORDER AT NO CHARGE

This type of permission/license, instead of the standard Terms & Conditions, is sent to you because no fee is being charged for your order. Please note the following:

- Permission is granted for your request in both print and electronic formats, and translations.
- If figures and/or tables were requested, they may be adapted or used in part.
- Please print this page for your records and send a copy of it to your publisher/graduate school.
- Appropriate credit for the requested material should be given as follows: "Reprinted (adapted) with permission from (COMPLETE REFERENCE CITATION). Copyright (YEAR) American Chemical Society." Insert appropriate information in place of the capitalized words.
- One-time permission is granted only for the use specified in your request. No additional uses are granted (such as derivative works or other editions). For any other uses, please submit a new request.

If credit is given to another source for the material you requested, permission must be obtained from that source.

Copyright Clearance Center RightsLink®

Home Create Account Help Live Chat

ACS Publications
Most Trusted. Most Cited. Most Read.

Title: Self-Assembled Monolayers of Thiolates on Metals as a Form of Nanotechnology
Author: J. Christopher Love, Lara A. Estroff, Jennah K. Kriebel, et al
Publication: Chemical Reviews
Publisher: American Chemical Society
Date: Apr 1, 2005

LOGIN

If you're a copyright.com user, you can login to RightsLink using your copyright.com credentials. Already **a RightsLink user** or want to learn more?

PERMISSION/LICENSE IS GRANTED FOR YOUR ORDER AT NO CHARGE

This type of permission/license, instead of the standard Terms & Conditions, is sent to you because no fee is being charged for your order. Please note the following:

- Permission is granted for your request in both print and electronic formats, and translations.
- If figures and/or tables were requested, they may be adapted or used in part.
- Please print this page for your records and send a copy of it to your publisher/graduate school.
- Appropriate credit for the requested material should be given as follows: "Reprinted (adapted) with permission from (COMPLETE REFERENCE CITATION). Copyright (YEAR) American Chemical Society." Insert appropriate information in place of the capitalized words.
- One-time permission is granted only for the use specified in your request. No additional uses are granted (such as derivative works or other editions). For any other uses, please submit a new request.

If credit is given to another source for the material you requested, permission must be obtained from that source.

BACK CLOSE WINDOW

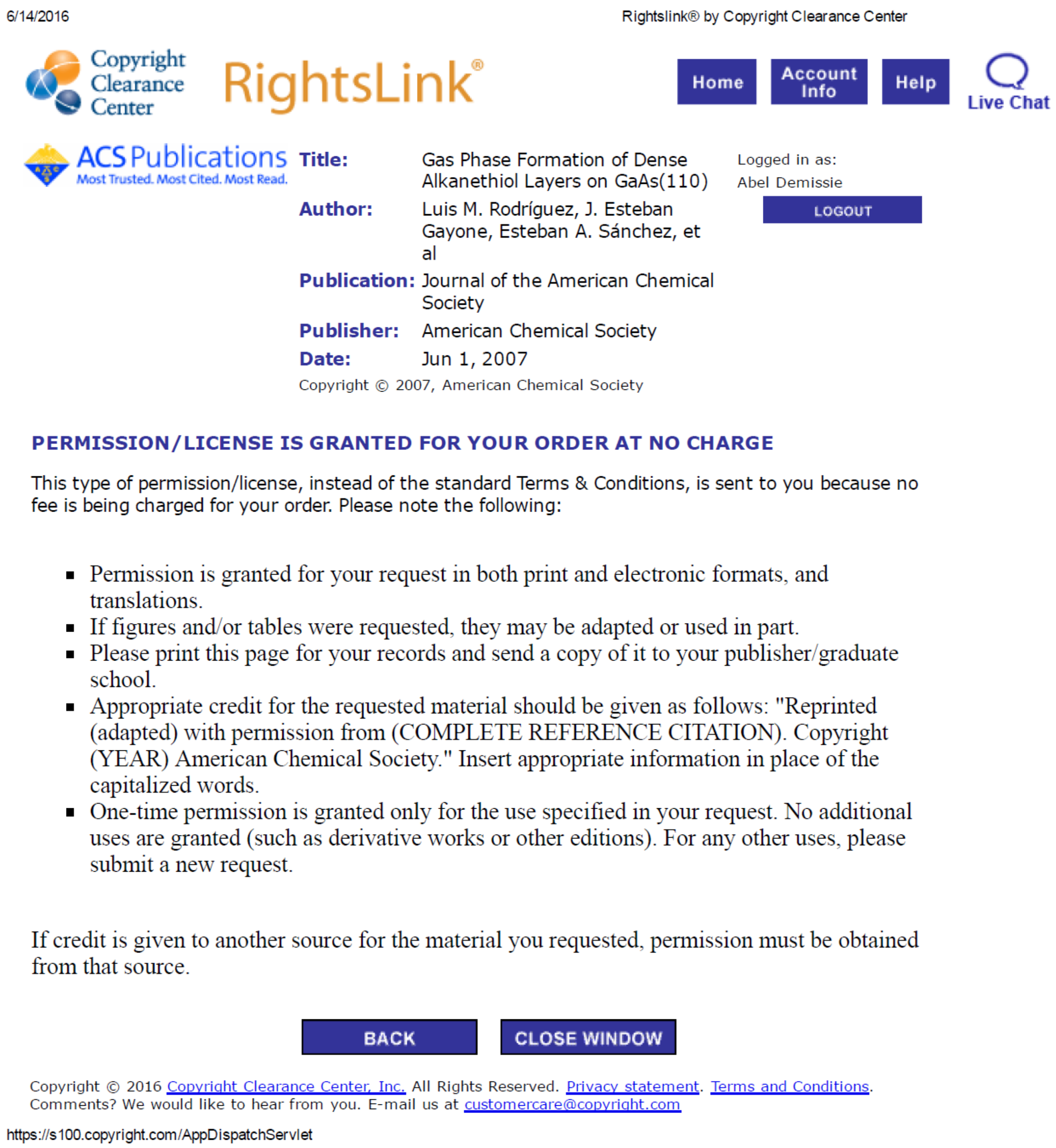

6/14/2016 Rightslink® by Copyright Clearance Center

Title:	Gas Phase Formation of Dense Alkanethiol Layers on GaAs(110)
Author:	Luis M. Rodríguez, J. Esteban Gayone, Esteban A. Sánchez, et al
Publication:	Journal of the American Chemical Society
Publisher:	American Chemical Society
Date:	Jun 1, 2007

Logged in as:
Abel Demissie

PERMISSION/LICENSE IS GRANTED FOR YOUR ORDER AT NO CHARGE

This type of permission/license, instead of the standard Terms & Conditions, is sent to you because no fee is being charged for your order. Please note the following:

- Permission is granted for your request in both print and electronic formats, and translations.
- If figures and/or tables were requested, they may be adapted or used in part.
- Please print this page for your records and send a copy of it to your publisher/graduate school.
- Appropriate credit for the requested material should be given as follows: "Reprinted (adapted) with permission from (COMPLETE REFERENCE CITATION). Copyright (YEAR) American Chemical Society." Insert appropriate information in place of the capitalized words.
- One-time permission is granted only for the use specified in your request. No additional uses are granted (such as derivative works or other editions). For any other uses, please submit a new request.

If credit is given to another source for the material you requested, permission must be obtained from that source.

https://s100.copyright.com/AppDispatchServlet

Copyright Clearance Center RightsLink®

Home | Account Info | Help | Live Chat

Title:	Conductance of a Molecular Junction
Author:	M. A. Reed,C. Zhou,C. J. Muller,T. P. Burgin,J. M. Tour
Publication:	Science
Publisher:	The American Association for the Advancement of Science
Date:	Oct 10, 1997

Logged in as:
Abel Demissie
Account #:
3001037225
LOGOUT

Order Completed

Thank you for your order.

This Agreement between Abel T Demissie ("You") and The American Association for the Advancement of Science ("The American Association for the Advancement of Science") consists of your license details and the terms and conditions provided by The American Association for the Advancement of Science and Copyright Clearance Center.

Your confirmation email will contain your order number for future reference.

Get the printable license.

License Number	3946680822111
License date	Sep 12, 2016
Licensed Content Publisher	The American Association for the Advancement of Science
Licensed Content Publication	Science
Licensed Content Title	Conductance of a Molecular Junction
Licensed Content Author	M. A. Reed,C. Zhou,C. J. Muller,T. P. Burgin,J. M. Tour
Licensed Content Date	Oct 10, 1997
Licensed Content Volume	278
Licensed Content Issue	5336
Volume number	278
Issue number	5336
Type of Use	Thesis / Dissertation
Requestor type	Scientist/individual at a research institution
Format	Print and electronic
Portion	Figure
Number of figures/tables	1
Order reference number	
Title of your thesis / dissertation	Surface and Electrical Characterization of Conjugated Molecular Wires
Expected completion date	Sep 2016
Estimated size(pages)	230
Requestor Location	Abel T Demissie 421 Washinton Ave SE MINNEAPOLIS, MN 55455 United States Attn: Abel T Demissie
Billing Type	Invoice
Billing address	

Copyright Clearance Center RightsLink®

Home | Account Info | Help | Live Chat

ACS Publications
Most Trusted. Most Cited. Most Read.

Title: Defining the Value of Injection Current and Effective Electrical Contact Area for EGaIn-Based Molecular Tunneling Junctions

Author: Felice C. Simeone, Hyo Jae Yoon, Martin M. Thuo, et al

Publication: Journal of the American Chemical Society

Publisher: American Chemical Society

Date: Dec 1, 2013

Copyright © 2013, American Chemical Society

Logged in as:
Abel Demissie
Account #:
3001037225

LOGOUT

PERMISSION/LICENSE IS GRANTED FOR YOUR ORDER AT NO CHARGE

This type of permission/license, instead of the standard Terms & Conditions, is sent to you because no fee is being charged for your order. Please note the following:

- Permission is granted for your request in both print and electronic formats, and translations.
- If figures and/or tables were requested, they may be adapted or used in part.
- Please print this page for your records and send a copy of it to your publisher/graduate school.
- Appropriate credit for the requested material should be given as follows: "Reprinted (adapted) with permission from (COMPLETE REFERENCE CITATION). Copyright (YEAR) American Chemical Society." Insert appropriate information in place of the capitalized words.
- One-time permission is granted only for the use specified in your request. No additional uses are granted (such as derivative works or other editions). For any other uses, please submit a new request.

If credit is given to another source for the material you requested, permission must be obtained from that source.

BACK | CLOSE WINDOW

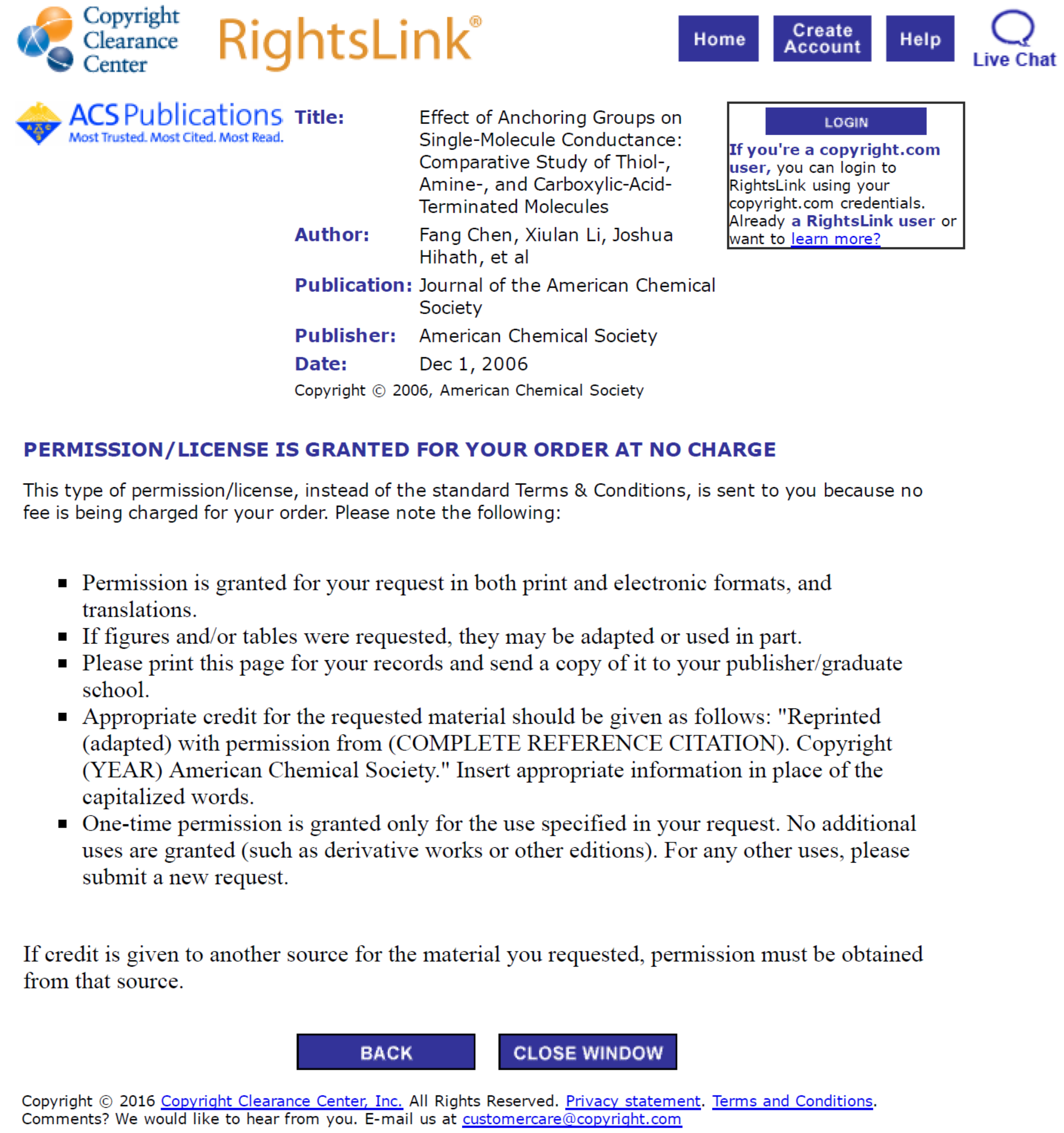

Title: Effect of Anchoring Groups on Single-Molecule Conductance: Comparative Study of Thiol-, Amine-, and Carboxylic-Acid-Terminated Molecules

Author: Fang Chen, Xiulan Li, Joshua Hihath, et al

Publication: Journal of the American Chemical Society

Publisher: American Chemical Society

Date: Dec 1, 2006

Copyright © 2006, American Chemical Society

If you're a copyright.com user, you can login to RightsLink using your copyright.com credentials. Already **a RightsLink user** or want to learn more?

PERMISSION/LICENSE IS GRANTED FOR YOUR ORDER AT NO CHARGE

This type of permission/license, instead of the standard Terms & Conditions, is sent to you because no fee is being charged for your order. Please note the following:

- Permission is granted for your request in both print and electronic formats, and translations.
- If figures and/or tables were requested, they may be adapted or used in part.
- Please print this page for your records and send a copy of it to your publisher/graduate school.
- Appropriate credit for the requested material should be given as follows: "Reprinted (adapted) with permission from (COMPLETE REFERENCE CITATION). Copyright (YEAR) American Chemical Society." Insert appropriate information in place of the capitalized words.
- One-time permission is granted only for the use specified in your request. No additional uses are granted (such as derivative works or other editions). For any other uses, please submit a new request.

If credit is given to another source for the material you requested, permission must be obtained from that source.

ROYAL SOCIETY OF CHEMISTRY LICENSE
TERMS AND CONDITIONS

Jun 14, 2016

This Agreement between Abel T Demissie ("You") and Royal Society of Chemistry ("Royal Society of Chemistry") consists of your license details and the terms and conditions provided by Royal Society of Chemistry and Copyright Clearance Center.

License Number	3887740758967
License date	Jun 14, 2016
Licensed Content Publisher	Royal Society of Chemistry
Licensed Content Publication	Chemical Society Reviews
Licensed Content Title	Self-assembled monolayers of thiols and dithiols on gold: new challenges for a well-known system
Licensed Content Author	C. Vericat,M. E. Vela,G. Benitez,P. Carro,R. C. Salvarezza
Licensed Content Date	Feb 24, 2010
Licensed Content Volume Number	39
Licensed Content Issue Number	5
Type of Use	Thesis/Dissertation
Requestor type	academic/educational
Portion	figures/tables/images
Number of figures/tables/images	2
Format	electronic
Distribution quantity	1
Will you be translating?	no
Order reference number	
Title of the thesis/dissertation	Surface and Electrical Characterization of Conjugated Molecular Wires
Expected completion date	Jun 2016
Estimated size	200

Requestor Location	Abel T Demissie 421 Washinton Ave SE MINNEAPOLIS, MN 55455 United States Attn: Abel T Demissie
Billing Type	Invoice
Billing Address	Abel T Demissie 421 Washinton Ave SE MINNEAPOLIS, MN 55455 United States Attn: Abel T Demissie
Total	0.00 USD

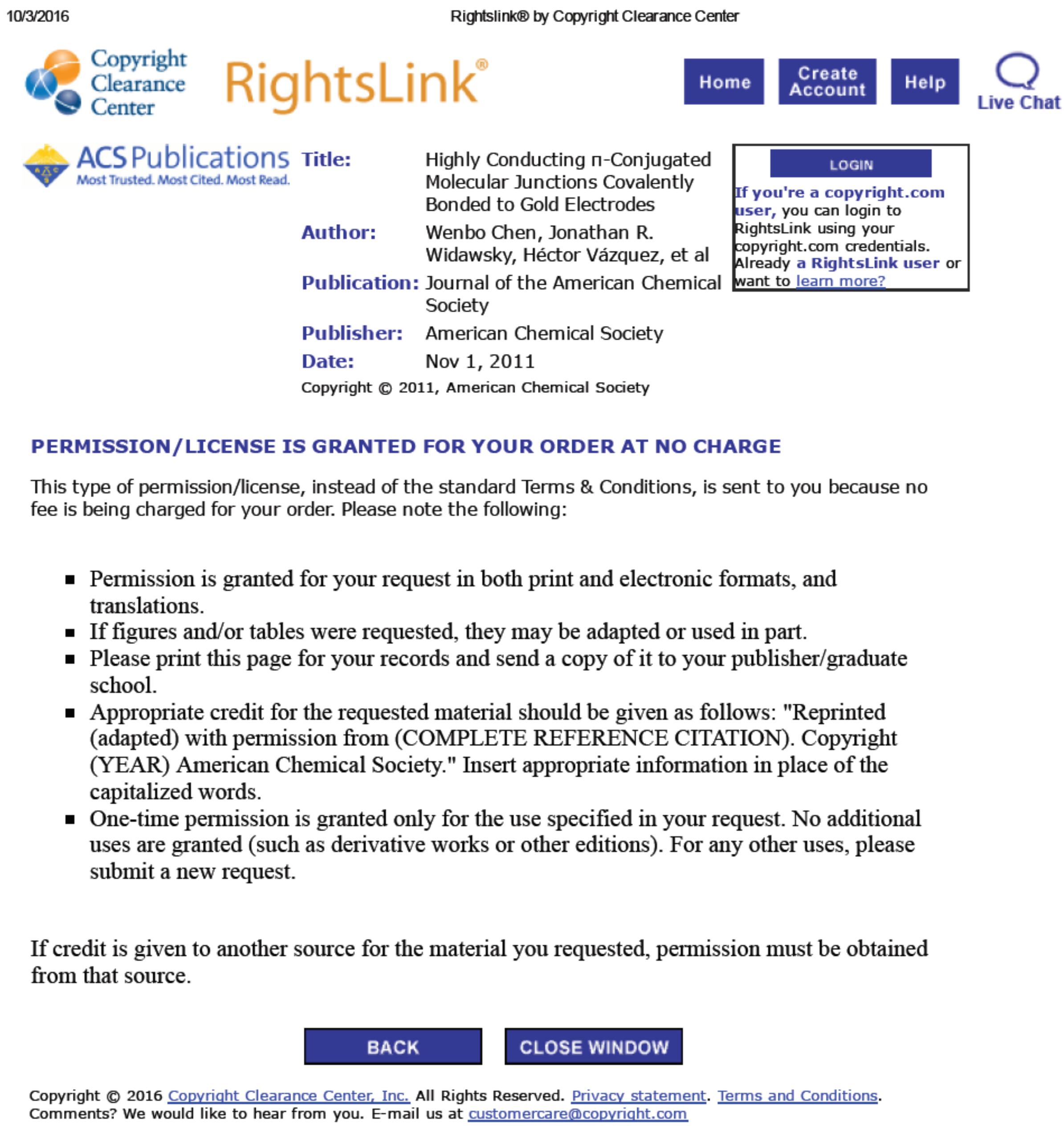

10/3/2016 Rightslink® by Copyright Clearance Center

Title:	Highly Conducting π-Conjugated Molecular Junctions Covalently Bonded to Gold Electrodes
Author:	Wenbo Chen, Jonathan R. Widawsky, Héctor Vázquez, et al
Publication:	Journal of the American Chemical Society
Publisher:	American Chemical Society
Date:	Nov 1, 2011

If you're a copyright.com user, you can login to RightsLink using your copyright.com credentials. Already **a RightsLink user** or want to learn more?

PERMISSION/LICENSE IS GRANTED FOR YOUR ORDER AT NO CHARGE

This type of permission/license, instead of the standard Terms & Conditions, is sent to you because no fee is being charged for your order. Please note the following:

- Permission is granted for your request in both print and electronic formats, and translations.
- If figures and/or tables were requested, they may be adapted or used in part.
- Please print this page for your records and send a copy of it to your publisher/graduate school.
- Appropriate credit for the requested material should be given as follows: "Reprinted (adapted) with permission from (COMPLETE REFERENCE CITATION). Copyright (YEAR) American Chemical Society." Insert appropriate information in place of the capitalized words.
- One-time permission is granted only for the use specified in your request. No additional uses are granted (such as derivative works or other editions). For any other uses, please submit a new request.

If credit is given to another source for the material you requested, permission must be obtained from that source.

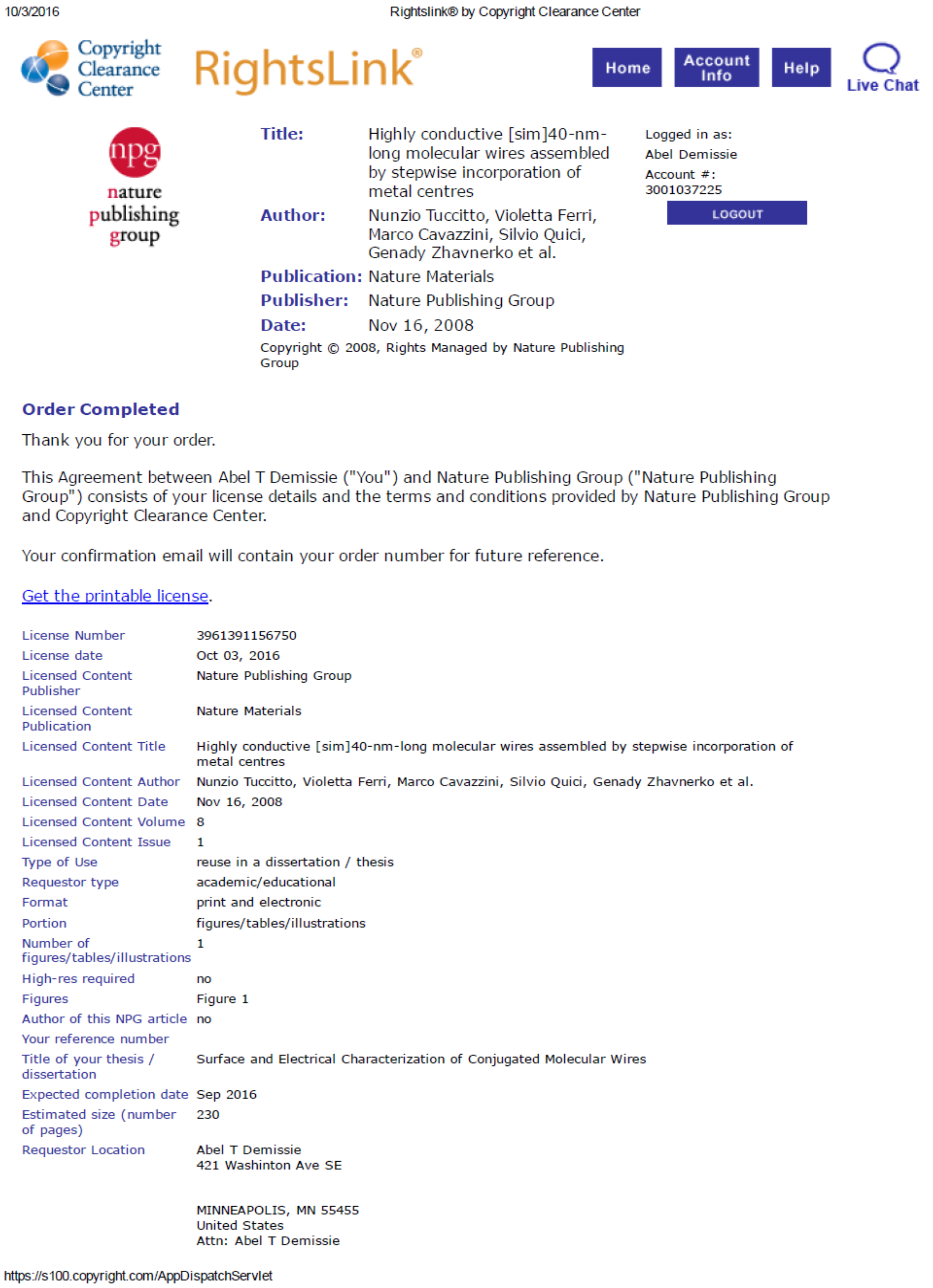

10/3/2016 Rightslink® by Copyright Clearance Center

Copyright Clearance Center RightsLink®

nature publishing group

Title: Highly conductive [sim]40-nm-long molecular wires assembled by stepwise incorporation of metal centres

Author: Nunzio Tuccitto, Violetta Ferri, Marco Cavazzini, Silvio Quici, Genady Zhavnerko et al.

Publication: Nature Materials

Publisher: Nature Publishing Group

Date: Nov 16, 2008

Copyright © 2008, Rights Managed by Nature Publishing Group

Logged in as:
Abel Demissie
Account #:
3001037225

Order Completed

Thank you for your order.

This Agreement between Abel T Demissie ("You") and Nature Publishing Group ("Nature Publishing Group") consists of your license details and the terms and conditions provided by Nature Publishing Group and Copyright Clearance Center.

Your confirmation email will contain your order number for future reference.

Get the printable license.

License Number	3961391156750
License date	Oct 03, 2016
Licensed Content Publisher	Nature Publishing Group
Licensed Content Publication	Nature Materials
Licensed Content Title	Highly conductive [sim]40-nm-long molecular wires assembled by stepwise incorporation of metal centres
Licensed Content Author	Nunzio Tuccitto, Violetta Ferri, Marco Cavazzini, Silvio Quici, Genady Zhavnerko et al.
Licensed Content Date	Nov 16, 2008
Licensed Content Volume	8
Licensed Content Issue	1
Type of Use	reuse in a dissertation / thesis
Requestor type	academic/educational
Format	print and electronic
Portion	figures/tables/illustrations
Number of figures/tables/illustrations	1
High-res required	no
Figures	Figure 1
Author of this NPG article	no
Your reference number	
Title of your thesis / dissertation	Surface and Electrical Characterization of Conjugated Molecular Wires
Expected completion date	Sep 2016
Estimated size (number of pages)	230
Requestor Location	Abel T Demissie 421 Washinton Ave SE MINNEAPOLIS, MN 55455 United States Attn: Abel T Demissie

https://s100.copyright.com/AppDispatchServlet

Bibliography

- *Charge and Exciton Transport through Molecular Wires*; Siebbeles, L. D. ., Grozeman, F. C., Eds.; John Wiley & Sons, 2011.

- Arrhenius, T. S.; Blanchard-Desce, M.; Dvolaitzky, M.; Lehn, J.-M.; Malthete, J. Molecular Devices: Caroviologens as an Approach to Molecular Wires--Synthesis and Incorporation into Vesicle Membranes. *Proc. Natl. Acad. Sci.* **1986**, *83* (15), 5355–5359.

- Nitzan, A.; Ratner, M. a. Electron Transport in Molecular Wire Junctions. *Science* **2003**, *300* (5624), 1384–1389.

- Davis, W. B.; Svec, W. A.; Ratner, M. A.; Wasielewski, M. R. Molecular-Wire Behaviour in P -Phenylenevinylene Oligomers. **1998**, *396* (6706), 60–63.

- Scheer, E. *Molecular Electronics: An Introduction to Theory and Experiment*; World Scientific, 2010.

- Aviram, A.; Ratner, M. A. Molecular Rectifiers. *Chem. Phys. Lett.* **1974**, *29* (2), 277–283.

- Cheng, H.; Shen, H.; Yang, F.; Tang, J. Cross Sections for Non-Rutherford Backscattering of 4He from Five Light Elements. *Nucl. Instruments Methods Phys. Res. Sect. B Beam Interact. with Mater. Atoms* **1994**, *85* (1-4), 47–50.

- Altmann, J. *Military Nanotechnology: Potential Applications and Preventive Arms Control*; Routledge, 2007.

- Natarajan, S.; Agostinelli, M.; Akbar, S.; Bost, M.; Bowonder, A.; Chikarmane, V.; Chouksey, S.; Dasgupta, A.; Fischer, K.; Fu, Q.; et al. A 14nm Logic Technology Featuring 2^{nd}-Generation FinFET, Air-Gapped Interconnects, Self-Aligned Double Patterning and a 0.0588 μm^2 SRAM Cell Size. In *2014 IEEE International Electron Devices Meeting*; IEEE, 2014; pp 3.7.1–3.7.3.

- Chen, W.; Widawsky, J. R.; Vázquez, H.; Schneebeli, S. T.; Hybertsen, M. S.; Breslow, R.; Venkataraman, L. Highly Conducting π-Conjugated Molecular Junctions Covalently Bonded to Gold Electrodes. *J. Am. Chem. Soc.* **2011**, *133* (43), 17160–17163.

- Perrin, M. L.; Frisenda, R.; Koole, M.; Seldenthuis, J. S.; Gil, J. A. C.; Valkenier, H.; Hummelen, J. C.; Renaud, N.; Grozema, F. C.; Thijssen, J. M.; et al. Large Negative Differential Conductance in Single-Molecule Break Junctions. *Nat. Nanotechnol.* **2014**, *9* (10), 830–834.

- Hines, T.; Diez-Perez, I.; Hihath, J.; Liu, H.; Wang, Z. S.; Zhao, J.; Zhou, G.; Müllen, K.; Tao, N. Transition from Tunneling to Hopping in Single Molecular Junctions by Measuring Length and Temperature Dependence. *J. Am. Chem. Soc.* **2010**, *132* (33), 11658–11664.

- Wold, D. J.; Frisbie, C. D. Fabrication and Characterization of Metal-Molecule-Metal Junctions by Conducting Probe Atomic Force Microscopy. *J. Am. Chem. Soc.* **2001**, *123*, 5549–5556.

- Lauhon, L. J.; Ho, W. Direct Observation of the Quantum Tunneling of Single Hydrogen Atoms with a Scanning Tunneling Microscope. *Phys. Rev. Lett.* **2000**, *85* (21), 4566–4569.

- Nijhuis, C. A.; Reus, W. F.; Whitesides, G. M. Molecular Rectification in Metal-SAM-Metal Oxide-Metal Junctions. *J. Am. Chem. Soc.* **2009**, *131*, 17814–17827.

- Nijhuis, C. A.; Reus, W. F.; Barber, J. R.; Whitesides, G. M. Comparison of SAM-Based Junctions with Ga 2 O 3 /EGaIn Top Electrodes to Other Large-Area Tunneling Junctions. *J. Phys. Chem. C* **2012**, *116* (26), 14139–14150.

- Chiechi, R. C.; Weiss, E. A.; Dickey, M. D.; Whitesides, G. M. Eutectic Gallium-Indium (EGaIn): A Moldable Liquid Metal for Electrical Characterization of Self-Assembled Monolayers. *Angew. Chem. Int. Ed. Engl.* **2008**, *47* (1), 142–144.

- Yaffe, O.; Ely, T.; Har-Lavan, R.; Egger, D. A.; Johnston, S.; Cohen, H.; Kronik, L.; Vilan, A.; Cahen, D. Effect of Molecule-Surface Reaction Mechanism on the Electronic Characteristics and Photovoltaic Performance of Molecularly Modified Si. *J. Phys. Chem. C. Nanomater. Interfaces* **2013**, *117* (43), 22351–22361.

- Tran, E.; Rampi, M. A.; Whitesides, G. M. Electron Transfer in a Hg-SAM//SAM-Hg Junction Mediated by Redox Centers. *Angew. Chem. Int. Ed. Engl.* **2004**, *43* (29), 3835–3839.

- Akkerman, H. B.; Blom, P. W. M.; de Leeuw, D. M.; de Boer, B. Towards Molecular Electronics with Large-Area Molecular Junctions. *Nature* **2006**, *441* (7089), 69–72.

- Neuhausen, A. B.; Hosseini, A.; Sulpizio, J. A.; Chidsey, C. E. D.; Goldhaber-Gordon, D. Molecular Junctions of Self-Assembled Monolayers with Conducting Polymer Contacts. *ACS Nano* **2012**, *6* (11), 9920–9931.

- Bonifas, A. P.; McCreery, R. L. “Soft” Au, Pt and Cu Contacts for Molecular Junctions through Surface-Diffusion-Mediated Deposition. *Nat. Nanotechnol.* **2010**, *5* (8), 612–617.

- Park, J.; Pasupathy, A. N.; Goldsmith, J. I.; Chang, C.; Yaish, Y.; Petta, J. R.; Rinkoski, M.; Sethna, J. P.; Abruña, H. D.; McEuen, P. L.; et al. Coulomb Blockade and the Kondo Effect in Single-Atom Transistors. *Nature* **2002**, *417* (6890), 722–725.

- Kubatkin, S.; Danilov, A.; Hjort, M.; Cornil, J.; Brédas, J.-L.; Stuhr-Hansen, N.; Hedegård, P.; Bjørnholm, T. Single-Electron Transistor of a Single Organic Molecule with Access to Several Redox States. *Nature* **2003**, *425* (6959), 698–701.

- Liao, J.; Agustsson, J. S.; Wu, S.; Schönenberger, C.; Calame, M.; Leroux, Y.; Mayor, M.; Jeannin, O.; Ran, Y.-F.; Liu, S.-X.; et al. Cyclic Conductance Switching in Networks of Redox-Active Molecular Junctions. *Nano Lett.* **2010**, *10* (3), 759–764.

- Rawlett, A. M.; Hopson, T. J.; Nagahara, L. A.; Tsui, R. K.; Ramachandran, G. K.; Lindsay, S. M. Electrical Measurements of a Dithiolated Electronic Molecule via Conducting Atomic Force Microscopy. *Appl. Phys. Lett.* **2002**, *81* (16), 3043.

- Yuan, L.; Nerngchamnong, N.; Cao, L.; Hamoudi, H.; del Barco, E.; Roemer, M.; Sriramula, R. K.; Thompson, D.; Nijhuis, C. A. Controlling the Direction of Rectification in a Molecular Diode. *Nat. Commun.* **2015**, *6*, 6324.

- Akkerman, H. B.; de Boer, B. Electrical Conduction through Single Molecules and Self-Assembled Monolayers. *J. Phys. Condens. Matter* **2008**, *20* (1), 013001.

- Rosink, J. J. W. M.; Blauw, M. A.; Geerligs, L. J.; van der Drift, E.; Rousseeuw, B. A. C.; Radelaar, S.; Sloof, W. G.; Fakkeldij, E. J. M. Self-Assembly of π-Conjugated Azomethine Oligomers by Sequential Deposition of Monomers from Solution. *Langmuir* **2000**, *16* (10), 4547–4553.

- Choi, S. H.; Kim, B.; Frisbie, C. D. Electrical Resistance of Long Conjugated Molecular Wires. *Science* **2008**, *320* (5882), 1482–1486.

- Luo, L.; Choi, S. H.; Frisbie, C. D. Probing Hopping Conduction in Conjugated Molecular Wires Connected to Metal Electrodes †. *Chem. Mater.* **2011**, *23* (3), 631–645.

- Choi, S. H.; Frisbie, C. D. Enhanced Hopping Conductivity in Low Band Gap Donor-Acceptor Molecular Wires up to 20 Nm in Length. *J. Am. Chem. Soc.* **2010**, *132*, 16191–16201.

- Choi, S. H.; Risko, C.; Delgado, M. C. R.; Kim, B.; Brédas, J.-L.; Frisbie, C. D. Transition from Tunneling to Hopping Transport in Long, Conjugated Oligo-Imine Wires Connected to Metals. *J. Am. Chem. Soc.* **2010**, *132* (12), 4358–4368.

- Luo, L.; Balhorn, L.; Vlaisavljevich, B.; Ma, D.; Gagliardi, L.; Frisbie, C. D. Hopping Transport and Rectifying Behavior in Long Donor–Acceptor Molecular Wires. *J. Phys. Chem. C* **2014**, *118* (46), 26485–26497.

- *Charge and Exciton Transport through Molecular Wires*; John Wiley & Sons, 2011.

- Eng, M. P.; Albinsson, B. Non-Exponential Distance Dependence of Bridge-Mediated Electronic Coupling. *Angew. Chem. Int. Ed. Engl.* **2006**, *45* (34), 5626–5629.

- Segawa, H.; Takehara, C.; Honda, K.; Shimidzu, T.; Asahi, T.; Mataga, N. Photoinduced Electron-Transfer Reactions of Porphyrin Heteroaggregates: Energy Gap Dependence of an Intradimer Charge Recombination Process. *J. Phys. Chem.* **1992**, *96* (2), 503–506.

- Segal, D.; Nitzan, A.; Davis, W. B.; Wasielewski, M. R.; Ratner, M. A. Electron Transfer Rates in Bridged Molecular Systems 2. A Steady-State Analysis of Coherent Tunneling and Thermal Transitions †. *J. Phys. Chem. B* **2000**, *104* (16), 3817–3829.

- Vericat, C.; Vela, M. E.; Corthey, G.; Pensa, E.; Cortés, E.; Fonticelli, M. H.; Ibañez, F.; Benitez, G. E.; Carro, P.; Salvarezza, R. C. Self-Assembled Monolayers of Thiolates on Metals: A Review Article on Sulfur-Metal Chemistry and Surface Structures. *RSC Adv.* **2014**, *4* (53), 27730.

- Blodgett, K. B. Monomolecular Films of Fatty Acids on Glass. *J. Am. Chem. Soc.* **1934**, *56* (2), 495–495.

- Blodgett, K. B. Films Built by Depositing Successive Monomolecular Layers on a Solid Surface. *J. Am. Chem. Soc.* **1935**, *57* (6), 1007–1022.

- Langmuir, I.; Schaefer, V. J. Composition of Fatty Acid Films on Water Containing Calcium or Barium Salts. *J. Am. Chem. Soc.* **1936**, *58* (2), 284–287.

- Cai, L.; Yao, Y.; Yang, J.; Price, D. W.; Tour, J. M. Chemical and Potential-Assisted Assembly of Thiolacetyl-Terminated Oligo(phenylene Ethynylene)s on Gold Surfaces. *Chem. Mater.* **2002**, *14* (7), 2905–2909.

- Küller, a.; El-Desawy, M. a.; Stadler, V.; Geyer, W.; Eck, W.; Gölzhäuser, a. Electron-Beam Lithography with Aromatic Self-Assembled Monolayers on Silicon Surfaces. *J. Vac. Sci. Technol. B Microelectron. Nanom. Struct.* **2004**, *22* (3), 1114.

- Zharnikov, M.; Küller, A.; Shaporenko, A.; Schmidt, E.; Eck, W. Aromatic Self-Assembled Monolayers on Hydrogenated Silicon. *Langmuir* **2003**, *19* (11), 4682–4687.

- Allara, D. L.; Nuzzo, R. G. Spontaneously Organized Molecular Assemblies. 2. Quantitative Infrared Spectroscopic Determination of Equilibrium Structures of Solution-Adsorbed N-Alkanoic Acids on an Oxidized Aluminum Surface. *Langmuir* **1985**, *1* (1), 52–66.

- Himmel, H.-J.; Kaschke, M.; Harder, P.; Wöll, C. Adsorption of Organic Monolayers on Pyrite (FeS2)(100). *Thin Solid Films* **1996**, *284-285*, 275–280.

- Frey, S.; Shaporenko, A.; Zharnikov, M.; Harder, P.; Allara, D. L. Self-Assembled Monolayers of Nitrile-Functionalized Alkanethiols on Gold and Silver Substrates. *J. Phys. Chem. B* **2003**, *107* (31), 7716–7725.

- Willicut, R. J.; McCarley, R. L. Surface-Confined Monomers on Electrode Surfaces. 1. Electrochemical and Microscopic Characterization of .omega.-(N-Pyrrolyl)alkanethiol Self-Assembled Monolayers on Au. *Langmuir* **1995**, *11* (1), 296–301.

- Han, S. W.; Lee, S. J.; Kim, K. Self-Assembled Monolayers of Aromatic Thiol and Selenol on Silver: Comparative Study of Adsorptivity and Stability. *Langmuir* **2001**, *17* (22), 6981–6987.

- Fadeev, A. Y.; Helmy, R.; Marcinko, S. Self-Assembled Monolayers of Organosilicon Hydrides Supported on Titanium, Zirconium, and Hafnium Dioxides. *Langmuir* **2002**, *18* (20), 7521–7529.

- Wollman, E. W.; Kang, D.; Frisbie, C. D.; Lorkovic, I. M.; Wrighton, M. S. Photosensitive Self-Assembled Monolayers on Gold: Photochemistry of Surface-Confined Aryl Azide and. *Society* **1994**, No. 8, 4395–4404.

- Love, J. C.; Estroff, L. A.; Kriebel, J. K.; Nuzzo, R. G.; Whitesides, G. M. Self-Assembled Monolayers of Thiolates on Metals as a Form of Nanotechnology. *Chem. Rev.* **2005**, *105* (4), 1103–1169.

- Beebe, J. M.; Engelkes, V. B.; Miller, L. L.; Frisbie, C. D. Contact Resistance in Metal-Molecule-Metal Junctions Based on Aliphatic SAMs: Effects of Surface Linker and Metal Work Function. *J. Am. Chem. Soc.* **2002**, *124*, 11268–11269.

- Nuzzo, R. G.; Allara, D. L. Adsorption of Bifunctional Organic Disulfides on Gold Surfaces. *J. Am. Chem. Soc.* **1983**, *105* (13), 4481–4483.

- Vericat, C.; Vela, M. E.; Benitez, G.; Carro, P.; Salvarezza, R. C. Self-Assembled Monolayers of Thiols and Dithiols on Gold: New Challenges for a Well-Known System. *Chem. Soc. Rev.* **2010**, *39* (5), 1805–1834.

- Rodríguez, L. M.; Gayone, J. E.; Sánchez, E. A.; Grizzi, O.; Blum, B.; Salvarezza, R. C.; Xi, L.; Lau, W. M. Gas Phase Formation of Dense Alkanethiol Layers on GaAs(110). *J. Am. Chem. Soc.* **2007**, *129* (25), 7807–7813.

- Caldwell, W. B.; Campbell, D. J.; Chen, K.; Herr, B. R.; Mirkin, C. A.; Malik, A.; Durbin, M. K.; Dutta, P.; Huang, K. G. A Highly Ordered Self-Assembled Monolayer Film of an Azobenzenealkanethiol on Au(111): Electrochemical Properties and Structural Characterization by Synchrotron in-Plane X-Ray Diffraction, Atomic Force Microscopy, and Surface-Enhanced Raman Spectroscopy. *J. Am. Chem. Soc.* **1995**, *117* (22), 6071–6082.

- Torrelles, X.; Barrena, E.; Munuera, C.; Rius, J.; Ferrer, S.; Ocal, C. New Insights in the c(4 X 2) Reconstruction of Hexadecanethiol on Au(111) Revealed by Grazing Incidence X-Ray Diffraction. *Langmuir* **2004**, *20* (21), 9396–9402.

- Walter, M.; Akola, J.; Lopez-Acevedo, O.; Jadzinsky, P. D.; Calero, G.; Ackerson, C. J.; Whetten, R. L.; Grönbeck, H.; Häkkinen, H. A Unified View of Ligand-Protected Gold Clusters as Superatom Complexes. *Proc. Natl. Acad. Sci. U. S. A.* **2008**, *105* (27), 9157–9162.

- Fuxen, C.; Azzam, W.; Arnold, R.; Witte, G.; Terfort, A.; Wöll, C. Structural Characterization of Organothiolate Adlayers on Gold: The Case of Rigid, Aromatic Backbones. *Langmuir* **2001**, *17* (12), 3689–3695.

- Kim, Y. T.; McCarley, R. L.; Bard, A. J. Scanning Tunneling Microscopy Studies of gold(111) Derivatized with Organothiols. *J. Phys. Chem.* **1992**, *96* (18), 7416–7421.

- Sabatani, E.; Cohen-Boulakia, J.; Bruening, M.; Rubinstein, I. Thioaromatic Monolayers on Gold: A New Family of Self-Assembling Monolayers. *Langmuir* **1993**, *9* (11), 2974–2981.

- Demissie, A. T.; Haugstad, G.; Frisbie, C. D. Growth of Thin, Anisotropic, π-Conjugated Molecular Films by Stepwise "Click" Assembly of Molecular Building Blocks: Characterizing Reaction Yield, Surface Coverage, and Film Thickness versus Addition Step Number. *J. Am. Chem. Soc.* **2015**, *137* (27), 8819–8828.

- Luo, L.; Frisbie, C. D. Length-Dependent Conductance of Conjugated Molecular Wires Synthesized by Stepwise "Click" Chemistry. *J. Am. Chem. Soc.* **2010**, *132* (26), 8854–8855.

- Ellipsometry http://america.pink/ellipsometry_1415432.html (accessed Apr 4, 2016).

- Ulman, A.; Eilers, J. E.; Tillman, N. Packing and Molecular Orientation of Alkanethiol Monolayers on Gold Surfaces. *Langmuir* **1989**, *5* (5).

- Smart, R.; McIntyre, S.; Bancroft, M.; Bello, I. X-ray Photoelectron Spectroscopy - Powerpoint slides http://mmrc.caltech.edu/SS_XPS/XPS_PPT/XPS_Slides.pdf (accessed Jan 20, 2004).

- Powell, C. J.; Jablonski, a. Progress in Quantitative Surface Analysis by X-Ray Photoelectron Spectroscopy: Current Status and Perspectives. *J. Electron Spectros. Relat. Phenomena* **2010**, *178-179*, 331–346.

- Powell, C. J.; Werner, W. S. M.; Smekal, W. Effects of Elastic Scattering and Analyzer-Acceptance Angle on the Analysis of Angle-Resolved X-Ray Photoelectron Spectroscopy Data. *Surf. Interface Anal.* **2011**, *43* (7), 1046–1056.

- Luo, L.; Choi, S. H.; Frisbie, C. D. Probing Hopping Conduction in Conjugated Molecular Wires Connected to Metal Electrodes. *Chem. Mater.* **2011**, *23*, 631–645.

- Chu, W.-K.; Mayer, J. W.; Nicolet, M. *Backscattering Spectrometry*; Academic Press, INC: New York, 1978.

- Haugstad, G. Ion Beam Analysis - Powerpoint Slides. Characterization Facility - University of Minnesota 2011, p 51.

- Chidsey, C. E. D.; Bertozzi, C. R.; Putvinski, T. M.; Mujsce, A. M. Coadsorption of Ferrocene-Terminated and Unsubstituted Alkanethiols on Gold: Electroactive Self-Assembled Monolayers. *J. Am. Chem. Soc.* **1990**, *112* (11), 4301–4306.

- Hines, T.; Díez-Pérez, I.; Nakamura, H.; Shimazaki, T.; Asai, Y.; Tao, N. Controlling Formation of Single-Molecule Junctions by Electrochemical Reduction of Diazonium Terminal Groups. *J. Am. Chem. Soc.* **2013**, *135* (9), 3319–3322.

- Cademartiri, L.; Thuo, M. M.; Nijhuis, C. A.; Reus, W. F.; Tricard, S.; Barber, J. R.; Sodhi, R. N. S.; Brodersen, P.; Kim, C.; Chiechi, R. C.; et al. Electrical Resistance of Ag TS –S(CH 2) N −1 CH 3 //Ga 2 O 3 /EGaIn Tunneling Junctions. *J. Phys. Chem. C* **2012**, *116* (20), 10848–10860.

- Yuan, L.; Jiang, L.; Zhang, B.; Nijhuis, C. A. Dependency of the Tunneling Decay Coefficient in Molecular Tunneling Junctions on the Topography of the Bottom Electrodes. *Angew. Chemie - Int. Ed.* **2014**, *53*, 3377–3381.

- (Sayed, S. Y.; Bayat, A.; Kondratenko, M.; Leroux, Y.; Hapiot, P.; McCreery, R. L. Bilayer Molecular Electronics: All-Carbon Electronic Junctions Containing Molecular Bilayers Made with “Click” Chemistry. *J. Am. Chem. Soc.* **2013**, *135* (35), 12972–12975.

- Alloway, D. M.; Graham, A. L.; Yang, X.; Mudalige, A.; Colorado, R.; Wysocki, V. H.; Pemberton, J. E.; Randall Lee, T.; Wysocki, R. J.; Armstrong, N. R. Tuning the Effective Work Function of Gold and Silver Using ω-Functionalized Alkanethiols: Varying Surface Composition through Dilution and Choice of Terminal Groups. *J. Phys. Chem. C* **2009**, *113* (47), 20328–20334.

- Reuter, M. G.; Solomon, G. C.; Hansen, T.; Seideman, T.; Ratner, M. A. Understanding and Controlling Crosstalk between Parallel Molecular Wires. *J. Phys. Chem. Lett.* **2011**, *2*, 1667–1671.

- Bâldea, I.; Xie, Z.; Frisbie, C. D. Uncovering a Law of Corresponding States for Electron Tunneling in Molecular Junctions. *Nanoscale* **2015**, *7* (23), 10465–10471.

- Taherinia, D.; Smith, C. E.; Ghosh, S.; Odoh, S. O.; Balhorn, L.; Gagliardi, L.; Cramer, C. J.; Frisbie, C. D. Charge Transport in 4 Nm Molecular Wires with Interrupted Conjugation: Combined Experimental and Computational Evidence for Thermally-Assisted Polaron Tunneling. *ACS Nano* **2016**.

- Smith, C. E.; Odoh, S. O.; Ghosh, S.; Gagliardi, L.; Cramer, C. J.; Frisbie, C. D. Length-Dependent Nanotransport and Charge Hopping Bottlenecks in Long Thiophene-Containing π-Conjugated Molecular Wires. *J. Am. Chem. Soc.* **2015**, *137* (50), 15732–15741.

- Sirringhaus, H. 25th Anniversary Article: Organic Field-Effect Transistors: The Path beyond Amorphous Silicon. *Adv. Mater.* **2014**, *26* (9), 1319–1335.

- Dou, L.; You, J.; Hong, Z.; Xu, Z.; Li, G.; Street, R. A.; Yang, Y. 25th Anniversary Article: A Decade of Organic/polymeric Photovoltaic Research. *Adv. Mater.* **2013**, *25* (46), 6642–6671.

- Samsung Galaxy S7 display, possibilities for future http://www.igalaxys7.com/samsung-galaxy-s7-display/ (accessed Apr 1, 2016).

- Nakasa, A.; Akiba, U.; Fujihira, M. Self-Assembled Monolayers Containing Biphenyl Derivatives as Challenge for Nc-AFM. *Appl. Surf. Sci.* **2000**, *157* (4), 326–331.

- Chen, F.; Li, X.; Hihath, J.; Huang, Z.; Tao, N. Effect of Anchoring Groups on Single-Molecule Conductance: Comparative Study of Thiol-, Amine-, and Carboxylic-Acid-Terminated Molecules. *J. Am. Chem. Soc.* **2006**, *128* (49), 15874–15881.

- Reed, M. a. Conductance of a Molecular Junction. *Science (80-.).* **1997**, *278* (5336), 252–254.

- Kim, B.; Choi, S. H.; Zhu, X.-Y.; Frisbie, C. D. Molecular Tunnel Junctions Based on π-Conjugated Oligoacene Thiols and Dithiols between Ag, Au, and Pt Contacts: Effect of Surface Linking Group and Metal Work Function. *J. Am. Chem. Soc.* **2011**, *133* (49), 19864–19877.

- Luo, L.; Benameur, A.; Brignou, P.; Choi, S. H.; Rigaut, S.; Frisbie, C. D. Length and Temperature Dependent Conduction of Ruthenium-Containing Redox-Active Molecular Wires. *J. Phys. Chem. C* **2011**, *115* (40), 19955–19961.

- Xie, Z.; Bâldea, I.; Smith, C. E.; Wu, Y.; Frisbie, C. D. Experimental and Theoretical Analysis of Nanotransport in Oligophenylene Dithiol Junctions as a Function of Molecular Length and Contact Work Function. *ACS Nano* **2015**, *9* (8), 8022–8036.

- Engelkes, V. B.; Beebe, J. M.; Frisbie, C. D. Analysis of the Causes of Variance in Resistance Measurements on Metal-Molecule-Metal Junctions Formed by Conducting-Probe Atomic Force Microscopy. *J. Phys. Chem. B* **2005**, *109* (35), 16801–16810.

- Cai, L. T.; Skulason, H.; Kushmerick, J. G.; Pollack, S. K.; Naciri, J.; Shashidhar, R.; Allara, D. L.; Mallouk, T. E.; Mayer, T. S. Nanowire-Based Molecular Monolayer Junctions: Synthesis, Assembly, and Electrical Characterization. *J. Phys. Chem. B* **2004**, *108* (9), 2827–2832.

- Engelkes, V. B.; Beebe, J. M.; Frisbie, C. D. Length-Dependent Transport in Molecular Junctions Based on SAMs of Alkanethiols and Alkanedithiols: Effect of Metal Work Function and Applied Bias on Tunneling Efficiency and Contact Resistance. *J. Am. Chem. Soc.* **2004**, *126*, 14287–14296.

- Wan, A.; Jiang, L.; Sangeeth, C. S. S.; Nijhuis, C. A. Reversible Soft Top-Contacts to Yield Molecular Junctions with Precise and Reproducible Electrical Characteristics. *Adv. Funct. Mater.* **2014**, *24* (28), 4442–4456.

- Sangeeth, C. S.; Wan, A.; Nijhuis, C. A. Probing the Nature and Resistance of the Molecule–electrode Contact in SAM-Based Junctions. *Nanoscale* **2015**, *7* (28), 12061–12067.

- Bonifas, A. P.; McCreery, R. L. Assembling Molecular Electronic Junctions One Molecule at a Time. *Nano Lett.* **2011**, *11* (11), 4725–4729.

- Bergren, A. J.; Harris, K. D.; Deng, F.; McCreery, R. L. Molecular Electronics Using Diazonium-Derived Adlayers on Carbon with Cu Top Contacts: Critical Analysis of Metal Oxides and Filaments. *J. Phys. Condens. Matter* **2008**, *20* (37), 374117.

- Kim, T.; Vázquez, H.; Hybertsen, M. S.; Venkataraman, L. Conductance of Molecular Junctions Formed with Silver Electrodes. *Nano Lett.* **2013**, *13* (7), 3358–3364.

- Sangeeth, C. S. S.; Wan, A.; Nijhuis, C. a. Equivalent Circuits of a Self-Assembled Monolayer-Based Tunnel Junction Determined by Impedance Spectroscopy. *J. Am. Chem. Soc.* **2014**, *136* (31), 11134–11144.

- Simeone, F. C.; Yoon, H. J.; Thuo, M. M.; Barber, J. R.; Smith, B.; Whitesides, G. M. Defining the Value of Injection Current and Effective Electrical Contact Area for EGaIn-Based Molecular Tunneling Junctions. *J. Am. Chem. Soc.* **2013**, *135* (48), 18131–18144.

- Lin, W.; Lin, W.; Wong, G. K.; Marks, T. J. Supramolecular Approaches to Second-Order Nonlinear Optical Materials. Self-Assembly and Microstructural Characterization of Intrinsically Acentric [(Aminophenyl)azo]pyridinium Superlattices. *J. Am. Chem. Soc.* **1996**, *118* (34), 8034–8042.

- Yoon, M.-H.; Facchetti, A.; Marks, T. J. Sigma-Pi Molecular Dielectric Multilayers for Low-Voltage Organic Thin-Film Transistors. *Proc. Natl. Acad. Sci. U. S. A.* **2005**, *102* (13), 4678–4682.

- DiBenedetto, S. A.; Facchetti, A.; Ratner, M. A.; Marks, T. J. Molecular Self-Assembled Monolayers and Multilayers for Organic and Unconventional Inorganic Thin-Film Transistor Applications. *Adv. Mater.* **2009**, *21* (14-15), 1407–1433.

- Tuccitto, N.; Ferri, V.; Cavazzini, M.; Quici, S.; Zhavnerko, G.; Licciardello, A.; Rampi, M. A. Highly Conductive Approximately 40-Nm-Long Molecular Wires Assembled by Stepwise Incorporation of Metal Centres. *Nat. Mater.* **2009**, *8* (1), 41–46.

- Luo, L.; Frisbie, C. D. Length-Dependent Conductance of Conjugated Molecular Wires Synthesized by Stepwise “Click” Chemistry. *J. Am. Chem. Soc.* **2010**, *132*, 8854–8855.

- Cabarcos, O. M.; Shaporenko, A.; Weidner, T.; Uppili, S.; Dake, L. S.; Zharnikov, M.; Allara, D. L. Physical and Electronic Structure Effects of Embedded Dipoles in Self-Assembled Monolayers: Characterization of Mid-Chain Ester Functionalized Alkanethiols on Au{111}. *J. Phys. Chem. C* **2008**, *112* (29), 10842–10854.

- Lavi, A.; Cohen, H.; Bendikov, T.; Vilan, A.; Cahen, D. Si-C-Bound Alkyl Chains on Oxide-Free Si: Towards Versatile Solution Preparation of Electronic Transport Quality Monolayers. *Phys. Chem. Chem. Phys.* **2011**, *13* (4), 1293–1296.

- Lewis, P. A.; Inman, C. E.; Maya, F.; Tour, J. M.; Hutchison, J. E.; Weiss, P. S. Molecular Engineering of the Polarity and Interactions of Molecular Electronic Switches. *J. Am. Chem. Soc.* **2005**, *127* (49), 17421–17426.

- Aradhya, S. V; Venkataraman, L. Single-Molecule Junctions beyond Electronic Transport. *Nat. Nanotechnol.* **2013**, *8*, 399–410.

- Hihath, J.; Tao, N. The Role of Molecule–electrode Contact in Single-Molecule Electronics. *Semicond. Sci. Technol.* **2014**, *29* (5), 054007.

- Heimel, G.; Zojer, E.; Romaner, L.; Brédas, J.-L.; Stellacci, F. Doping Molecular Wires. *Nano Lett.* **2009**, *9* (7), 2559–2564.

- Bergfield, J. P.; Ratner, M. A. Forty Years of Molecular Electronics: Non-Equilibrium Heat and Charge Transport at the Nanoscale. *Phys. status solidi* **2013**, *250* (11), n/a – n/a.

- Alloway, D. M.; Hofmann, M.; Smith, D. L.; Gruhn, N. E.; Graham, A. L.; Colorado, R.; Wysocki, V. H.; Lee, T. R.; Lee, P. A.; Armstrong, N. R. Interface Dipoles Arising from Self-Assembled Monolayers on Gold: UV−Photoemission Studies of Alkanethiols and Partially Fluorinated Alkanethiols. *J. Phys. Chem. B* **2003**, *107* (42), 11690–11699.

- Golchoubian, H.; Hosseinpoor, F. Effective Oxidation of Sulfides to Sulfoxides with Hydrogen Peroxide under Transition-Metal-Free Conditions. *Molecules* **2007**, *12* (3), 304–311.

- Norman Young, R.; Yves Gauthier, J.; Coombs, W. The Methyl Group as a Protectinq Group for Arylthiols: A Mild and Efficient Method for the Conversion of Methyl Aryl Sulfides to Arylthiols. *Tetrahedron Lett.* **1984**, *25* (17), 1753–1756.

- Feng, Y.; Zhou, Z.; Zhou, Y.; Zhao, G. Cross Sections for 165° Backscattering of 2.0–9.0 MeV 4He from Carbon. *Nucl. Instruments Methods Phys. Res. Sect. B Beam Interact. with Mater. Atoms* **1994**, *86* (3-4), 225–230.

- Lin-Vien, D.; Colthup, N. B.; Fateley, W. G.; Grasselli, J. G. *The Handbook of Infrared and Raman Characteristic Frequencies of Organic Molecules*; Elsevier, 1991.

- Ledbetter, J. W. Infrared Spectra of N-Aryl Imines of O-Hydroxybenzaldehyde between 2000 and 1500 Cm-1. *J. Phys. Chem.* **1977**, *81* (1), 54–59.

- Smalley, J. F.; Sachs, S. B.; Chidsey, C. E. D.; Dudek, S. P.; Sikes, H. D.; Creager, S. E.; Yu, C. J.; Feldberg, S. W.; Newton, M. D. Interfacial Electron-Transfer Kinetics of Ferrocene through Oligophenyleneethynylene Bridges Attached to Gold Electrodes as Constituents of Self-Assembled Monolayers: Observation of a Nonmonotonic Distance Dependence. *J. Am. Chem. Soc.* **2004**, *126* (44), 14620–14630.

- Sikes, H. D.; Smalley, J. F.; Dudek, S. P.; Cook, A. R.; Newton, M. D.; Chidsey, C. E.; Feldberg, S. W. Rapid Electron Tunneling through Oligophenylenevinylene Bridges. *Science* **2001**, *291* (5508), 1519–1523.

- Valincius, G.; Niaura, G.; Kazakeviciene, B.; Talaikyte, Z.; Kazemekaite, M.; Butkus, E.; Razumas, V. Anion Effect on Mediated Electron Transfer through Ferrocene-Terminated Self-Assembled Monolayers. *Langmuir* **2004**, *20* (16), 6631–6638.

- Walczak, M. M.; Popenoe, D. D.; Deinhammer, R. S.; Lamp, B. D.; Chung, C.; Porter, M. D. Reductive Desorption of Alkanethiolate Monolayers at Gold: A Measure of Surface Coverage. *Langmuir* **1991**, *7* (11), 2687–2693.

- Colvin, V. L.; Goldstein, A. N.; Alivisatos, A. P. Semiconductor Nanocrystals Covalently Bound to Metal Surfaces with Self-Assembled Monolayers. *J. Am. Chem. Soc.* **1992**, *114* (13), 5221–5230.

- Wohlfart, P.; Weiβ, J.; Käshammer, J.; Winter, C.; Scheumann, V.; Fischer, R. A.; Mittler-Neher, S. Selective Ultrathin Gold Deposition by Organometallic Chemical Vapor Deposition onto Organic Self-Assembled Monolayers (SAMs). *Thin Solid Films* **1999**, *340* (1-2), 274–279.

- Beebe, J. M.; Engelkes, V. B.; Liu, J.; Gooding, J. J.; Eggers, P. K.; Jun, Y.; Zhu, X.; Paddon-Row, M. N.; Frisbie, C. D. Length Dependence of Charge Transport in Nanoscopic Molecular Junctions Incorporating a Series of Rigid Thiol-Terminated Norbornylogs. *J. Phys. Chem. B* **2005**, *109*, 5207–5215.

- *Surface and Thin Film Analysis: A Compendium of Principles, Instrumentation and Applications*; Bubert, H., Jenett, H., Eds.; John Wiley & Sons: Dortmund, 2002.

- Scofield, J. H. Hartree-Slater Subshell Photoionization Cross-Sections at 1254 and 1487 eV. *J. Electron Spectros. Relat. Phenomena* **1976**, *8* (2), 129–137.

- Berry, G. M.; Bravo, B. G.; Bothwell, M. E.; Cali, G. J.; Harris, J. E.; Mebrahtu, T.; Michelhaugh, S. L.; Rodriguez, J. F.; Soriaga, M. P. Spectroscopic and Electrochemical Studies of Iodine Coordinated to Noble-Metal Electrode Surfaces. *Langmuir* **1989**, *5* (3), 707–713.

- Reilman, R. F.; Msezane, A.; Manson, S. T. Relative Intensities in Photoelectron Spectroscopy of Atoms and Molecules. *J. Electron Spectros. Relat. Phenomena* **1976**, *8* (5), 389–394.

- Seah, M. P.; Gilmore, I. S. Quantitative AES. VIII: Analysis of Auger Electron Intensities from Elemental Data in a Digital Auger Database. *Surf. Interface Anal.* **1998**, *26* (12), 908–929.

- Yarzhemsky, V. G.; Nefedov, V. I.; Trzhaskovskaya, M. B.; Band, I. M.; Szargan, R. The Influence of Core Hole Relaxation on the Main-Line Intensities in X-Ray Photoelectron Spectra. *J. Electron Spectros. Relat. Phenomena* **2002**, *123* (1), 1–10.

- Bain, C. D.; Troughton, E. B.; Tao, Y. T.; Evall, J.; Whitesides, G. M.; Nuzzo, R. G. Formation of Monolayer Films by the Spontaneous Assembly of Organic Thiols from Solution onto Gold. *J. Am. Chem. Soc.* **1989**, *111* (1), 321–335.

- Tour, J. M.; Jones, L.; Pearson, D. L.; Lamba, J. J. S.; Burgin, T. P.; Whitesides, G. M.; Allara, D. L.; Parikh, A. N.; Atre, S. Self-Assembled Monolayers and Multilayers of Conjugated Thiols, .alpha.,.omega.-Dithiols, and Thioacetyl-Containing Adsorbates. Understanding Attachments between Potential Molecular Wires and Gold Surfaces. *J. Am. Chem. Soc.* **1995**, *117* (37), 9529–9534.

- Abu-Husein, T.; Schuster, S.; Egger, D. A.; Kind, M.; Santowski, T.; Wiesner, A.; Chiechi, R.; Zojer, E.; Terfort, A.; Zharnikov, M. The Effects of Embedded Dipoles in Aromatic Self-Assembled Monolayers. *Adv. Funct. Mater.* **2015**, *25* (25), 3943–3957.

- Ulman, A. Formation and Structure of Self-Assembled Monolayers. *Chem. Rev.* **1996**, *96* (4), 1533–1554.

- Schlenoff, J. B.; Li, M.; Ly, H. Stability and Self-Exchange in Alkanethiol Monolayers. *J. Am. Chem. Soc.* **1995**, *117* (50), 12528–12536.

- Camillone, N.; Chidsey, C. E. D.; Eisenberger, P.; Fenter, P.; Li, J.; Liang, K. S.; Liu, G.-Y.; Scoles, G. Structural Defects in Self-Assembled Organic Monolayers via Combined Atomic Beam and X-Ray Diffraction. *J. Chem. Phys.* **1993**, *99* (1), 744.

- Park, J.-S.; Vo, A. N.; Barriet, D.; Shon, Y.-S.; Lee, T. R. Systematic Control of the Packing Density of Self-Assembled Monolayers Using Bidentate and Tridentate Chelating Alkanethiols. *Langmuir* **2005**, *21* (7), 2902–2911.

- Lee, S.; Shon, Y.-S.; Colorado, R.; Guenard, R. L.; Lee, T. R.; Perry, S. S. The Influence of Packing Densities and Surface Order on the Frictional Properties of Alkanethiol Self-Assembled Monolayers (SAMs) on Gold: A Comparison of SAMs Derived from Normal and Spiroalkanedithiols. *Langmuir* **2000**, *16* (5), 2220–2224.

- Rittikulsittichai, S.; Jamison, A. C.; Lee, T. R. Self-Assembled Monolayers Derived from Alkoxyphenylethanethiols Having One, Two, and Three Pendant Chains. *Langmuir* **2011**, *27* (16), 9920–9927.

- Gardner, T. J.; Frisbie, C. D.; Wrighton, M. S. Systems for Orthogonal Self-Assembly of Electroactive Monolayers on Au and ITO: An Approach to Molecular Electronics. *J. Am. Chem. Soc.* **1995**, *117* (26), 6927–6933.

- Creager, S.; Yu, C. J.; Bamdad, C.; O'Connor, S.; MacLean, T.; Lam, E.; Chong, Y.; Olsen, G. T.; Luo, J.; Gozin, M.; et al. Electron Transfer at Electrodes through Conjugated "Molecular Wire" Bridges. *J. Am. Chem. Soc.* **1999**, *121* (5), 1059–1064.

- Leavitt, J. A.; McIntyre, L. C.; Ashbaugh, M. D.; Oder, J. G.; Lin, Z.; Dezfouly-Arjomandy, B. Cross Sections for 170.5° Backscattering of 4He from Oxygen for 4He Energies between 1.8 and 5.0 MeV. *Nucl. Instruments Methods Phys. Res. Sect. B Beam Interact. with Mater. Atoms* **1990**, *44* (3), 260–265.

- Leung. Ph.D. Thesis, University of Kentucky, 1972.

- Perrin, M. L.; Verzijl, C. J. O.; Martin, C. A.; Shaikh, A. J.; Eelkema, R.; van Esch, J. H.; van Ruitenbeek, J. M.; Thijssen, J. M.; van der Zant, H. S. J.; Dulić, D. Large Tunable Image-Charge Effects in Single-Molecule Junctions. *Nat. Nanotechnol.* **2013**, *8* (4), 282–287.

- Wang, L.; Rangger, G. M.; Romaner, L.; Heimel, G.; BucÌŒko, T.; Ma, Z.; Li, Q.; Shuai, Z.; Zojer, E. Electronic Structure of Self-Assembled Monolayers on Au(111) Surfaces: The Impact of Backbone Polarizability. *Adv. Funct. Mater.* **2009**, *19* (23), 3766–3775.

- Heimel, G.; Brédas, J.-L. Molecular Electronics: Reflections on Charge Transport. *Nat. Nanotechnol.* **2013**, *8* (4), 230–231.

- Capozzi, B.; Xia, J.; Adak, O.; Dell, E. J.; Liu, Z.-F.; Taylor, J. C.; Neaton, J. B.; Campos, L. M.; Venkataraman, L. Single-Molecule Diodes with High Rectification Ratios through Environmental Control. *Nat. Nanotechnol.* **2015**, *10* (6), 522–527.

- Heimel, G.; Rissner, F.; Zojer, E. Modeling the Electronic Properties of Pi-Conjugated Self-Assembled Monolayers. *Adv. Mater.* **2010**, *22* (23), 2494–2513.

- Egger, D. A.; Rissner, F.; Zojer, E.; Heimel, G. Polarity Switching of Charge Transport and Thermoelectricity in Self-Assembled Monolayer Devices. *Adv. Mater.* **2012**, *24* (32), 4403–4407.

- Toledano, T.; Sazan, H.; Mukhopadhyay, S.; Alon, H.; Lerman, K.; Bendikov, T.; Major, D. T.; Sukenik, C. N.; Vilan, A.; Cahen, D. Odd-Even Effect in Molecular Electronic Transport via an Aromatic Ring. *Langmuir* **2014**, *30* (45), 13596–13605.

- Fereiro, J. A.; Kondratenko, M.; Bergren, A. J.; McCreery, R. L. Internal Photoemission in Molecular Junctions: Parameters for Interfacial Barrier Determinations. *J. Am. Chem. Soc.* **2015**, *137* (3), 1296–1304.

- Motiei, L.; Lahav, M.; Gulino, A.; Iron, M. A.; van der Boom, M. E. Electrochemical Characteristics of a Self-Propagating Molecular-Based Assembly. *J. Phys. Chem. B* **2010**, *114* (45), 14283–14286.

- Sakamoto, R.; Wu, K.-H.; Matsuoka, R.; Maeda, H.; Nishihara, H. π-Conjugated Bis(terpyridine)metal Complex Molecular Wires. *Chem. Soc. Rev.* **2015**, *44* (21), 7698–7714.

- Wold, D. J.; Frisbie, C. D. Formation of Metal−Molecule−Metal Tunnel Junctions: Microcontacts to Alkanethiol Monolayers with a Conducting AFM Tip. *J. Am. Chem. Soc.* **2000**, *122* (12), 2970–2971.

- Salomon, A.; Cahen, D.; Lindsay, S.; Tomfohr, J.; Engelkes, V. B.; Frisbie, C. D. Comparison of Electronic Transport Measurements on Organic Molecules. *Adv. Mater.* **2003**, *15* (22), 1881–1890.

- McCreery, R. L.; Bergren, A. J. Progress with Molecular Electronic Junctions: Meeting Experimental Challenges in Design and Fabrication. *Adv. Mater.* **2009**, *21* (43), 4303–4322.

- (Milani, F.; Grave, C.; Ferri, V.; Samorì, P.; Rampi, M. A. Ultrathin Pi-Conjugated Polymer Films for Simple Fabrication of Large-Area Molecular Junctions. *Chemphyschem* **2007**, *8* (4), 515–518.

- Wold, D. J.; Frisbie, C. D. Fabrication and Characterization of Metal−Molecule−Metal Junctions by Conducting Probe Atomic Force Microscopy. *J. Am. Chem. Soc.* **2001**, *123* (23), 5549–5556.

- Heitzer, H. M.; Marks, T. J.; Ratner, M. A. Maximizing the Dielectric Response of Molecular Thin Films via Quantum Chemical Design. *ACS Nano* **2014**, *8* (12), 12587–12600.

- Yu, X.; Wilhelmi, O.; Moser, H. O.; Vidyaraj, S. V.; Gao, X.; Wee, A. T. S.; Nyunt, T.; Qian, H.; Zheng, H. New Soft X-Ray Facility SINS for Surface and Nanoscale Science at SSLS. *J. Electron Spectros. Relat. Phenomena* **2005**, *144-147*, 1031–1034.

- Stöhr, J. *NEXAFS Spectroscopy*; Springer Science & Business Media, 1992.

- Yuan, L.; Jiang, L.; Zhang, B.; Nijhuis, C. A. Dependency of the Tunneling Decay Coefficient in Molecular Tunneling Junctions on the Topography of the Bottom Electrodes. *Angew. Chem. Int. Ed. Engl.* **2014**, *53* (13), 3377–3381.

- Jiang, L.; Sangeeth, C. S. S.; Wan, A.; Vilan, A.; Nijhuis, C. A. Defect Scaling with Contact Area in EGaIn-Based Junctions: Impact on Quality, Joule Heating, and Apparent Injection Current. *J. Phys. Chem. C* **2015**, *119* (2), 960–969.

- Goldsmith, R. H.; Sinks, L. E.; Kelley, R. F.; Betzen, L. J.; Liu, W.; Weiss, E. A.; Ratner, M. A.; Wasielewski, M. R. Wire-like Charge Transport at near Constant Bridge Energy through Fluorene Oligomers. *Proc. Natl. Acad. Sci. U. S. A.* **2005**, *102* (10), 3540–3545.

- Marcus, R. A. On the Theory of Electron-Transfer Reactions. VI. Unified Treatment for Homogeneous and Electrode Reactions. *J. Chem. Phys.* **1965**, *43* (2), 679.

- Wang, D.; Fracasso, D.; Nurbawono, A.; Annadata, H. V; Sangeeth, C. S. S.; Yuan, L.; Nijhuis, C. A. Tuning the Tunneling Rate and Dielectric Response of SAM-Based Junctions via a Single Polarizable Atom. *Adv. Mater.* **2015**, n/a – n/a.

- *Impedance Spectroscopy: Theory, Experiment, and Applications*; Barsoukvo, E., Macdonald, J. R., Eds.; John Wiley & Sons, 2005.

- Landau, A.; Kronik, L.; Nitzan, A. No Title. *J.Comput. Theor. Nanosci* **2008**, *5*, 534–544.

- Holm, R. *Electric Contacts: Theory and Application*; Springer Berlin Heidelberg, 1999; Vol. 1.

- Kim, B.; Beebe, J. M.; Jun, Y.; Zhu, X. Y.; Frisbie, G. D. Correlation between HOMO Alignment and Contact Resistance in Molecular Junctions: Aromatic Thiols versus Aromatic Isocyanides. *J. Am. Chem. Soc.* **2006**, *128*, 4970–4971.

- Huang, M.-J.; Hsu, L.-Y.; Fu, M.-D.; Chuang, S.-T.; Tien, F.-W.; Chen, C.-H. Conductance of Tailored Molecular Segments: A Rudimentary Assessment by Landauer Formulation. *J. Am. Chem. Soc.* **2014**, *136* (5), 1832–1841.

- Kim, T.; Liu, Z.-F.; Lee, C.; Neaton, J. B.; Venkataraman, L. Charge Transport and Rectification in Molecular Junctions Formed with Carbon-Based Electrodes. *Proc. Natl. Acad. Sci.* **2014**, *111* (30), 10928–10932.

- Castañeda Ocampo, O. E.; Gordiichuk, P.; Catarci, S.; Gautier, D. A.; Herrmann, A.; Chiechi, R. C. Mechanism of Orientation-Dependent Asymmetric Charge Transport in Tunneling Junctions Comprising Photosystem I. *J. Am. Chem. Soc.* **2015**, *137* (26), 8419–8427.

- Wang, L.; Chen, W.; Huang, C.; Chen, Z.-K.; Wee, A. T. S. Ultrafast Electron Transfer from Oligo(p-Phenylene-Ethynylene)thiol to Gold. *J. Phys. Chem. B* **2006**, *110* (2), 674–676.

- Cao, L.; Yang, M.; Yuan, L.; Nerngchamnong, N.; Feng, Y.-P.; Wee, A. T. S.; Qi, D.-C.; Nijhuis, C. A. Orbital Dependent Ultrafast Charge Transfer Dynamics of Ferrocenyl-Functionalized SAMs on Gold Studied by Core-Hole Clock Spectroscopy. *J. Phys. Condens. Matter* **2016**, *28* (9), 094006.

- Kao, P.; Neppl, S.; Feulner, P.; Allara, D. L.; Zharnikov, M. Charge Transfer Time in Alkanethiolate Self-Assembled Monolayers via Resonant Auger Electron Spectroscopy. *J. Phys. Chem. C* **2010**, *114* (32), 13766–13773.

- Vandenberg, E. T.; Bertilsson, L.; Liedberg, B.; Uvdal, K.; Erlandsson, R.; Elwing, H.; Lundström, I. Structure of 3-Aminopropyl Triethoxy Silane on Silicon Oxide. *J. Colloid Interface Sci.* **1991**, *147* (1), 103–118.

- Kumar, K. S.; Pasula, R. R.; Lim, S.; Nijhuis, C. A. Charge Transport: Long-Range Tunneling Processes across Ferritin-Based Junctions (Adv. Mater. 9/2016). *Adv. Mater.* **2016**, *28* (9), 1900–1900.

- Yan, H.; Bergren, A. J.; McCreery, R.; Della Rocca, M. L.; Martin, P.; Lafarge, P.; Lacroix, J. C. Activationless Charge Transport across 4.5 to 22 Nm in Molecular Electronic Junctions. *Proc. Natl. Acad. Sci. U. S. A.* **2013**, *110* (14), 5326–5330.

- Love, J. C.; Estroff, L. a.; Kriebel, J. K.; Nuzzo, R. G.; Whitesides, G. M. Self-Assembled Monolayers of Thiolates on Metals as a Form of Nanotechnology. *Chemical Reviews*. 2005, pp 1103–1169.

- Chen, W.; Widawsky, J. R.; Vázquez, H.; Schneebeli, S. T.; Hybertsen, M. S.; Breslow, R.; Venkataraman, L. Highly Conducting π-Conjugated Molecular Junctions Covalently Bonded to Gold Electrodes. *J. Am. Chem. Soc.* **2011**, *133* (43), 17160–17163.

- Zaba, T.; Noworolska, A.; Bowers, C. M.; Breiten, B.; Whitesides, G. M.; Cyganik, P. Formation of Highly Ordered Self-Assembled Monolayers of Alkynes on Au(111) Substrate. *J. Am. Chem. Soc.* **2014**, *136* (34), 11918–11921.

- Kim, B.; Beebe, J. M.; Olivier, C.; Rigaut, S.; Touchard, D.; Kushmerick, J. G.; Zhu, X. Y.; Frisbie, C. D. Temperature and Length Dependence of Charge Transport in Redox-Active Molecular Wires Incorporating ruthenium(II) Bis(σ-Arylacetylide) Complexes. *J. Phys. Chem. C* **2007**, *111*, 7521–7526.

- Haensch, C.; Chiper, M.; Ulbricht, C.; Winter, A.; Hoeppener, S.; Schubert, U. S. Reversible Supramolecular Functionalization of Surfaces: Terpyridine Ligands as Versatile Building Blocks for Noncovalent Architectures. *Langmuir* **2008**, *24* (22), 12981–12985.

- Thompson, B. C.; Fréchet, J. M. J. Polymer-Fullerene Composite Solar Cells. *Angew. Chem. Int. Ed. Engl.* **2008**, *47* (1), 58–77.

- Shirai, Y.; Cheng, L.; Chen, B.; Tour, J. M. Characterization of Self-Assembled Monolayers of Fullerene Derivatives on Gold Surfaces: Implications for Device Evaluations. *J. Am. Chem. Soc.* **2006**, *128* (41), 13479–13489.

- Hau, S. K.; Cheng, Y.-J.; Yip, H.-L.; Zhang, Y.; Ma, H.; Jen, A. K.-Y. Effect of Chemical Modification of Fullerene-Based Self-Assembled Monolayers on the Performance of Inverted Polymer Solar Cells. *ACS Appl. Mater. Interfaces* **2010**, *2* (7), 1892–1902.